COXSACKIEVIRUS B3 SUBVERSION OF THE AUTOPHAGY PATHWAY

by

Yasir Mohamud

B.Sc., University of Ottawa, 2012

M.Sc., University of Ottawa, 2015

A THESIS SUBMITTED IN PARTIAL FULFILLMENT OF THE REQUIREMENTS FOR THE DEGREE OF

DOCTOR OF PHILOSOPHY

in

THE FACULTY OF GRADUATE AND POSTDOCTORAL STUDIES

(Pathology and Laboratory Medicine)

THE UNIVERSITY OF BRITISH COLUMBIA

(Vancouver)

June 2021

The following individuals certify that they have read, and recommend to the Faculty of Graduate and Postdoctoral Studies for acceptance, the dissertation entitled:

Coxsackievirus B3 subversion of the autophagy pathway

submitted by Yasir Mohamud in partial fulfillment of the requirements for the degree of Doctor of Philosophy in Pathology and Laboratory Medicine

Examining Committee:

Dr. Honglin Luo, Professor, Pathology and Laboratory Medicine, UBC
Supervisor

Dr. Bruce McManus, Professor Emeritus, Pathology and Laboratory Medicine, UBC
Supervisory Committee Member

Dr. Calvin Yip, Associate Professor, Biochemistry and Molecular Biology, UBC
Supervisory Committee Member

Dr. Decheng Yang, Professor, Pathology and Laboratory Medicine, UBC
University Examiner

Dr. Robert Nabi, Professor, Cellular and Physiological Sciences, UBC
University Examiner

Additional Supervisory Committee Members:

Dr. Thibault Mayor, Professor, Biochemistry and Molecular Biology, UBC
Supervisory Committee Member

Dr. David Granville, Professor and Associate Dean Research, UBC
Supervisory Committee Member

Abstract

Coxsackievirus B3 (CVB3) is a positive single-strand RNA virus of the enterovirus genus that is implicated in diverse human pathologies from viral myocarditis to neurological disorders. CVB3 infection has been linked to the cellular activation of the host autophagy pathway but the underlying mechanisms remain unclear. The central hypothesis of the current dissertation is that that CVB3 usurps the host autophagy pathway to promote viral propagation. To address this hypothesis, I proposed to investigate how CVB3 disrupts important steps in the autophagy pathway including the initiation of autophagosome biogenesis, selective recruitment of cargo, fusion of autophagosomes with lysosomes, and overall lysosomal function. I have demonstrated that CVB3 infection disrupts multiple stages of the autophagy pathway to favor viral pathogenesis, including the initiation of autophagosome biogenesis, the selective recruitment of substrates, the fusion of autophagosomes with lysosomes, as well as lysosomal function. In particular, I uncovered that CVB3 targets autophagy initiation factors such as ULK1/2, through viral proteinase-mediated cleavage, to disrupt canonical autophagy signaling that is activated following physiological stimuli such as starvation. Instead, I showed that CVB3 utilizes viral proteins to initiate non-canonical autophagy that relies on PI4PKIIIβ kinase. In addition to disrupted autophagosome biogenesis, I reported that CVB3 also targets the selective autophagy process by cleaving autophagy adaptor proteins NDP52/CALCOCO2 through the activity of viral proteinase 3C, consistent with our previous reports on adaptor proteins SQSTM1/p62 and NBR1. Furthermore, I uncovered that CVB3 impairs the clearance function of autophagy by disrupting the autophagosome-lysosome fusion process, in part through the cleavage of fusion adaptor and tethering factors SNAP29 and PLEKHM1, respectively. Lastly, I identified that CVB3 targets the master regulator of lysosomal biology, TFEB, through viral proteinase 3C-mediated cleavage to disrupt lysosome function. Collectively, I identify viral proteinases as important pathogenic factors that not only facilitate viral maturation but also disrupt the cellular recycling machinery of autophagy at multiple stages. These findings are significant because they provide a strong foundation for targeting autophagy as a strategy to combat viral pathogenesis.

Lay Summary

Coxsackievirus B3 (CVB3) is a dangerous virus that can infect humans and lead to diseases of the pancreas, brain, and heart by replicating inside the cells of these tissues. Recent evidence shows that CVB3 disrupts autophagy inside cells to promote virus growth and cell death. Autophagy is a self-digestion process that takes place inside cells to recycle damaged cellular parts or invading pathogens. To counteract the efforts of the cell to defend itself from viral infection, CVB3 has evolved to disrupt autophagy at multiple stages including the initial construction of the autophagosome, the recruitment of cargo, and the late-stage fusion of autophagosome with a degradative chamber called the lysosome. This thesis outlines the molecular components of autophagy that are targeted by CVB3 to compromise this process in favor of viral pathogenesis. Given that many viruses use autophagy to promote disease, the current research provides insight into potential anti-viral therapy.

Preface

The contents of this dissertation are my original work and obtained during my doctoral training under the supervision of Dr. Honglin Luo, and the guidance of my supervisory committee members. The work presented herein is derived from one review article and four original research papers, all completed during the tenure of my graduate training at UBC. I am the primary author of these work and was responsible for >90% of the conception of projects, conduction of experiments, organization and analysis of data, composition of manuscripts, and presentation and dissemination of research findings. At the same time, I wish to acknowledge all co-authors who were instrumental in their contributions to the published work. all co-authors provided support in replicating experiments, revision efforts, and finalizing manuscripts. I wish to especially acknowledge the contributions of Dr. Junyan Shi and Dr. Gabriel Fung for providing training during the early phase of my PhD. Please see the detailed author contributions as published in the journals below.

Chapter 2: Conceptualization, Y.M. and H. Luo; Methodology, Y.M. and H. Luo; Investigation, Y.M., J.S., H.T., P.X., Y.C.X., H. Li, and C.S.N.; Formal analysis, Y.M. and H. Luo; Writing—original draft, Y.M. and H. Luo; Writing—reviewing and editing, Y.M. J.S., H.T., P.X., Y.C.X., H. Li, C.S.N. and H. Luo.

Chapter 3: Y.M. and H.Luo designed the research and wrote the manuscript. Y.M., J.Q., Y.C.X., H.L., and H.D. performed the experimental studies and analyzed the data.

Chapter 4: Y.M. and H.Luo designed the research and wrote the manuscript. T.P., J.S., and J.Z. conducted the animal experiments. Y.M., J.S., J.Q., Y.C.X., and H.D. performed the cell culture studies and analyzed the data.

Chapter 5: Conceptualization, Y.M. and H. Luo; Methodology, Y.M. and H. Luo; Investigation, Y.M., H.T., Y.C.X., H. Li, and C.S.N., and A.B; Formal analysis, Y.M. and H. Luo; Writing—original draft, Y.M. and H. Luo; Writing—reviewing and editing, Y.M. H.T., Y.C.X., H. Li, and C.S.N., A.B., and H. Luo.

Chapter 1 is an introduction that was composed from a published review article I co-wrote with Dr. Honglin Luo of which I am the first-author. This is an accepted manuscript of an article published by Taylor & Francis in Journal of Virulence on 03 Dec 2018, available online: https://doi.org/10.1080/21505594.2018.1551010 [**Mohamud Y**, Luo H. Intertwined lifecycles of enterovirus and autophagy. *Virulence.* 2019. 10(1):470-480].

Chapter 2 is based on primary research that was published in the journal *Scientific Reports.* [**Mohamud Y,** Shi J, Tang H, Xiang P, Xue YC, Liu H, Ng CS, Luo H. (2020). Coxsackievirus infection induces a non-canonical autophagy independent of the ULK1 and PI3K complexes. *Sci Rep.* 10, 19068]. Initial publication source: https://doi.org/10.1038/s41598-020-76227-7

Chapter 3 is based on primary research that was published in the journal *Cell Death and Differentiation* of which I am a first author [**Mohamud Y,** Qu J, Xue YC, Liu H, Deng H, Luo H. (2019). CALCOCO2/NDP52 and SQSTM1/p62 differentially regulate coxsackievirus B3 propagation. *Cell Death and Differentiation.* 26(6): 1062-10]. Initial publication source: https://doi.org/10.1038/s41418-018-0185-5. Special acknowledgement to Dr. Junyan Qu for her contributions as a second author of this manuscript.

Chapter 4 is based on primary research that was published in the journal *Cell Reports* [**Mohamud Y**, Shi J, Qu J, Poon T, Xue YC, Deng H, Zhang J, Luo H. (2018). Enteroviral Infection Inhibits Autophagic Flux via Disruption of the SNARE Complex to Enhance Viral Replication. *Cell Reports.* 22(12):3292-303]. Initial publication source: https://doi.org/10.1016/j.celrep.2018.02.090. Special acknowledgement to Dr. Junyan Shi, Tak Poon, and Jingchun Zhang for their contributions to animal studies presented in this chapter.

Chapter 5 is based on a primary research article currently in press of which I am the first-author. This is an accepted manuscript of an article published by Taylor & Francis in Journal of *Autophagy*, available online: 10.1080/15548627.2021.1896925 [**Mohamud Y,** Tang H, Xue YC, Liu H, Ng CS, Bahreyni A, Luo H. (2021). Coxsackievirus B3 targets TFEB to disrupt lysosomal function. *Autophagy.* 1-15, DOI: 10.1080/15548627.2021.1896925]. Special acknowledgment to Dr. Hui Tang for her contributions as a second author of this manuscript.

The reuse and reprint of all published work is with permission from the indicated journals. All viral and animal studies were approved by the University of British Columbia Research Ethics Board (certificate number A13-0321 and B14-0190).

Table of Contents

List of Figures

List of Abbreviations

2A: viral proteinase 2A

3C: viral proteinase 3C

3D: viral RNA-dependent RNA polymerase

ACTB: actin *beta* (also ß-actin)

AMBRA: autophagy and beclin 1 regulator 1

ATG: autophagy related

ATG2: autophagy related 2

ATG3: autophagy related 3 (E2-enzyme, ATG-conjugation system)

ATG5: autophagy related 5 (component of ATG-conjugation system)

ATG7: autophagy related 7 (E1-like enzyme, ATG-conjugation system)

ATG9: autophagy related 9 (transmembrane autophagy protein)

ATG12: autophagy related 12 (component of ATG-conjugation system)

ATG13: autophagy related 13 (component of ULK1/2 complex)

ATG14: autophagy related 14 (component of BECN1 complex)

ATG16L1: autophagy related 16L1 (component of ATG-conjugation system)

ATG5-12-16L1: autophagy related 5-12-16L1 complex (E3-like enzyme)

ATG101: autophagy related 101

BAF: bafilomycin A1

ß-actin: beta actin (also ACTB)

BECN1: beclin 1

CALCOCO2: calcium-binding and coil-coil domain-containing protein 2 (also NDP52)

CRISPR: clustered regularly interspaced short palindromic repeats

CVB3: coxsackievirus B3

DAPI: 4, 6-diamidino-2-phenylindole

DMEM: Dulbecco's modified Eagle’s medium

DMSO: dimethyl sulfoxide

DMV: double-membrane vesicle

DPBS: Dulbecco’s phosphate-buffered saline

ER: endoplasmic reticulum

EV-A71: enterovirus A71

EV-D68: enterovirus D68

FBS: fetal bovine serum

FIP200: FAK family kinase-interacting protein of 200 kDa

GFP: green fluorescent protein

gRNA: guide RNA

HA-tag: Human influenza hemagglutinin tag

HBSS: Hank’s balanced salt solution

HeLa: Human cervical cancer cell

HEK293: Human embryonic kidney 293

IFN1: interferon type 1

IFNß: interferon *beta*

IRES: internal ribosome entry site

K48: lysine (K) 48

K63: lysine (K) 63

LAP: LC3-associated phagocytosis

LAMP1: lysosome associated protein 1

LC3: microtubule-associated protein 1 light chain 3

LIR: LC3-interaction region

LTR: Lysotracker Red

MAVS: mitochondrial antiviral-signaling protein

MOI: multiplicity of infection

MOSLB: modified oncogene science lysis buffer

mTOR: mammalian target of rapamycin

mTORC1: mammalian target of rapamycin complex 1

NBR1: neighbor of BRCA1

NDP52: nuclear dot protein 52 (also CALCOCO2)

NSC-34: mouse motor neuron-like hybrid cell line

p62: ubiquitin-binding protein 62 (also SQSTM1)

PFU: plaque forming unit

PFU/mL: plaque forming unit per milliliter

PE: phosphatidylethanoleamine

PI: phosphoinositide

PI3KC3C: phosphatidylinositol 3-kinase catalytic subunit type 3

PI4KIIIb: phosphoinositide 4 kinase III beta

PIKfyve: phosphoinositide kinase, FYVE-type zinc finger containing

PLEKHM1: plekstrin homology domain-containing family M member 1

PV: poliovirus

PCR: polymerase chain reaction

Poly IC: polyinosilic:polycytidylic

PPP3: Protein phosphatase 3 / calcineurin

q-PCR: quantitative polymerase chain reaction

RB1CC1: RB1-inducible coiled-coil protein 1

RFP: red fluorescent protein

RNA: ribonucleic acid

RT-q-PCR: quantitative reverse transcription polymerase chain reaction

RUBCN: Rubicon autophagy regulator

siRNA: small interfering RNA (abbreviated as “si-”)

SDS-PAGE: sodium dodecyl sulfate- polyacrylamide gel electrophoresis

SD: standard deviation

SNAP29: synaptosome-associated protein 29

SQSTM1: sequestome 1

ssRNA: single stranded ribonucleic acid

STX17: syntaxin-17

TBK1: TANK-binding kinase 1

$TCID^{50}$: median tissue culture infectious dose

TFEB: Transcription Factor EB

UBA: ubiquitin-binding domain

ULK1/2: unc-51 like autophagy activating kinase

VAMP8: vesicle-associated membrane protein 8

VP1: viral capsid protein 1

VPS34: vacuolar protein sorting 34 (also PIK3C3)

WIPI2: WD repeat domain phosphoinositide-interacting protein 2

WT: wildtype

Z-VAD-FMK: Z-Valine-Alanine-Aspartate-fluoromethylketone

Acknowledgements

It is with great honour and privilege that I have this opportunity to acknowledge the wonderful individuals who have contributed to my training and education here at UBC. First and foremost, I am forever grateful to my amazing supervisor, Dr. Honglin Luo, who saw my potential early on and helped me to become the researcher that I am today. A true advocate for the wellbeing and academic success of her trainees, Dr. Honglin Luo has provided me with an excellent training environment to not only grow into a confident scientist but also a mature human being. Her mentorship style is the perfect blend of fostering independence and providing personalized guidance. Dr. Honglin Luo was very generous with her time and allowed me to learn firsthand how she manages the various demands of her productive lab. Her above and beyond mentorship has allowed me to gain the most out of my Ph.D. training. I would also like to thank my thesis committee members Dr. Bruce McManus, Dr. Calvin Yip, Dr. Thibault Mayor, and Dr. David Granville for sharing their kind support and expertise and always providing insightful directions during my graduate studies.

I am very thankful to all the members of the Luo lab, past and present, who have helped me during my training. My sincere gratitude to Dr. Gabriel Fung, Dr. Junyan Shi, and John Zhang for helping me begin my studies when I first joined the lab. A heartfelt thank you to Dr. Eric Deng, Tim Xue, Huitao Liu, Dr. Chen Seng Ng and Amirhossein Bahreyni for being excellent colleagues. Their enthusiasm for science and research continues to be an inspiration. A special thank you to Dr. Junyan Qu and Dr. Hui Tang who were instrumental in several studies and provided unique expertise. I would like to thank Eric Xiang for being an extremely hardworking and inquisitive student. My sincere gratitude to members of the Yang lab, especially Dr. Mary Zhang and Guangze Zhao for their kindness and generosity. A heartfelt thank you to Dr. Gurpreet Singhera, Dr. Paul Hanson, Basak Sahin, and Beth Whalen for always sharing with me their expertise and knowledge in navigating both science and life! I would also like to thank all the wonderful colleagues at the Centre for Heart Lung Innovation, affectionately known as HLI. This diverse community of trainees, staff, and principal investigators has been a positive force for my personal and professional growth.

Most importantly, I want to share my gratitude towards my dear parents and loving family for their encouragement and support without which none of this would be possible.

Dedicated to my loving family.

Chapter 1: Introduction

Intertwined within the life cycle of enterovirus is the host autophagy pathway, which in itself follows a perpetual cycle to maintain cellular homeostasis.[1] In 1963, the Belgian biochemist Christian de Duve first coined the term ***'auto-phagy'*** from the Greek word '*autophagos'* meaning 'self-digestion'. In 1965, the group of George Emil Palade, a Romanian-American cell-biologist, first described the emergence of 'membrane-enclosed structures' following poliovirus infection.[2, 3] Nine years later, both scientists would go on to share the Nobel Prize in Medicine (1974) for their pioneering discoveries of previously unknown cellular organelles, most notably the lysosome and ribosome. These early discoveries piqued the interests of many researchers seeking to unravel the relationship between enteroviruses (EVs) and the autophagy pathway. The current dissertation describes novel molecular insights gained from exploring this relationship with the ultimate goal of identifying targets for anti-viral therapy.

EVs, of the *Picornaviridae* family, are a genus of pathogenic viruses that cause diverse human disorders. The major members of the EV genus include poliovirus (PV), echovirus, coxsackievirus, enterovirus, and rhinovirus[4]. These medically important viruses pose a significant health burden as evidenced by recent global epidemics across Asia and North America[5, 6]. EVs are associated with broad human pathologies, ranging from the common cold to neurological disorder (i.e., encephalitis, aseptic meningitis, and flaccid paralysis)[7], cardiovascular damage (i.e., viral myocarditis and dilated cardiomyopathy)[8], and metabolic disease (i.e., type 1 diabetes)[9]. With the exception of the successful PV vaccination beginning in the 1950s, non-polio EVs continue to be a global health issue.

EVs are a family of small, non-enveloped viruses containing a positive, single-stranded RNA genome of ~7.5 kb that encodes a single open reading frame flanked by 5' and 3' untranslation regions (UTRs)[4]. The life cycle of an EV begins with viral attachment to one or multiple designated cellular receptors. Following internalization, viral RNA is released into the cytoplasm, where it serves as a template for the translation of the viral polyprotein and for the replication of the viral genome. The 5'UTR of EV genome contains an internal ribosome entry site (IRES) for viral translation initiation, which allows EVs to bypass the shutoff of cap-dependent protein translation that occurs during viral infection[10]. Viral proteins are initially synthesized as a single polyprotein, which is subsequently processed into structural proteins (VP1, VP2, VP3, and VP4), nonstructural proteins (2A, 2B, 2C, 3A, 3B, 3C, and 3D), and cleavage intermediates by

virus-encoded proteinases 2A and 3C (or 3CD, the precursor) (**Figure 1**). The viral RNA-dependent RNA polymerase 3D then uses protein 3B (also known as viral protein genome-linked (VPg) that covalently linked to the 5'-end of viral genome) as a primer for both negative- and positive-stranded RNA synthesis. Viral replication takes place on virus-modified intracellular membranous structures that not only serve as physical scaffolds but also provide favorable lipid compositions for viral RNA assembly and replication[11, 12]. The viral proteins 2B, 2C (or their precursor 2BC), and 3A (or its precursor 3AB) regulate cellular permeability and vesicular transport, and constitute essential components of the viral replication complexes[13]. Finally, the newly synthesized RNA genome is packaged into a viral capsid of ~30 nm in size to generate the nascent infectious viral particle. The life cycle is completed when viral progeny are released from the infected cells following cell lysis or non-cytolytically prior to cell rupture through extracellular microvesicles[14, 15, 16, 17].

EVs can infect across various age groups and are associated with diverse human pathologies. EV specific disorders include hand-foot-and-mouth disease, poliomyelitis, and herpangina. Additionally, EVs are associated with viral meningitis, myopericarditis, and respiratory infections [18]. In particular, Coxsackievirus B family have been linked with additional chronic autoimmune diseases such as type 1 diabetes [19]. The wide spectrum of EV-associated disease reflects the inherent broad tropism of individual viruses. Infections may be self-limiting and require no treatment or progressive in nature leading to systemic viremia and worst outcomes [20]. Currently, there is a lack of FDA-approved treatments available for non-polio EV infections. Various anti-viral drugs have previously been developed to target multiple stages of the EV replication life cycle. Capsid-binding drugs such as pleconaril have shown promising anti-viral efficacy by binding to the hydrophobic pockets of viral capsid proteins to limit receptor attachment and subsequent uncoating. However, moderate side effects and adverse drug cross-reactions have precluded pleconaril from receiving FDA approval. The guanosine analog, Ribavarin has demonstrated anti-viral efficacy against various EVs through its ability to integrate into nascent viral RNA and generate defective viral mutants. Additionally, anti-EV strategies have included the targeting of viral proteinase 3C, through peptidomimetic drugs such as Rupintrivir. Although effective against experimental rhinoviral infections in healthy individuals, a lack of efficacy against natural infections in clinical trials has halted further development of Rupintrivir [21]. Except

for the successful poliovirus vaccination campaign, therapeutic efforts to combat non-polio EVs have remained an ongoing challenge.

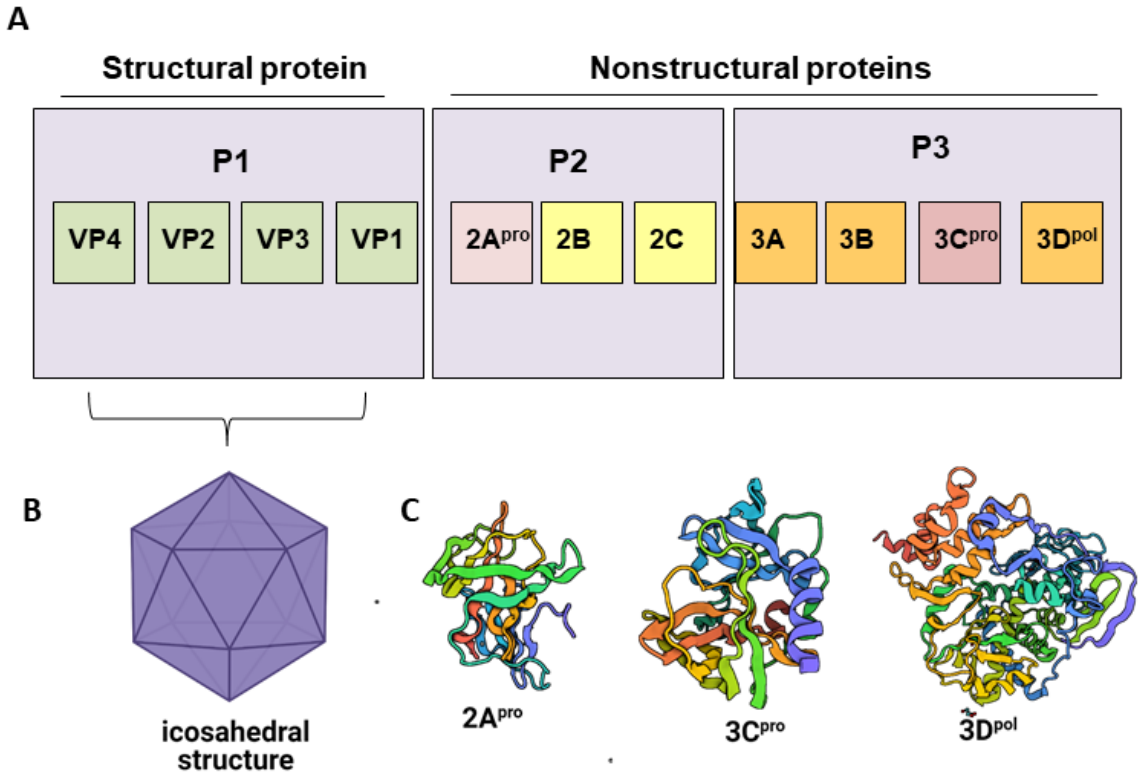

Figure 1. Structure of enterovirus polyprotein. The polyprotein is the translational product of the single open reading frame of enteroviral positive strand RNA. The Coxsackievirus B3 (Nancy strain) polyprotein is comprised of 2,185 amino acids encoding 11 viral proteins (**A**) - 4 structural capsid proteins (VP1-VP4) that generate the icosahedral structure (**B**), and 7 non-structural proteins ($2A^{pro}$, 2B, 2C, 3A, 3B, $3C^{pro}$, and $3D^{pol}$). The polyprotein is processed by two internal viral proteinases ($2A^{pro}$ and $3C^{pro}$) into intermediate fragments and individual proteins. The RNA-dependent RNA polymerase $3D^{pol}$ plays an essential role in the formation of viral replication complexes (**C**).

Autophagy

Autophagy is a cellular process that targets cytoplasmic proteins and/or organelles to the lysosomes for degradation[22, 23]. Over the past decade, extensive research has been conducted to explore how EVs evolve to harness the cellular autophagy pathway to facilitate the successful completion of their life cycle. The current review will focus on the recent progress in understanding the interplay between EV infection and the autophagy pathway. Specifically, I will provide an overview of how EVs hijack components of this cellular process at the different steps of viral life cycle to promote viral growth and for immune evasion.

Autophagy is an evolutionarily conserved intracellular degradation pathway that plays a key role in maintaining cellular homeostasis under both normal and stress conditions[22, 23]. It exists in three forms, i.e., macroautophagy, chaperone-mediated autophagy, and microautophagy[24]. In this review, I focus on macroautophagy as all current literature about EV-autophagy interaction has been on this type of autophagy. The process of macroautophagy (or simply referred to as autophagy) begins with the formation of phagophore (also known as the isolation membrane), a cup-shaped double-membraned structure that sequesters cellular components. Although the origin(s) of the phagophore membrane remain not fully elucidated, multiple sources, including the endoplasmic reticulum (ER)[25], mitochondria[26], ER-mitochondria contact sites/mitochondria-associated membranes[27], ER-Golgi intermediate compartments[28], endosomes, and plasma membrane[29], have been proposed. Following the closure of the phagophore, a double-membraned vesicle, so-called autophagosome, is generated. The autophagosome or amphisome (the latter is formed by the merge of an autophagosome with an endosome) then fuses with a lysosome to form autolysosome and the cargo enwrapped including the inner membrane of the autophagosome is degraded by hydrolyses[23].

In mammalian cells, the molecular processes of autophagy are controlled by a set of more than 30 ‘autophagy-related’ (ATG) proteins. Proteins encoded by these genes participate in the initiation and formation of autophagosomes through the action of several protein complexes and molecules[30, 31]. Upon autophagy stimulation, the uncoordinated (UNC)-51-like (ULK) complex, consisting of ULK1/2, ATG13, RB1CC1 (RB1 inducible coiled-coil 1)/FIP200 (focal adhesion kinase family interacting protein of 200 kDa), and ATG101, translocates to the autophagy initiation sites and facilitates the recruitment of the class III phosphatidylinositol-3-kinase (PI3K) complex (**Figure 2**). The PI3K complex is composed of PI3KC3 (phosphatidylinositol 3-kinase

catalytic subunit type 3)/VPS34 (vacuolar protein sorting 34), PIK3R4 (phosphoinositide 3-kinase regulatory subunit 4)/VPS15, AMBRA1 (activating molecule in beclin-1-regulated autophagy protein 1), ATG14, and Beclin-1, which promote autophagosome formation by providing PtdIns(3)P (PI3P) to the phagophores. The PI3P then recruits the downstream ATG2-WIPI (WD-repeat protein interacting with phosphoinositides) complex, comprising of transmembrane protein ATG9, WIPI, and ATG2, to the phagophore, which in turn facilitates the recruitment of ATG5-ATG12-ATG16L1 complex and covalent association of LC3 (microtubule-associated protein light chain 3) to phosphatidylethanolamine (PE) on the nascent autophagosome membrane, allowing for autophagosome maturation.

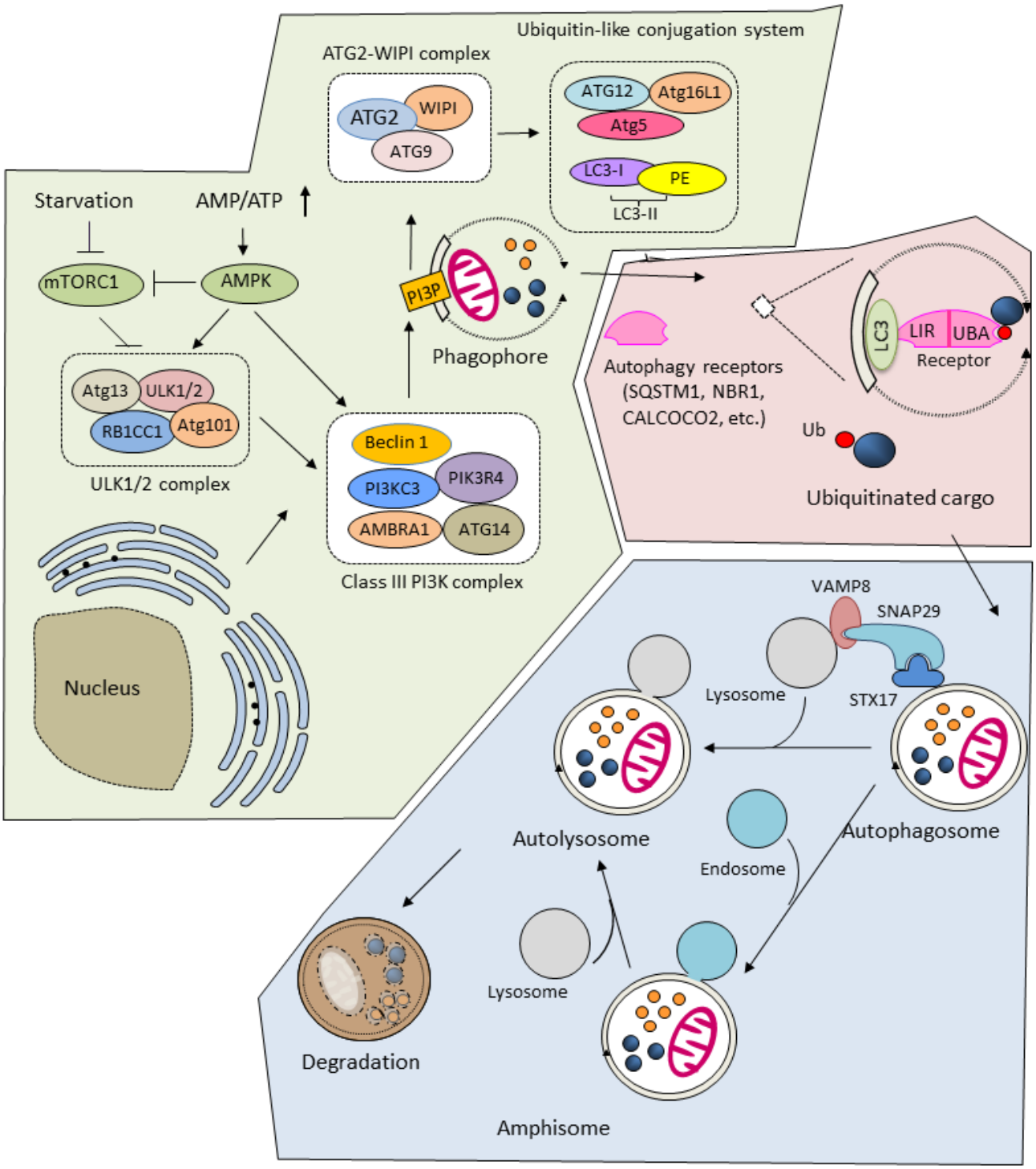
Ubiquitin-like conjugation system
ATG2-WIPI complex
ATG2
WIPI
ATG9
ATG12
Atg16L1
Atg5
LC3-I
PE
LC3-II
Starvation
AMP/ATP
mTORC1
AMPK
PI3P
Phagophore
Autophagy receptors
(SQSTM1, NBR1,
CALCOCO2, etc.)
LC3
LIR
UBA
Receptor
Ub
Ubiquitinated cargo
Atg13
ULK1/2
RB1CC1
Atg101
ULK1/2 complex
Beclin 1
PI3KC3
PIK3R4
AMBRA1
ATG14
Class III PI3K complex
Nucleus
VAMP8
SNAP29
Lysosome
STX17
Autolysosome
Autophagosome
Endosome
Degradation
Lysosome
Amphisome

Figure 2. Schematic overview of the molecular mechanism of autophagy. Autophagosome formation is initiated by the nutrient sensing kinases (i.e., mTORC1 and AMPK) and through the function of three protein complexes (i.e., ULK1/2 complex, class III PI3K complex, and ATG2-WIPI complex) and two ubiquitin-like conjugation systems (i.e., ATG12-ATG5-ATG16L1 and LC3-PE). Once formed, the autophagosome then fuses with the lysosome to produce an autolysosome. Autophagosome can also merge with the endosome to form an amphisome, which then fuse with a lysosome for cargo degradation. The fusion between an autophagosome and a lysosome is regulated by multiple proteins, particularly the (STX17-SNAP29-VAMP8) SNARE complex. Selective cargo degradation is mediated by autophagy receptors, such as SQSTM1, NBR1, and CALCOCO2, which harbor a UBA domain for substrate recognition, and a LIR for binding to autophagosome-anchored LC3-II, thereby bridging the substrate to the autophagosome for degradation. mTORC1, mechanistic target of rapamycin complex 1; AMPK, AMP activated protein kinase; ATG, autophagy-related; ULK, uncoordinated (UNC)-51-like kinase; RB1CC1, RB1 inducible coiled-coil 1; PI3KC3, phosphatidylinositol 3-kinase catalytic subunit type 3; PIK3R4, phosphoinositide 3-kinase regulatory subunit 4; AMBRA1, activating molecule in Beclin-1-regulated autophagy protein 1; PI3P, PtdIns(3)P; WIPI, WD-repeat protein interacting with phosphoinositides; LC3, microtubule-associated protein light chain 3; PE, phosphatidylethanolamine; SQSTM1, sequestosome 1, NBR1, neighbor of BRCA1; CALCOCO2, calcium binding and coiled coil domain-containing protein 2; SNAP29, synaptosomal-associated protein 29; STX17, syntaxin 17; VAMP8, vesicle-associated membrane protein 8; LIR, LC3-interacting region; UBA, ubiquitin-associated; Ub, ubiquitin.

The fusion between autophagosomes and lysosomes is regulated by multiple proteins involved in the intracellular membrane trafficking, including the Rab GTPases, the soluble N-ethylmaleimide-sensitive factor (NSF)-activating protein receptor (SNARE) proteins, and the membrane-tethering proteins[32] (**Figure 2**). Upon autophagy induction, the SNARE protein syntaxin 17 (STX17), is recruited to autophagosomes, where it binds to another autophagosomal SNARE protein, the synaptosomal-associated protein 29 (SNAP29) to form a binary SNARE protein complex (STX17-SNAP29)[33, 34]. ATG14 is then recruited to the binary SNARE complex to facilitate the generation of a ternary SNARE complex with the lysosome/endosome-localized SNARE protein, vesicle-associated membrane protein 8 (VAMP8), driving autophagosome-lysosome fusion[35]. Beyond the SNARE proteins, several membrane-tethering proteins are also involved in the fusion step of autophagy. For example, the pleckstrin homology domain containing protein family member 1 (PLEKHM1) protein was reported to interact with Rab7, homotypic fusion and protein sorting (HOPS), and LC3 to promote the formation of SNARE complexes during autophagosome fusion[36, 37]. For a more in-depth review of autophagic fusion requirements, please refer to Corona *et al*.[38].

Autophagy can be induced by various stimuli and stressors, including nutrient starvation, metabolic and oxidative stress (reactive oxygen and nitrogen species), ER stress, hypoxia, infectious agents, and the presence of damaged organelle, through either a cargo-selective or a cargo–non-selective pathway[39, 40]. Under nutrient-stress or normal conditions, autophagy initiates a non-selective degradation of cytoplasmic contents for energy preservation. However, autophagy can also facilitate selective clearance of cytoplasmic materials in response to specific cellular and/or environmental stimuli (termed selective or precision autophagy), such as protein aggregates, damaged mitochondria, and invading pathogens in a process termed the aggrephagy, mitophagy, and xenophagy, respectively[23]. Cargo specificity is mediated by a family of multivalent autophagy receptors, which harbor ubiquitin-association domains (e.g., UBA (ubiquitin-associated) or UBZ (ubiquitin-binding zinc finger)) for substrate recognition, and LC3-interacting regions (LIRs) for binding to the autophagosome-localized LC3, thereby bridging ubiquitinated substrates to the autophagosomes for degradation[41, 42]. To date, a number of autophagy receptors have been identified, including sequestosome 1 (SQSTM1)/p62, neighbor of BRCA1 (NBR1), optineurin, calcium binding and coiled-coil domain-containing protein 2 (CALCOCO2)/nuclear dot 10 protein 52 (NDP52), and CALCOCO3/Tax1-binding protein1 (TAX1BP1).

Autophagy is generally considered cytoprotective at both baseline and under various forms of stresses by providing energy and degrading damaged proteins/organelles. In addition, autophagy also plays a critical role in host defense[43, 44]. As part of the cell autonomous innate immunity, autophagy functions to defend individual cells from invading pathogens such as bacteria, fungi, parasites, and viruses. At the same time, autophagy initiates signals within infected cells to induce systemic immune responses[43, 44]. Notably, autophagy-mediated degradation in lysosomal compartments can generate immunogenic peptides that may be loaded onto major histocompatibility complexes (MHC) for presentation to $CD4^+$ T cells (via MHC class II) or $CD8^+$ T cells (via MHC class I) [45]. of In the context of virus infection, autophagy is classically regarded as an anti-viral mechanism that selectively degrades viral particles or viral components inside lysosomes in a process referred to as virophagy[23]. However, many viruses, including EVs, have evolved to subvert this pathway for pro-viral purposes[46, 47].

Endocytic function of autophagy and EV entry

EVs initiate infections by attachment to host receptors, resulting in receptor-mediated endocytosis, and then undergo uncoating for delivery of the viral genome into the cytoplasm of a target cell (**Figure 3**). The cellular tropism observed within EVs relies largely on specific receptors available on the target cells. For example, PV receptor (PVR, also known as CD155)[48], intercellular adhesion molecule 1 (ICAM-1)[49], coxsackievirus adenovirus receptor (CAR)[50] and co-receptor decay accelerating factor (DAF, also known as CD55)[51], have been identified as the receptors for PVes, major groups of rhinoviruses, and type B coxsackieviruses (CVB), respectively. Despite the discoveries of majority of EV receptors, including the recently identified EV-D68 and coxsackievirus A (CVA)10 receptors[52, 53], the precise mechanism of EV entry and the exact site of viral genome penetration and uncoating remain poorly understood. Clathrin-mediated endocytosis is the best-studied, receptor-mediated endocytic pathway for EV internalization. In addition, caveolin-dependent and clathrin/caveolin-independent (macropinocytosis is an example of the latter) endocytic mechanisms are also reported[54].

Echovirus 7 enters polarized intestinal epithelial cells through a clathrin-mediated endocytic mechanism and then proceeds to early and late endosomes for viral genome release[55]. This process was shown to be independent of endosomal acidification, but require the function of Rab7[55]. Rab7 is a small GTPase critical for both endocytosis and autophagy by controlling endo-

lysosomal trafficking and autophagosome fusion with lysosomes, respectively[56]. In addition to Rab7, several other core components of autophagy were also discovered to be involved in the regulation of the endocytic pathway. For instance, Beclin 1 was shown to control early endosome formation as well as late endosome trafficking and maturation through the UVRAG (UV radiation resistance-associated gene)-PI3KC3/VPS34 complex[57]. It was also reported that conjugation of the ubiquitin-like molecule ATG12 to ATG3 (an E2-like enzyme that catalyzes LC3 lipidation) mediates endo-lysosomal trafficking and late endosome function beyond autophagy[58]. Furthermore, ATG5 and ATG16L have recently been linked to endosomal acidification and exosome biogenesis independent of the canonical autophagy machinery[59]. Given the demonstrated significance of autophagy core proteins in regulating the endocytic pathway and the recognized cross-talk between the endosomal and autophagic pathways via the formation of amphisomes, Kim *et al.*[60] further investigated the possible involvement of other autophagy-related proteins in echovirus 7 entry. They found that depletion of Beclin-1, ATG12, ATG14, ATG16, or LC3 prevents internalization of echovirus 7 but not CVB3 at a step after viral attachment to its receptor but prior to uncoating[60]. The process of uncoating in these studies, defined as the release of viral genome from its proteinaceous capsid, appears to be independent of autophagosome and amphisome formation[60]. The mechanism associated with this virus-specific requirement for autophagy proteins in EV entry is not clear; it may be related to differential endocytotic mechanism (clathrin-dependent versus caveolin-dependent for echovirus 7 and CVB3 entry, respectively) in polarized cells[61].

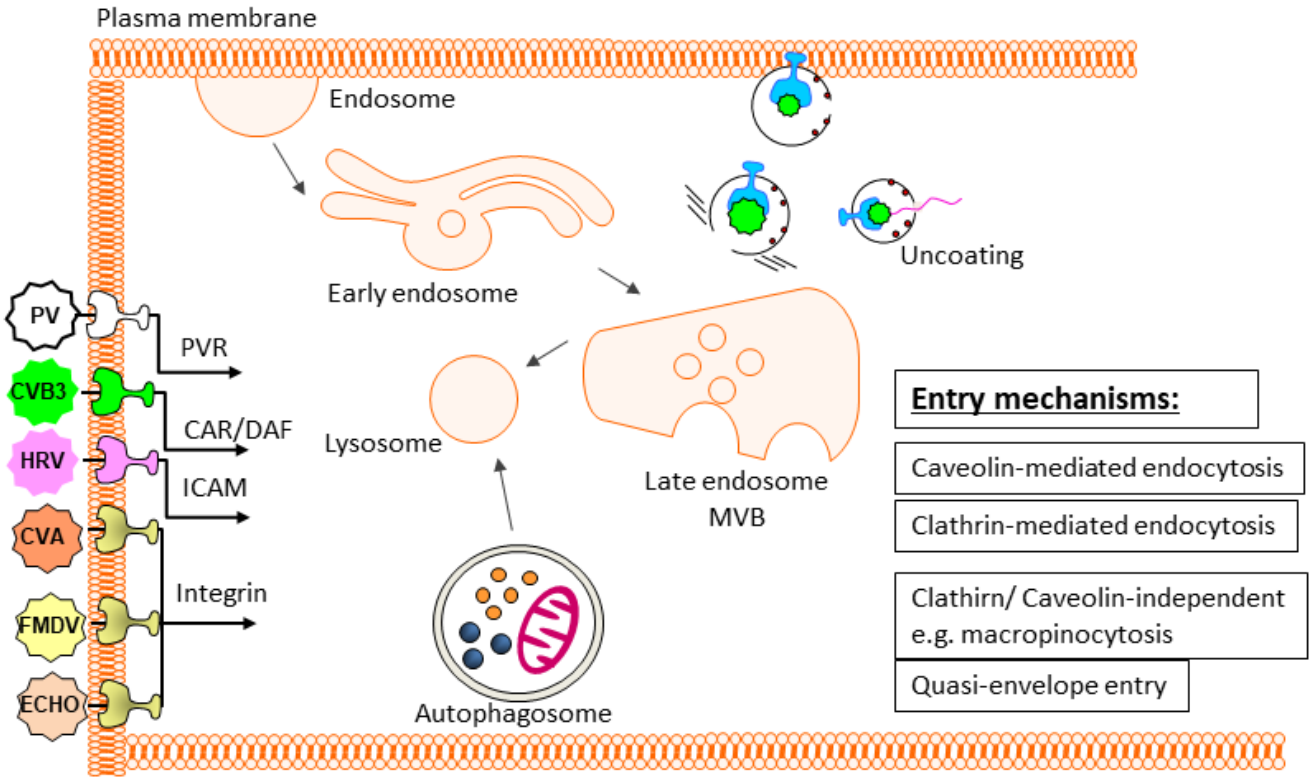

Figure 3. Intersection of endocytosis, autophagy, and EV entry. EV cellular tropism is determined by various viral receptors on host cell plasma membrane. Poliovirus (PV) entry requires the poliovirus receptor (PVR). Coxsackievirus and adenovirus receptor (CAR) and decay accelerating factor (DAF) facilitate CVB3 entry. Intercellular adhesion molecule 1 (ICAM1) facilitates the entry of several human rhinoviruses (HRV). Integrins serve as entry factors for Coxsackievirus A, foot and mouth disease (FMDV), and echovirus. EV entry can be clathrin-mediated, caveolin-mediated, or through clathrin/caveolin-independent mechanisms. Upon entry, endocytic vesicles may traffick through a series of compartments including the early endosome, late endosome or multivesicular bodies (MVBs), and finally the lysosome. Uncoating of RNA from viral capsid can occur at different stages along the endocytic pathway.

Another example linking autophagy to EV entry is the recent finding that during early viral infection (PV, CVB1, and CVB3) host factors are recruited to the ruptured endosomes to escape the autophagy-mediated degradation of viral RNA[62] (**Figure 3**). Using haploid genetic screens, Staring *et al.*[62] identified PLA2G16, a small phospholipase, to be a key regulator of the uncoating process whereby viral genome is delivered from its proteinaceous capsid into the cytoplasm. Further screen for gene mutations that can rescue viral infection in PLA2G16-deficient cells demonstrated an inhibitory role for galectin-8 in EV infection by promoting autophagy degradation of viral RNA genome[62]. A model is proposed to explain the competitive determination of the fate of viral RNA at the interface of endosomes: after viral endocytosis, endosome fragmentation occurs, leading to the exposure of β-galactosides on the luminal side of the endosomes to galectin-8 and consequently initiating selective autophagy for viral clearance; to compete with this process, PLA2G16 is recruited to the permeated endosomes, allowing for effective viral RNA release into the cytoplasm for translation[62] (**Figure 4**).

Induction of autophagy and EV replication

Similar to other positive-strand RNA viruses, replication of EVs occurs on distinct intracellular membranes, which are modified both architecturally and chemically by EVs to assemble viral replication complexes (also defined as viral replication organelles[63])[11, 12]. Studies have revealed that EVs modulate host lipid metabolism/distribution and utilize membrane complexes enriched in phosphatidylinositol 4-phosphate (PI4P) and cholesterol for replication[63, 64, 65]. Despite notable progress in understanding cellular membrane remodeling and its significance in EV infection, the contribution of autophagy in such event remains largely undefined.

It has been well documented that EV infection induces the formation of autophagy-associated membrane scaffolds, favoring viral RNA synthesis. Almost all major groups of the EVs, including PV[66], CVB3[67, 68], CVB4[69], CVA16[70], EV-A71[71, 72], EV-D68[73], and human rhinovirus 2 (HRV2)[74], have been shown to facilitate the production of autophagosomes, as demonstrated by LC3 lipidation and puncta formation, as well as detection of intracellular double-membraned vesicles. Disruption of autophagy using chemical inhibitors (such as 3-methyladenine, a class III PI3K inhibitor) or through deletion of critical genes involved in autophagosome formation/maturation (such as ATG5, ATG7, Beclin 1, PI3KC3/VPS34, ATG14, and UVRAG) inhibits viral replication both *in vitro* and *in vivo*[68, 73, 75, 76, 77]. The mechanism underlying the pro-

viral function of autophagy is still unclear. Electron microscopy analysis of CVB3-infected acinar cells revealed that the highly organized lattice structures (likely viral replication organelles) observed in normal mice are barely detected in ATG5-deficient mice[67, 75]. In addition, research utilizing an antibody against double-stranded RNA (dsRNA, a replicating intermediate of viral RNA used as a marker for viral replication complexes) showed that dsRNA colocalizes with LC3-positive puncta (as a marker for autophagosomes and autophagy-independent LC3 accumulation) during late PV infection[78], in line with the 3D ultrastructural results that PV induces early convoluted single-membraned structures and late autophagosome-like double-membraned vesicles[79]. These findings, together with recent evidence that PI4P lipids accumulate on autophagosomes upon autophagy stress to promote autophagosome-lysosome fusion[80], support the premise that autophagosomes serve as sites, at least during late phase of maximal viral replication, for viral RNA replication. It is important to note that previous studies on the role of autophagy in EV replication have been conducted predominantly through deletion of individual autophagy-related genes. Some of the ATG proteins are known to have unconventional functions beyond autophagy[81, 82]. Thus, further investigations are required to determine whether the pro-viral role of these ATG proteins is truly or exclusively via the autophagy pathway. Indeed, both autophagy-dependent and –independent function of LC3 has been described to benefit CVB3 replication *in vivo*[83]. Moreover, knockdown of ATG13 and RB1CC1/FIP200, components of the ULK1/2 complex, has been found to enhance CVB3, EV-A71, and CVA21 replication; this effect seems to be unrelated to autophagy function as depletion of genes encoded for other ULK1/2 components (such as ULK1, ULK2, and ATG101) does not affect viral replication[84].

Although the precise mechanism by which EVs induce autophagy remains to be elucidated, several studies have examined the upstream pathways that can potentially be co-opted to initiate autophagy. Canonical autophagy receives signaling input through nutrient-sensing kinases such as AMP activated protein kinase (AMPK) and mechanistic target of rapamycin complex 1 (mTORC1) that converge on autophagy initiating kinase complexes, such as the ULK1/2 complex and the class III PI3K complex[23]. In response to augmented AMP/ATP ratio, AMPK is activated, which in turn deactivates mTORC1 and/or provokes ULK1 and Beclin1 activity directly. The nutrient sensing kinase mTORC1 is a negative regulator of autophagy through inhibitory phosphorylation of ATG13 and ULK1[23]. Monitoring of mTORC1 activity by checking the phosphorylation status of its substrates has revealed controversial results in EV infection. It was

reported that infection with CVA16 and EV-A71 results in a reduction of mTORC1 activity[70, 72], whereas CVB3 infection presented no evident changes in the activity of mTORC1[68, 84]. Consistent with the latter result, a recent study showed that phosphorylation and activity of mTORC1 do not alter throughout PV infection[85]. Further study demonstrates that PV-induced autophagy is independent of the ULK1 complex[85], suggesting the existence of alternate mechanisms by which EV induces autophagy. Similarly, CVB3 was shown to benefit from a non-canonical form of autophagy that appears to bypass the requirement for core autophagy initiation components, such as Beclin 1, UVRAG, and ATG14[76]. Finally, several studies revealed that viral components of the RNA replication machinery, such as viral proteins 2B, 2BC, 3A, and 3AB, are sufficient to induce LC3-lipidation and/or autophagosome formation[66, 86, 87, 88, 89]. Collectively, the current evidence suggests that EVs can employ multiple strategies to induce the accumulation of autophagosomes; however, the mechanism is likely independent of the canonical autophagy pathway.

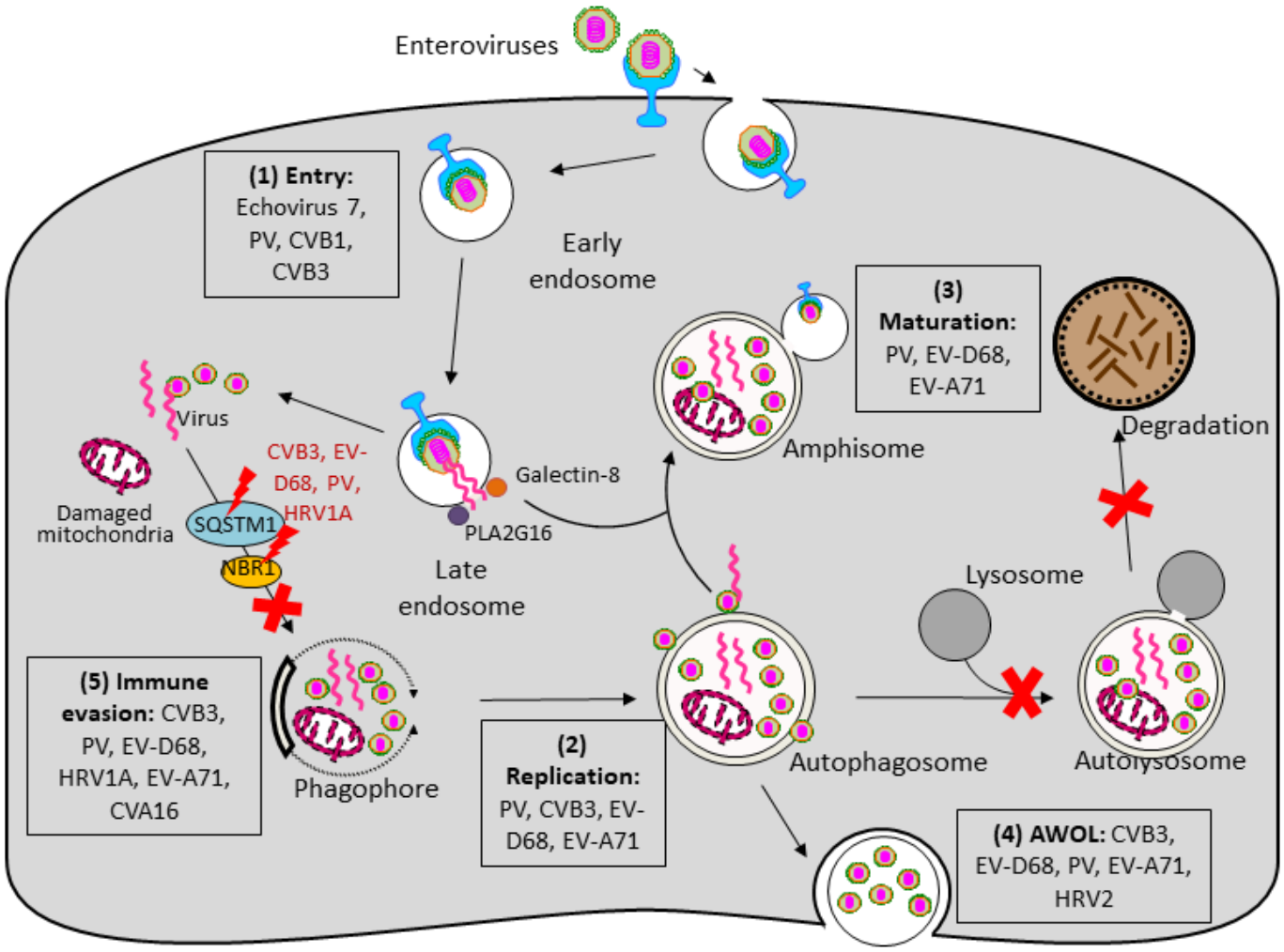

Figure 4. Interplay between enteroviruses and the host autophagy pathway. Major members of enteroviruses have been shown to subvert the host autophagy machinery at different phases of viral life cycle to enhance viral growth and for immune escape. (1) Viral entry. Autophagy core proteins benefit echovirus 7 entry, likely through regulation of the endocytic pathway. During PV, CVB1, and CVB3 infection, PLA2G16 is recruited to the fragmented endosome to antagonize the function of galectin-8 in initiating autophagic degradation of viral RNA genome. (2) Viral replication. Autophagosome-lysosome fusion is blocked during CVB3, PV, and EV-D68 infection. Accumulation of autophagosomes appears to favor viral replication by offering replication membranes for PV, CVB3, EV-D68, and EV-A71. (3) Viral maturation. Formation of acidified amphisomes is required for EV (e.g., PV, EV-D68, EV-A71) maturation to generate infectious viruses. (4) Viral release through AWOL. EVs (e.g., PV, EVD68, EV-A71, CVB3, and HRV2)

utilize autophagosomes as envelopes for non-lytic viral exit. (4) Immune evasion. Autophagy receptor SQSTM1 is cleaved by viral proteinase 2A during CVB3, PV, EV-D68, and HRV1A infection (cleavage of NBR1 is also observed during CVB3 infection) to counteract virophagy-mediated clearance of viral particles/components. Enhanced autophagy during EV-A71 and CVA16 infection was shown to benefit viruses by suppressing TLR7-mediated type I IFN signaling. PV, poliovirus; CVB, coxsackievirus B; CVA, coxsackievirus A; EV, enterovirus; HRV, human rhinovirus; SQSTM1, sequestosome 1, NBR1, neighbor of BRCA1; AWOL, autophagosome-mediated exit without lysis; IFN, interferon.

Fusion machinery of autophagy, EV maturation and release

As noted earlier, autophagy is a dynamic process starting with autophagosome formation, followed by fusion with lysosomes and consequent degradation of enclosed cargo. It is now clear that accumulation of autophagosomes could be due to increased induction of autophagosome biogenesis and/or reduced autophagosome fusion with lysosomes. To evaluate the effects of EV infection on autophagy flux (a measure of the completion of degradative autophagy), early research focused on monitoring the stability of the cargo receptor SQSTM1/p62 that is well known to be degraded during complete autophagy[90]. It was found that PV infection causes a decrease in protein levels of SQSTM1/p62, prompting the authors to conclude that PV infection enhances autophagy flux[91]. However, it was later revealed that SQSTM1/p62 is not only a substrate of autophagy, but also targeted by viral proteinase 2A during CVB3 infection[92], raising the concern whether it serves as a dependable marker to assess autophagy flux. The cleavage of SQSTM1/p62 was recently confirmed upon PV, EV-D68, and HRV1A infection[73]. Therefore, the question of whether EVs increase or decrease autophagic flux still remains.

EVs have traditionally been considered to escape the infected cell by causing it to rupture. However, emerging evidence highlights the significance of EVs in being able to spread through non-lytic mechanisms[93], such as via autophagosome-mediated exit without lysis (AWOL)[94]. Apart from its central role in cargo degradation, autophagy also has a function in unconventional secretion of cytosolic proteins, such as the release of inflammatory cytokines[95]. Secretory autophagy' is originally identified as an alternative disposal strategy under conditions of impaired lysosomal function[95]. A growing body of work has documented that EVs, including PV, EV-D68, EV-A71, CVB3, HRV2, can indeed hijack the autophagic machinery to usurp its abundant membranes by repurposing them as envelopes for non-lytic viral egress[14, 15, 17, 73, 96, 97]. This strategy seems to provide unique advantages for EV[93]. For example, by cloaking inside host-derived vesicles, EVs adopt a Trojan horse-like strategy to propagate within their host organism, thereby shielding their pathogen-associated patterns from the adaptive immune detection. In addition, the use of quasi-envelopes that enclose multiple viral particles within a single vesicle was discovered to deliver viral particles more efficiently than infection with individual "naked" virions[15]. The mechanisms by which EVs use autophagy as a means of non-lytic spread is largely undefined. Recent studies on CVB3 and EV-D68 postulate that inhibition of autophagosome-lysosome fusion benefits viruses by re-directing autophagosome and/or amphisome vesicles from

degradative autophagy to secretory autophagy, ultimately resulting in AWOL[73, 98, 99]. Similarly, there was a report describing that CVB3 infection induces the generation of mitochondrion-containing autophagosomes (coined mitophagosomes)[96]. Instead of being targeted and degraded by lysosomes, these mitophagosomes are released along with the enclosed viral particles from the infected cells[96]. However, the process of how autophagosomes and/or amphisomes are guided to merge with plasma membranes for viral release remains elusive. The SNARE proteins are known to have an important role in vesicle exocytosis via regulating membrane fusion[100] (**Figure 5**); however, the exact SNARE(s) that mediate docking and subsequent fusion of autophagosomes with the plasma membranes have not been identified, and warrants further investigations.

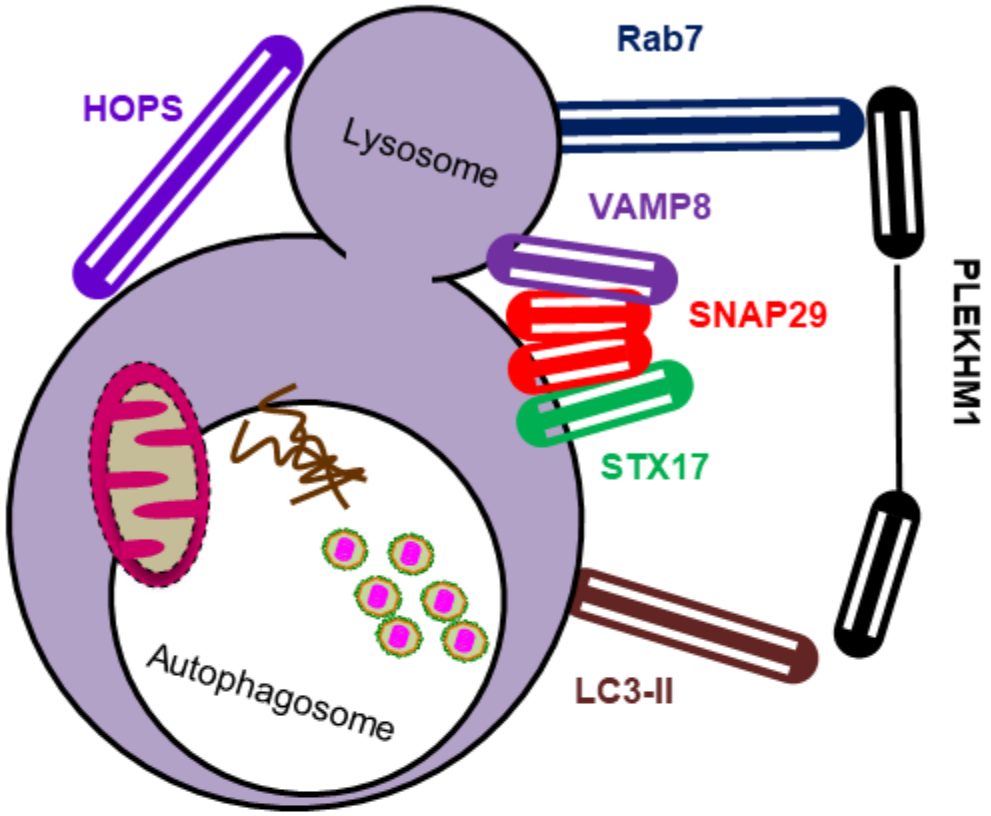

Figure 5. Autophagosome-lysosome fusion machinery. Autophagic vesicles are positioned in close proximity to lysosomes by tethering factor pleckstrin homology domain containing, family M (PLEKHM1) through direct interaction with autophagosome-anchored LC3-II and lysosome-anchored Rab7. The homotypic fusion and protein sorting (HOPS) complex is a multi-subunit tethering complex that also participates in this process. Membrane fusion between the outer membrane of autophagosome and lysosomes is mediated by autophagic soluble NSF attachment protein REceptors (SNARE) composed of autophagosome-localized Qa SNARE syntaxin17 (STX17) and the R-SNARE vesicle-associated membrane protein 8 (VAMP8). The Qbc SNARE synaptosomal-associated protein 29 (SNAP29) bridges with STX17 and VAMP8 to form a ternary SNARE complex that drives membrane fusion.

Selective autophagy and EV evasion of host anti-viral immunity

It is well documented that autophagy are involved in both innate and adaptive immunity[44, 101]. One of the best-appreciated functions for autophagy in immunity is to defend against microbial invasion[102, 103]. For this reason, autophagy has traditionally been considered an anti-viral machinery. In particular, autophagy can selectively target invading viruses through a process, called virophagy, for clearance[23] (**Figure 6**). Similar to other types of selective autophagy, virophagy is mediated through autophagy receptors, including SQSTM1/p62, NBR1, optineurin, CALCOCO2/NDP52, and TAXBP1[104]. The first-identified virophagy receptor is SQSTM1/p62 that was discovered to interact with capsid proteins of Sindbis and Chikungunya viruses, which are positive-sense RNA viruses in the *Togaviridae* family, and target viral particles and/or capsid proteins for autophagic degradation[105, 106]. To counteract the anti-viral action of virophagy, EVs have developed strategies to directly target autophagy receptors. For example, infection with several EVs, including CVB3, EV-D68, PV, and HRV1A, has been shown to cause the cleavage of SQSTM1/p62[73, 92], suggesting a conserved EV strategy to subvert the host virophagy efforts. Additional research demonstrated that NBR1, a functional homolog of SQSTM1/p62, is also cleaved upon CVB3 infection, excluding a possible compensatory role for NBR1 when SQSTM1/p62 is disturbed. Of note, it was found that cleavage of SQSTM1/p62 and NBR1 not only results in a loss-of-function but also produces a dominant-negative fragment against native proteins[92].

Toll-like receptors (TLRs) are important mediators in innate anti-viral immunity. It is well characterized that EV infection activates the TLR signaling to initiate the host innate immune response[107]. Current evidence suggests a dual role for autophagy in the regulation of the TLR signaling during EV infection[108, 109]. Research of CVB3 demonstrated that virus-activated, TLR3-dependent type I interferon signaling requires autophagy[108]. Results from this study support a model that autophagosomes fuse with TLR3-positive endosomes to form amphisomes, which serve as platforms to sense the viral pathogen-associated molecular patterns (delivered by autophagosomes) and consequently activate the downstream anti-viral signaling. In contrast, it was recently reported that enhanced autophagy in response to EV-A71 and CVA16 infection benefits viruses by inhibiting TLR7-mediated type I interferon signaling, although the detailed mechanism remains to be determined[109].

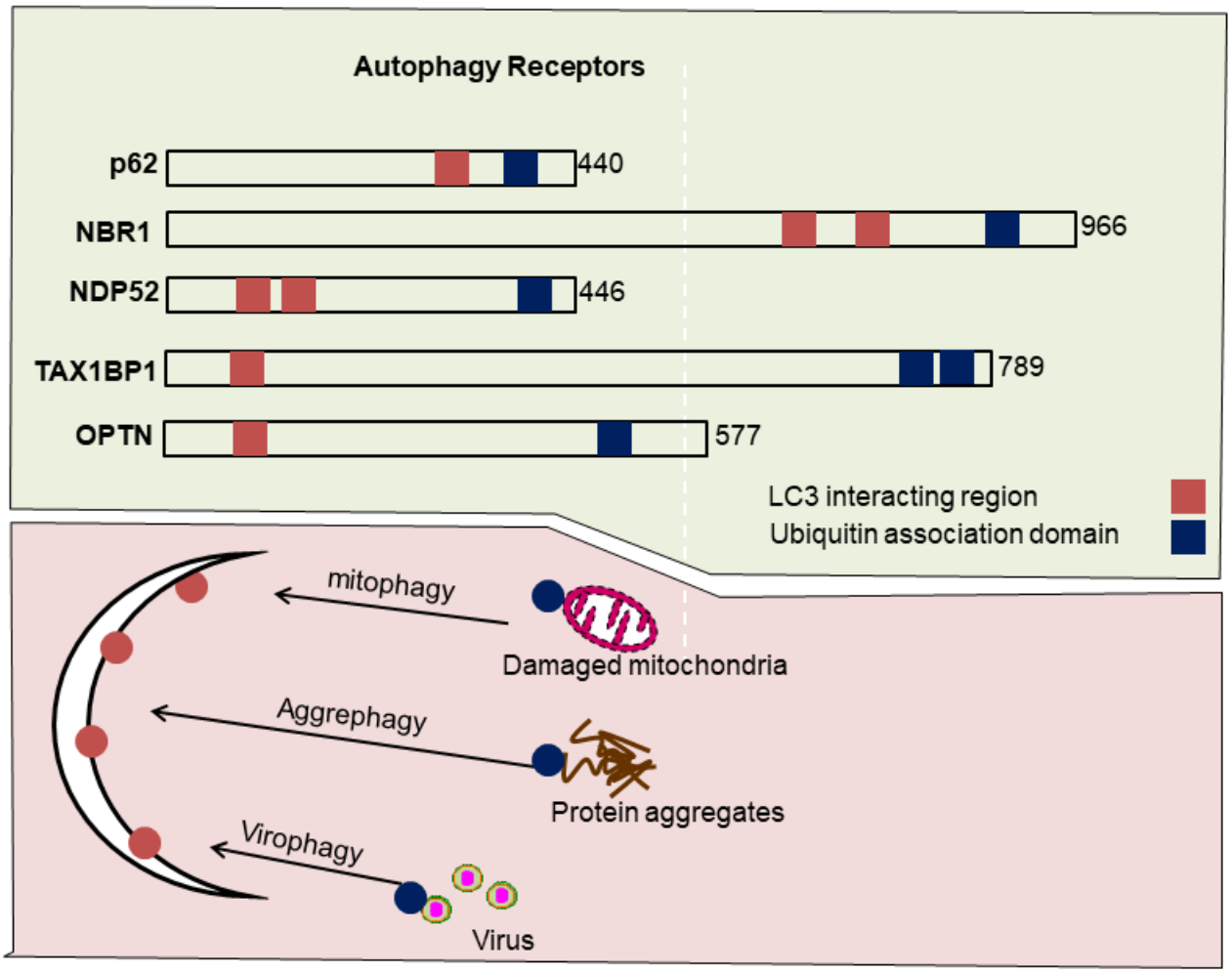

Figure 6. Selective autophagy receptors. Selective autophagy provides specificity to substrate degradation through the autophagy pathway. Selective autophagy receptors harbor domains that recognize and bind ubiquitin (e.g. UBA, UBZ) as well as LC3-interaction regions (LIR) that bridge various ubiquitinated substrates for autophagy mediated clearance. Sequestosome 1 (SQSTM1/p62), neighbor of BRCA1 (NBR1), calcium binding and coiled-coil domain 2/ nuclear dot protein 52 (CALCOCO2/NDP52), calcium binding and coiled-coil domain 3/Tax1-binding protein 1 (CALCOCO3/TAX1BP1), and optineurin (OPTN) are among the first identified autophagy receptors. E.g. of selective autophagy include mitophagy, the selective degradation of damaged mitochondria; aggrephagy, the selective degradation of protein aggregates; virophagy, the selective degradation of virus and/or viral components through autophagy.

Rationale, hypothesis, and specific aims:

Collectively, current evidence highlights a convergence between EV and the host autophagy pathway, but the underlying molecular mechanisms require further elucidation. The goal of this thesis project is to further characterize the molecular details by which EVs subvert the autophagy pathway. To accomplish this, four specific aims are proposed:

The **central hypothesis** of my thesis is that CVB3 hijacks the host autophagy pathway at multiple stages to promote viral propagation. To address this hypothesis, I have proposed the following aims.

Specific aims:

Aim 1: Characterize the mechanism by which CVB3 initiates autophagy.

Aim 2: Elucidate the role of selective autophagy receptors in CVB3 propagation.

Aim 3: Determine the mechanism by which CVB3 disrupts autophagy flux.

Aim 4: Investigate the mechanism by which CVB3 impairs host lysosomal function.

The specific aims have been structured to reflect the natural progression of the autophagy process. In **aim 1**, I explored the early stages of autophagy and how CVB3 targets protein complexes (e.g. ULK1/2 complex) required for autophagosome biogenesis. In **aim 2**, I explored the mechanism of viral subversion that disrupts cargo recruitment to autophagosomes by identifying novel host proteins (e.g. NDP52/CALCOCO2) that are targeted by CVB3. In **aim 3,** I studied the underlying mechanism by which CVB3 targets the autophagosome-lysosome fusion process by identifying novel host factors (e.g. SNAP29 and PLEKHM1) which are bona fide substrates of viral proteinases. Lastly, in **aim 4**, I investigated the mechanism by which CVB3 disrupts lysosomal function by identifying TFEB, a master regulator of lysosome biogenesis, as a novel viral target. Each specific aim demonstrates CVB3's capacity to target distinct stages of the autophagic process and reveals a unique theme of pathogenic viral proteinases targeting critical autophagy proteins.

This thesis is composed of an introductory **Chapter 1**. The research derived from specific aims 1-4 is discussed in **Chapters 2-5**. A brief summary chapter is provided in **Chapter 6**.

Chapter 2: Coxsackievirus B3 initiates non-canonical autophagy

Background

Evidence dating back to the 1950s revealed the emergence of double-membrane vesicular structures following PV infection of HeLa cells[3]. The resemblance of these virus-induced structures to autophagosomes prompted researchers to closely examine the potential relationship between EV infection and autophagy. Despite numerous studies that have linked EV infection to autophagosome induction[110], very little is known about the underlying mechanism.

Rationale: Available evidence has suggested that EVs may initiate autophagy through a novel mechanism that is distinct from the well characterized starvation-induced 'canonical' autophagy pathway. It was shown that PV induces autophagy independent of the ULK1/2 complex[111]. Further, CVB3 was demonstrated to initiate autophagy independent of BECN1, ATG14, UVRAG [76]. The **objective** of this chapter is to characterize the role of canonical factors in CVB3-induced autophagy as well as identify novel protein(s) involved in CVB3-induced autophagy. The **specific aims** of chapter 2 are to **(1)** investigate the role of ULK1/2 complex, PI3K-complex, WIPI2-ATG9 complex, as well as the ubiquitin-like ATG conjugation system in CVB3-induced autophagy, and **(2)** investigate the role of phosphoinositide kinase(s) as potential novel host factors involved in this process.

Materials and methods

Cell culture, viral infection, and chemicals

HeLa, HEK293A, and NSC-34 were from American Type Culture Collection (ATCC). $ATG5^{-/-}$ and $ATG5^{+/+}$ mouse embryonic fibroblasts (MEF) were kind gifts from Dr. Noboru Mizushima[112], and obtained through BIKEN BioResource Research Center (RCB2711 and RCB2710, respectively). These cells were cultured in Dulbecco's Modified Eagle's Medium (DMEM) supplemented with 10% fetal bovine serum (FBS) and a penicillin/streptomycin cocktail (100 µg/mL). Jurkat cells were from ATCC and cultured in Roswell Park Memorial Institute (RPMI) 1640 medium.

For CVB3 infection, cells were seeded at a density of approximately 0.5×10^6 cells/mL. Upon reaching ~70% confluency (16h-24h), cells were either sham-infected with PBS or inoculated with CVB3 (Kandolf strain) at multiplicity of infections (MOI) of 100 or as specified

in the Figure Legends. The following chemicals were used for the treatment of cells: general caspase inhibitor Z-VAD-FMK (BD Biosciences, #550377), lysosome inhibitor bafilomycin A1 (Sigma-Aldrich, B1793), ULK1/2 kinase inhibitor MRT68921 HCl (Selleck, S7949). Cells were starved by culturing in Hank's Balanced Salt Solution (HBSS) medium (Thermofisher Scientific, 14025076) for 2h.

Generation of knockout cells using CRISPR-Cas9 system

Knockout (KO) HEK293A cell lines for ATG5, ATG16L1, FIP200, BECN1, WIPI2, ATG9A, and PI4KIIIβ were generated using the CRISPR-Cas9 system as previously described[113]. Briefly, custom synthesized guide RNA (gRNA) (IDT) were cloned into the pSpCas9 (BB)-2A-Puro V2.0 (Addgene #62988) following BbsI digestion. Positive insertion of guide RNA was verified by Sanger sequencing using at UBC Sequencing + Bioinformatics Consortium. The gRNA sequences used in this study are ATG5(5'-GAACTTGTTTCACGCTATATC-3'), ATG16L1(5'-GATTCTCTGCATTAAG CCGAT-3'), FIP200 (5′-CAGGTGCTGGTGGTCAATGG -3′), BECN1(5'-GCACA CGAAGCTCACCTGCA-3'),WIPI2(5'-GCAGCTACTCCAACACGATTC-3'),ATG9A(5'-GCCTGTTGGTGCACGTCG CCG-3'), and PI4KIIIβ (5'-GTGTGGGGTACACGGACC ACG-3'). Positive clones from plasmid-transfected cells were isolated by single-cell selection using serial dilution in 96-well plates following 48h puromycin treatment (2-7 μg/ml). Colonies from single cells were monitored for up to 14 days before splitting and re-seeding in 6-well plates. Growing clones were verified for knockout efficiency by western blot analysis.

Plasmids and small interfering RNA (siRNA)

The myc-tagged wild-type CVB3-3C (3Cwt) and C147A mutant CVB3-3C (3Cmut) constructs were generous gifts from Dr. Carolyn Coyne at the University of Pittsburgh [114]. The GFP-LC3 plasmid was from Dr. Sharon Tooze at the Francis Crick Institute London [115]. The mRFP-GFP-LC3 plasmid was a gift from Dr. Tamotsu Yoshimori (Addgene, 21074). The GFP-STX17TM was generated by cloning STX17TM into the pEGF-C1 backbone at the BglII and EcoRI cut-sites with the following primers (forward: 5'-AGATCTCTGGCAGCTCTGCCTGTGG-3'; reverse: 5'-

GAATTCTTAACTGCATTTCTTGTCAGTTTGGCTGGGAAGAT-3'). The 3×Flag-ULK1, 3×Flag-ATG16L1, and 3×Flag-PI4KIIIβ plasmids were generated using a multiple cloning site modified CMV10 vector backbone with the corresponding cut sites for ULK1 (EcorI/BamHI), ATG16L1 (EcorI/XbaI) and PI4KIIIβ (EcoRV/XbaI). Mutant 3×Flag-ULK1 Q524L was generated using a gBLOCKS fragment (Integrated DNA Technologies) harbouring the point mutation A1571T in the ULK1 coding sequence and cloned using restriction enzymes FseI and AflII. The GFP-UVRAG was generated using the pEGF-C1 backbone at the BspEI and KpnI cut sites. The scrambled siRNA (sc-37007) and the siRNAs targeting FIP200 (sc-38211), ATG13 (sc-97013), BECN1 (sc-29797), PIK3C3 (sc-62802), WIPI2 (sc-72212), ATG9 (sc-72586), and PIKfyve (sc-39142) were purchased from Santa Cruz Biotechnology. The siRNA targeting PI4KIIIβ was obtained from Dharmacon (D-006777-02). For transfection, cells were transiently transfected with plasmid cDNAs or siRNAs using Lipofectamine 2000 (Invitrogen, 11668-019) following the manufacturer's instructions.

Western blot analysis

Cells were lysed for 15min on ice in lysis buffer (10mM HEPES pH 7.4, 50mM NaPyrophosphate, 50 mM NaF, 50mM NaCl, 5 mM EDTA, 5mM EGTA, 100 µM Na_3VO_4, 0.1% Triton X-100) supplemented with cOmplete Mini, EDTA-free protease inhibitor cocktail tablets (Sigma, #11836170001). Lysates were centrifuged at 4°C for 15min at 12,000g and supernatant transferred to new Eppendorf tubes. Protein concentration was measured using Bio-Rad Protein Assay Dye Reagent (Bio-Rad, #5000006). Equal concentration of protein (~30ug) was used for western analysis. Western blotting was conducted using the following primary antibodies: LC3 (Novus Biologicals, NB100-2220), actin-*beta* (ACTB, Sigma-Aldrich, A5316), ATG5 (Santa Cruz, sc-33210), FIP200 (Cell Signaling Technology, D10D11), ATG13 (Cell Signaling Technology, D4P1K), BECN1 (Santa Cruz, sc-48341), PIK3C3 (Santa Cruz, sc365404), WIPI2 (Cell Signaling Technology, #8567), ATG9A (Cell Signaling Technology, D4O9D), ULK1 (Santa Cruz, sc-390904), ULK2 (GeneTex, GTX111476), UVRAG (Santa Cruz, sc-293268), ATG14 (Cell Signaling Technology, #5504), ATG7 (Santa Cruz, sc-376212), ATG12 (Santa Cruz, sc-271688), ATG16L1 (Santa Cruz, sc-393274), cleaved-caspase 3 (Cell Signaling Technology, #9661), viral capsid protein 1 (VP1, Dako, M706401-1), FLAG (Sigma, F1804), GFP (Life Technologies, A-6455), PI4KIIIβ (Sigma 06578), PIKfyve (Santa Cruz, sc-100408), and Rubicon

(Cell Signaling Technology, D8B2). Primary antibodies were used at 1:1000 dilution. Secondary anti-mouse HRP (Invitrogen, #31430) or anti-rabbit HRP (Invitrogen, # 31460) were used at 1:5000 dilution. Western blotting was performed on a Bio-Rad Mini Trans-Blot Electrophoretic System (Bio-Rad, #1703930).

Densitometry Analysis

Densitometry of protein bands was measured using NIH Image J software. Briefly, gel images were saved in high resolution TIFF format using Syngene software of the GBOX (Model: Chemi XRQ). Images were exported to Image J software and manually processed using the gel analysis function. Images were carefully selected to avoid oversaturation and non-linear signal intensities. Individual bands were selected to generate intensity peaks, and each intensity peak was segregated to generate area under measurements. Background intensity was equally subtracted from all intensity peaks using the linear segregation tool. Area under the curve was averaged among biological replicates (n=3) for quantification analysis.

Immunofluorescence and confocal microscopy

After fixation with 4% paraformaldehyde and permeabilization (0.1% Triton), cells were blocked for 1h with 3% bovine serum albumin, followed by incubation with primary antibodies at 4ºC overnight and then secondary antibodies at room temperature for 1h. After PBS washes, coverslips were mounted using Fluoroshield with 4, 6-diamidino-2-phenylindole (DAPI, Sigma-Aldrich, F6057). Images were captured with the Zeiss LSM 880 Inverted Confocal Microscopy/ Zen Black Software using the 63x oil immersion objective. LC3 puncta per cell was quantified using the Spot Detector plugin in the open source bio-imaging software Icy 1.9.5.0. as previously described [116].

Animals

The breeding pairs of autophagic reporter mice expressing GFP-LC3 were obtained from the RIKEN BioResource Center (#00806) and the background C57BL/6 mice were purchased from the Jackson Laboratories (#000664). These mice were bred in the Center for Heart Lung Innovation animal facility. PCR genotyping was performed to identify wild-type (WT), hemizygous (WT/Tg) and homozygous (Tg/Tg) GFP-LC3 mice as described [117]. Male

homozygous GFP-LC3 and C57BL/6 mice at the age of ~5 weeks were inoculated intraperitoneally with 10^4 plaque-forming units (pfu) of CVB3 (Charles Gauntt strain) or sham-infected with PBS as previously described [118]. At 3 or 9 days post-infection, mice were sacrificed and tissues were harvested for confocal imaging, immunohistochemical staining, Western blotting, and plaque assay. Heart tissue was perfused with PBS to remove excess blood and equally portioned into three segment separating the base (for plaque assay), mid-section (for ICC and H&E staining), and apex (for western analysis). Base segment was weighed and supplemented with sterile DMEM at a ratio of 50mg tissue/ 1 mL DMEM. Tissue was crushed in a sterile dounce homogenizer and subjected to serial dilution for subsequent plaque assay. Cardiac mid-segment was placed in tissue cassette and fixed for 24h in 4% formalin. Tissue blocks where submitted to HLI Histology Laboratory for embedding/cutting of paraffin blocks and routine hematoxylin and eosin staining. Apex segment was frozen in mortar chamber containing liquid nitrogen and crushed to fine powder. Dried tissue was reconstituted in MOSLB lysis buffer and protein concentration was assessed with Bio-Rad Protein Assay Dye Reagent. All mouse studies were carried out in accordance with the Guide for the Care and Use of Laboratory Animals of the Canadian Council on Animal Care. The protocol (A13-0321) for this research was approved by the Animal Care Committee of the University of British Columbia.

Results

CVB3-induced LC3 puncta and lipidation require ATG5 and ATG16L1

To measure the effect of CVB3 infection on autophagy initiation, human embryonic kidney (HEK293A) cells were selected due to their low levels of background autophagy under basal conditions[119, 120]. HEK293A cells were infected with CVB3 for different time-points. Protein expression of autophagosome-associated LC3-II, a marker of autophagosomes, was analyzed by western blotting. **Figure 7A** demonstrated that, as compared to sham-infected cells, there was a significant increase in LC3-II protein levels upon CVB3 infection, starting at ~8h and persisting for up to 24h post-infection. To determine the molecular mechanism by which CVB3 triggers autophagy, I first examined the role of canonical autophagy factors in this process. The established upstream autophagy pathways induced by amino acid deprivation are illustrated in **Figure 7B**. A previous study made the surprising observation that Vaccinia virus can induce LC3 lipidation independent of ATG5 and ATG7 [121]. Thus, I initially investigated whether ubiquitin-like

conjugation systems are required for CVB3-induced LC3 lipidation. Utilizing the CRISPR-Cas9 system, I knocked out (KO) ATG5 or ATG16L1 in HEK293A cells. As shown in **Figure 7C**, compared to wild-type (WT) cells, CVB3 infection failed to induce LC3-II formation in both ATG5-KO and ATG16L1-KO cells, suggesting an ATG5- and ATG16L1-dependent process. This finding was confirmed in $ATG5^{-/-}$ mouse embryonic fibroblasts (MEFs) transiently transfected with mRFP-GFP-LC3 plasmid that has been widely used to monitor autophagic flux [122]. **Figure 7D** showed that, in WT-MEFs, CVB3 infection led to a marked increase of cells with LC3 puncta. However, cells positive for LC3 puncta were significantly reduced when ATG5 was deleted. Together, these results suggest that unlike Vaccinia virus, CVB3-induced LC3 lipidation and puncta require the ubiquitin-like conjugation enzymes of the autophagy pathway.

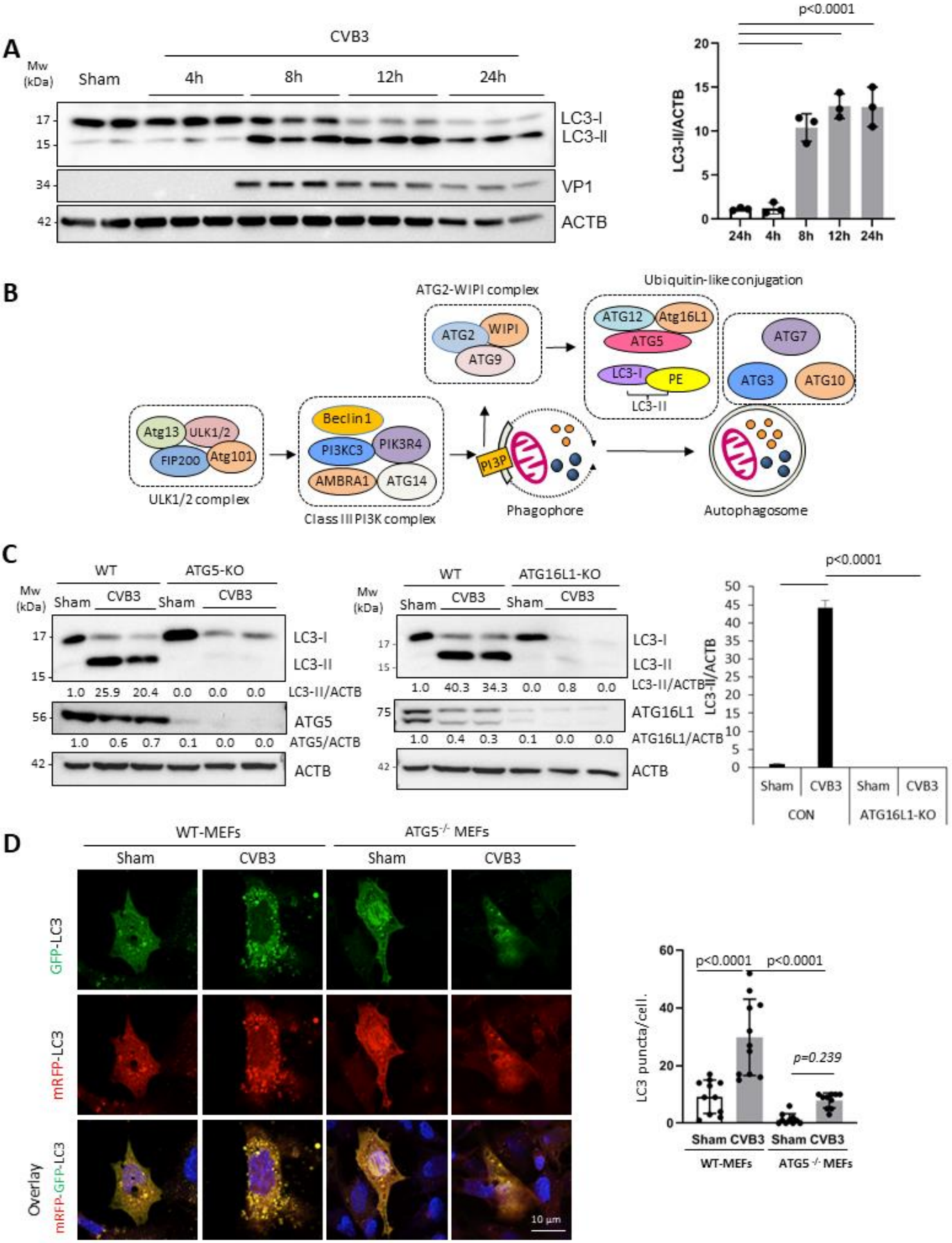
A
CVB3
Mw (kDa)
Sham
4h
8h
12h
24h
17
15
34
42
LC3-I
LC3-II
VP1
ACTB
p<0.0001
LC3-II/ACTB
20
15
10
5
0
24h
4h
8h
12h
24h
B
ATG2-WIPI complex
ATG2
WIPI
ATG9
Ubiquitin-like conjugation
ATG12
Atg16L1
ATG5
LC3-I
PE
LC3-II
ATG7
ATG3
ATG10
Atg13
ULK1/2
FIP200
Atg101
ULK1/2 complex
Beclin1
PI3KC3
PIK3R4
AMBRA1
ATG14
Class III PI3K complex
PI3P
Phagophore
Autophagosome
C
WT
ATG5-KO
Mw (kDa)
Sham
CVB3
Sham
CVB3
17
15
LC3-I
LC3-II
1.0 25.9 20.4 0.0 0.0 0.0
LC3-II/ACTB
56
ATG5
1.0 0.6 0.7 0.1 0.0 0.0
ATG5/ACTB
42
ACTB
WT
ATG16L1-KO
Mw (kDa)
Sham
CVB3
Sham
CVB3
17
15
LC3-I
LC3-II
1.0 40.3 34.3 0.0 0.8 0.0
LC3-II/ACTB
75
ATG16L1
1.0 0.4 0.3 0.1 0.0 0.0
ATG16L1/ACTB
42
ACTB
p<0.0001
LC3-II/ACTB
50
45
40
35
30
25
20
15
10
5
0
Sham
CVB3
Sham
CVB3
CON
ATG16L1-KO
D
WT-MEFs
ATG5-/- MEFs
Sham
CVB3
Sham
CVB3
GFP-LC3
mRFP-LC3
Overlay
mRFP-GFP-LC3
10 μm
LC3 puncta/cell.
60
40
20
0
p<0.0001
p<0.0001
p=0.239
Sham
CVB3
Sham
CVB3
WT-MEFs
ATG5-/- MEFs

Figure 7. CVB3-induced LC3 puncta and lipidation are dependent on ATG5 and ATG16L1. **(A)** HEK293A were either sham-infected with PBS or infected with CVB3 (MOI=100) for indicated time-points. Western blotting was performed to detect LC3 lipidation and ACTB expression (loading control). Levels of LC3-II were quantified by densitometric analysis as described in materials and methods, normalized to ACTB and presented as fold changes in the right panel (mean±SD, n=3, analyzed by one-way ANOVA with Tukey's post-test). **(B)** Schematic diagram of canonical autophagy pathway induced by amino acid deprivation. **(C)** ATG5- or ATG16L1-knockout (KO) HEK293A cells generated *via* CRISPR-Cas9 editing, or wildtype (WT)-HEK293A cells were either sham- or CVB3-infected for 16h. Cell lysates were harvested and probed for LC3, ATG5, and ATG16L1 by Western blotting. Densitometric analysis was carried out as above (the first lane is arbitrarily set a value of 1) and the results are presented under each blot. **(D)** WT- or $Atg5^{-/-}$ MEFs transfected with mRFP-GFP-LC3 construct were sham- or CVB3-infected for 8h. GFP and RFP signal was captured by confocal microscopy. Mean LC3 puncta per cell was quantified (n≥10 cells) and analyzed by one-way ANOVA with Tukey post-test (right).

CVB3-induced LC3 lipidation occurs independent of FIP200 and ATG13

Next I sought to more closely address whether CVB3-induced LC3 lipidation utilizes the upstream canonical autophagy initiation machinery. As illustrated in **Figure 7B**, during starvation, autophagy induction is regulated by the ULK complex that consists of ULK1/2 kinases, ATG13, RB1CC1/FIP200, and ATG101 [123]. RB1CC1/FIP200 is an essential component of the ULK complex and its genetic ablation was previously demonstrated to abrogate the canonical autophagy pathway [124]. FIP200-KO HEK293A cells were generated through CRISPR-Cas9 gene editing (**Figure 8A, left**). To recapitulate previous findings and validate our FIP200-KO cells, I performed starvation treatment in the absence or presence of bafilomycin A1 (BAF), a vacuolar-ATPase inhibitor that blocks the autophagosome-lysosome fusion process required for degradative autophagy. Autophagy flux can be measured by comparing the levels of LC3-II in the absence or presence of BAF. As expected, starvation-induced autophagy flux was dramatically impaired in FIP200-KO compared to WT cells, supporting an important role for FIP200 in starvation-induced autophagy (**Figure 8A, middle**). Following the recommended guidelines for the use and interpretations of assays for monitoring autophagy, LC3-II was normalized to the loading control, ACTB, as opposed to LC3-I. These recommendations take into account the instability of LC3-I during freeze-thaw processing of lysates, differential abundance of LC3-I across multiple tissues, and differential sensitivity of anti-LC3 antibodies for LC3-I. It was previously reported that modulation of vesicle acidification, including treatment with BAF1, significantly impairs enteroviral replication [73, 91]. To eliminate this confounding variable, CVB3 infected cells were not treated with BAF-A1. I next tested whether loss of FIP200 would have an effect on CVB3-induced LC3 lipidation. Compared to control cells, FIP200-KO HEK293A cells that are infected with CVB3 demonstrated comparable accumulation of LC3-II (**Figure 8A, right**). Similar buildup of LC3-II was observed in CVB3-infected cells in which FIP200 was transiently silenced using siRNA as compared to cells treated with a scrambled siRNA (**Figure 8B**). To corroborate these observations, I also examined whether gene-silencing of ATG13, another essential component of the ULK complex [125], would impact CVB3-induced LC3 lipidation. Indeed, knockdown of ATG13 using siRNA resulted in a comparable accumulation of LC3-II in CVB3-infected cells as that observed in control siRNA-treated cells **(Figure 8C)**. Given that ULK1/2 are required for starvation-induced autophagy, I also tested whether ULK1/2 kinase activity plays a role in CVB3-induced LC3 lipidation using the chemical compound MRT68921, a potent inhibitor of both

ULK1/2 [126]. Whereas treatment of HEK293A cells with MRT68921 completely abrogated starvation-induced autophagy, similar treatment in CVB3-infected cells did not reduce LC3-II accumulation (**Figure 8D)**. Collectively, these data suggest that the ULK complex is dispensable for CVB3-induced LC3 lipidation, in agreement with a previous finding with PV [111].

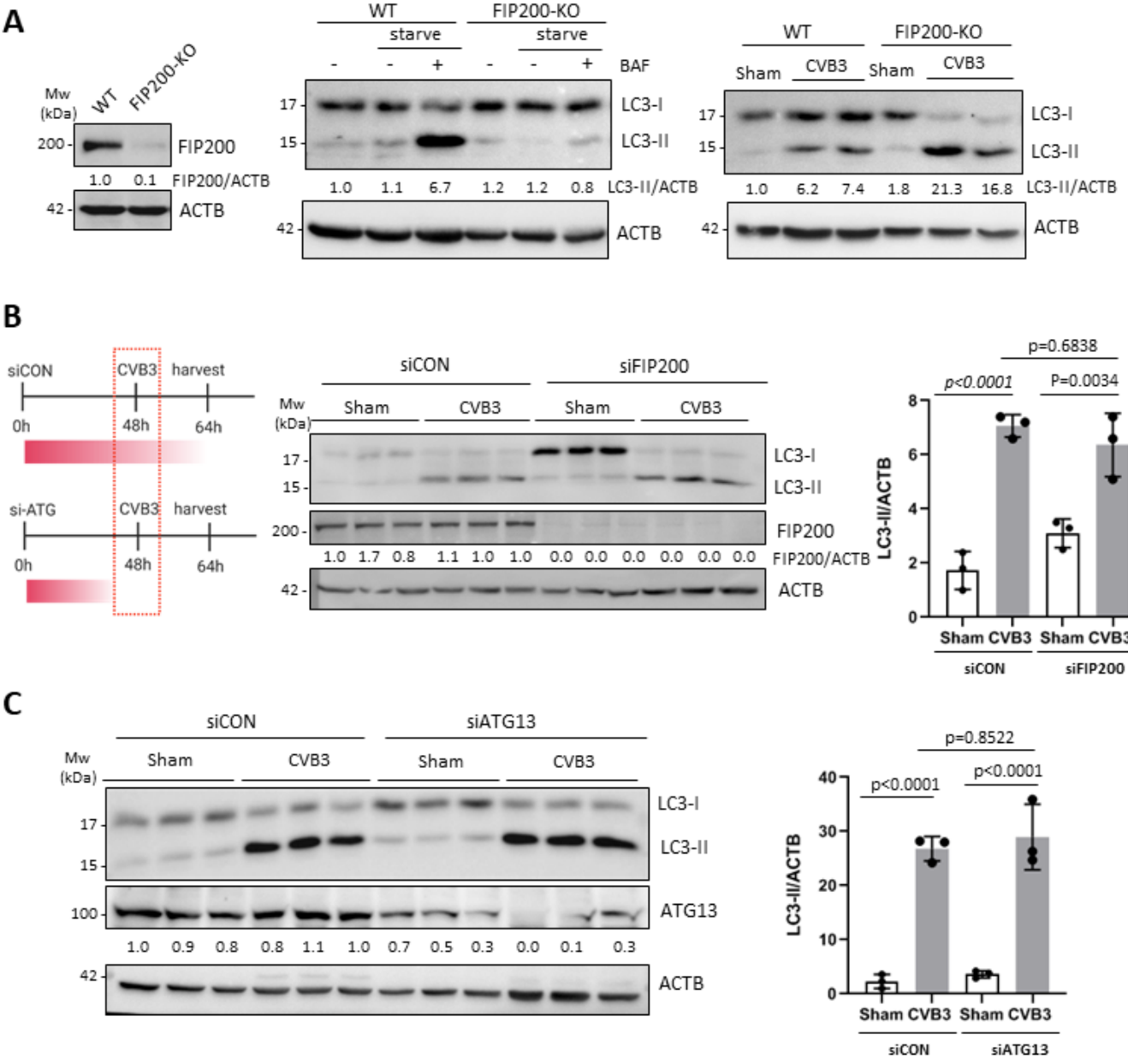
A
WT
FIP200-KO
starve
BAF
Mw (kDa)
200
FIP200
1.0 0.1 FIP200/ACTB
42
ACTB
17
15
LC3-I
LC3-II
1.0 1.1 6.7 1.2 1.2 0.8 LC3-II/ACTB
Sham
CVB3
1.0 6.2 7.4 1.8 21.3 16.8 LC3-II/ACTB
B
siCON
CVB3
harvest
0h
48h
64h
si-ATG
siFIP200
1.0 1.7 0.8 1.1 1.0 1.0 0.0 0.0 0.0 0.0 0.0 0.0 FIP200/ACTB
p=0.6838
p<0.0001
P=0.0034
LC3-II/ACTB
Sham CVB3 Sham CVB3
siCON
siFIP200
C
siATG13
100
ATG13
1.0 0.9 0.8 0.8 1.1 1.0 0.7 0.5 0.3 0.0 0.1 0.3
p=0.8522
p<0.0001
p<0.0001
siATG13
D
Starve
MRT68921
1.0 5.2 0.9 0.9 LC3-II/ACTB
1.0 2.7 0.5 6.2 LC3-II/ACTB

Figure 8. CVB3-induced LC3 lipidation occurs independent of FIP200 and ATG13. (A) FIP200-KO HEK293A cells were established through CRISPR-Cas9 gene editing. Knockout efficiency was validated by western blotting (left panel). WT-HEK293A or FIP200-KO cells were cultured in either normal medium, HBSS starvation medium, or starvation medium supplemented with 200nM bafilomycin (BAF) for 2h (middle panel). WT or FIP200-KO cells were sham (PBS) - or CVB3-infected (MOI=100) for 16h (right panel). Western blotting was performed for analysis of LC3 lipidation. Multiple FIP200-KO clones were assessed during screening of CRISPR-KO cells whereas data presented in panel A is representative of a single FIP200-KO clone. **(B & C)** Schematic of siRNA-based gene silencing and CVB3 infection schedule (left), HEK293A cells were transiently transfected with scrambled siRNA control (siCON) or siRNAs against FIP200 (B) or ATG13 (C) for 48h. Cells were then subjected to sham or CVB3 infection for an additional 16h. Western blotting was conducted to determine knockdown efficiency and LC3 lipidation. Densitometry was measured as above and the results are presented either underneath the blots or in the right panel (mean±SD, n=3, analyzed by one-way ANOVA with Tukey's post-test). **(D)** HEK293A cells were treated with a selective ULK1/2 kinase inhibitor (MRT68921, 5μM) under starvation for 2h in the presence or absence of 200nM BAF (left panel). HEK293A cells were sham- or CVB3-infected for 16h with or without 5μM MRT68921 (right panel). Western blotting was performed to examine LC3 levels and the quantified results are shown underneath the blots.

CVB3-induced LC3 lipidation is independent of BECN and PIK3C3

Downstream of the ULK complex is the PI3P-generating PI3K complex that consists of BECN1, ATG14, PIK3C3, PIK3R4, and AMBRA1 (**Figure 7B**) [127]. To determine the possible involvement of the PI3K complex in CVB3-induced LC3 lipidation, BECN1-KO HEK293A cells were generated using CRISPR-Cas 9 approach. Upon verification of the KO efficiency through western blot analysis **(Figure 9A, left)**, the cells were subjected to starvation treatment in the presence or absence of BAF. Similar to the observation in FIP200-KO cells, starvation-induced autophagy was impaired in BECN1-KO cells (**Figure 9A, middle**). However, CVB3-induced LC3-II accumulation was comparable between control and BECN1-KO cells, suggesting that the process is independent of BECN1 **(Figure 9A, right)**. LC3-II accumulation was also observed in CVB3-infected cells subjected to transient silencing of BECN1 **(Figure 9B)** or PIK3C3, the active catalytic subunit of the PI3K complex **(Figure 9C)**. Taken together, these data suggest that CVB3 infection promotes LC3-II production independent of BECN1 and PIK3C3.

CVB3-induced LC3 lipidation is independent of ATG9 and WIPI2

With the evidence that CVB3-induced autophagy is independent of the ULK1/2 and PI3K complexes, I next set out to address whether CVB3 can bypass upstream autophagy initiators to directly influence autophagosome biogenesis. During canonical autophagy, the activity of the lipid kinase PI3K complex results in the enrichment of autophagic membranes with PI3P. Phosphorylated lipids then serve as recruitment hubs for downstream proteins harboring PI3P interacting domains such as WIPI2 and DFCP1, that may further recruit LC3-lipidation complexes and membranes *via* ATG9 (**Figure 7B**) [128, 129]. WIPI2 and ATG9A were transiently silenced in HEK293A cells using siRNAs, followed by sham or CVB3 infection. Similar to the observations above, LC3 lipidation was induced upon CVB3 infection independent of WIPI2 and ATG9 **(Figure 10A & B)**. Moreover, WIPI2-KO and ATG9A-KO cells generated *via* CRISPR-Cas9 engineering showed no significant impairment in CVB3-induced LC3 lipidation (**Figure 10C**). Collectively, these data indicate that CVB3 initiates autophagy independent of ATG9 and WIPI2.

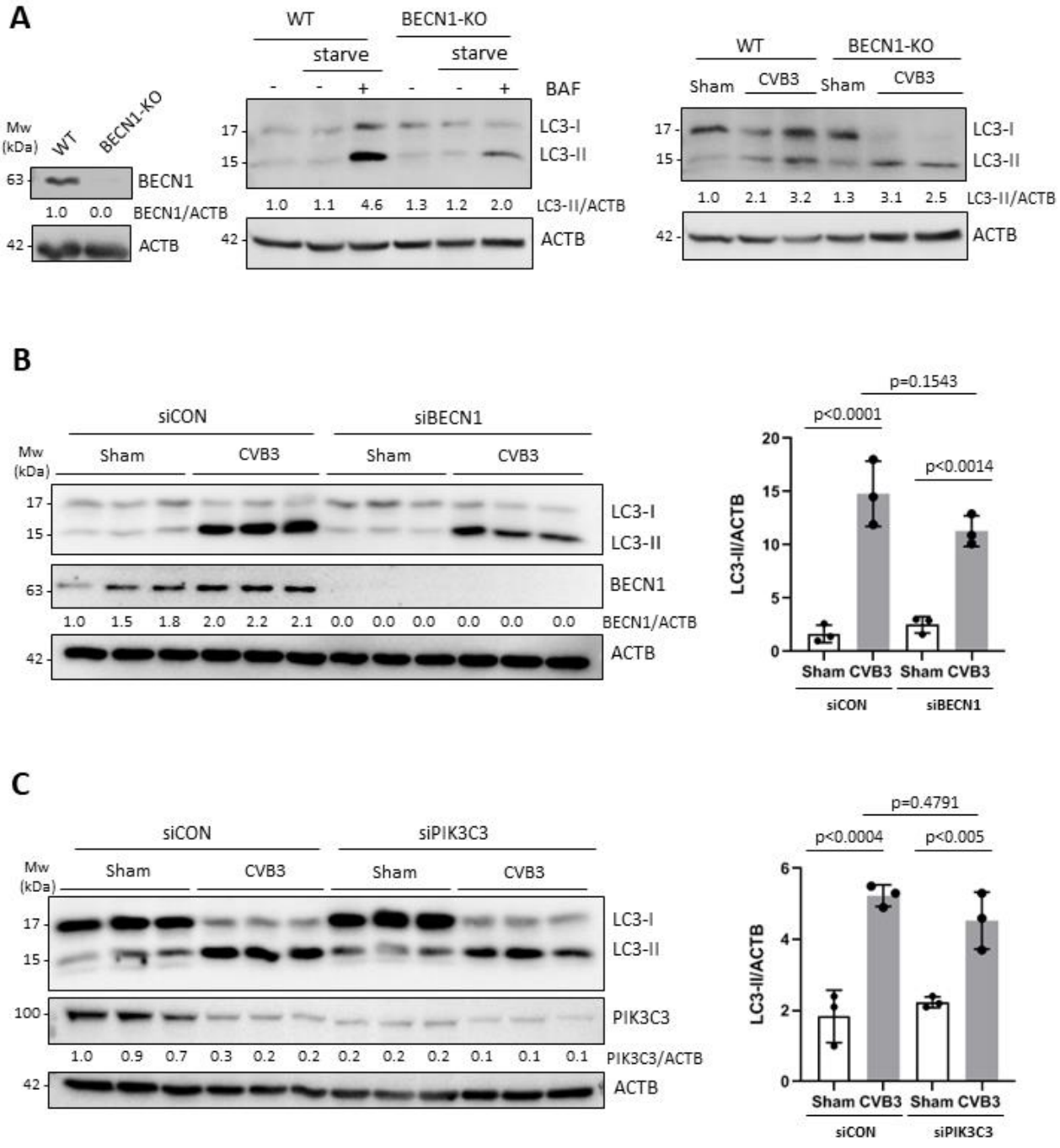
A
WT
BECN1-KO
starve
starve
BAF
Mw (kDa)
WT
BECN1-KO
63
BECN1
1.0 0.0
BECN1/ACTB
42
ACTB
17
15
LC3-I
LC3-II
1.0 1.1 4.6 1.3 1.2 2.0
LC3-II/ACTB
ACTB
WT
BECN1-KO
Sham
CVB3
Sham
CVB3
17
15
LC3-I
LC3-II
1.0 2.1 3.2 1.3 3.1 2.5
LC3-II/ACTB
42
ACTB
B
siCON
siBECN1
Mw (kDa)
Sham
CVB3
Sham
CVB3
17
15
LC3-I
LC3-II
63
BECN1
1.0 1.5 1.8 2.0 2.2 2.1 0.0 0.0 0.0 0.0 0.0 0.0
BECN1/ACTB
42
ACTB
p=0.1543
p<0.0001
p<0.0014
LC3-II/ACTB
20
15
10
5
0
Sham CVB3 Sham CVB3
siCON
siBECN1
C
siCON
siPIK3C3
Mw (kDa)
Sham
CVB3
Sham
CVB3
17
15
LC3-I
LC3-II
100
PIK3C3
1.0 0.9 0.7 0.3 0.2 0.2 0.2 0.2 0.2 0.1 0.1 0.1
PIK3C3/ACTB
42
ACTB
p=0.4791
p<0.0004
p<0.005
LC3-II/ACTB
6
4
2
0
Sham CVB3 Sham CVB3
siCON
siPIK3C3

Figure 9. CVB3-induced LC3 lipidation is independent of BECN1 and PIK3C3. (A) BECN1-KO HEK293A cells were established through CRISPR-cas9 editing. Knockout efficiency was verified by western blotting (left panel). WT or BECN1-KO cells were cultured in either normal medium, HBSS starvation medium, or starvation medium supplemented with 200nM BAF for 2h, followed by western blot analysis of LC3 (middle panel). Multiple BECN1-KO clones were assessed during screening of CRISPR-KO cells whereas data presented in panel A is representative of a single BECN1-KO clone. WT or BECN1-KO cells were sham (PBS)- or CVB3-infected (MOI=100) for 16h, followed by western blot assessment of LC3 (right panel). **(B & C)** BECN1 (B) and PIK3C3 (C) were transiently silenced in HEK293A cells *via* siRNA treatment for 48h. Cells were then subjected to sham or CVB3 infection for 16h. Cells were harvested and subjected to western blot analysis of LC3, BECN1, and PIK3C3. Densitometric results are presented either underneath the blots or in the right panel (mean±SD, n=3, analyzed by one-way ANOVA with Tukey's post-test).

A

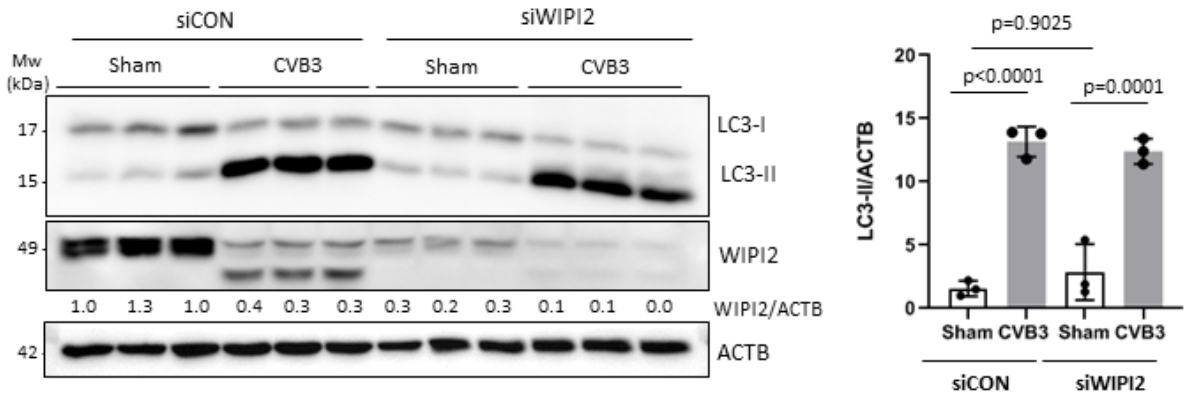
siCON
siWIPI2
Mw (kDa)
Sham
CVB3
Sham
CVB3
17
15
LC3-I
LC3-II
49
WIPI2
1.0 1.3 1.0 0.4 0.3 0.3 0.3 0.2 0.3 0.1 0.1 0.0
WIPI2/ACTB
42
ACTB
p=0.9025
p<0.0001
p=0.0001
LC3-II/ACTB
Sham CVB3 Sham CVB3
siCON
siWIPI2

B

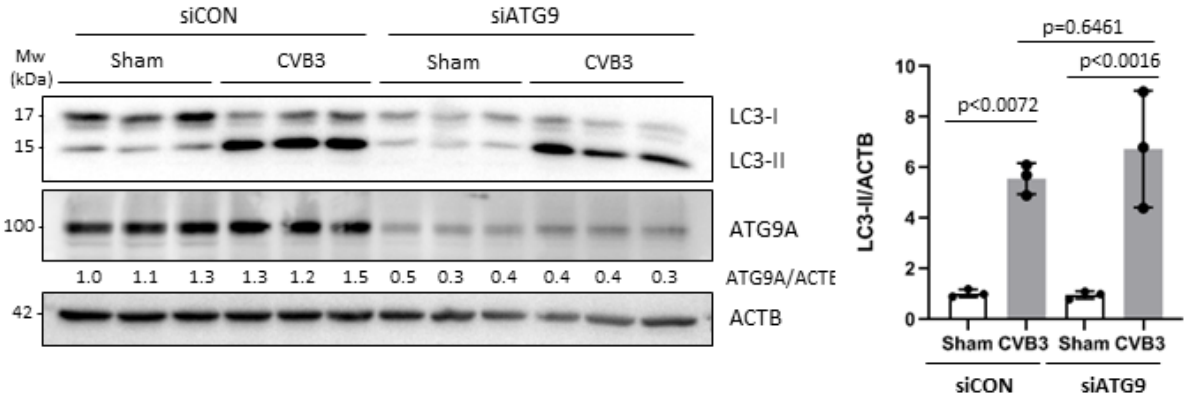
siCON
siATG9
Mw (kDa)
Sham
CVB3
Sham
CVB3
17
15
LC3-I
LC3-II
100
ATG9A
1.0 1.1 1.3 1.3 1.2 1.5 0.5 0.3 0.4 0.4 0.4 0.3
ATG9A/ACTB
42
ACTB
p=0.6461
p<0.0016
p<0.0072
LC3-II/ACTB
Sham CVB3 Sham CVB3
siCON
siATG9

C

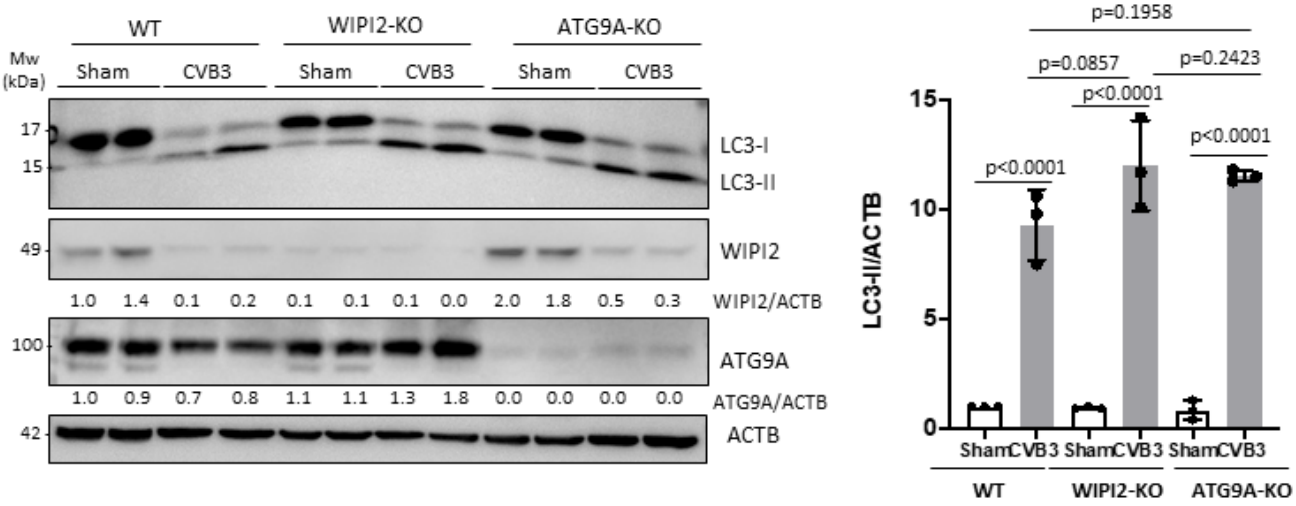
WT
WIPI2-KO
ATG9A-KO
Mw (kDa)
Sham
CVB3
Sham
CVB3
Sham
CVB3
17
15
LC3-I
LC3-II
49
WIPI2
1.0 1.4 0.1 0.2 0.1 0.1 0.1 0.0 2.0 1.8 0.5 0.3
WIPI2/ACTB
100
ATG9A
1.0 0.9 0.7 0.8 1.1 1.1 1.3 1.8 0.0 0.0 0.0 0.0
ATG9A/ACTB
42
ACTB
p=0.1958
p=0.0857
p=0.2423
p<0.0001
p<0.0001
p<0.0001
LC3-II/ACTB
Sham CVB3 Sham CVB3 Sham CVB3
WT
WIPI2-KO
ATG9A-KO

Figure 10. CVB3-induced LC3 lipidation is independent of ATG9 and WIPI2. (A & B) WIPI2 (A) and ATG9A (B) were transiently silenced in HEK293 cells through siRNA treatment for 48h. Cells were then sham- or CVB3-infected for 16h. Western blotting was conducted to verify the knockdown efficiency and to examine LC3 levels. Densitometric results are presented either underneath the blots or in the right panel (mean±SD, n=3, analyzed by one-way ANOVA with Tukey's post-test). **(C)** WIPI2-KO and ATG9A-KO HEK293A cells, generated through CRISPR-Cas9 gene editing, were sham (PBS)- or CVB3-infected (MOI=100) as above, followed by western blot analysis of LC3, WIPI2, and ATG9A. Densitometry was measured as described in materials and methods and presented as above.

Several autophagy proteins are targeted during CVB3 infection

To investigate the direct effects of CVB3 infection on critical components of the canonical autophagy pathway, I proceeded to closely measure the levels of autophagy proteins during a 24h time-course of CVB3 infection in HEK293A cells. I first examined components of the ULK1/2 complex and observed a significant reduction in protein levels of ULK1, ULK2, RB1CC1/FIP200, and ATG13. Of note, the protein loss of ULK1 was accompanied by the emergence of lower molecular weight fragments (~75kDa) at ~8h post-infection **(Figures 11A)**. Similarly, protein levels of major components of the PI3K and WIPI complexes, including BECN1, UVRAG, PIK3C3, ATG14, WIPI2, and ATG9A, were also decreased following CVB3 infection (**Figures 11B-C).** The decrease in autophagy proteins following CVB3 infection was most pronounced when cells were infected in the absence of transient transfection (e.g. during RNAi or plasmid overexpression) as transient transfection was previously reported to impair and/or delay viral replication [130].

The significant reduction in ULK1 protein levels accompanied by the detection of lower molecular weight fragments prompted us to explore the potential role of virus-encoded proteinases. *In vitro* cleavage assay was performed using cell lysates incubated with either vehicle control, purified WT viral proteinase 3C ($3C^{wt}$) or catalytically inactive 3C (C147A) mutant ($3C^{mut}$). I found that $3C^{wt}$, but not $3C^{mut}$, was able to significantly reduce the full-length proform and recapitulate cleavage fragments observed in CVB3-infected cells (**Figure 12A)**. Similarly, cells co-transfected with 3×Flag-ULK1 (~135 kDa) and myc-tagged $3C^{wt}$ but not myc-$3C^{mut}$ displayed the 75kDa-cleavage fragments **(Figure 12B**). To exclude the possible role of host caspases that are activated during the late stage of CVB3 infection in the cleavage of ULK1, I utilized the pan-caspase inhibitor zVAD-fmk. I found that caspase inhibition failed to attenuate CVB3-induced cleavage of ULK1 **(Figure 13C**). Site-directed mutagenesis was utilized to further identify the site of viral proteinase 3C cleavage of ULK1. **Figure 13D** showed that ULK^{Q524L} mutant was resistant to CVB3-induced cleavage, suggesting that the cleavage takes place at this position although it cannot be excluded that additional cleavages may take place. This cleavage led to the separation of the N-terminal kinase domain and the GABARAP interacting region (GIR) from the C-terminal domain (CTD) of substrate binding (**Figure 12E)**. Of interest, expression of wild-type ULK1 led to impaired viral replication compared to vector control while non-cleavable $ULK1^{Q524L}$ further reduced viral titers (**Figure 12F**). Taken together, these data support that viral proteinase 3C is

responsible for the cleavage of ULK1 during CVB3 infection and that cleavage of ULK1 may enhance viral replication.

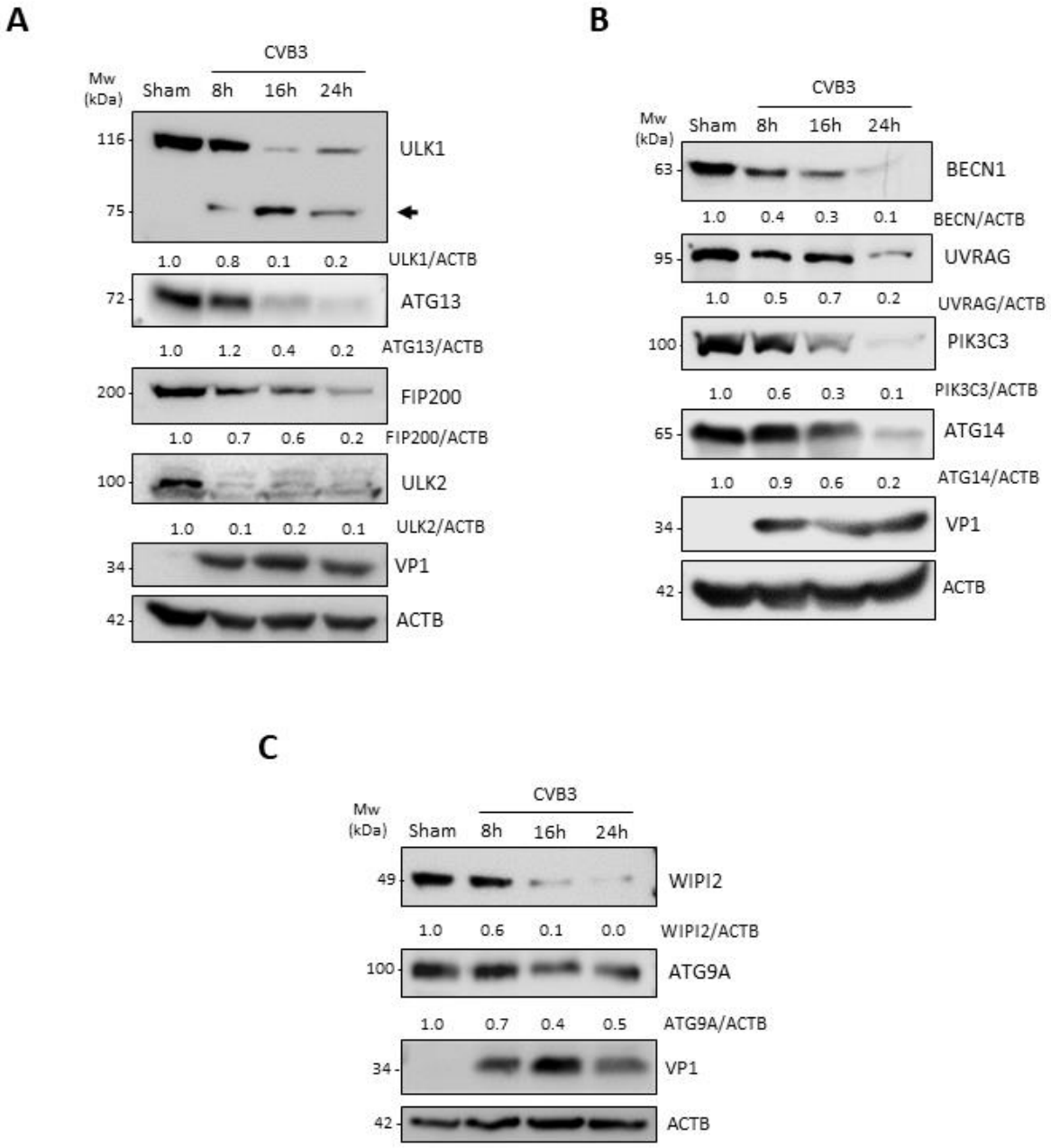
A
CVB3
Mw (kDa)
Sham
8h
16h
24h
116
ULK1
75
1.0 0.8 0.1 0.2
ULK1/ACTB
72
ATG13
1.0 1.2 0.4 0.2
ATG13/ACTB
200
FIP200
1.0 0.7 0.6 0.2
FIP200/ACTB
100
ULK2
1.0 0.1 0.2 0.1
ULK2/ACTB
34
VP1
42
ACTB
B
CVB3
Mw (kDa)
Sham
8h
16h
24h
63
BECN1
1.0 0.4 0.3 0.1
BECN/ACTB
95
UVRAG
1.0 0.5 0.7 0.2
UVRAG/ACTB
100
PIK3C3
1.0 0.6 0.3 0.1
PIK3C3/ACTB
65
ATG14
1.0 0.9 0.6 0.2
ATG14/ACTB
34
VP1
42
ACTB
C
CVB3
Mw (kDa)
Sham
8h
16h
24h
49
WIPI2
1.0 0.6 0.1 0.0
WIPI2/ACTB
100
ATG9A
1.0 0.7 0.4 0.5
ATG9A/ACTB
34
VP1
42
ACTB

Figure 11. CVB3 targets several autophagy proteins in HEK293A cells. (A-C) HEK293A cells were sham (PBS) - or CVB3-infected (MOI=100) for 8h, 16h, or 24h as indicated. Cell lysates were harvested and probed for ULK1, ATG13, FIP200, and ULK2, components of the ULK1/2 complex (A), BECN1, UVRAG, PIK3C3, and ATG14, components of the PI3K complex (B), and WIPI2 and ATG9A, components of the WIPI complex (C). Protein levels were quantified and presented underneath each western blot as described in materials and methods.

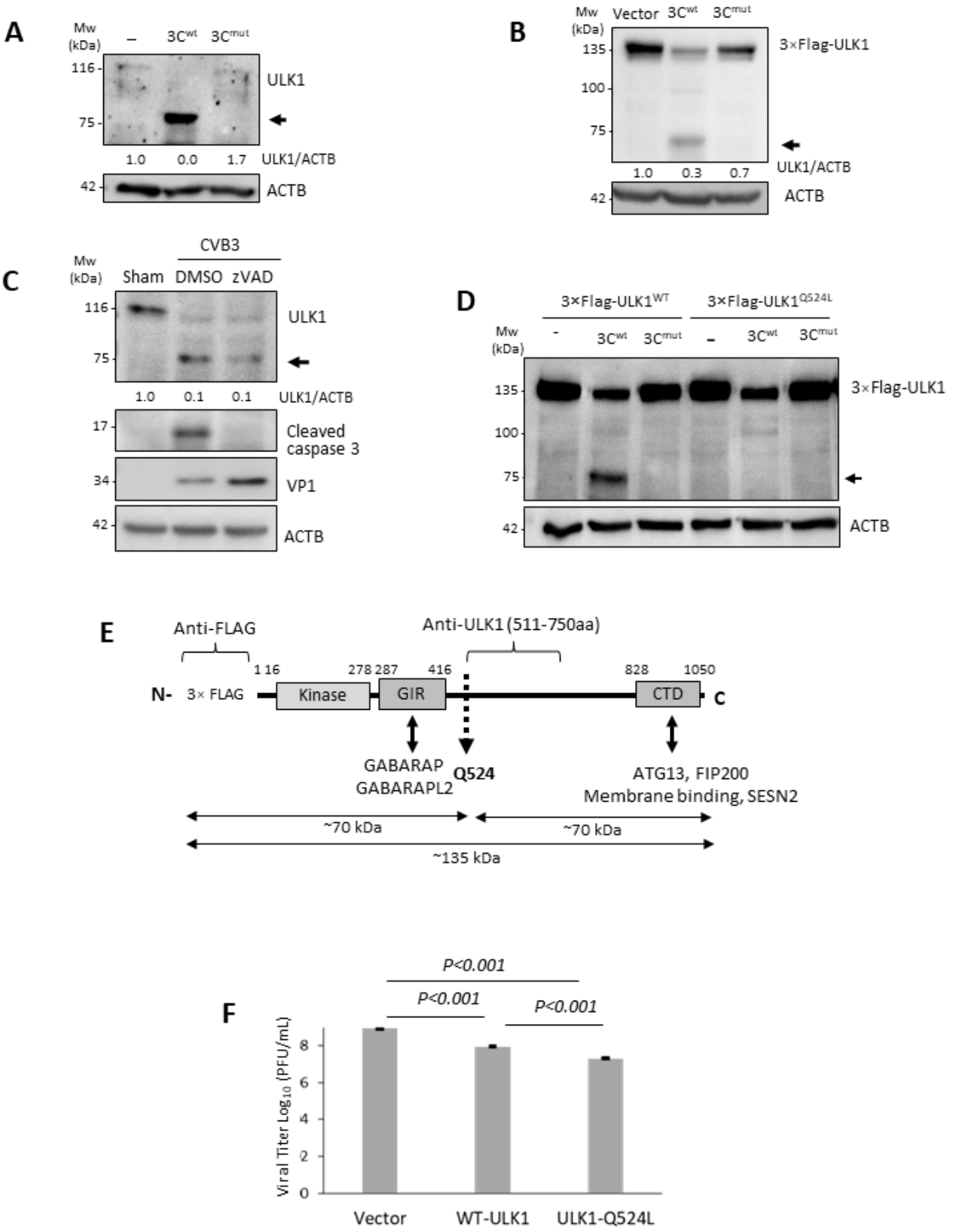
A
Mw (kDa)
–
3C^wt
3C^mut
116
75
ULK1
1.0
0.0
1.7
ULK1/ACTB
42
ACTB
B
Mw (kDa)
Vector
3C^wt
3C^mut
135
100
75
3×Flag-ULK1
1.0
0.3
0.7
ULK1/ACTB
42
ACTB
C
CVB3
Mw (kDa)
Sham
DMSO
zVAD
116
75
ULK1
1.0
0.1
0.1
ULK1/ACTB
17
Cleaved caspase 3
34
VP1
42
ACTB
D
3×Flag-ULK1^WT
3×Flag-ULK1^Q524L
Mw (kDa)
-
3C^wt
3C^mut
–
3C^wt
3C^mut
135
100
75
3×Flag-ULK1
42
ACTB
E
Anti-FLAG
Anti-ULK1 (511-750aa)
1 16
278 287
416
828
1050
N-
3× FLAG
Kinase
GIR
CTD
C
GABARAP
GABARAPL2
Q524
ATG13, FIP200
Membrane binding, SESN2
~70 kDa
~70 kDa
~135 kDa
F
P<0.001
P<0.001
P<0.001
Viral Titer Log10 (PFU/mL)
0
2
4
6
8
Vector
WT-ULK1
ULK1-Q524L

Figure 12. Viral proteinase 3C cleaves ULK1 after glutamine 524. (A) *In vitro* cleavage assay was performed by incubating lysates from HeLa cells with vehicle (−), purified wildtype 3C ($3C^{wt}$), or catalytically inactive 3C (C147A) mutant ($3C^{mut}$) proteins, followed by western blot analysis of ULK1 using an antibody that recognizes an internal region (amino acids 511 to 750) of ULK1. Arrow denotes the cleavage fragment. **(B)** HeLa cells were transfected with 3×Flag-ULK1 together with either empty vector, myc-$3C^{wt}$, or myc-$3C^{mut}$ as indicated. After 24h, cell lysates were collected and analyzed by western blotting with antibodies against FLAG. **(C)** HeLa cells were infected with CVB3 for 7h in the presence or absence of a pan-caspase inhibitor z-VAD-FMK (zVAD, 50 μM) or DMSO (vehicle). Western blotting was performed with antibodies against ULK1. Activation of caspase-3 was examined using an anti-cleaved caspase-3 antibody. Densitometry was measured as above. **(D)** HeLa cells were co-transfected with 3×FLAG-$ULK1^{WT}$ or 3×FLAG-$ULK1^{Q524L}$ (Glutamine 524 mutated to Leucine), together with empty vector, myc-$3C^{wt}$, or myc-$3C^{mut}$. Western blotting was performed with an anti-FLAG antibody. **(E)** Schematic illustration of the structural domains, the identified cleavage site, the antibody recognition regions, and the resulting cleavage products of ULK1. *GIR*, GABARAP interacting region; *CTD*, C-terminal domain. (F) HEK293 cells were transfected with either vector control, WT-ULK1 or non-cleavable ULK1 (ULK1-Q524L) for 24 h followed by CVB3 infection for an additional 8 h. Supernatant was collected for viral titer measurement (mean±SD, n=3, analyzed by unpaired Student t-test).

PI4KIIIβ is an upstream factor in CVB3-induced autophagy

Our observations that canonical autophagy factors are dispensable for CVB3-induced autophagy, coupled with the findings that viral proteinase(s) target key autophagy proteins for degradation, suggest the existence of non-canonical, alternate autophagy pathways in initiating CVB3-induced autophagy. In addition to PI3P, both PI4P and PI5P have been identified as alternative phospholipids to induce autophagy [131, 132]. During EV infection, membrane-anchored viral protein 3A has been shown to recruit PI4KIIIβ to the viral replication organelles to promote the production of PI4P. PI4P in turn recruits viral polymerase 3D to initiate viral RNA synthesis (**Figure 13A**) [63, 133]. To test the role of PI4P in CVB3-induced autophagy, I genetically silenced PI4KIIIβ, a major enzyme regulating PI4P synthesis. I discovered that CVB3-induced LC3 lipidation is markedly inhibited in cells depleted of PI4KIIIβ compared to control siRNA-treated cells, suggesting a PI4P-dependent mechanism (**Figure 13B**). I next compared the role of PI4KIIIβ to PIK3C3 (a PI3P kinase) and PIKfyve (FYVE finger-containing phosphoinositide kinase, a PI5P kinase) in a single experiment. I found that the viral dose utilized in this study (MOI=100) had no major influence on viral replication, as evidenced by equal viral protein production among three groups. I confirmed that gene-silencing of PI4KIIIβ, but not PIK3C3 or PIKfyve, was responsible for the attenuation of CVB3-induced LC3 lipidation (**Figure 13C**).

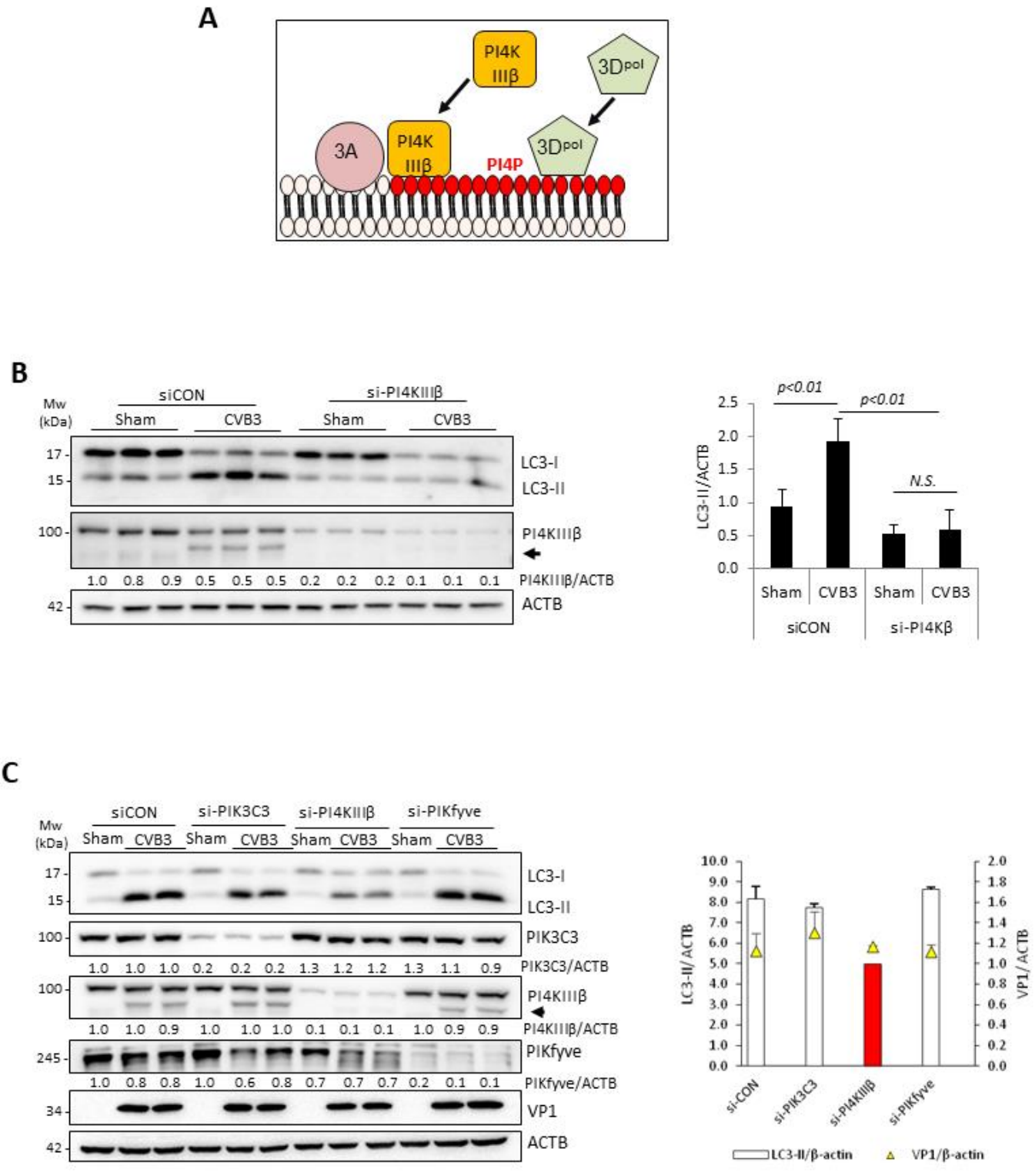
A
PI4K IIIβ
3Dpol
3A
PI4K IIIβ
3Dpol
PI4P
B
Mw (kDa)
siCON
si-PI4KIIIβ
Sham
CVB3
Sham
CVB3
17
15
LC3-I
LC3-II
100
PI4KIIIβ
1.0 0.8 0.9 0.5 0.5 0.5 0.2 0.2 0.2 0.1 0.1 0.1
PI4KIIIβ/ACTB
42
ACTB
p<0.01
p<0.01
N.S.
LC3-II/ACTB
2.5
2.0
1.5
1.0
0.5
0.0
Sham
CVB3
Sham
CVB3
siCON
si-PI4Kβ
C
Mw (kDa)
siCON
si-PIK3C3
si-PI4KIIIβ
si-PIKfyve
Sham
CVB3
Sham
CVB3
Sham
CVB3
Sham
CVB3
17
15
LC3-I
LC3-II
100
PIK3C3
1.0 1.0 1.0 0.2 0.2 0.2 1.3 1.2 1.2 1.3 1.1 0.9
PIK3C3/ACTB
100
PI4KIIIβ
1.0 1.0 0.9 1.0 1.0 1.0 0.1 0.1 0.1 1.0 0.9 0.9
PI4KIIIβ/ACTB
245
PIKfyve
1.0 0.8 0.8 1.0 0.6 0.8 0.7 0.7 0.7 0.2 0.1 0.1
PIKfyve/ACTB
34
VP1
42
ACTB
LC3-II/ACTB
VP1/ACTB
10.0
9.0
8.0
7.0
6.0
5.0
4.0
3.0
2.0
1.0
0.0
2.0
1.8
1.6
1.4
1.2
1.0
0.8
0.6
0.4
0.2
0.0
si-CON
si-PIK3C3
si-PI4KIIIβ
si-PIKfyve
LC3-II/β-actin
VP1/β-actin

Figure 13. PI4KIIIβ is involved in CVB3-induced LC3 lipidation. (A) Schematic diagram of the proposed role of PI4KIIIβ in autophagy (left) and the known function in enterovirus replication (right). **(B)** PI4KIIIβ was transiently silenced in HEK293A cells using siRNA for 48h. Cells were then subjected to sham or CVB3 infection for 16h, followed by western blot analysis of LC3 and PI4KIIIβ. Arrow indicates the cleavage product. **(C)** HEK293A cells, transfected with control or PIK3C3, PI4KIIIβ, or PIKfyve siRNAs for 48h, were sham- or CVB3-infected. Western blotting was performed for detection of LC3, VP1, PIK3C3, PI4KIIIβ, or PIKfyve. Right panel, LC3-II protein densitometry was quantified and normalized to ACTB as described in materials and methods and presented as bar plots (mean±SD, n=3). Viral capsid VP1 was normalized to ACTB and presented as yellow triangles (mean±SD, n=3).

Discussion

EVs have been shown to induce autophagosome accumulation as a viral strategy to facilitate productive infection. The initiation of autophagy allows EVs to hijack autophagic membranes as topological surfaces that can be repurposed as replication organelles for viral RNA synthesis [66, 67, 75]. Additionally, the acidification of autophagosomes/amphisomes has been proposed to act as a maturation chamber for newly synthesized virions [73, 91], which may also commandeer autophagosomes as quasi-envelopes that act as vehicles for non-lytic viral propagation [14, 15, 17]. These insights have established a complex relationship between EV and the autophagic process during various stages of the viral life cycle.

The production of double-membraned vesicles, development of LC3 puncta, and accumulation of LC3-II marker following viral infection have been documented for many EVs [66, 67, 68, 72, 73]. A recent study has provided evidence that PV-induced autophagy is independent of the ULK complex [111]; however the precise mechanisms by which EVs initiate autophagy remain to be fully elucidated. The current study was designed to use CVB3 as a model system to investigate how EVs trigger autophagosome biogenesis. Lipidation of LC3 by the ubiquitin-like ATG conjugation system plays an essential role in host autophagy by facilitating membrane curvature, recruitment of selective autophagy receptors and/or cargo, closure of autophagosomes, and membrane fusion with endolysosmal compartments [134]. Our present study has uncovered that CVB3-induced LC3 lipidation requires the ATG ubiquitin-like conjugation system, but independent of the canonical starvation-induced upstream signaling pathways such as ULK1/2

signaling and PI3P production. In addition, PI3P-binding effectors, such as WIPI2 that facilitates LC3 lipidation by recruitment of ATG5-ATG12-ATG16L1 complex, were also found to be dispensable for CVB3-induced LC3 lipidation.

Our observations that canonical autophagy factors are not required for CVB3-induced autophagy, coupled with the findings that viral proteinase(s) target key autophagy proteins for cleavage, suggest the existence of non-canonical, alternate autophagy pathways in initiating CVB3-induced autophagy. Several instances of non-canonical autophagy have been previously described, such as ULK1/2-independent autophagy. It was shown that ammonia-induced autophagy is dependent on ATG5, but does not require ULK1/2 [135]. Rubicon was identified as a key modulator of ULK-independent, LC3-associated phagocytosis (LAP) [136, 137], a form of 'non-canonical' autophagy that occurs in immune cells and utilizes some components of the autophagy machinery (e.g. ATG conjugation machinery) to process extracellular cargo through single membrane endocytic vesicles [138]. Interestingly, I found that the protein levels of Rubicon were undetectable in neural cells and very low in HeLa and HEK293 cells compared to Jurkat cell (**not shown),** indicating that Rubicon may not play a major role in CVB3-induced autophagy.

Class III PI3K-independent autophagy was also previously reported [132]. It was shown that PIK3C3-dependent PI3P production is dispensable for glucose deprivation-induced autophagy [132]. Further research identified PI5P, synthesized by PIKfyve (FYVE finger-containing phosphoinositide kinase), as an alternative phospholipid to induce autophagy [132]. However, I found that knockdown of PIKfyve was unable to block CVB3-elicited LC3 lipidation (**not shown**), suggesting that PI5P is not a key autophagy initiating factor upon CVB3 infection.

In addition to PI3P and PI5P, recent studies also suggest a role for PI4P in autophagosome biogenesis. PI4P is a lipid that is predominantly found on the membranes of the trans Golgi network (TGN) [63, 139]. It was recently shown that ATG9A recruits PI4KIIIβ, a major enzyme regulating PI4P synthesis, to the autophagosome initiation site for PI4P production and deletion of PI4KIIIβ disrupts the process of autophagy [131]. Interestingly, during CVB3 and PV infection, the replication organelles of viruses were found to be enriched in PI4P, partly through the TGN-anchored viral membrane protein 3A that recruits PI4KIIIβ to the viral replication organelles. Enhanced PI4P production further recruits viral polymerase 3D to initiate viral RNA synthesis [63, 65]. I discovered that CVB3-induced LC3 lipidation is markedly inhibited in cells depleted of

PI4KIIIβ compared to control siRNA-treated cells. Since PI4KIIIβ is needed for effective viral replication, knockdown of this gene results in reduced viral growth, interfering with the data interpretation of LC3-II accumulation. Therefore, a firm conclusion about the role of PI4KIIIβ-PI4P in CVB3-induced autophagy initiation cannot be made at this moment and further investigation is needed.

In conclusion, our study reveals that CVB3 initiates a novel form of autophagy depending on ATG5-ATG12-ATG16L1 complex, but being distinct from the physiological, starvation-induced 'canonical' autophagy. The current study adds CVB3 as a novel stimulus in the emerging field of non-canonical autophagy.

In **Chapter 2**, I explored the mechanisms by which CVB3 initiates autophagy. Given that cells can initiate different forms of autophagy to target diverse cellular cargo, in **Chapter 3** I sought to further explore the mechanism by which CVB3 disrupts selective autophagy.

Chapter 3: NDP52/CALCOCO2 and p62/SQSTM1 differentially regulate CVB3 propagation

Background

Cells are evolutionarily equipped with a defense system to combat invading pathogens that is broadly described as cell autonomous immunity. Selective autophagy proteins are components of this defense system that are able to detect, sequester, and eliminate invading microbes including EV, but the mechanisms remain poorly defined. Previous evidence demonstrated that CVB3 can target selective autophagy receptors SQSTM1 and NBR1 through viral proteinase-mediated degradation [92, 140], however the functional consequence of such targeting and whether other autophagy receptors are also targeted remains unclear.

Rationale: To better understand how CVB3 evades cell autonomous immunity, I sought to investigate the relationship between CVB3 and the host selective autophagy receptors CALCOCO2 and SQSTM1. These autophagy receptors were selected in particular because of their previously reported interactions with other viral pathogens such as Sindbis and Chikungunya virus [105, 106]. The **specific aim** of this chapter is to define the role of CALCOCO2 and SQSTM1 in CVB3 replication and characterize the mechanism of viral subversion.

Materials and methods

Cell culture and viral infection

HeLa cells (American Type Culture Collection) were cultured in Dulbecco's Modified Eagle's Medium (DMEM) supplemented with 10% fetal bovine serum (FBS) and a penicillin/streptomycin cocktail (100 µg/mL). CALCOCO2 knockout (KO) HeLa cells were generated through the CRISPR-Cas9 system[141]. The guide RNA sequence targeting exon 6 of CALCOCO2 was: 5'-GAAGCAGAACTCAGACATGC-3', which was cloned into pSpCas9(BB)-2A-Puro vector (Addgene #62988). Following transfection, positive cells were selected using puromycin (7 µg/ml) for up to two days. For CVB3 infection, cells were either sham-infected with PBS or inoculated with CVB3 (Kandolf strain) at different multiplicity of infection (MOI=0.1,1, or 10) as specified in the Figure Legends.

Plasmids and small interfering RNA (siRNA)

The myc-tagged wild-type CVB3-3C ($3C^{wt}$) and C147A mutant CVB3-3C ($3C^{mut}$) constructs were generous gifts from Dr. Carolyn Coyne at the University of Pittsburgh[114]. The PHAGE-GFP-CALCOCO2 plasmid was a kind gift from Dr. Richard Youle at the National Institute of Neurological Disorders and Stroke, USA[142]. Flag-N-SQSTM1 (aa 1-241) and Flag-C-SQSTM1 (aa 242-440) was generated as previously described [92]. The 3×Flag-CALCOCO2, 3×Flag-N-CALCOCO2, 3×Flag-C-CALCOCO2 constructs were generated using CMV10 backbone with the following primers: full-length CALCOCO2 (forward: AAA TTT GAA TTC C ATG GAG GAG ACC ATC AAA GAT C; reverse: AAA TTT GGA TCC TCA GAG AGA GTG GCA GAA CA); N-CALCOCO2 (forward: AAA TTT GAA TTC CAT GGA GGA GAC CAT CAA AG; reverse: AAA TTT GGA TCC TCA CTG AGT GGT AAC AAC C); C-CALCOCO2 (forward: AAA TTT GAA TTC CGG AGA GGT GGA AGA GAT TGA G; reverse: AAA TTT GGA TCC TCA GAG AGA GTG GCA GAA CAC). GFP-$CALCOCO2^{Q139L}$ mutant was generated using the QuikChange Site-Directed Mutagenesis kit (Agilent, #200518) according to the manufacture's protocol with the following primers: forward: CTG GTT GTT ACC ACT CTG GGA GAG GTG GAA GAG; reverse: CTC TTC CAC CTC TCC CAG AGT GGT AAC AAC CAG. The siRNAs targeting CALCOCO2 (sc-93738) and SQSTM1 (M-010230-00-0005) were purchased from Santa Cruz Biotechnology and Dharmacon, respectively. The scrambled siRNA (sc-37007) was purchased from Santa Cruz Biotechnology. For transfection, HeLa cells were transiently transfected with plasmid cDNAs or siRNAs using Lipofectamine 2000 (Invitrogen, 11668-019) following the manufacturer's instructions.

Real-time quantitative RT-PCR

Total RNA was extracted using the RNeasy Mini kit (Qiagen, 74104). To determine the expression level of IFN-α and IFN-β, quantitative PCR targeting IFN-α (forward primer: GCC TCG CCC TTT GCT TTA CT; reverse primer: CTG TGG GTC TCA GGG AGA TCA), and IFN-β (forward primer: GTC TCC TCC AAA TTG CTC TC; reverse primer: ACA GGA GCT TCT GAC ACT GA) was performed in a 10-μl reaction containing 1 μg of RNA, using the TaqMan™ RNA-to-CT™ 1-Step Kit (Life Technologies, 4392653) and normalized to GAPDH mRNA according to the manufacturer's instructions. The PCR reaction was performed on a ViiA 7 Real-Time PCR System (Applied Biosystems). Samples were run in triplicate and analyzed using

comparative CT (2-ΔΔCT) method with control samples and presented as relative quantitation (RQ).

Western blot analysis

Cells were lysed in buffer (10 mM HEPES pH 7.4, 50 mM NaPyrophosphate, 50 mM NaF, 50 mM NaCl, 5 mM EDTA, 5 mM EGTA, 100 µM Na_3VO_4, 0.1% Triton X-100) supplemented with cOmplete Mini, EDTA-free protease inhibitor cocktail tablets (Sigma, #11836170001). Western blotting was conducted using the following primary antibodies: CALCOCO2/NDP52 (Santa Cruz Biotechnology, sc-376540), SQSTM1/p62 (PROGEN Biotechnik GmbH, GSQSTM1-C), cleaved-caspase 3 (Cell Signaling Technology, #9661), LC3 (MBL International, PM036), VP1 (Dako, M706401-1), NBR1 (Santa Cruz Biotechnology, sc-130380), HA (Roche, 11867423001), Flag (Sigma, F1804), ubiquitin (Cell Signaling Technology, #3933), GFP (Life Technologies, A-6455), K63-ubiquitin (Cell Signaling Technology, #12930), K48-ubiquitin (Cell Signaling Technology, #12805), MAVS (Cell Signaling Technology, #24930), p-TBK1 (Cell Signaling Technology, #5483), TBK1 (Cell Signaling Technology, #3504), ACTB (Sigma-Aldrich, A5316), and GAPDH (Cell Signaling Technology, 14C10). Primary antibodies were used at 1:1000 dilution. Secondary anti-mouse HRP (Invitrogen, #31430) or anti-rabbit HRP (Invitrogen, # 31460) were used at 1:5000 dilution. Western blotting was performed on a Bio-Rad Mini Trans-Blot Electrophoretic System (Bio-Rad, #1703930).

Densitometry Analysis

Densitometry of protein bands was measured using NIH Image J software. Briefly, gel images were saved in high resolution TIFF format using Syngene software of the GBOX (Model: Chemi XRQ). Images were exported to Image J software and manually processed using the gel analysis function. Images were carefully selected to avoid oversaturation and non-linear signal intensities. Individual bands were selected to generate intensity peaks, and each intensity peak was segregated to generate area under measurements. Background intensity was equally subtracted from all intensity peaks using the linear segregation tool. Area under the curve was averaged among biological replicates (n=3) for quantification analysis.

Immunoprecipitation

Immunoprecipitation was performed using EZview™ Red ANTI-FLAG ® M2 Affinity Gel (Sigma-Aldrich, F2426) according to the manufacturer's instructions. Immunoprecipitation (IP) of VP1 was performed using anti-VP1 antibody (Dako, M706401-1) pre-incubated with Dynabeads Protein G (Invitrogen, 1003D) according to the manufacturer's instructions. In brief, HeLa cells were lysed with Flag Lysis Buffer (50 mM Tris HCl, pH 7.4, with 150 mM NaCl, 1 mM EDTA, and 1% TX-100) for 15min on ice. Lysates were cleared with a centrifugation at 12,000g for 15min. Supernatants (50uL) was partitioned for input control and the remaining lysate was incubated overnight with anti-Flag M2 agarose beads with end-over-end rotation at 4°C. After three washes with lysis buffer, the bound proteins were eluted with 2× SDS sample buffer and then subjected to Western blot analysis.

Immunofluorescence and confocal microscopy

HeLa cells were fixed in methanol-free 4% PFA for 15min at room temperature. Cells were rinsed with 100mM glycine/PBS solution for 15min and subsequently permeabilized with a 3-minute incubation in 0.1% Triton X-100. Fixed and permeabilized cells were blocked for 1 h with 3% bovine serum albumin, followed by incubation with primary antibodies overnight at 4ºC. After 15min washes with PBS, cells were incubated with fluorescent secondary antibodies (Anti Rb-Alexa 488 and Anti-Ms-Alexa 647 at 1:1000 dilution) for 1 h. After the final 15min washes, coverslips were mounted using Fluoroshield with DAPI (Sigma-Aldrich, F6057). Images were captured with the Zeiss LSM 880 Inverted Confocal Microscopy.

Results

CALCOCO2/NDP52 and SQSTM1/p62 differentially regulate CVB3 propagation

To determine the role of autophagy receptors, SQSTM1 and CALCOCO2, in coxsackievirus infection, I first examined the effects of gene-silencing of each receptor on viral propagation. As shown in **Figure 14A & B**, knockdown of SQSTM1 led to enhanced viral capsid protein (VP1) expression and increased cell-associated viral titers after 24 h infection with a low dose of CVB3 (multiplicities of infection (MOI) of 0.1). In contrast, depletion of CALCOCO2 caused a significant attenuation of viral growth. Given the possible impacts of different viral dosages and infectious cycles, I further confirmed our observations in CALCOCO2-depleted cells by treating the cells with 3 logarithmic doses of CVB3 (MOI of 10, 1, and 0.1) for 3 respective

time-points (7 h, 16 h, 24 h) that spanned 3 viral replication cycles. In agreement, results from all 3 conditions concluded that depletion of CALCOCO2 resulted in a concomitant decrease of viral protein synthesis as well as infectious viral titers **(Figure 14C & D)**. In line with these observations, ectopic expression of 3×Flag-tagged CALCOCO2 showed an enhancement in both VP1 expression and intracellular viral titers **(Figure 14E & F)**, whereas cells expressing exogenous Flag-SQSTM1 exhibited a reduction in both metrics **(Figure 14G & H)**. Collectively, our results demonstrated opposing roles for SQSTM1 and CALCOCO2 in CVB3 infection.

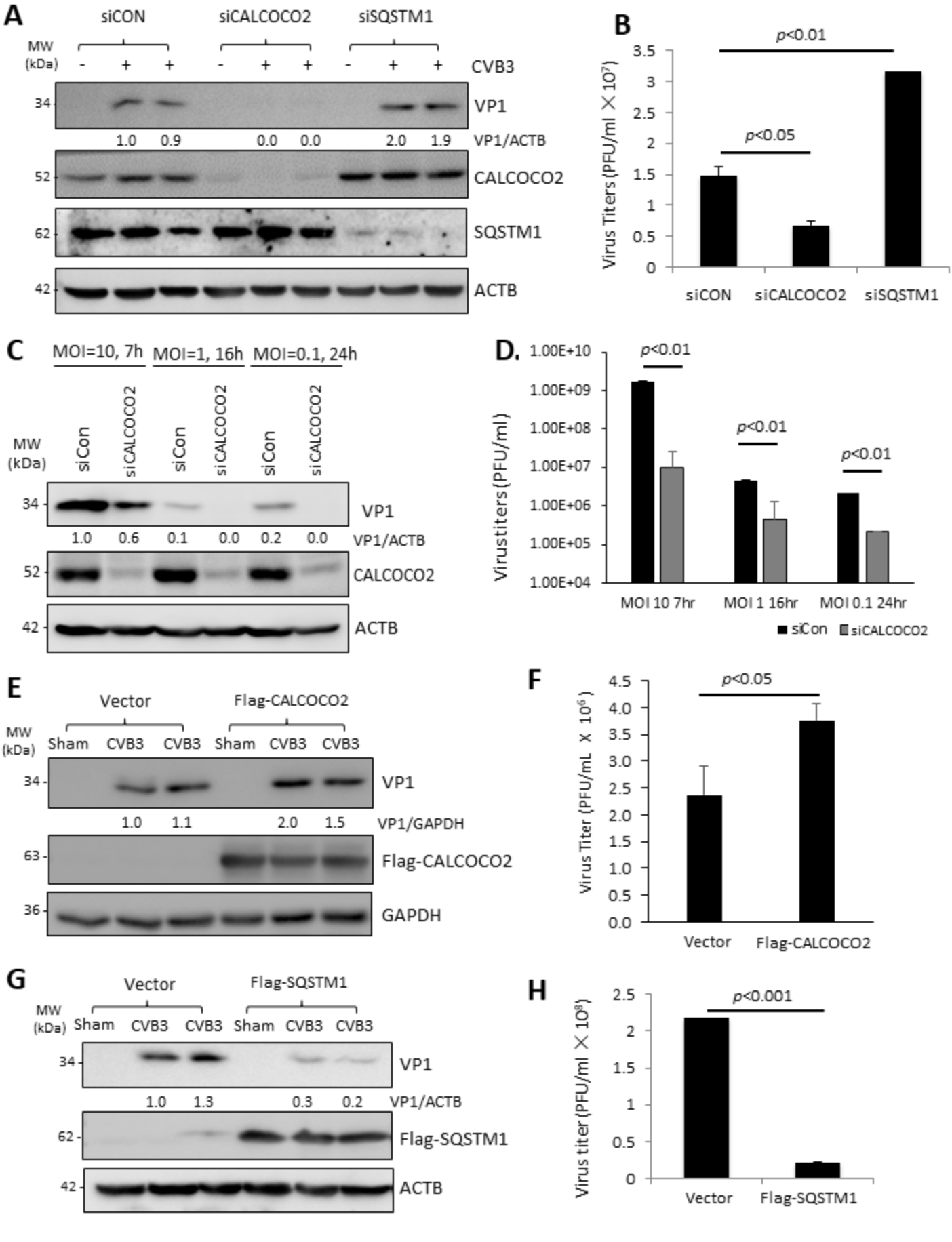
A
siCON
siCALCOCO2
siSQSTM1
MW (kDa)
CVB3
VP1
VP1/ACTB
CALCOCO2
SQSTM1
ACTB
B
p<0.01
p<0.05
Virus Titers (PFU/ml × 10^7)
siCON
siCALCOCO2
siSQSTM1
C
MOI=10, 7h
MOI=1, 16h
MOI=0.1, 24h
siCon
siCALCOCO2
D.
p<0.01
Virustiters(PFU/ml)
MOI 10 7hr
MOI 1 16hr
MOI 0.1 24hr
siCon
siCALCOCO2
E
Vector
Flag-CALCOCO2
Sham
CVB3
VP1/GAPDH
Flag-CALCOCO2
GAPDH
F
p<0.05
Virus Titer (PFU/mL X 10^6)
Vector
Flag-CALCOCO2
G
Vector
Flag-SQSTM1
VP1/ACTB
Flag-SQSTM1
ACTB
H
p<0.001
Virus titer (PFU/ml × 10^8)
Vector
Flag-SQSTM1

Figure 14. CALCOCO2 and SQSTM1 differentially regulate CVB3 propagation. (A) HeLa cells were transiently transfected with siRNAs targeting CALCOCO2 (siCALCOCO2) or SQSTM1 (siSQSTM1), or a scramble siRNA control (siCON) for 48 h, followed by CVB3 infection (MOI=0.1) for 24 h. Western blotting was performed to examine protein expression of CALCOCO2, SQSTM1, VP1, and ACTB. Protein levels of VP1 were quantified by densitometric analysis using NIH ImageJ, normalized to ACTB and presented underneath as fold changes compared to sham (the first lane of sham is arbitrarily set a value of 1). **(B)** HeLa cells were treated as above. Cell-associated virus titers were determined by $TCID_{50}$. Data are represented as mean ± SD from 3 replicates. **(C, D)** HeLa cells were treated with siCALCOCO2 as above, and then subjected to infection with different doses of CVB3 for various times as indicated. Western blotting and densitometric analysis were conducted (C) and virus titers (mean ± SD, n=3) were measured (D) as above. **(E-H)** HeLa cells were transfected with constructs overexpressing Flag-CALCOCO2 **(E, F)** or Flag-SQSTM1 **(G, H)** for 24 h and then subjected to CVB3 infection (MOI=0.1) for 16 h. Cell lysates were analyzed by Western blotting for VP1 protein levels (E, G) and cell-associated virus titers were quantified as above (F, H). Results in this Figure represent data from 2 to 3 independent experiments.

Both SQSTM1 and CALCOCO2 physically interact with CVB3 capsid protein VP1

Previous studies have shown that SQSTM1 can interact with capsid proteins of Sindbus virus[143] and Chikungunya virus[105]. I therefore questioned whether CVB3 capsid proteins are also recognized by SQSTM1. HeLa cells transiently expressing Flag-SQSTM1 were infected with CVB3 at an MOI of 10 for 5 h, followed by co-immunoprecipitation using anti-Flag M2 beads. **Figure 15A** showed that Flag-SQSTM1, but not a vector control, was able to immunoprecipitate viral capsid protein, VP1. Likewise, immunostaining revealed the co-localization of viral capsid protein and SQSTM1 in CVB3-infected cells **(Figure 15B)**. I have previously demonstrated that SQSTM1 is cleaved before glycine 241 during CVB3 infection through the activity of CVB3-encoded proteinase 2A[92]. Here I found that the binding affinity to VP1 for both the resulting N- and C-terminal cleavage fragments of SQSTM1 was markedly decreased (**Figure 15C**). Furthermore, immunoprecipitation also demonstrated the interaction between CALCOCO2 and viral protein VP1 (**Figure 15D**). Given the pro-viral role of CALCOCO2, I further examined its interaction with VP1 through co-localization studies. Similar to SQSTM1, depletion of CALCOCO2 in virus-infected cells showed impaired co-localization with the autophagosome marker (LC3). However, the association of VP1 with the lysosomal and late endosome marker LAMP2 was only reduced in SQSTM1-silenced cells but not CALCOCO2 (**Figure 15E**). Together, our data suggest a potential role for SQSTM1 in virophagy through interacting with viral capsid proteins. Our findings in this study also indicate that cleavage of SQSTM1 may serve as a viral strategy to counteract the role of SQSTM1 in viral clearance.

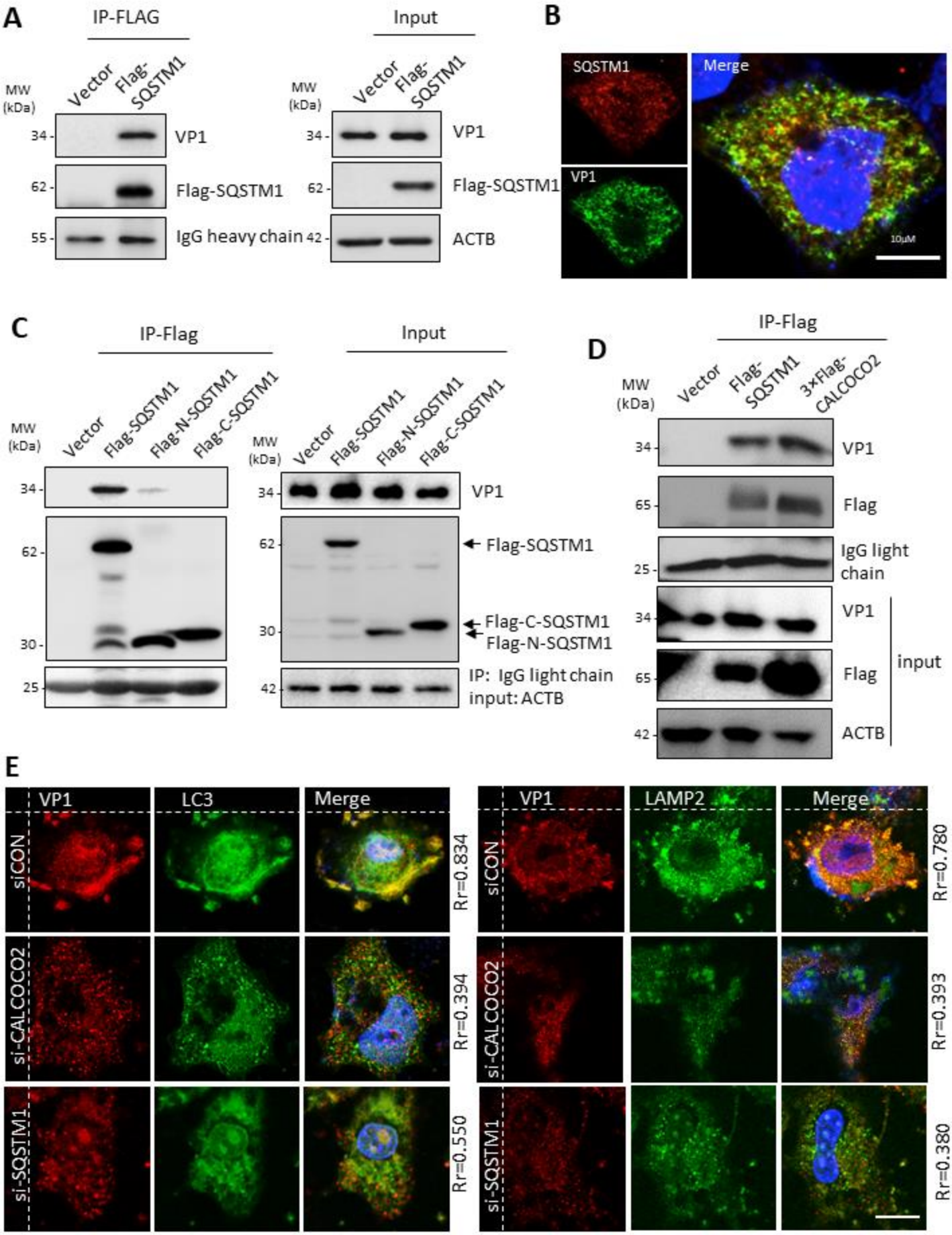
A
IP-FLAG
Input
MW (kDa)
Vector
Flag-SQSTM1
34
62
55
42
VP1
Flag-SQSTM1
IgG heavy chain
ACTB
B
SQSTM1
Merge
VP1
10μM
C
IP-Flag
Input
Vector
Flag-SQSTM1
Flag-N-SQSTM1
Flag-C-SQSTM1
30
25
Flag-C-SQSTM1
Flag-N-SQSTM1
IP: IgG light chain
input: ACTB
D
IP-Flag
3×Flag-CALCOCO2
65
IgG light chain
input
Flag
E
VP1
LC3
Merge
LAMP2
siCON
si-CALCOCO2
si-SQSTM1
Rr=0.834
Rr=0.780
Rr=0.394
Rr=0.393
Rr=0.550
Rr=0.380

Figure 15. SQSTM1 and CALCOCO2 physically interact with CVB3 capsid protein VP1. **(A)** HeLa cells were transfected with Flag-tagged SQSTM1 for 24 h, followed by CVB3 infection (MOI=10) for 5 h. After immunoprecipitation (IP) with an anti-Flag antibody, Western blotting was performed for detection of viral capsid protein 1 (VP1) and Flag-SQSTM1. Blots for antibody IgG heavy chain and ACTB were shown as loading controls for IP and input, respectively. **(B)** Confocal microscopy analysis of the co-localization of endogenous SQSTM1 and viral capsid protein VP1. HeLa cells were infected with CVB3 (MOI=10) for 3 h. Cells were then fixed and immunostained for SQSTM1 and VP1. The nucleus was stained with DAPI. **(C, D)** HeLa cells were transfected with Flag-SQSTM1, Flag-N-SQSTM1 (aa 1-241), Flag-C-SQSTM1 (aa 242-440), 3×Flag-tagged CALCOCO2, or empty vector as indicated for 24 h, followed by CVB3 infection (MOI=10) for 5 h. Co-IP and Western blotting were conducted as above in (A). Blots for IgG light chain and ACTB were used as loading controls for IP and input, respectively. Similar results were observed in 2 independent experiments. **(E)** Confocal microscopy analysis of the co-localization of VP1 and LC3 (autophagosome marker) or LAMP2 (lysosome marker). HeLa cells were treated with either control siRNA (siCON), si-CALCOCO2, or si-SQSTM1 for 48 h, followed by CVB3 infection (MOI=10) for 3 h. Cells were then immunostained for VP1, LC3, and LAMP2 as indicated. The nucleus was stained with DAPI. Co-localization between VP1 and LC3 or VP1 and LAMP2 was quantified using ImageJ and presented as Pearson Correlation (Rr).

CVB3 capsid protein VP1 undergoes ubiquitination

Since autophagy receptors recognize the targets via their ubiquitin-association domains, I then questioned whether ubiquitin or ubiquitination process plays a role in linking SQSTM1/CALCOCO2 with viral capsid protein. To test this model, I initially examined whether VP1 itself can associate with ubiquitin by performing co-immunoprecipitation of exogenously expressed HA-ubiquitin in CVB3-infected HeLa cells. I found that VP1 indeed interacted either directly or indirectly, with ubiquitin or ubiquitinated proteins **(Figure 16A)**. Moreover, reverse immunoprecipitation of VP1 from CVB3-infected HeLa cells revealed a significant pull-down of ubiquitinated species, which may include ubiquitinated VP1 and other viral and host ubiquitinated proteins (**Figure 16B)**. Of note, immunoprecipitation of VP1 routinely showed the presence of 4 distinct protein bands in immunoblots incubated with anti-VP1 antibody (**Figure 16B**). **I** concurred that these 4 distinct bands likely represent VP1-positive fragments, which are generated following viral processing of the polyprotein **(Figure 16C)**. To further characterize the status of ubiquitinated species observed following VP1 immunoprecipitation, I utilized the ubiquitin-specific antibodies, which recognize lysine-63 (K63) or lysine-48 (K48) linkages, in the presence or absence of the lysosome (bafilomycin A1) or proteosome (MG132) inhibitors. Western blotting with anti-K63-ubiquitin or anti-K48-ubiquitin antibody showed the detection of distinct protein bands that were unresponsive to degradative blockade and migrated at the same molecular weight as those observed following VP1 immunoprecipitation, suggesting that the ubiquitin-specific antibodies recognize VP1-associated fragments (**Figure 16D)**. Our data indicate a possible mechanism by which autophagy receptors recognize the invading viral pathogens through association with viral capsid proteins.

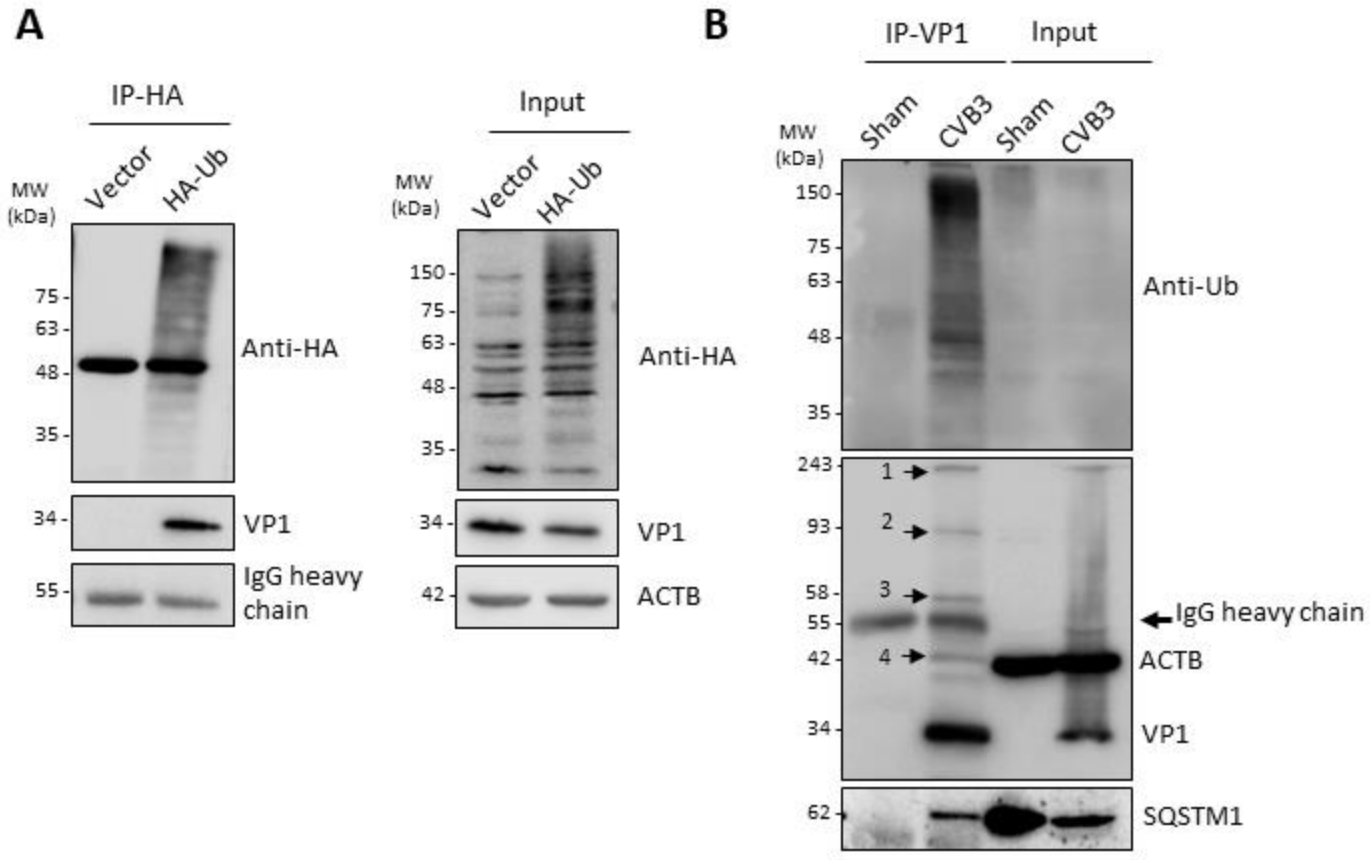
A
IP-HA
Input
MW (kDa)
Vector
HA-Ub
75
63
48
35
Anti-HA
34
VP1
55
IgG heavy chain
150
42
ACTB
B
IP-VP1
Input
Sham
CVB3
Anti-Ub
243
93
58
1
2
3
4
IgG heavy chain
ACTB
VP1
62
SQSTM1

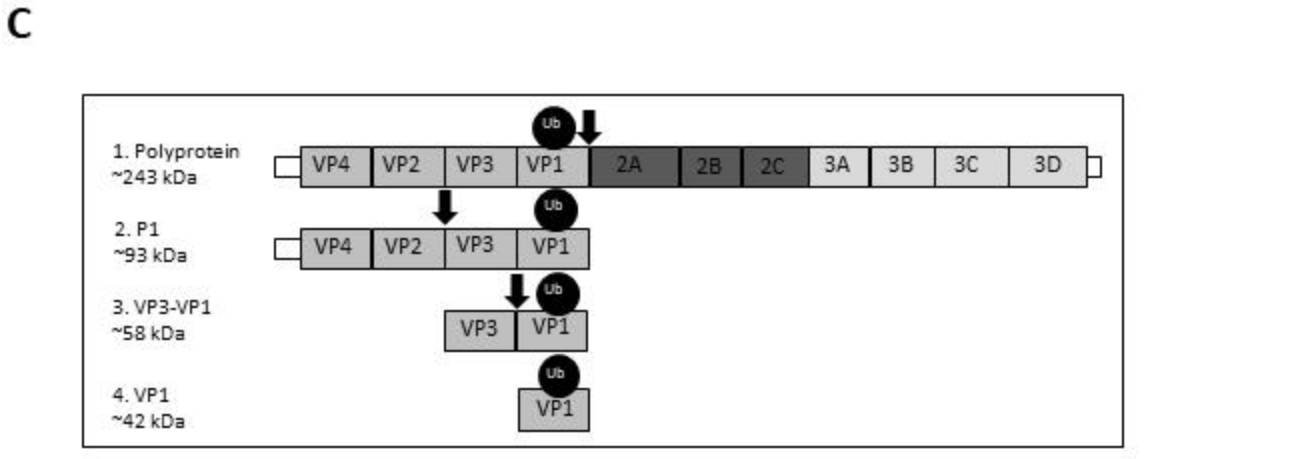
C
1. Polyprotein
~243 kDa
2. P1
~93 kDa
3. VP3-VP1
~58 kDa
4. VP1
~42 kDa
Ub
VP4
VP2
VP3
VP1
2A
2B
2C
3A
3B
3C
3D

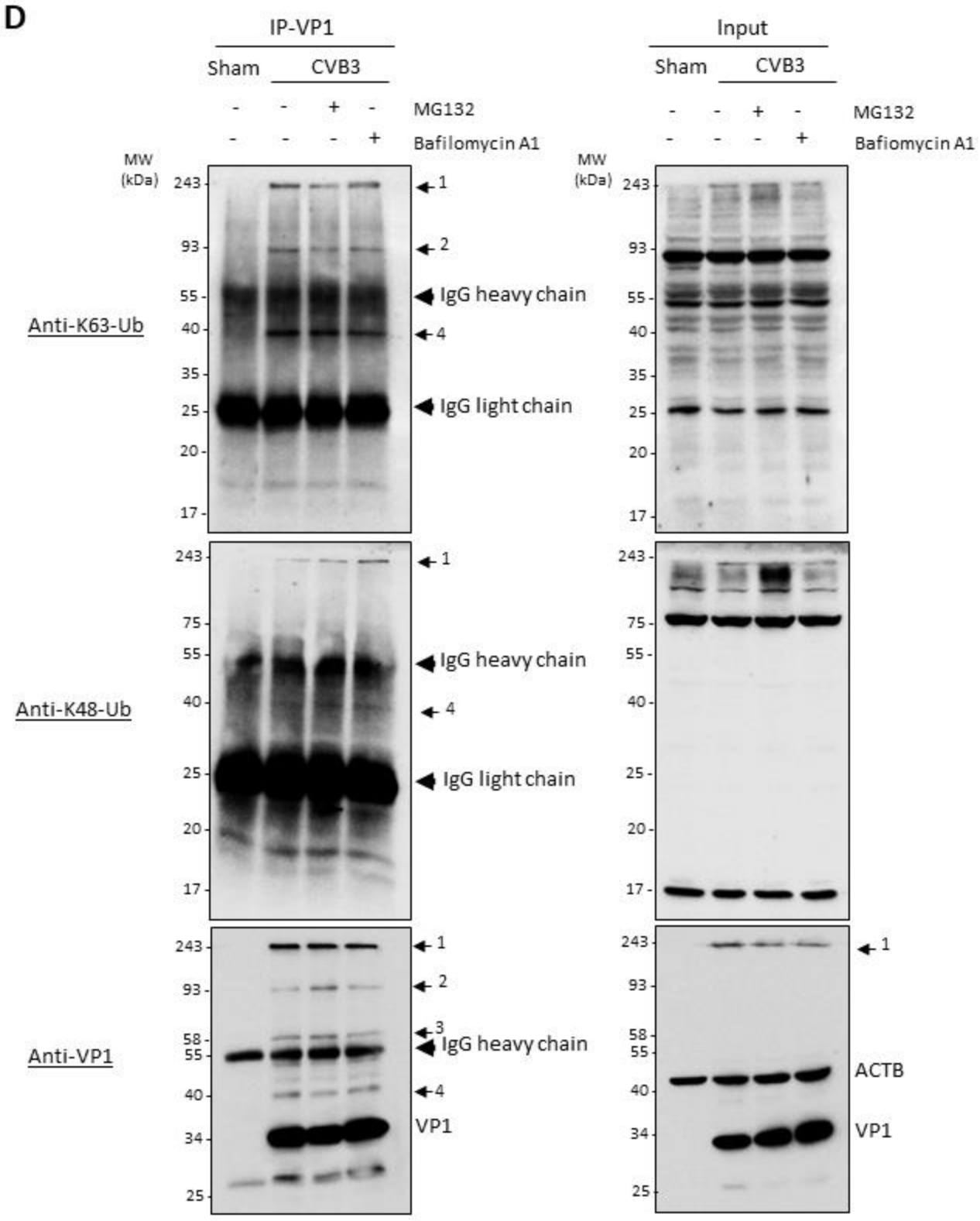
D
IP-VP1
Input
Sham
CVB3
MG132
Bafilomycin A1
MW (kDa)
Anti-K63-Ub
Anti-K48-Ub
Anti-VP1
IgG heavy chain
IgG light chain
VP1
ACTB

Figure 16. CVB3 capsid protein VP1 undergoes ubiquitination. (A) HeLa cells were transiently transfected with HA-tagged ubiquitin (HA-Ub) or empty vector for 24 h, and then infected with CVB3 (MOI=10) for 5 h. Co-IP was performed with an anti-HA antibody, followed by Western blot analysis of HA-Ub using antibodies against HA tag or VP1. **(B)** HeLa cells were infected with CVB3 (MOI=10) for 5 h, followed by IP using anti-VP1 antibody. Western blotting was conducted using antibodies against Ub, VP1, or SQSTM1 as indicated. **(C)** Schematic illustration of the CVB3 polyprotein and the respective VP1-linked ubiquitinated fragments. Arrows depict sites of cleavage by virus-encoded proteinases. **(D)** HeLa cells were infected with CVB3 (MOI=10) for 5 h in the presence or absence of a proteasome inhibitor MG132 (10 μM) or a lysosome inhibitor bafilomycin A1 (200 nM) as indicated. IP was conducted using an anti-VP1 antibody, followed by Western blotting was performed using anti-K63-linked or anti-K48-linked Ub antibody and anti-VP1 antibody as indicated. Similar results were observed in 3 independent experiments.

CALCOCO2 attenuates type I interferon signaling

Despite the possible role of CALCOCO2 in virophagy, the overall function of CALCOCO2 is to enhance CVB3 infection (**Figure 14**). Thus, I next sought to determine the pro-viral mechanism of CALCOCO2. Type I interferon (IFN) signaling is a broad anti-viral pathway and was previously reported to inhibit CVB3 replication[144, 145]. Recent studies have suggested an important role for CALCOCO2 in the deactivation of type I IFN signaling through autophagy-mediated clearance of the mitochondrial anti-viral signaling (MAVS)[146]. To test the hypothesis that CALCOCO2 facilitates CVB3 replication by inhibiting the type I IFN response, I examined the effects of knockdown of CALCOCO2 on the protein levels of MAVS, phosphorylation of TANK-binding kinase 1 (TBK1, a downstream target of MAVS[147]), and mRNA production of IFN-α/IFN-β. I showed that depletion of CALCOCO2 led to increased protein accumulation of MAVS (**Figure 17A**) and elevated phosphorylation of TBK1 (**Figure 17C**). No evident effects of knockdown of SQSTM1 on MAVS accumulation (**Figure 17B**) and TBK1 phosphorylation (**Figure 17D**) were observed. Lastly, quantitative PCR results demonstrated that gene-silencing of CALCOCO2, but not SQSTM1, caused increased mRNA levels of IFN-α/IFN-β **(Figure 17E & F)**. Taken together, our data suggest that CALCOCO2 acts as a suppressor of type I IFN signaling, which likely contributes to its pro-viral activity.

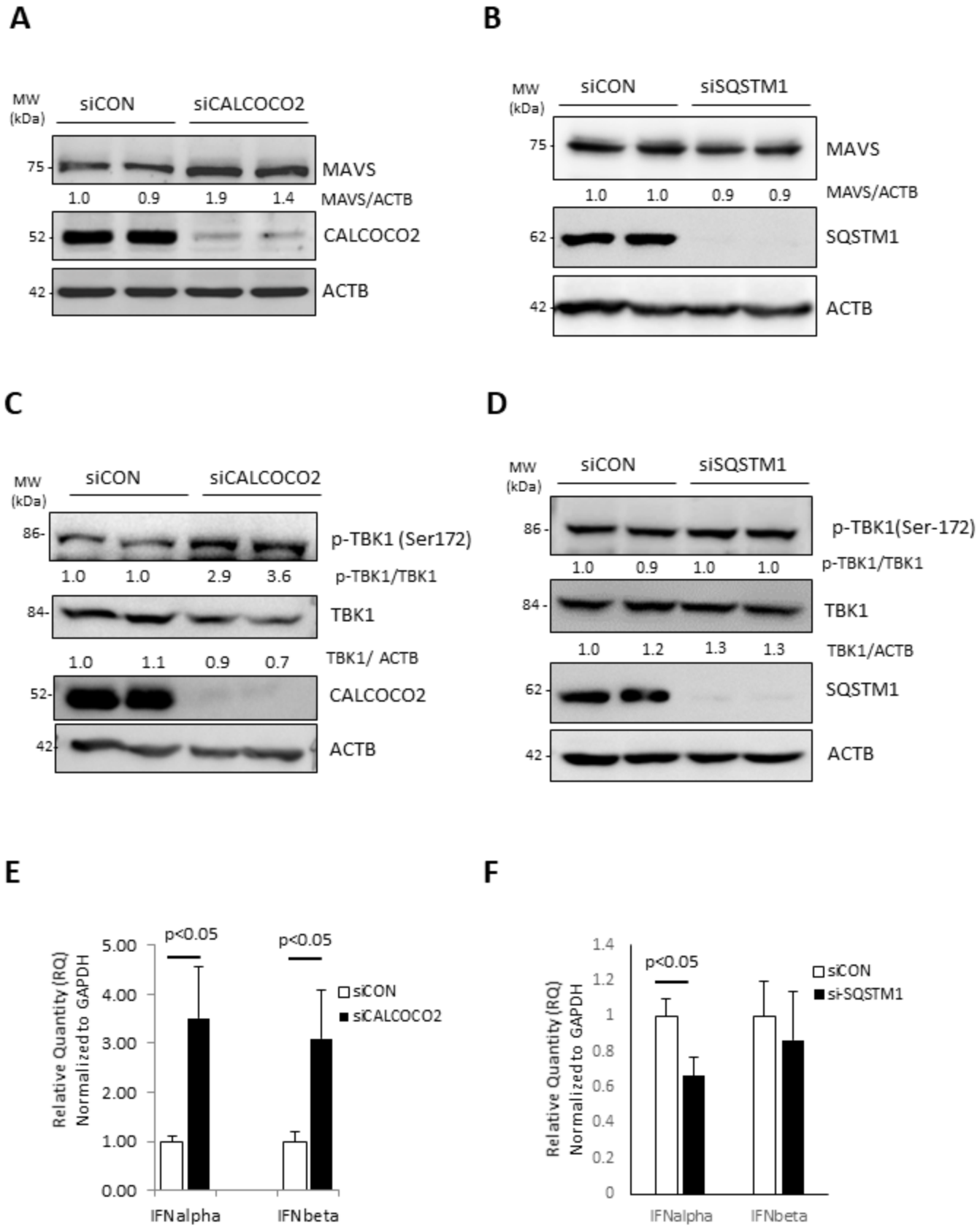
A
MW (kDa)
siCON
siCALCOCO2
75
MAVS
1.0 0.9 1.9 1.4
MAVS/ACTB
52
CALCOCO2
42
ACTB
B
MW (kDa)
siCON
siSQSTM1
75
MAVS
1.0 1.0 0.9 0.9
MAVS/ACTB
62
SQSTM1
42
ACTB
C
MW (kDa)
siCON
siCALCOCO2
86
p-TBK1 (Ser172)
1.0 1.0 2.9 3.6
p-TBK1/TBK1
84
TBK1
1.0 1.1 0.9 0.7
TBK1/ ACTB
52
CALCOCO2
42
ACTB
D
MW (kDa)
siCON
siSQSTM1
86
p-TBK1(Ser-172)
1.0 0.9 1.0 1.0
p-TBK1/TBK1
84
TBK1
1.0 1.2 1.3 1.3
TBK1/ACTB
62
SQSTM1
42
ACTB
E
Relative Quantity (RQ) Normalized to GAPDH
5.00
4.00
3.00
2.00
1.00
0.00
p<0.05
p<0.05
siCON
siCALCOCO2
IFNalpha
IFNbeta
F
Relative Quantity (RQ) Normalized to GAPDH
1.4
1.2
1
0.8
0.6
0.4
0.2
0
p<0.05
siCON
si-SQSTM1
IFNalpha
IFNbeta

Figure 17. Knockdown of CALCOCO2 results in increased protein levels of MAVS and p-TBK1 as well as elevated production of type I interferons. (A, C, E) HeLa cells were treated with siCALCOCO2 or siCON for 48 h. Cell lysates were harvested and probed for MAVS (A), p-TBK1/TBK1 (C) by Western blotting. Knockdown efficiency was verified by probing with anti-CALCOCO2 antibody. Densitometry was carried out as above. Total RNA was extracted and real-time qRT-PCR was performed to measure mRNA levels of IFN-α and IFN-β normalized to GAPDH mRNA (E), and presented as relative quantification (RQ) with respect to siCON (RQ ± SE, n=3, confidence interval at 95%). **(B, D, F)** HeLa cells were transfected with siSQSTM1 or siCON for 48 h, followed by Western blot analysis of MAVS (B) and p-TBK1/TBK1 (D) and qRT-PCR measurement of IFN-α and IFN-β (F) as above. Similar results were observed in 3 independent experiments.

CALCOCO2 is cleaved after Q139 following CVB3 infection by viral proteinase 3C

During our characterization of CALCOCO2 as a pro-viral autophagy receptor, I made the surprising observation that CVB3 infection resulted in a marked reduction in CALCOCO2 protein levels, accompanied by the appearance of a ~36-kDa protein fragment using an anti-CALCOCO2 antibody targeting to the C-terminal region (**Figure 18A**). This result suggests a likely cleavage of CALCOCO2. In line with this, HeLa cells transiently expressing 3×Flag-CALCOCO2 showed an equally significant decrease in full-length CALCOCO2 levels following CVB3 infection, although no apparent fragment was observed with the N-terminal anti-Flag antibody (**Figure 18B**). Further ectopic expression using an N-terminally tagged GFP-CALCOCO2 demonstrated a decrease in full-length GFP-CALCOCO2 and the detection of an additional band at ~42 kDa using anti-GFP antibody (**Figure 18C**), corresponding to an N-terminal cleavage fragment of CALCOCO2 which complemented our previously observed endogenous CALCOCO2 C-terminal fragment (**Figure 18C**).

We then studied whether CVB3-encoded proteinases are responsible for the cleavage of CALCOCO2. Co-transfection of GFP-CALCOCO2 with constructs expressing viral proteinase $3C^{wt}$, but not a catalytically inactive 3C mutant ($3C^{mut}$), led to the production of the same ~42 kDa N-terminal cleavage fragment, as that observed following CVB3 infection **(Figure 18D)**. Similarly, *in vitro* cleavage assays using recombinant proteinases $3C^{wt}$, but not $3C^{mut}$, showed the detection of CALCOCO2 cleavage fragment (**Figure 18E**), suggesting that viral proteinase 3C is responsible for the cleavage of CALCOCO2. To rule out the possible involvement of viral proteinase 2A and host caspases, which are activated during CVB3 infection, I conducted an *in vitro* cleavage assay using recombinant $2A^{wt}$ or $2A^{mut}$ (**Figure 18F**) and Western blotting using the pan-caspase inhibitor zVAD-fmk (**Figure 18G**). I found that addition of viral proteinase $2A^{wt}$ or inhibition of general caspase activity failed to induce the cleavage of CALCOCO2, indicating that CALCOCO2 cleavage is independent of 2A and caspase activation.

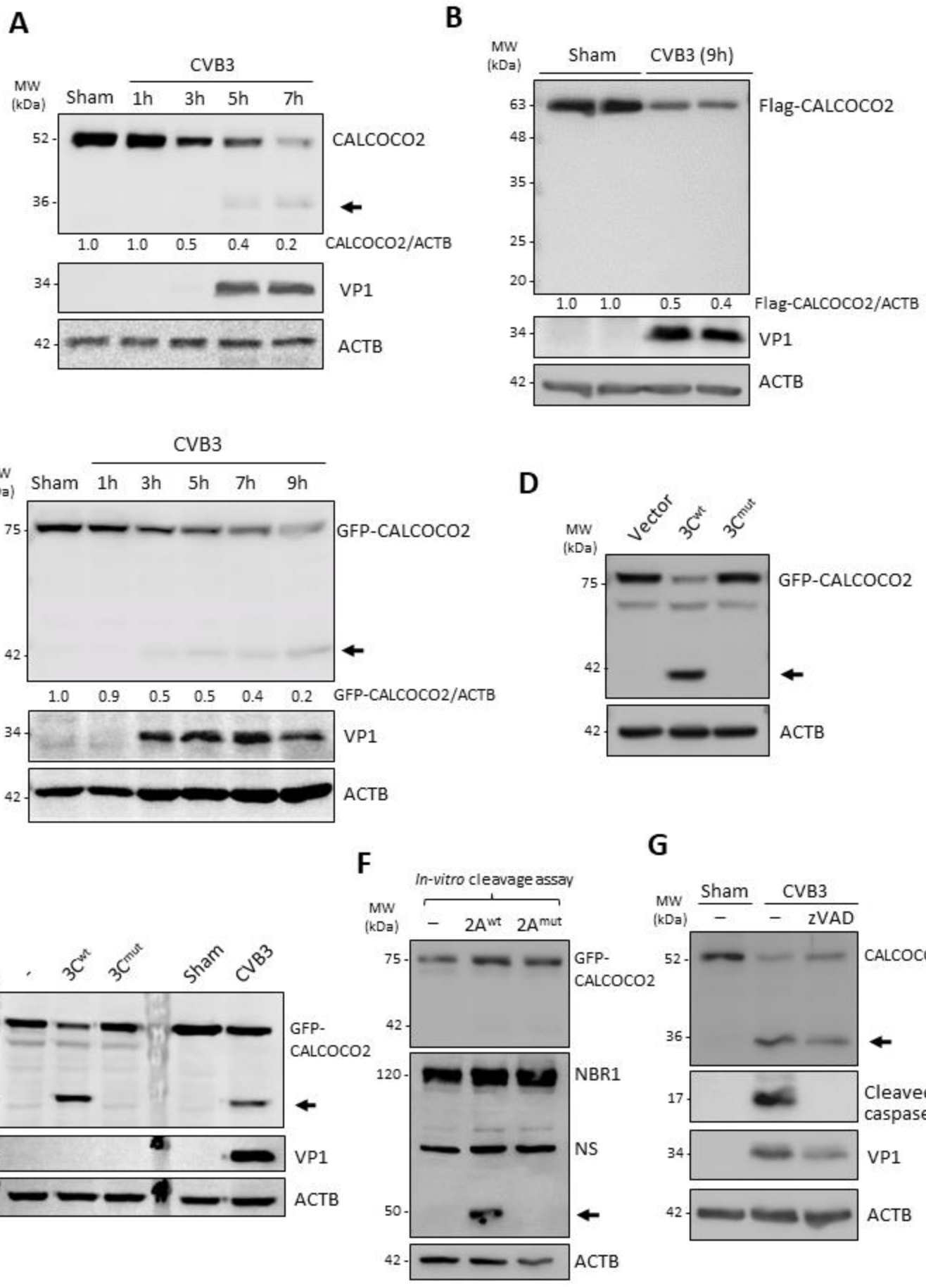
A
CVB3
MW (kDa)
Sham
1h
3h
5h
7h
52
36
CALCOCO2
1.0 1.0 0.5 0.4 0.2
CALCOCO2/ACTB
34
VP1
42
ACTB
B
MW (kDa)
Sham
CVB3 (9h)
63
48
35
25
20
Flag-CALCOCO2
1.0 1.0 0.5 0.4
Flag-CALCOCO2/ACTB
34
VP1
42
ACTB
C
CVB3
MW (kDa)
Sham
1h
3h
5h
7h
9h
75
42
GFP-CALCOCO2
1.0 0.9 0.5 0.5 0.4 0.2
GFP-CALCOCO2/ACTB
34
VP1
42
ACTB
D
MW (kDa)
Vector
3Cwt
3Cmut
75
42
GFP-CALCOCO2
42
ACTB
E
MW (kDa)
-
3Cwt
3Cmut
Sham
CVB3
75
42
GFP-CALCOCO2
34
VP1
42
ACTB
F
In-vitro cleavage assay
MW (kDa)
–
2Awt
2Amut
75
42
GFP-CALCOCO2
120
NBR1
NS
50
42
ACTB
G
MW (kDa)
Sham
CVB3
–
–
zVAD
52
36
CALCOCO2
17
Cleaved caspase 3
34
VP1
42
ACTB

Figure 18. CALCOCO2 is cleaved following CVB3 infection by viral proteinase 3C. (A-C) HeLa cells (A), HeLa cells transfected with 3×Flag-CALCOCO2 (B), or GFP-CALCOCO2 (C) for 24 h, were sham- or CVB3-infected (MOI=10) for the indicated time-points. Western blotting was conducted for detection of CALCOCO2 using anti-CALCOCO2 that recognizes the C-terminal region of CALCOCO2 (A), anti-Flag (B), or anti-GFP antibody (C). Densitometry was carried out as above. **(D)** HeLa cells were transfected with GFP-CALCOCO2, together with either empty vector, wild-type 3C ($3C^{wt}$), or catalytically inactive 3C (C147A) mutant ($3C^{mut}$). After 24 h, cells lysates were collected and analyzed by Western blotting with an anti-GFP antibody. **(E)** *In vitro* cleavage assay was performed by incubation of lysates (30 μg) from HeLa cells transfected with GFP-CALCOCO2 with vehicle (-), purified $3C^{wt}$, or $3C^{mut}$ proteins (0.1 μg) for 16 h. Sham- and CVB3-infected (MOI=10, 7 h) HeLa cell lysates were included (right two lanes) as a control. Cleavage products of CALCOCO2 were analyzed by Western blotting with anti-GFP antibody. **(F)** *In vitro* cleavage assay was conducted as above with vehicle (-), recombinant $2A^{wt}$, or $2A^{mut}$ proteins (0.3 μg) for 16 h. Cleavage of NBR1 by 2A, which was previously demonstrated [140], was shown as evidence of the activity of 2A. **(G)** HeLa cells were infected with CVB3 (MOI=10) for 7 h in the presence or absence of a pan-caspase inhibitor z-VAD-FMK (zVAD, 50 μM) or vehicle (-). Western blotting was then performed with an anti-CALCOCO2 antibody. Activation of caspase-3 was examined using an anti-cleaved caspase-3 antibody. Results in this Figure represent data from 3 independent experiments.

Having identified that CALCOCO2 is cleaved by viral proteinase 3C, I performed site-directed mutagenesis based on the enteroviral 3C consensus sequence[148] to identify the potential cleavage sites on CALCOCO2. Both *in vivo* (in cells transfected with $3C^{wt}$ proteinase construct, **Figure 19A**) and *in vitro* (using recombinant purified viral proteinase, **Figure 19B**) cleavage assay showed that GFP-$CALCOCO2^{Q139L}$ (glutamine 139 mutated to leucine) is resistant to 3C-mediated cleavage, suggesting that CALCOCO2 is cleaved by viral proteinase 3C after Q139. This cleavage separates the N-terminal skeletal and kidney-enriched inosital phosphatase (SKIP) carboxyl homology (SKICH) and LC3C-interacting region (CLIR) of CALCOCO2 from its C-terminal LIR, coiled-coil (CC) and ubiquitin-binding zinc finger (UBZ) domains (**Figure 19C**).

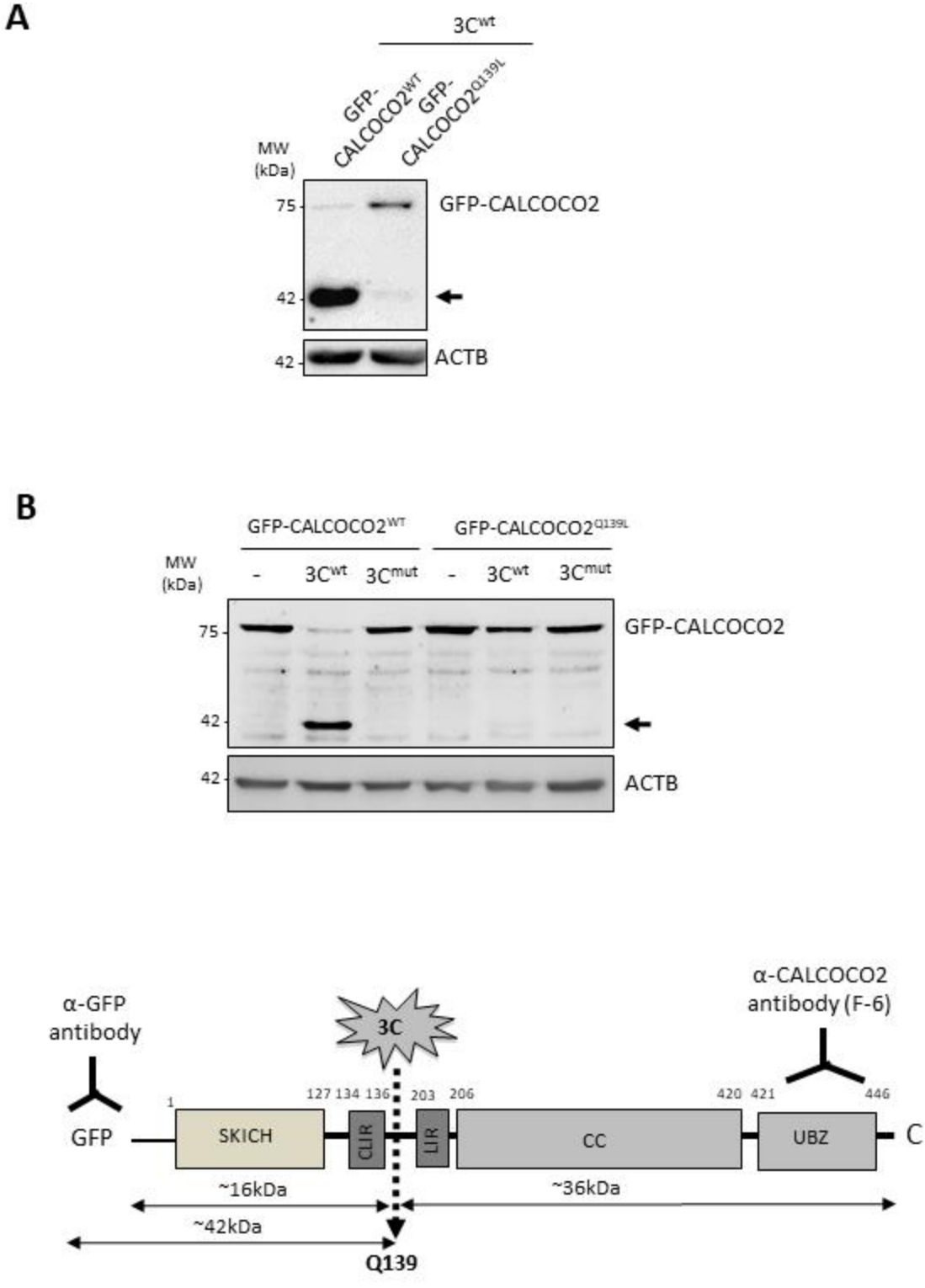
A
3C^wt
GFP-CALCOCO2^WT
GFP-CALCOCO2^Q139L
MW (kDa)
75
42
GFP-CALCOCO2
42
ACTB
B
GFP-CALCOCO2^WT
GFP-CALCOCO2^Q139L
MW (kDa)
-
3C^wt
3C^mut
-
3C^wt
3C^mut
75
42
GFP-CALCOCO2
42
ACTB
C
α-GFP antibody
3C
α-CALCOCO2 antibody (F-6)
GFP
1
127 134 136
203 206
420 421
446
SKICH
CLIR
LIR
CC
UBZ
C
~16kDa
~36kDa
~42kDa
Q139

Figure 19. CALCOCO2 is cleaved after Q139 by viral proteinase 3C. (A) HeLa cells were transfected with $3C^{wt}$ together with GFP-$CALCOCO2^{WT}$ or GFP-$CALCOCO2^{Q139L}$ as indicated. After 24 h, cell lysates were harvested and subjected to Western blot analysis using an anti-GFP antibody. **(B)** *In vitro* cleavage assay was conducted by incubation of lysates of HeLa cells transfected with GFP-$CALCOCO2^{WT}$ or GFP-$CALCOCO2^{Q139L}$ with recombinant $3C^{wt}$, $3C^{mut}$, or vehicle (-) as above in (E). **(C)** Schematic illustration of the structural domains, the identified cleavage site, the antibody recognition regions, and the resulting cleavage products of CALCOCO2. SKICH, skeletal muscle and kidney-enriched inositol phosphatase (SKIP) carboxyl homology; CLIR, LC3C-interacting region; LIR, LC3-interacting region; CC, coiled-coil domain; UBZ, ubiquitin-binding zinc-finger region. Arrows denote the cleavage fragments. NS, non-specific bands. Results in this Figure represent data from 2 independent experiments.

The C-terminal cleavage fragment of CALCOCO2 retains the function of full-length CALCOCO2 in promoting viral replication

We next sought to evaluate the functional consequence of CALCOCO2 cleavage by generating recombinant fragments corresponding to the N-terminal (N1-139) and C-terminal (C140-446) cleavage products. Of note, I found that the N-CALCOCO2 fragment was less stable as compared to full-length and C-CALCOCO2 fragment (**Figure 20A & B**), consistent with the finding that the Flag-N-CALCOCO2 was undetectable following CVB3 infection (**Figure 18B**). Further experiments using proteasome and lysosome inhibitors showed that the N-CALCOCO2 fragment was degraded mainly through the proteasome pathway, as evidenced by the accumulation of N-CALCOCO2 in the presence of proteasome inhibitor MG132 (**Figure 20A**), but not lysosome inhibitor bafilomycin A1 (**Figure 20B**)**.** Based on these findings, our study hereafter focused on the C-CALCOCO2 fragment to further elucidate its functional significance. Similar to full-length $CALCOCO2^{WT}$, I found that expression of C-CALCOCO2 caused a significant increase in viral titers (**Figure 20C**), suggesting that viral cleavage of CALCOCO2 does not impair its pro-viral activity. To further understand the pro-viral mechanism of C-CALCOCO2, I examined whether C-CALCOCO2 has a direct effect on MAVS. To rule out the possible interference from endogenous CALCOCO2, I utilized CRISPR-Cas9 gene editing system to generate CALCOCO2 knockout cells (**Figure 20D).** The cells were then reconstituted with either a vector control, $CALCOCO2^{WT}$, or truncated C-CALCOCO2 by transient transfection. As shown in **Figure 20E**,

protein levels of MAVS were reduced in CALCOCO2 knockout cells expressing either CALCOCO2^{WT} or C-CALCOCO2 as compared to vector control, indicating that MAVS is also a target of C-CALCOCO2. I further examined whether C-CALCOCO2 retains its capacity to behave as an autophagy receptor by evaluating its ability to interact with the autophagosome marker LC3 as well as degradative signals such as ubiquitin. Consistent with the observation that both wild-type and truncated CALCOCO2 can degrade MAVS, both forms demonstrated the capacity to interact with exogenously expressed GFP-LC3 as well as HA-Ubiquitin conjugates **(Figure 20F & 20G).** Finally, I assessed the effects of C-CALCOCO2 on IFN-β production induced by poly I:C (a synthetic analogue of double-stranded RNA). I found that treatment with poly I:C for 12 h resulted in a marked increase in IFN-β transcript levels (**Figure 20H**). Addition of CALCOCO2^{WT} or C-CALCOCO2 significantly decreased mRNA and protein levels of IFN-β (**Figures 20H & 20I).** Collectively, our results support a pro-viral mechanism of the C-CALCOCO2 fragment through attenuating the IFN-β signaling by targeting the MAVS protein.

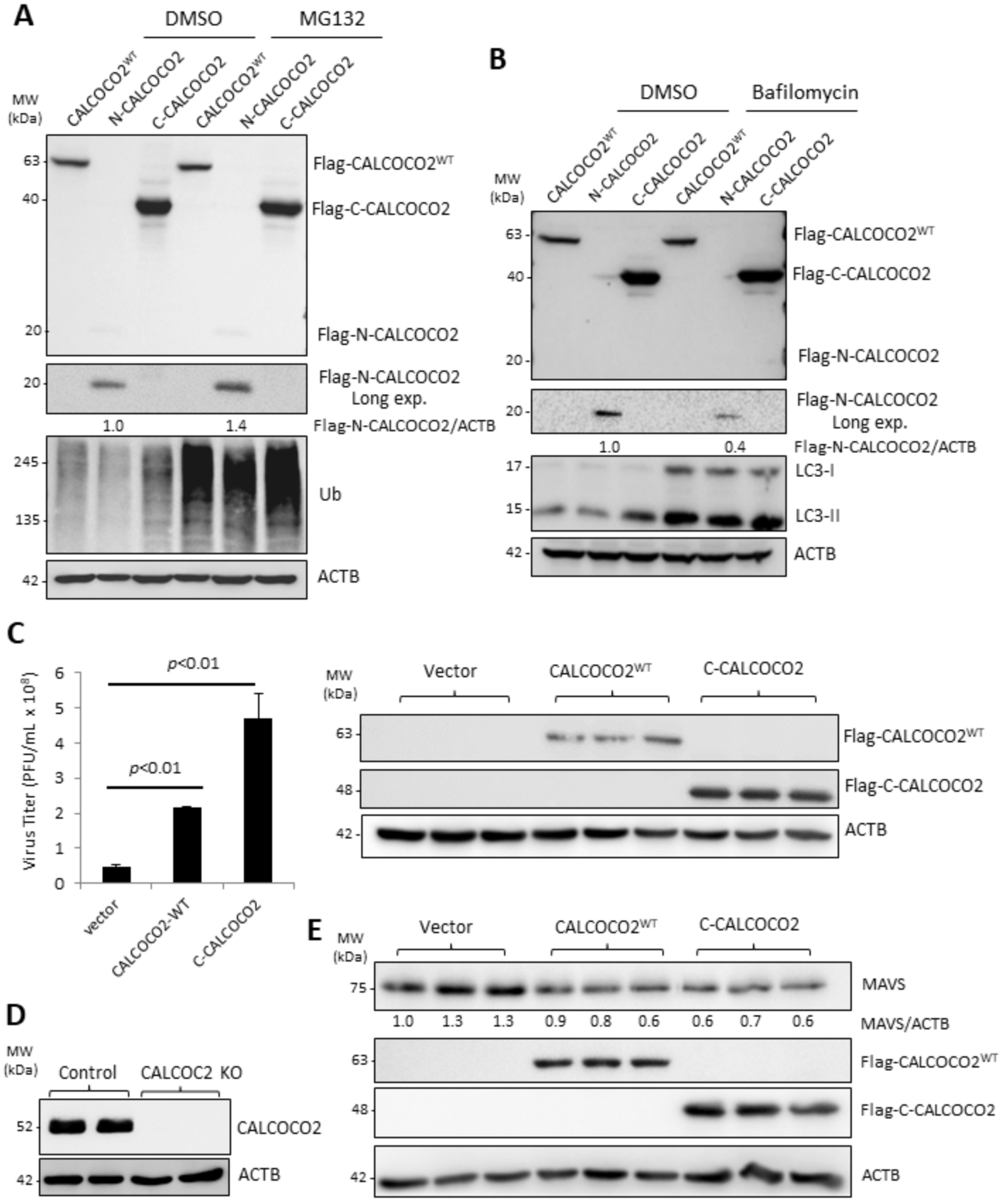
A
DMSO
MG132
MW (kDa)
CALCOCO2WT
N-CALCOCO2
C-CALCOCO2
CALCOCO2WT
N-CALCOCO2
C-CALCOCO2
63
40
20
Flag-CALCOCO2WT
Flag-C-CALCOCO2
Flag-N-CALCOCO2
20
Flag-N-CALCOCO2
Long exp.
1.0
1.4
Flag-N-CALCOCO2/ACTB
245
135
Ub
42
ACTB
B
DMSO
Bafilomycin
MW (kDa)
CALCOCO2WT
N-CALCOCO2
C-CALCOCO2
CALCOCO2WT
N-CALCOCO2
C-CALCOCO2
63
40
20
Flag-CALCOCO2WT
Flag-C-CALCOCO2
Flag-N-CALCOCO2
20
Flag-N-CALCOCO2
Long exp.
1.0
0.4
Flag-N-CALCOCO2/ACTB
17
15
LC3-I
LC3-II
42
ACTB
C
p<0.01
p<0.01
Virus Titer (PFU/mL x 10^8)
6
5
4
3
2
1
0
vector
CALCOCO2-WT
C-CALCOCO2
MW (kDa)
Vector
CALCOCO2WT
C-CALCOCO2
63
Flag-CALCOCO2WT
48
Flag-C-CALCOCO2
42
ACTB
D
MW (kDa)
Control
CALCOC2 KO
52
CALCOCO2
42
ACTB
E
MW (kDa)
Vector
CALCOCO2WT
C-CALCOCO2
75
MAVS
1.0
1.3
1.3
0.9
0.8
0.6
0.6
0.7
0.6
MAVS/ACTB
63
Flag-CALCOCO2WT
48
Flag-C-CALCOCO2
42
ACTB

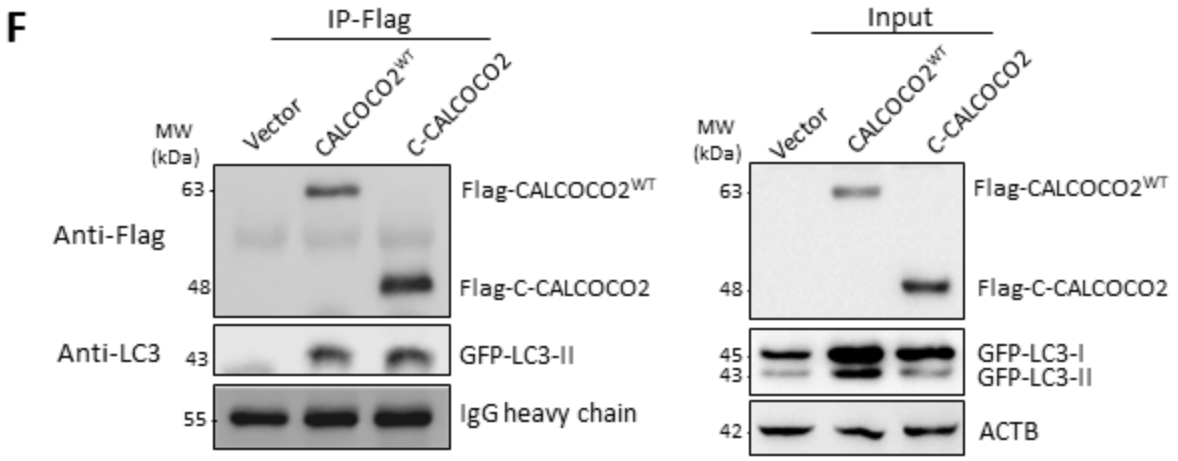
F
IP-Flag
Input
Vector
CALCOCO2WT
C-CALCOCO2
MW (kDa)
63
48
43
55
45
42
Anti-Flag
Anti-LC3
Flag-CALCOCO2WT
Flag-C-CALCOCO2
GFP-LC3-II
IgG heavy chain
GFP-LC3-I
GFP-LC3-II
ACTB

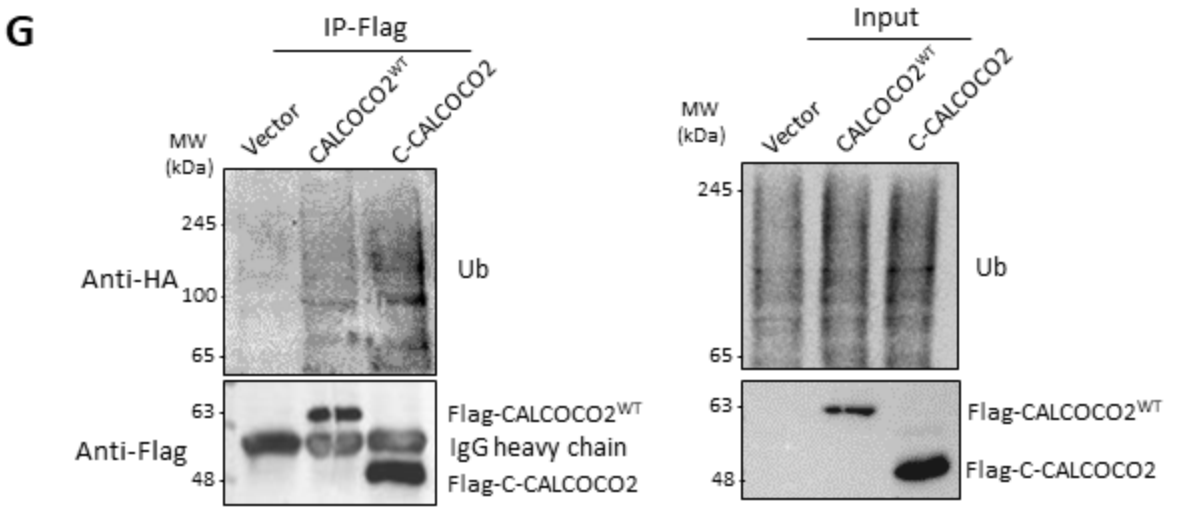
G
IP-Flag
Input
Vector
CALCOCO2WT
C-CALCOCO2
MW (kDa)
245
100
65
63
48
Anti-HA
Anti-Flag
Ub
Flag-CALCOCO2WT
IgG heavy chain
Flag-C-CALCOCO2

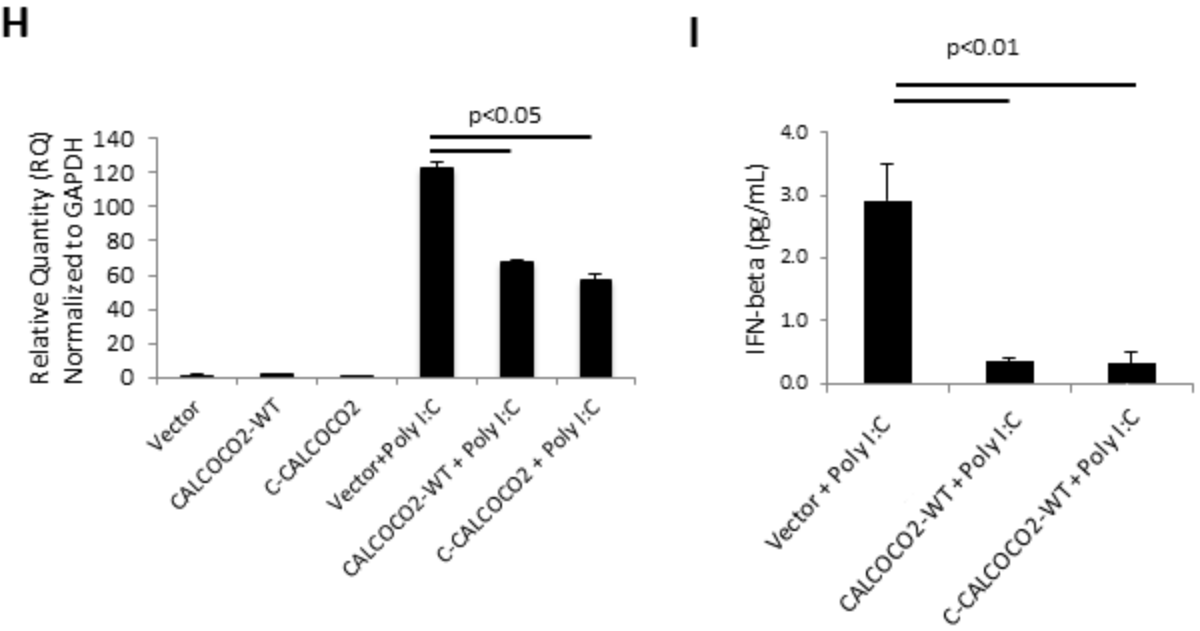
H
Relative Quantity (RQ) Normalized to GAPDH
140
120
100
80
60
40
20
0
p<0.05
Vector
CALCOCO2-WT
C-CALCOCO2
Vector+Poly I:C
CALCOCO2-WT + Poly I:C
C-CALCOCO2 + Poly I:C
I
p<0.01
IFN-beta (pg/mL)
4.0
3.0
2.0
1.0
0.0
Vector + Poly I:C
CALCOCO2-WT + Poly I:C
C-CALCOCO2-WT + Poly I:C

Figure 20. The C-terminal cleavage fragment of CALCOCO2 retains the function of full-length CALCOCO2 in promoting CVB3 growth. (A, B) HeLa cells were transfected with 3×FLAG-tagged CALCOCO2^{WT}, N- or C-terminal cleavage fragments of CALCOCO2 **(**N-CALCOCO2 or C-CALCOCO2) in the presence of vehicle (DMSO), proteasomal inhibitor (MG132, 10μM) (A), or lysosome inhibitor (bafilomycin, 200nM) (B) for 6 h. Protein levels of full-length and the respective cleavage fragments of CALCOCO2 were verified by Western blotting with an anti-Flag antibody. Ubiquitin (A) and LC3 (B) were probed by Western blotting to confirm the inhibition of proteasome and lysosome activities, respectively. Densitometry was conducted as above. **(C)** HeLa cells were transfected with 3×FLAG-tagged CALCOCO2^{WT}, C-CALCOCO2, or empty vector for 24 h, followed by CVB3 infection (MOI=10) for 7 h. Virus titer (mean ± SD, n=3) were measured by $TCID_{50}$ and Western blotting was performed to confirm the expression of exogenous CALCOCO2 using an anti-Flag antibody. **(D)** Knockout (KO) efficiency of the CALCOCO2 KO HeLa cells was verified by Western blotting with anti-CALCOCO2 antibody. **(E)** CALCOCO2 KO cells were transfected with empty vector, 3×FLAG-tagged CALCOCO2^{WT}, or C-CALCOCO2 for 16 h. Western blot analysis was conducted to examine the protein expression of MAVS, CALCOCO2, and ACTB. Protein levels of MAVS were quantitated by densitometric analysis, normalized to ACTB, and presented as fold changes (mean±SD, n=3) compared to vector control. **(F,G)** HeLa cells were transfected with 3×FLAG-tagged CALCOCO2^{WT}, C-CALCOCO2, or empty vector and co-transfected with either GFP-LC3 **(F)** or HA-Ubiquitin **(G)** for 16 h. Co-IP and Western blotting were conducted as above. Blots for IgG light chain and ACTB were used as loading controls for IP and input, respectively. Similar results were observed in 2 independent experiments. (**H, I**) CALCOCO2 KO cells were transfected with empty vector, 3×FLAG-tagged CALCOCO2^{WT}, or C-CALCOCO2 for 16 h, followed by addition of poly I:C (1 μg/ml) or vehicle for another 12 h. Cells were collected for RNA extraction and qRT-PCR was conducted to determine the mRNA levels of IFN-β (F, mean ± SD, n=3). Culture supernatants were harvested for the measurement of IFN-β secretion by ELISA (G, mean ± SD, n=3). Results in this Figure represent data from 2-3 independent experiments.

Discussion

Enterovirus replication is tightly associated with host cellular machinery, including the autophagy pathway, which has been previously shown to be beneficial for viral growth by providing physical scaffolds for viral replication[68, 75, 149], and through facilitating autophagosome-associated non-lytic viral spread[15, 17, 97]. Additional support was provided from a recent study, which used a high-throughput genetic screen to identify autophagy and membrane trafficking genes as critical regulators of susceptibility to *Picornaviruses* infection[150]. I have previously demonstrated that CVB3 infection promotes the formation of autophagosomes while at the same time targeting several autophagy receptor and adaptor proteins, including SQSTM1/p62, NBR1, synaptosomal-associated protein 29 (SNAP29), and pleckstrin homology domain-containing family M member 1(PLEKHM1) to disrupt its degradative capacity [68, 92, 140, 151]. The current study provides further insights into the mechanism by which CVB3 subverts autophagy by identifying the autophagy receptor CALCOCO2 as a novel viral substrate that is co-opted to facilitate viral propagation.

CALCOCO2 is generally considered a xenophagic receptor; this is mainly based on previous evidence on bacteria, most notably Salmonella[152, 153, 154]. For viral infection, it was previously reported that CALCOCO2 binds the non-structural protein 2 of Chikungunya virus to promote viral replication in humans but not mice, suggesting not only a pro-viral function but also a species-specific role for CALCOCO2[105]. Other studies also showed a pro-viral role for CALCOCO2 in Influenza and Measles viral infection[155, 156]. However, the mechanism has not been investigated and CALCOCO2 interaction with various viral proteins has been proposed to be relevant[105, 155, 157]. In this study, I demonstrated that in addition to its role in selective autophagy, CALCOCO2 has an indirect effect on CVB3 propagation by regulating a broader host anti-viral response. Type I IFN signaling provides a potent host innate immunity against enteroviral infection. Indeed, CVB3 has been shown to disrupt this pathway through virus-mediated cleavage of MAVS protein[158, 159]. Consistent with a recent report[146], I found that loss of CALCOCO2 causes increased accumulation of MAVS and phosphorylation of TBK1, a prerequisite for the downstream production of IFN α/β cytokines. I also showed that depletion of CALCOCO2, but not SQSTM1, results in an elevated production of IFN-α/IFN-β mRNA, providing a plausible mechanism by which autophagy receptors differentially regulate CVB3 replication.

We previously reported that perturbation of SQSTM1, either through genetic silencing or exogenous overexpression, does not contribute to viral replication[92]. The current study addresses the limitations of our previous research, in which viral propagation was assessed after challenging cells with a high dose of CVB3, which I now realize may fail to capture the subtle nuances of viral replication. The present study utilized a low dose of CVB3 infection to re-examine the role of SQSTM1 in viral propagation and demonstrated an anti-viral function of SQSTM1.

It was first identified by Beth Levine's laboratory that SQSTM1 binds and targets the capsid proteins of Sindbis virus for autophagic degradation[143]. Later, SQSTM1 interaction with capsid proteins was also reported during Chikungunya viral infection[105]. Our current study revealed that both SQSTM1 and CALCOCO2 are able to interact with CVB3 capsid protein VP1. I further demonstrated that VP1 undergoes ubiquitination, a substrate signal recognized by autophagy receptors, but whether intact infectious capsids are also ubiquitinated remains to be shown[160]. Autophagy receptors can initiate virophagy either in a ubiquitin-dependent or independent manner[161]. With regards to SQSTM1, both ubiquitin-dependent and independent targeting have been reported for Chikungunya and Sindbis virus[105, 143]. An important consideration in virophagy is the nature of ubiquitin-association i.e. whether autophagy substrates, such as viral capsid proteins, are either directly ubiquitinated via the activity of E3 ubiquitin ligases, or rather indirectly associate with host ubiquitinated factors. In both cases, the presence of ubiquitin can signal for the recruitment of autophagy receptors[162]. But an additional consideration should be made for the former in which direct ubiquitin-conjugation can occur through various linkages. Using linkage-specific ubiquitin antibodies, our study revealed that CVB3 capsid proteins can potentially exhibit multiple forms, including K48 and/or K63–linked ubiquitination by a yet unidentified E3 ligase, although the precise number of ubiquitin linkages is not clear. One potential candidate, the E3 ligase SMURF1 (Smad ubiquitin regulatory factor 1), was previously shown to not only interact with SQSTM1 but to also regulate virophagy of Sindbis and herpes simplex virus, albeit in a ubiquitin-conjugation independent manner[163]. Another likely candidate is the SQSTM1-associoated E3 ligase TRAF6 (tumor necrosis factor receptor (TNF)-associated factor 6), which plays an important role in anti-viral signaling via the NF-κB pathway. Of note, our previous report demonstrated that CVB3-mediated cleavage of SQSTM1 occurs within its respective TRAF6-binding domain, leading to disrupted NF-κB signaling[92]. In addition to CVB3, cleavage of

SQSTM1 has recently been confirmed upon poliovirus, rhinovirus, and enterovirus D68 infection[164], suggesting a common enteroviral strategy to counteract selective autophagy receptor.

In summary, our study provides novel insight into the mechanisms by which CVB3 evades host virophagy, through viral-mediated cleavage of CALCOCO2 and SQSTM1, to promote viral propagation.

In **Chapter 3**, I demonstrated that CVB3 can target selective autophagy receptors for cleavage as a strategy to enhance viral propagation and disrupt the innate immune function of autophagy receptors. In addition to disrupting the normal function of selective autophagy, I sought to explore additional mechanisms by which CVB3 evades autophagic degradation. In **Chapter 4**, I identified novel molecular insights by which CVB3 targets the autophagosome-lysosome fusion process to impair autophagic clearance.

Chapter 4: CVB3 Inhibits Autophagic Flux Via Disruption of the SNARE Complex

Background

Numerous studies have reported that EVs initiate autophagy to facilitate viral replication. Given that autophagy is generally regarded as an anti-microbial pathway, the question emerged as to how EVs circumvent the anti-viral capacity of autophagy. Research presented in ***Chapter 3*** revealed that CVB3 can degrade selective autophagy receptors such as SQSTM1 and CALCOCO2 to evade capture inside autophagosomes. However, it remains unclear whether EV infection can regulate the late stage autophagosome-lysosome fusion process. Recent advances in the field of autophagy have identified SNARE proteins as critical factors for autophagosome-lysosome fusion [34, 35]. In particular, the SNARE complex of syntaxin 17/STX17, SNAP29, and VAMP8 was shown to be a major driver of autophagic membrane fusion. The **rationale** of this study was to understand the underlying mechanism by which CVB3 regulates autophagosome-lysosome fusion. The **specific aim** was to investigate whether CVB3 targets the autophagic SNARE complex, particularly the STX17-SNAP29-VAMP8 complex that is implicated in autophagosome-lysosome fusion processes.

Materials and methods

Animals

The breeding pairs of autophagic reporter mice expressing GFP-LC3 were obtained from the RIKEN BioResource Center (00806), and the background C57BL/6 mice were purchased from the Jackson Laboratories (000664). These mice were bred at the Center for Heart Lung Innovation animal facility. PCR genotyping was performed to identify wild-type (WT), hemizygous (WT/ Tg), and homozygous (Tg/Tg) GFP-LC3 mice as previously described (Kuma and Mizushima, 2008). Male homozygous GFP-LC3 and C57BL/6 mice at the age of 5 weeks were inoculated intraperitoneally with 104 plaque-forming units (pfu) of CVB3 (Charles Gauntt strain) or sham-infected with PBS as previously described (Wang et al., 2015). At 3 or 9 days post-infection, mice were sacrificed, and tissues were harvested for confocal imaging, immunohistochemical staining,

western blotting, and plaque assay. All mouse studies were carried out in accordance with the Guide for the Care and Use of Laboratory Animals of the Canadian Council on Animal Care. The protocol (A13- 0321) for this research was approved by the Animal Care Committee of the University of British Columbia. Statistical Analysis Results are presented as mean ± SD. Statistical analysis was performed using unpaired Student's t test. A p value < 0.05 was considered to indicate statistical significance. The survival curves were plotted using Kaplan-Meier methods, and significance was determined using the log rank test.

Cell culture and viral infection

HEK293 cells stably expressing mRFP-EGFP-LC3 were provided from Dr. Sharon Gorski at the BC Cancer Agency (Vancouver, BC, Canada). HEK293 and HeLa cells (American Type Culture Collection) were cultured in Dulbecco's Modified Eagle's Medium (DMEM) supplemented with 10% fetal bovine serum (FBS) and a penicillin/streptomycin cocktail (100 µg/mL). Cell starvation was induced by incubating cells in Hank's Balanced Salt Solution (Invitrogen, #14175095) for the indicated times. For CVB3 infection, cells were either sham-infected with PBS or inoculated with CVB3 (Kandolf strain) at different multiplicity of infection (MOI) as indicated. The following chemicals were used for the treatment of cells: general caspase inhibitor Z-VAD-FMK (BD Biosciences, #550377), proteasome inhibitor MG132 (Sigma-Aldrich, C2211), lysosome/endosome inhibitor bafilomycin A1 (Sigma-Aldrich, B1793), autophagy activator rapamycin (Sigma-Aldrich, R8781).

Plasmids and small interfering RNA (siRNA)

The myc-tagged wild-type CVB3-3C ($3C^{wt}$) and C147A mutant CVB3-3C ($3C^{mut}$) constructs were generous gifts from Dr. Carolyn Coyne at the University of Pittsburgh [114]. The 3×Flag-SNAP29, Flag-STX17, and Flag-VAMP8 constructs were gifts from Dr. Qing Zhong at the University of Texas Southwestern Medical Center [35]. The PLEKHM1-HA plasmid was purchased from Addgene (#89300). 3×Flag-$SNAP29^{Q161L}$ and $PLEKHM^{Q668L}$-HA mutants were generated using the QuikChange Site-Directed Mutagenesis kit (Agilent, #200518) according to the manufacture's protocol with the following primers: SNAP29 forward - CAG GAA GCA AAG TAC CTG GCC AGC CAC CCA AAC; SNAP29 reverse - GTT TGG GTG GCT GGC CAG GTA CTT TGC TTC CTG; PLEKHM1 forward-CCC GCG GCC CTC CTG GGC ACA CAG TTT G,

PLEKHM1 reverse - CAA ACT GTG TGC CCA GGA GGG CCG CGG G. HA-VAMP8 and HA-STX17 constructs were generous gifts from Dr. Mingzhou Chen at the Wuhan University, China [165]. The siRNAs targeting SNAP29 (sc-76531) and PLEKHM1 (sc-93882), and the scrambled siRNAs (sc-37007) were purchased from Santa Cruz Biotechnology. For transfection, HeLa cells were transiently transfected with plasmid cDNAs or siRNAs using Lipofectamine 2000 (Invitrogen, 11668-019) following the manufacturer's instructions.

Western blot analysis

Cells were lysed in buffer (10mM HEPES pH 7.4, 50mM NaPyrophosphate, 50 mM NaF, 50mM NaCl, 5 mM EDTA, 5mM EGTA, 100 µM Na_3VO_4, 0.1% Triton X-100) supplemented with cOmplete Mini, EDTA-free protease inhibitor cocktail tablets (Sigma, #11836170001) . Western blotting was conducted using the following primary antibodies: p-eIF2α (Cell Signaling Technology, #9721), eIF2α (Cell Signaling Technology, #9722), ATG5 (Novus Biologicals, NB110-53818), Rab7 (Santa Cruz Biotechnology, sc-10767), LAMP2 (Santa Cruz Biotechnology, sc-8101), SNAP29 (Abcam, ab181151), STX17 (Sigma-Aldrich, HPA001204), VAMP8 (Abcam, ab76021), cleaved-caspase 3 (Cell Signaling Technology, #9661), p62/SQSTM1 (PROGEN Biotechnik GmbH, GSQSTM1-C), LC3 (MBL International, PM036), PLEKHM1 (Cell Signaling Technology, #66012), VP1 (Dako, M706401-1), Nbr1 (Santa Cruz Biotechnology, sc-130380), EGFR (Cell Signaling Technology, #4267), HA (Roche, 11867423001), Flag (Sigma, F1804), ubiquitin (Cell Signaling Technology, #3933), LRP6 (Cell Signaling Technology, #2560), β-actin (Sigma-Aldrich, A5316), GAPDH (Cell Signaling Technology, 14C10), and GFP (Life Technologies, A-6455).

Immunofluorescence and confocal microscopy

Cells were fixed in 4% methanol-free paraformaldehyde for 15min at room temperature. Unreacted aldehyde was quenched with 100 mM glycine/PBS solution for 15min. Cells were subsequently permeabilized with 3-minute incubation in 0.1% Triton X-100. Fixed and permeabilized cells were blocked for 1 h with 3% bovine serum albumin, followed by incubation with primary antibodies (anti-LC3, anti-VP1, anti-STX17, and anti-dsRNA) at 4ºC overnight and then secondary antibodies for 1 h. After washes, coverslips were mounted using Fluoroshield with DAPI (Sigma-Aldrich, F6057). Lysosomes and late endosomes were visualized using Lysotracker Red DND-99 (life technologies, L7528) according to the manufacturer's instructions. Images were

captured with the Zeiss LSM 880 Inverted Confocal Microscopy. Quantification of the localization of LC3 and Lysotracker Red (LTR) was conducted using ImageJ and presented as Pearson coefficient (Rr) by counting at least 50 $LC3^{+}/LTR^{+}$ cells. HeLa cells positive for LC3 peripheral staining were counted and normalized to total cells (70+ cells) and expressed as % positive cells (mean ± SD) with LC3 periphery accumulation.

Histological examination

Heart specimens were stained with hematoxylin and eosin (H&E) as described previously [118]. Sections were then graded blindly for the damage of heart based on the relative lesion area, cellular vacuolization, calcification, necrosis, and inflammatory infiltration, with the following scales: 0, no or questionable presence; 1, limited focal distribution; 2-3, intermediate severity; and 4-5, coalescent and extensive foci over the entirety of the transversely sectioned tissue.

Extracellular microvesicle (EMV) isolation

EMV isolation was performed as previously described [97]. Briefly, cell culture medium was harvested from HeLa cells infected with CVB3 at an MOI of 0.1 for 16 h. After spinning down to pellet cellular debris, the supernatant was collected and incubated with exosome isolation reagent (Life Technologies, #4478359) overnight at 4°C. Following centrifugation at 14,000g for 1 h, the EMVs were resuspended in PBS and air-dried on coverslips for subsequent analysis by immunostaining.

Cell fractionation

Following infection, cells were incubated with hypotonic lysis buffer (20 mM HEPES, pH 7.4, 10 mM KCl with phosphatase and protease inhibitors) for 20 minutes on ice. Cell lysates were subjected to 25 strokes of dounce homogenization followed by a brief centrifugation to remove cell debris. The supernatant was further centrifuged at 64,000 g for 1 h to separate the membrane from the cytoplasm fraction. The membrane fraction was confirmed by the detection of the membrane protein, low-density lipoprotein receptor-related protein 6 (LRP6).

Plaque assay

Following CVB3 infection of HeLa cells, cell supernatant was harvested for the measurement of extracellular virus titers. Intracellular virus was extracted from infected cells using hypotonic burst lysis as described previously [166]. In brief, cells were scraped and agitated through

repeated pipetting to ensure complete lysis. Cellular debris and nuclei were cleared and the supernatant containing intracellular virus was resuspended in equal volume 2×DMEM for viral titer measurement. The amount of extracellular and intracellular CVB3 titers in cultures and total virus titers in CVB3-infected hearts were determined by agar overlay plaque assay as previously described [92]. The samples were serially diluted and overlaid on 6-well plates of ~90% confluent HeLa cells. Following a period of 1-h incubation at 37ºC, medium was replaced with 0.75% agar overlay for 72 h. Cells were then fixed in Carnoy's fixative of 75% ethanol and 25% acetic acid. The numbers of plaques were quantified in triplicates and viral titers were measured as pfu/ml or g of tissue.

Statistical analysis

Results are presented as mean ± standard deviation (SD). Statistical analysis was performed with unpaired Student's *t*-test or analysis of variance (ANOVA). A P-value <0.05 was considered to be statistically significant. The survival curves were plotted using the Kaplan-Meier methods and significance was determined by the log-rank test.

Results

CVB3 infection results in an increased accumulation of autophagosomes *in vivo*

Our previous *in-vitro* study has found that autophagosome is accumulated in CVB3-infected cells and serves as a site for viral replication [68]. Here I explored the interplay between CVB3 and the autophagic pathway *in-vivo* using the autophagy reporter mice with GFP-labeled microtubule-associated protein 1 light chain 3 (LC3) [167]. After verification by genotyping (**Figure 21A**), adolescent male homozygous GFP-LC3 mice or the background C57BL/6 mice were inoculated with CVB3 or sham-infected for 3 or 9 days. Confocal microscopy analysis showed that, in sham-infected heart, GFP-LC3 signal was low and diffusely distributed in the cytosol of cardiomyocytes, while in virus-infected heart, the signal of GFP-LC3 was markedly increased and formed puncta (a marker of autophagosomes) (**Figure 21B**). In line with this observation, Western blotting demonstrated elevated conversion of both endogenous and exogenous non-modified LC3-I to lipidated LC3-II in infected heart (**Figure 21C**), suggesting an augmented autophagosome formation and/or a blockade of autophagosome fusion with lysosomes/endosomes. The eukaryotic initiation factor 2α (eIF2α) signaling is an important upstream regulator shown to control autophagosome formation/maturation in response to viral infection and under ER stress [168]. Similar to our findings *in-vitro* [68], I showed here that phosphorylation of eIF2α was greatly increased in virus-infected heart (**Figure 21D**), revealing a possible upstream mechanism contributing to elevated autophagosome formation. Interestingly, consistent with a previous report [83], I found that GFP-LC3 mice were more permissive to CVB3 infection than the control mice. When compared with the C57BL/6 littermates, GFP-LC3 mice had a significantly higher mortality rate (**Figure 21E**), greater viral loads (**Figure 21F**), and developed more severe virus-induced myocarditis (**Figure 1G**), indicating a pro-viral role for LC3, probably by providing autophagy-dependent and –independent intracellular membrane scaffolds for viral replication as proposed previously [83]. Together, our *in-vivo* data suggest that CVB3 infection induces an accumulation of autophagosomes in virus-infected heart, which is partly attributable to increased formation as a consequence of the activation of the upstream signaling pathway. However, whether the accumulation of LC3 puncta could also be caused by decreased autophagosome clearance remains elusive.

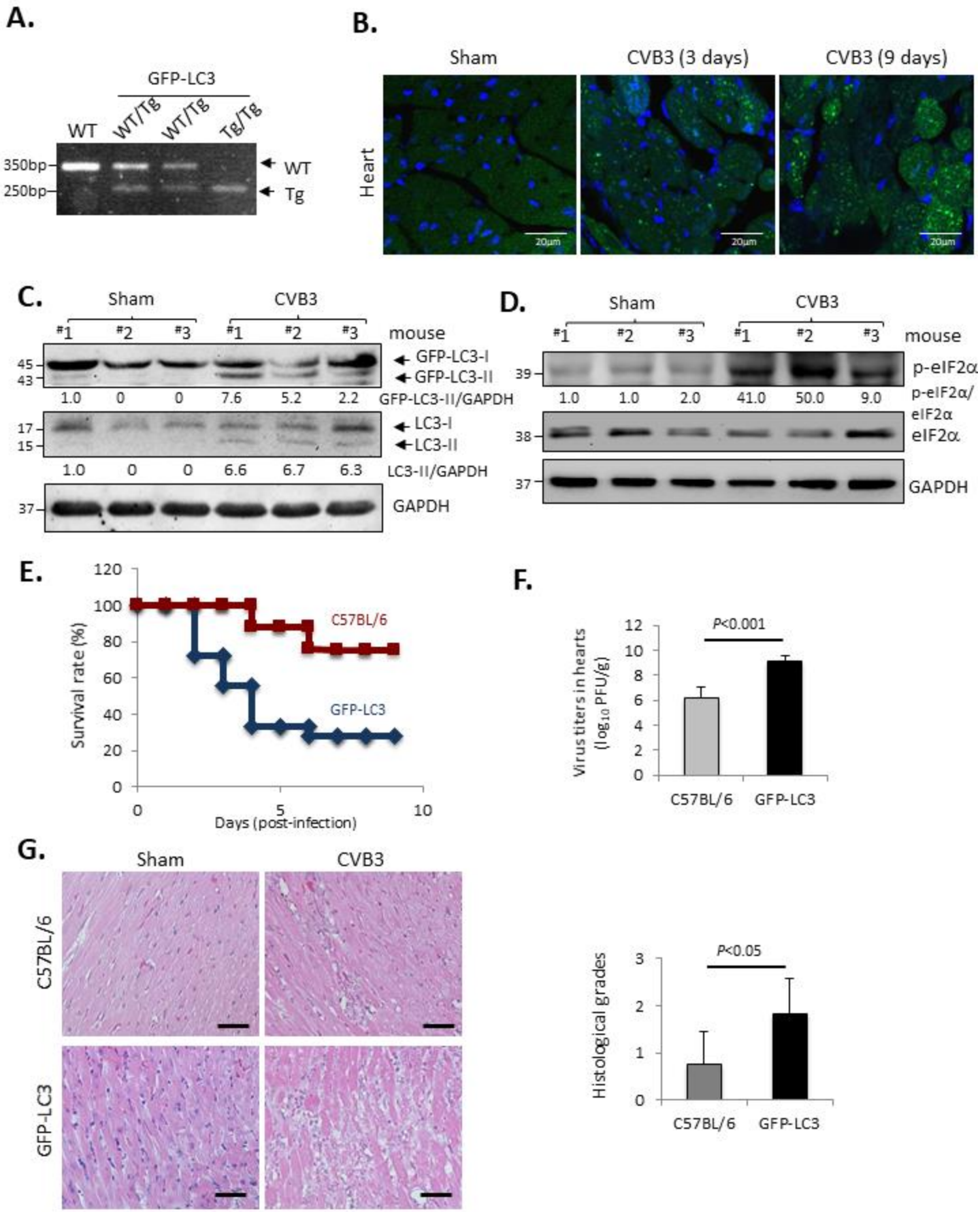
A.
GFP-LC3
WT
WT/Tg
WT/Tg
Tg/Tg
350bp
250bp
WT
Tg
B.
Sham
CVB3 (3 days)
CVB3 (9 days)
Heart
20μm
C.
Sham
CVB3
#1 #2 #3 #1 #2 #3
mouse
45
43
GFP-LC3-I
GFP-LC3-II
1.0 0 0 7.6 5.2 2.2
GFP-LC3-II/GAPDH
17
15
LC3-I
LC3-II
1.0 0 0 6.6 6.7 6.3
LC3-II/GAPDH
37
GAPDH
D.
Sham
CVB3
#1 #2 #3 #1 #2 #3
mouse
39
p-eIF2α
1.0 1.0 2.0 41.0 50.0 9.0
p-eIF2α/eIF2α
38
eIF2α
37
GAPDH
E.
Survival rate (%)
120
100
80
60
40
20
0
C57BL/6
GFP-LC3
0
5
10
Days (post-infection)
F.
Virus titers in hearts (log10 PFU/g)
P<0.001
12
10
8
6
4
2
0
C57BL/6
GFP-LC3
G.
Sham
CVB3
C57BL/6
GFP-LC3
Histological grades
P<0.05
3
2
1
0
C57BL/6
GFP-LC3

Figure 21. CVB3 infection leads to an increased accumulation of autophagosomes *in vivo*. Male homozygous GFP-LC3 transgenic mice or the background C57BL/6 control mice at ~5 weeks were infected intraperitoneally with 10^4 pfu of CVB3 or sham-infected with PBS for 3 or 9 days. **(A)** Genotyping identification of wild-type (WT), hemizygous (WT/Tg), and homozygous (Tg/Tg) GFP-LC3 mice by PCR. **(B)** Representative confocal images of GFP-LC3 signal (green) in mouse heart at 3 or 9 days post-infection. The nucleus was counterstained with DAPI (blue). The LC3 puncta was detected at different virus-infected area across the whole section (n=3, in each group). **(C and D)** Western blot analysis of endogenous LC3 and exogenous GFP-LC3 (C), p-eIF2α and total eIF2α (D) in three independent mouse hearts using antibodies against LC3, GFP, p-eIF2α, and eIF2α. GAPDH was probed as a protein loading control. Protein levels of LC3-II and p-eIF2α were quantitated by densitometric analysis using NIH ImageJ, normalized to GAPDH and eIF2α, respectively, and presented underneath as fold changes compared to sham (the first lane of sham is arbitrarily set a value of 1). **(E)** Kaplan-Meier survival curves of GFP-LC3 (n=18) and C57BL/6 control mice (n=8) over a time-course of 9-day infection. $P<0.05$ between two groups by the log-rank test. **(F)** Virus titers in CVB3-infected mouse heart at 9 days post-infection by plaque assay. Data are presented as mean ± SD (n=5 mice in each group). **(G)** Histological examination of CVB3-infected heart at 9 days post-infection by H&E staining. The level of virus-induced myocarditis was graded based on the intensity and character of injury and inflammatory and expressed as mean ± SD (n=6 mice in each group) in the right panel. Scale bar=50μM

CVB3 infection inhibits autophagic flux *in-vitro*

Autophagy is a dynamic process comprised of autophagosome formation and degradation, termed autophagic flux, thus autophagosome accumulation could be a result of increased production and/or decreased clearance. To measure autophagic flux in the context of CVB3 infection, I utilized a tandem fluorescent-tagged mRFP-GFP-LC3 reporter construct that monitors autophagosome-lysosome/endosome fusion based on different pH stability of GFP and RFP [122]. This system is advantageous because the GFP fluorescence signal is unstable in acidic environments, such as lysosomal and late endosomal compartments. For this reason, following autophagosome-lysosome/endosome fusion in response to autophagic stimuli, i.e., starvation (**Figure 22A**, HEK293 cells stably expressing mRFP-GFP-LC3), the GFP signal was lost due to quenching while RFP fluorescence remained strong. Addition of bafilomycin A1, an inhibitor of vacuolar type proton ATPase that prevents the fusion of autophagosomes with lysosomes/endosomes, rescued the loss of GFP-LC3 puncta. Following CVB3 infection, I found that puncta GFP and RFP signal increased and always co-localized with or without bafilomycin A1, indicating an inhibition of autophagosome fusion (**Figure 22A**).

Furthermore, I assessed the turnover of p62/sequestosome1 (SQSTM1), a target of autophagy and widely used as a marker for monitoring autophagic flux. I recognized that endogenous p62/SQSTM1 could not be used to measure flux as it is cleaved upon CVB3 infection by virus-encoded proteinase 2A [92]. Here I applied a CVB3 non-cleavable form of p62 ($p62^{G241E}$) to monitor its stability. As shown in **Figure 22B**, after 2-h starvation, the protein levels of $p62^{G241E}$ decreased, suggesting a degradation event or complete autophagy. However, no apparent reduction in $p62^{G241E}$ protein levels was seen after CVB3 infection, indicating an inhibition of autophagic flux. Lastly, I used Lysotracker Red, a weak base that accumulates in acidic organelles, to visualize lysosomes and late endosomes. To avoid potential artifacts with overexpression system, I stained for endogenous LC3 instead of using GFP-LC3 construct. **Figure 22C** showed that the co-localization of LC3 puncta and the LysoTracker dye, which was observed in starved cells, significantly reduced in virus-infected cells, further supporting a blockade in the late stage of autophagy following infection.

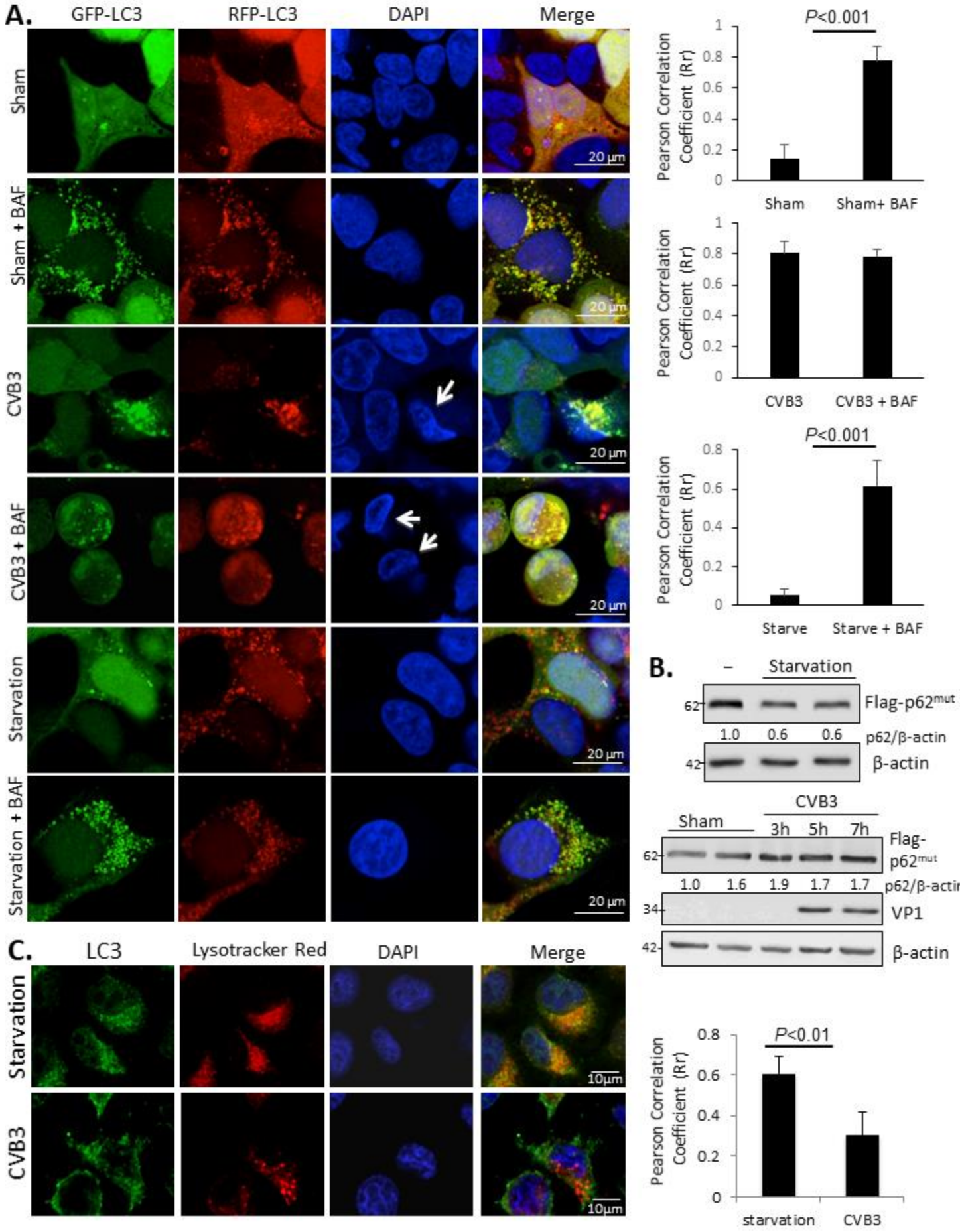
A.
GFP-LC3
RFP-LC3
DAPI
Merge
Sham
Sham + BAF
CVB3
CVB3 + BAF
Starvation
Starvation + BAF
20 μm
Pearson Correlation Coefficient (Rr)
P<0.001
Sham
Sham+ BAF
CVB3
CVB3 + BAF
Starve
Starve + BAF
B.
Starvation
Flag-p62mut
p62/β-actin
β-actin
CVB3
Sham
3h
5h
7h
VP1
C.
LC3
Lysotracker Red
10μm
P<0.01
starvation

Figure 22. CVB3 infection inhibits autophagic flux *in vitro*. (A) Monitoring of autophagic flux in CVB3-infected reporter cells by confocal microscopy. HEK293 cells stably expressing mRFP-EGFP-LC3 were either sham- or CVB3-infected (MOI=20) for 7 h in the presence or absence of a lysosome/endosome inhibitor bafilomycin A1 (BAF, 200 nM). Cells underwent starvation for 6 h were included as a positive control for autophagy. Co-localization between GFP-LC3 and mRFP-LC3 puncta was quantified using ImageJ and presented as Pearson Correlation (Rr). Arrows indicate nuclear condensation, a marker of CVB3-induced apoptosis. **(B)** Stability of viral proteinase-resistant p62/SQSTM1 in CVB3-infected cells. HeLa cells were transfected with Flag-$p62^{G241E}$, a CVB3 non-cleavable p62 mutant, for 24 h, followed by 2-h starvation or CVB3 infection (MOI=10) for various time-courses. Protein level of Flag-p62-G241E was measured by Western blotting with an anti-Flag antibody. Densitometry was conducted as above. Similar results were observed 2 independent experiments. **(C)** Confocal microscopy analysis of the co-localization of LC3 and Lysotracker Red. HeLa cells were starved for 6h or infected with CVB3 (MOI=10) for 5 h, followed by an additional hour of incubation with Lysotracker Red (LTR). Cells were then immunostained for LC3. Co-localization between LC3 and LTR was quantified as in (A).

SNAP29 and PLEKHM1 are cleaved following CVB3 infection by viral proteinase 3C

We next sought to delineate the mechanisms responsible for the impaired fusion. I focused on proteins previously reported to be involved in such process. Firstly, I examined the protein levels of Ras-related protein in brain 7 (Rab7, a small GTPase localized on lysosomes and late endosomes) and lysosome-associated membrane protein 2 (LAMP2, a major component of lysosomal and late endosomal membrane), two proteins shown to play a role in autophagosome-lysosome/endosome fusion [169, 170]. However, no evident changes over the course of CVB3 infection were observed.

We then analyzed the soluble N-ethylmaleimide-sensitive factor activating protein receptor (SNARE) proteins that were identified to be key regulators for autophagosome fusion [33]. It was demonstrated that upon autophagic stimulation, the SNARE protein syntaxin 17 (STX17), is recruited specifically to mature autophagosomes where it interacts with another autophagosomal SNARE protein, synaptosomal-associated protein 29 (SNAP29), and the lysosomal/endosomal SNARE protein, vesicle-associated membrane protein 8 (VAMP8), driving the fusion of autophagosomes with lysosomes/endosomes. As shown in **Figure 23A**, following infection, protein levels of all three SNARE proteins decreased, with the highest reduction being observed in SNAP29. Of interest, decreases in full-length SNAP29 were accompanied by the appearance of an additional band at ~19 kDa, suggesting a possible cleavage of SNAP29. Experiments in HeLa cells transiently expressing 3×Flag-SNAP29 confirmed SNAP29 cleavage by the detection of a comparable N-terminal cleavage fragment with an anti-Flag antibody (**Figure 23B**). The cleavage products of SNAP29 detected by different antibodies are illustrated in **Figure 24B**. Moreover, I conducted both *in-vivo* (in cells transfected with proteinase constructs) and *in-vitro* (using recombinant purified proteinases) cleavage assay to identify the proteinase that contributes to this cleavage. **Figure 23C** showed that expression of a wild-type CVB3 proteinase 3C ($3C^{wt}$), but not its catalytically inactive mutant ($3C^{mut}$) in cells, caused the generation of a similar cleavage product of SNAP29 as observed under viral infection, indicating that SNAP29 is a target of 3C. The role of 3C in SNAP29 processing was verified by an *in-vitro* cleavage assay using recombinant proteinases (**Figure 23D**). **Figure 23D** also showed that poliovirus infection resulted in a similar cleavage of SNAP29 as detected upon CVB3 infection. No effects of viral proteinase 2A on SNAP29 were observed (**Figure 23E**). Lastly, I investigated the possible participation of the apoptotic, proteasomal, and lysosomal pathways in the regulation of SNAP29 stability using a

general caspase inhibitor (Z-VAD-FMK), a proteasome inhibitor (MG132), and a lysosome/endosome inhibitor (bafilomycin A1). Our data revealed that SNAP29 cleavage upon infection was independent of caspase activation (**Figure 23F**) and proteasome/lysosome-mediated degradation (data not shown).

In addition to SNARE proteins, adaptor/tethering proteins, such as pleckstrin homology domain containing protein family member 1 (PLEKHM1), also participate in the fusion step by facilitating the formation of SNARE complexes via its interaction with homotypic fusion and protein sorting (HOPS), Rab7, and LC3 [37]. Similar to what I have observed for SNAP29, I found that both endogenous and exogenous PLEKHM1 were cleaved upon infection (**Figure 23G & H**) via the catalytic activity of CVB3 proteinase 3C (**Figure 23I & J**), independent of the activation of 2A (**Figure 23K**) and caspase (**Figure 23L**). The cleavage fragments of PLEKHM1 detected by different antibodies are elucidated in **Figure 24D.** Collectively, our results suggest a potential mechanism by which CVB3 inhibits autophagic flux via dysregulating proteins involved in SNARE-mediated autophagosome fusion.

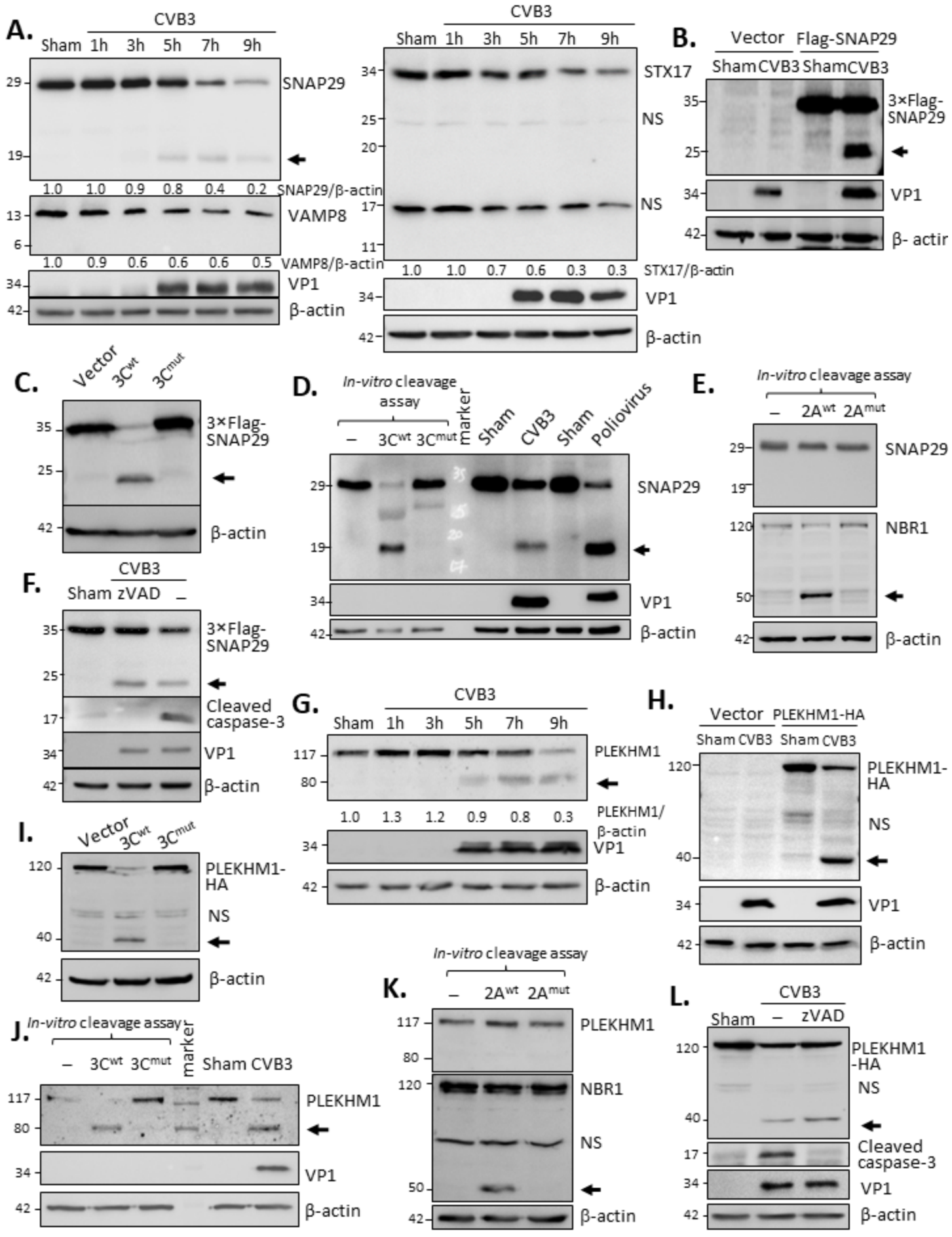
A.
CVB3
Sham 1h 3h 5h 7h 9h
SNAP29
SNAP29/β-actin
VAMP8
VAMP8/β-actin
VP1
β-actin
STX17
NS
STX17/β-actin
B.
Vector Flag-SNAP29
Sham CVB3 Sham CVB3
3×Flag-SNAP29
VP1
β- actir
C.
Vector 3Cwt 3Cmut
3×Flag-SNAP29
β-actin
D.
In-vitro cleavage assay
– 3Cwt 3Cmut marker Sham CVB3 Sham Poliovirus
SNAP29
VP1
β-actin
E.
In-vitro cleavage assay
– 2Awt 2Amut
SNAP29
NBR1
β-actin
F.
CVB3
Sham zVAD –
3×Flag-SNAP29
Cleaved caspase-3
VP1
β-actin
G.
CVB3
Sham 1h 3h 5h 7h 9h
PLEKHM1
PLEKHM1/β-actin
VP1
β-actin
H.
Vector PLEKHM1-HA
Sham CVB3 Sham CVB3
PLEKHM1-HA
NS
VP1
β-actin
I.
Vector 3Cwt 3Cmut
PLEKHM1-HA
NS
β-actin
J.
In-vitro cleavage assay
– 3Cwt 3Cmut marker Sham CVB3
PLEKHM1
VP1
β-actin
K.
In-vitro cleavage assay
– 2Awt 2Amut
PLEKHM1
NBR1
NS
β-actin
L.
CVB3
Sham – zVAD
PLEKHM1-HA
NS
Cleaved caspase-3
VP1
β-actin

Figure 23. SNAP29 and PLEKHM1 are cleaved following CVB3 infection by viral proteinase 3C. (A, G) Western blot analysis of SNARE proteins (A) and PLEKHM1 (G) in CVB3-infected cells. HeLa cells were sham- or CVB3-infected (MOI=10) for various time-points. Western blotting was conducted for detection of SNAP29, STX17, and VAMP8 (A), or PLEKHM1 (G). Densitometry was carried out as above. NS = non-specific bands. **(B, H)** Cleavage of exogenously expressed SNAP29 (B) or PLEKHM1 (H). Hela cells were transfected with an empty vector or a plasmid expressing 3×Flag-SNAP29 (B) or PLEKHM1-HA (H) for 24 h, followed by CVB3 infection (MOI=10) for 7 h. Western blotting was carried out with anti-Flag (B) or anti-HA (H) antibodies. **(C, I)** Viral proteinase 3C-dependent cleavage of SNAP29 (C) and PLEKHM1 (I). HeLa cells were transfected with 3×Flag-SNAP29 (C) or PLEKHM1-HA (I), together with either empty vector, wild-type 3C ($3C^{wt}$), or catalytically inactive 3C (C147A) mutant ($3C^{mut}$). After 24 h, cells lysates were collected and analyzed by Western blotting with anti-Flag (C) or anti-HA (I) antibodies. **(D, J)** Cleavage of SNAP29 (D) or PLEKHM1 (J) by recombinant 3C. *In vitro* cleavage assay was performed by incubation of HeLa cell lysates (30 μg) with vehicle (-), purified $3C^{wt}$, or $3C^{mut}$ proteins (0.1 μg) for 16 h. Sham- and CVB3- or poliovirus-infected HeLa cell lysates were included (right four lanes) as controls. Cleavage products of SNAP29 or PLEKHM1 were analyzed by Western blotting with anti-SNAP29 (D) or anti-PLEKHM1 (J) antibodies, respectively. **(E, K)** Viral proteinase 2A-independent cleavage of SNAP29 (E) and PLEKHM1 (K). *In vitro* cleavage assay was conducted as above with vehicle (-), recombinant $2A^{wt}$, or $2A^{mut}$ proteins (0.3 μg) for 16 h. Cleavage of Nbr1 by 2A, which was previously demonstrated [140], was shown as evidence of the activity of 2A. **(F, L)** Caspase-independent cleavage of SNAP29 (F) and PLEKHM1 (L) in CVB3-infected cells. HeLa cells were transfected with 3×Flag-SNAP29 (F) or PLEKHM1-HA (L) for 24 h, followed by CVB3 infection (MOI=10) for 7 h in the presence or absence of a pan-caspase inhibitor Z-VAD-FMK (zVAD, 50 μM) or vehicle (-). Western blotting was performed with an anti-Flag (F) or an anti-HA (L). Activation of caspase-3 was examined using an anti-cleaved caspase-3 antibody. Arrows denote the cleavage fragments. Results in this Figure represent data from 2 to 4 independent experiments. NS = non-specific bands.

SNAP29 is cleaved after Q161 and PLEKHM1 after Q668

Having confirmed that SNAP29 and PLEKHM1 undergo cleavage by 3C, I next wished to identify the cleavage site. Using a bioinformatics approach tailored towards mapping of 3C consensus sequence [171], I identified several potential cleavage sites. To verify our prediction, I constructed individual point mutation plasmids by site-directed mutagenesis. I found that wild-type SNAP29 and PLEKHM1, but not the $SNAP29^{Q161L}$ [the glutamine (Q) residue at position 161 was replaced with leucine (L)] and $PLEKHM1^{Q668L}$ mutants, were able to yield cleavage fragments when co-expressed with $3C^{wt}$ but not with $3C^{mut}$ (**Figure 24A & C**), suggesting that Q161 and Q668 are the cleavage sites on SNAP29 and PLEKHM1, respectively. As illustrated in **Figure 24B & D**, CVB3-induced cleavage of SNAP29 separates its N-terminal coiled-coil domain from the C-terminal SNARE motif, while cleavage of PLEKHM1 results in the dissociation of the N-terminal RUN (RPIP8, UNC-14, and NESCA), PH1 (Pleckstrin homology 1), and LIR (LC3-interacting region) domains from the C-terminal PH2 and C1 (Cysteine-rich) domains.

CVB3 infection leads to impaired formation of SNARE complexes

Given the established role of SNAP29 and PLEKHM1 in the formation of SNARE complexes, I suspected that the STX17-SNAP29-VAMP8 complex is disrupted upon CVB3 infection as a result of SNAP29/PLEKHM1 cleavage. To address this hypothesis, I conducted studies to assess the physical interaction between STX17 and VAMP8 under viral challenge. Co-immunoprecipitation with pull-down of Flag-STX17 using anti-Flag M2 beads revealed that the STX17-VAMP8 interaction was markedly reduced following infection (**Figure 25A**), which was further confirmed by reverse co-IP (**Figure 25B**). Our data here support a model that CVB3 reduces autophagic flux by disrupting the formation of SNARE complexes.

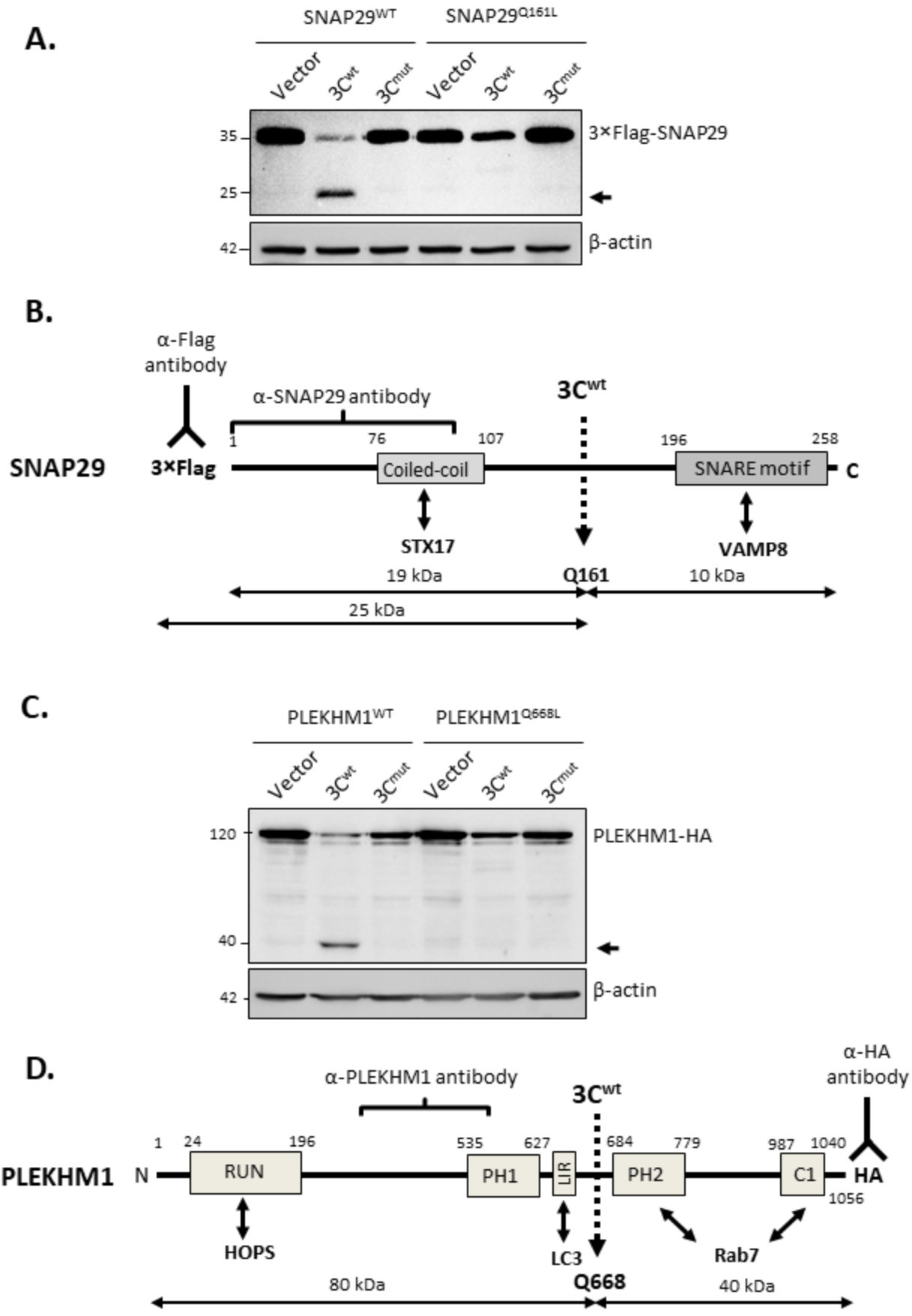
A.
SNAP29WT
SNAP29Q161L
Vector
3Cwt
3Cmut
Vector
3Cwt
3Cmut
35
25
42
3×Flag-SNAP29
β-actin
B.
α-Flag antibody
α-SNAP29 antibody
3Cwt
SNAP29
3×Flag
1
76
107
196
258
Coiled-coil
SNARE motif
C
STX17
VAMP8
19 kDa
Q161
10 kDa
25 kDa
C.
PLEKHM1WT
PLEKHM1Q668L
Vector
3Cwt
3Cmut
Vector
3Cwt
3Cmut
120
40
42
PLEKHM1-HA
β-actin
D.
α-PLEKHM1 antibody
3Cwt
α-HA antibody
PLEKHM1
N
1
24
196
535
627
684
779
987
1040
1056
RUN
PH1
LIR
PH2
C1
HA
HOPS
LC3
Rab7
Q668
80 kDa
40 kDa

Figure 24. SNAP29 is cleaved after Q161 and PLEKHM1 after Q668 following CVB3 infection. (A, C) Identification of the cleavage sites on SNAP29 (A) and PLEKHM1 (C). HeLa cells were transfected with $3C^{wt}$ or $3C^{mut}$, together with 3×Flag-$SNAP29^{WT}$ or 3×Flag-$SNAP29^{Q161L}$ (A), or with $PLEKHM1^{WT}$-HA or $PLEKHM1^{Q668L}$-HA (C) as indicated. After 24 h, cell lysates were harvested and subjected to Western blot analysis using anti-Flag (A) or anti-HA antibodies (C). Data are representative of 3 independent experiments. **(B, D)** Schematic illustration of the structural domains, the interacting proteins, the identified cleavage sites, the antibody recognition regions, and the resulting cleavage products of SNAP29 (B) and PLEKHM1 (D). RUN = RPIP8, UNC-14, and NESCA; PH = pleckstrin homology; LIR = LC3-interacting region; C1 = cysteine-rich domain/zinc-finger-like motif; HOPS = homotypic fusion and protein sorting.

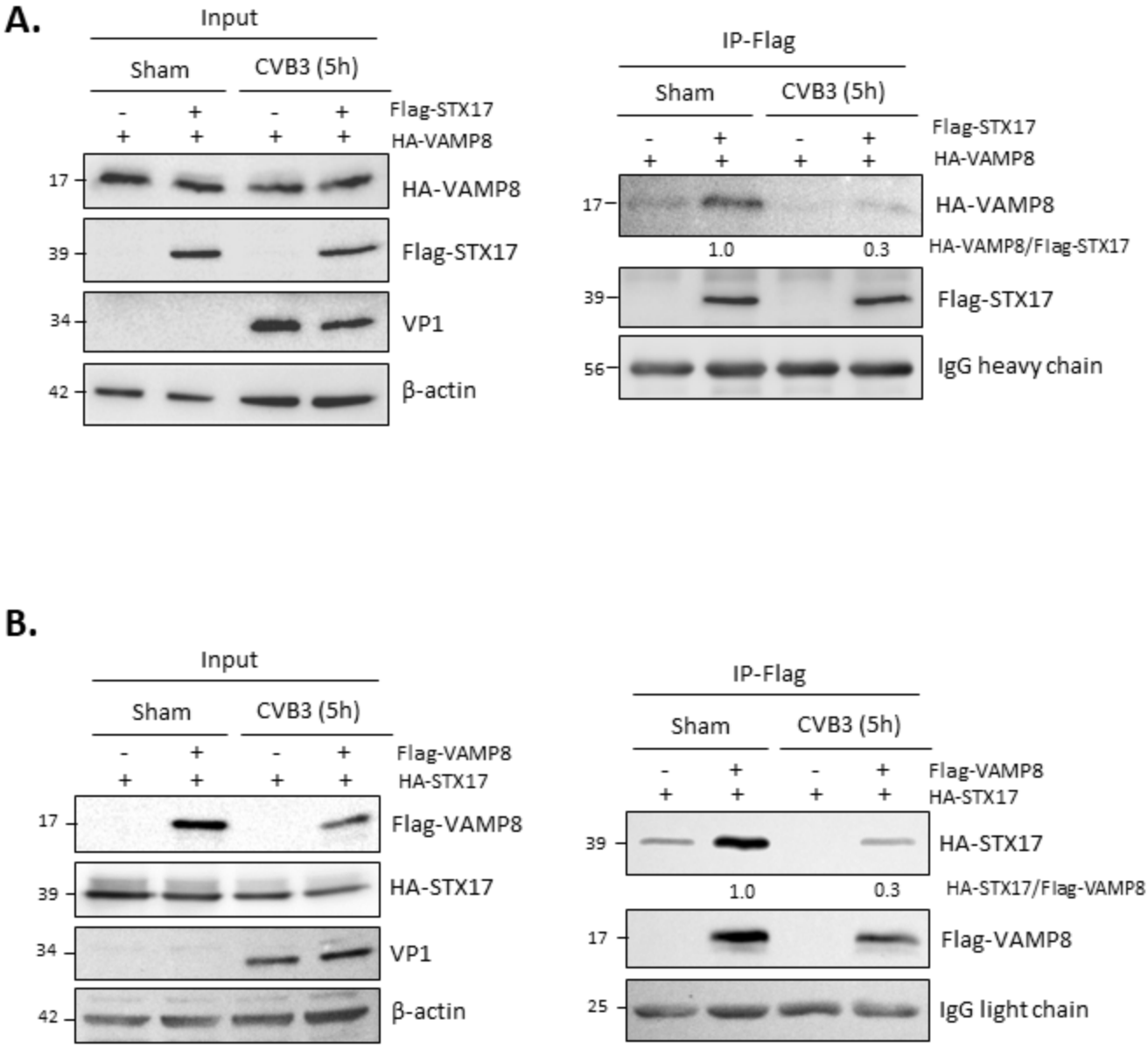
A.
Input
Sham
CVB3 (5h)
- + - +
+ + + +
Flag-STX17
HA-VAMP8
17
HA-VAMP8
39
Flag-STX17
34
VP1
42
β-actin
IP-Flag
Sham
CVB3 (5h)
- + - +
+ + + +
Flag-STX17
HA-VAMP8
17
HA-VAMP8
1.0
0.3
HA-VAMP8/Flag-STX17
39
Flag-STX17
56
IgG heavy chain
B.
Input
Sham
CVB3 (5h)
- + - +
+ + + +
Flag-VAMP8
HA-STX17
17
Flag-VAMP8
39
HA-STX17
34
VP1
42
β-actin
IP-Flag
Sham
CVB3 (5h)
- + - +
+ + + +
Flag-VAMP8
HA-STX17
39
HA-STX17
1.0
0.3
HA-STX17/Flag-VAMP8
17
Flag-VAMP8
25
IgG light chain

Figure 25. Physical interaction between STX17 and VAMP8 is decreased after CVB3 infection. (A, B) Reduced STX17-VAMP8 interaction in CVB3-infected cells. HeLa cells were co-transfected with Flag-STX17 and HA-VAMP8 (A), or Flag-VAMP8 and HA-STX17 (B) for 24 h, followed by CVB3 infection (MOI=10) for 5 h. After immunoprecipitation with an anti-Flag antibody, Western blotting was conducted for detection of HA-VAMP8 (A, right panels) or HA-STX17 (B, right panels) by anti-HA antibody. Immunoprecipitated STX17 (A, right panels) or VAMP8 (B, right panels) was verified by Western blot analysis using anti-Flag antibody, Blots for antibody IgG heavy or light chain were shown as loading controls. Densitometry was conducted to quantify the amount of HA-VAMP8 or HA-STX17 over precipitated Flag-STX17 or Flag-VAMP8, respectively. Western blots of inputs for immunoprecipitation were shown in the left panels. Similar results were observed in 3 independent experiments.

Knockdown of SNAP29/PLEKHM1 inhibits autophagic flux and facilitates viral replication

Since multiple proteins involved in autophagosome fusion, including (but probably not to limited to) SNAP29, PLEKHM1, STX17, and VAMP8, are targeted by CVB3, it would be difficult to rescue this process by introducing one or two proteins. In fact, I observed no significant differences in LC3 levels and viral replication between control and cells expressing cleavage-resistant $SNAP29^{Q161L}$ and/or $PLEKHM1^{Q668L}$ mutants (data not shown). Thus, to elucidate the functional significance of SNAP29/PLEKHM1 cleavage, I decided to knock down their expression by small-interfering RNAs (siRNAs) in cells infected with a low titer of CVB3. By lowering the virus titers, I minimized the amount of SNAP29/PLEKHM1 that are cleaved in control siRNA-treated cells (**Figure 26A**), thus providing an accurate comparison between control and siSNAP29/siPLEKHM1 cells. Consistent with previous reports [33, 37], ablation of either SNAP29 or PLEKHM1 alone was able to induce an accumulation of LC3-II**,** indicative of reduced autophagic flux (**Figure 26A**). However, the inhibitory effect was notably much more profound in cells depleted of SNAP29 than PLEKHM1. Apart from their function in autophagosome fusion, SNAP29 and PLEKHM1 are also implicated in vesicular trafficking of the endocytic pathway [172, 173]. As expected, knockdown of SNAP29/PLEKHM1 resulted in an increase of epidermal growth factor receptor (EGFR), an endocytic cargo degraded by lysosome, suggesting a likely engagement of the endocytic pathway in viral infection (**Figure 26A**). Of note, combined knockdown had no evident synergy in blocking LC3-II and EGFR degradation, indicating a shared common downstream pathway.

Following CVB3 infection, viral capsid protein was barely detectable in control cells by Western blotting due to low-dose of viral infection, whereas in cells depleted of SNAP29/PLEKHM1 viral protein synthesis was markedly elevated (**Figure 26A**). Furthermore, plaque assay demonstrated significantly higher cell-associated virus yields in SNAP29/PLEKHM1-depleted cells as compared to control cells (**Figure 26B**), corresponding well with the elevated levels of LC3-II and EGFR. The big differences in fold-changes between viral protein expression and titers may reflect the variation of methodological sensitivities. Finally, cell fractionation experiment revealed a strong association of viral protein with membrane fraction of the cells (**Figure 26C**). Together, our data suggest that loss of SNAP29/PLEKHM1 blocks autophagy flux, resulting in the accumulation of LC3-II-positive membrane structures that likely provide sites for viral assembly and replication.

Ablation of SNAP29 restricts CVB3 spread

Previous studies also suggest a role for autophagy in non-lytic spread of CVB3 [17]. I next decided to determine whether CVB3 inhibition of autophagic flux promotes viral release. I found that CVB3 infection led to increased peripheral accumulation of LC3 puncta (data not shown). Similar to previous report, autophagosome marker LC3 was detected in EMVs isolated from CVB3-infected cells and co-localized with viral protein (**Figure 27A)**, supporting a non-lytic egress route for CVB3 via autophagosomes. I further demonstrated that EMVs isolated from virus-infected cells contained infectious viral particles as evidenced by the detection of double-stranded RNA (dsRNA), an intermediate of viral RNA during replication, and viral protein in EMV-treated cells (**Figure 27B**). To investigate the impact of SNAP29/PLEKHM1 loss on viral spread, I conducted plaque assay to examine intracellular and extracellular virus titers in HeLa cells undergoing a single life-cycle of viral infection. No cell death was observed for this infection (data not shown), indicating that the extracellular virus particles are mainly released via a non-lytic pathway. As shown in **Figure 27C**, knockdown of PLEKHM1 resulted in a significant increase in extracellular virus yields, suggesting that increased viral release is likely a result of elevated intracellular viruses. Of note, depletion of SNAP29 alone or together with PLEKHM1 significantly facilitated intracellular virus growth, but had no apparent influences on virus yields in the supernatant, suggesting a possible role for SNAP29 in suppressing viral spread.

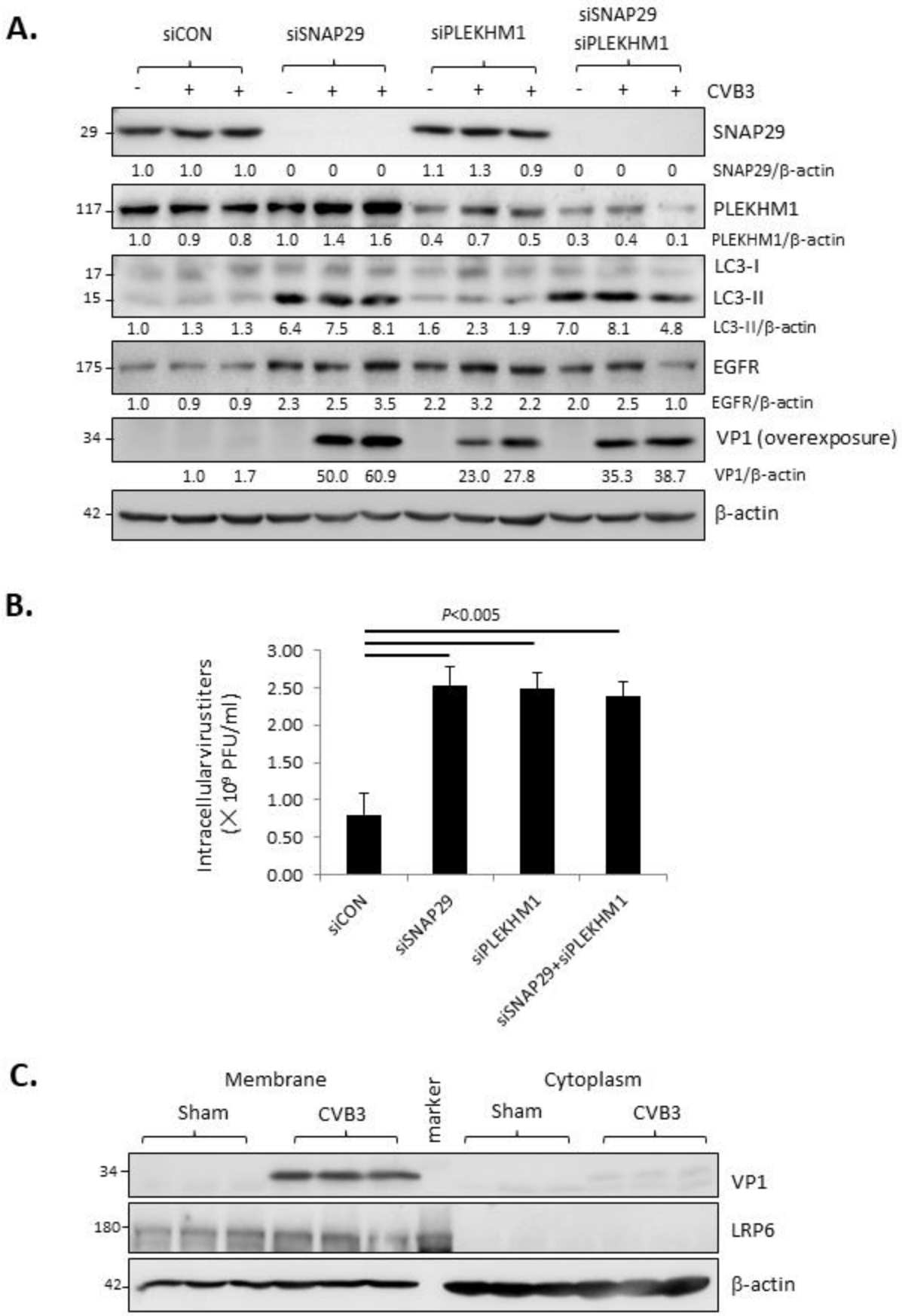
A.
siCON
siSNAP29
siPLEKHM1
siSNAP29
siPLEKHM1
- + + - + + - + + - + + CVB3
29
SNAP29
1.0 1.0 1.0 0 0 0 1.1 1.3 0.9 0 0 0 SNAP29/β-actin
117
PLEKHM1
1.0 0.9 0.8 1.0 1.4 1.6 0.4 0.7 0.5 0.3 0.4 0.1 PLEKHM1/β-actin
17
15
LC3-I
LC3-II
1.0 1.3 1.3 6.4 7.5 8.1 1.6 2.3 1.9 7.0 8.1 4.8 LC3-II/β-actin
175
EGFR
1.0 0.9 0.9 2.3 2.5 3.5 2.2 3.2 2.2 2.0 2.5 1.0 EGFR/β-actin
34
VP1 (overexposure)
1.0 1.7 50.0 60.9 23.0 27.8 35.3 38.7 VP1/β-actin
42
β-actin
B.
P<0.005
Intracellularvirustiters
(× 10⁹ PFU/ml)
3.00
2.50
2.00
1.50
1.00
0.50
0.00
siCON
siSNAP29
siPLEKHM1
siSNAP29+siPLEKHM1
C.
Membrane
Cytoplasm
Sham
CVB3
marker
Sham
CVB3
34
VP1
180
LRP6
42
β-actin

Figure 26. Knockdown of SNAP29 and PLEKHM1 inhibits autophagic flux and facilitates viral replication. (A) Induction of viral protein synthesis by gene-silencing of SNAP29/PLEKHM1. HeLa cells were transfected with siRNAs targeting SNAP29 (siSNAP29) and/or PLEKHM1 (siPLEKHM1), or a scramble siRNA control (siCON) for 48 h, followed by CVB3 infection (MOI=0.1) for 16 h. Western blotting was performed to examine protein expression of SNAP29, PLEKHM1, EGFR, LC3, VP1, and β-actin. Densitometry was carried out as above. **(B)** Elevated CVB3 yields in cells depleted of SNAP29/PLEKHM1. HeLa cells were treated as above. Intracellular virus titers were determined by plaque assay. Data are represented as mean ± SD from 3 replicates. **(C)** Association of viral protein with cellular membrane fraction. HeLa cells infected with CVB3 (MOI=10) were harvested for cell fractionation, followed by Western blot detection of VP1, LRP6 (a membrane marker), and β-actin. Data in this Figure are representative of 2 to 4 independent experiments.

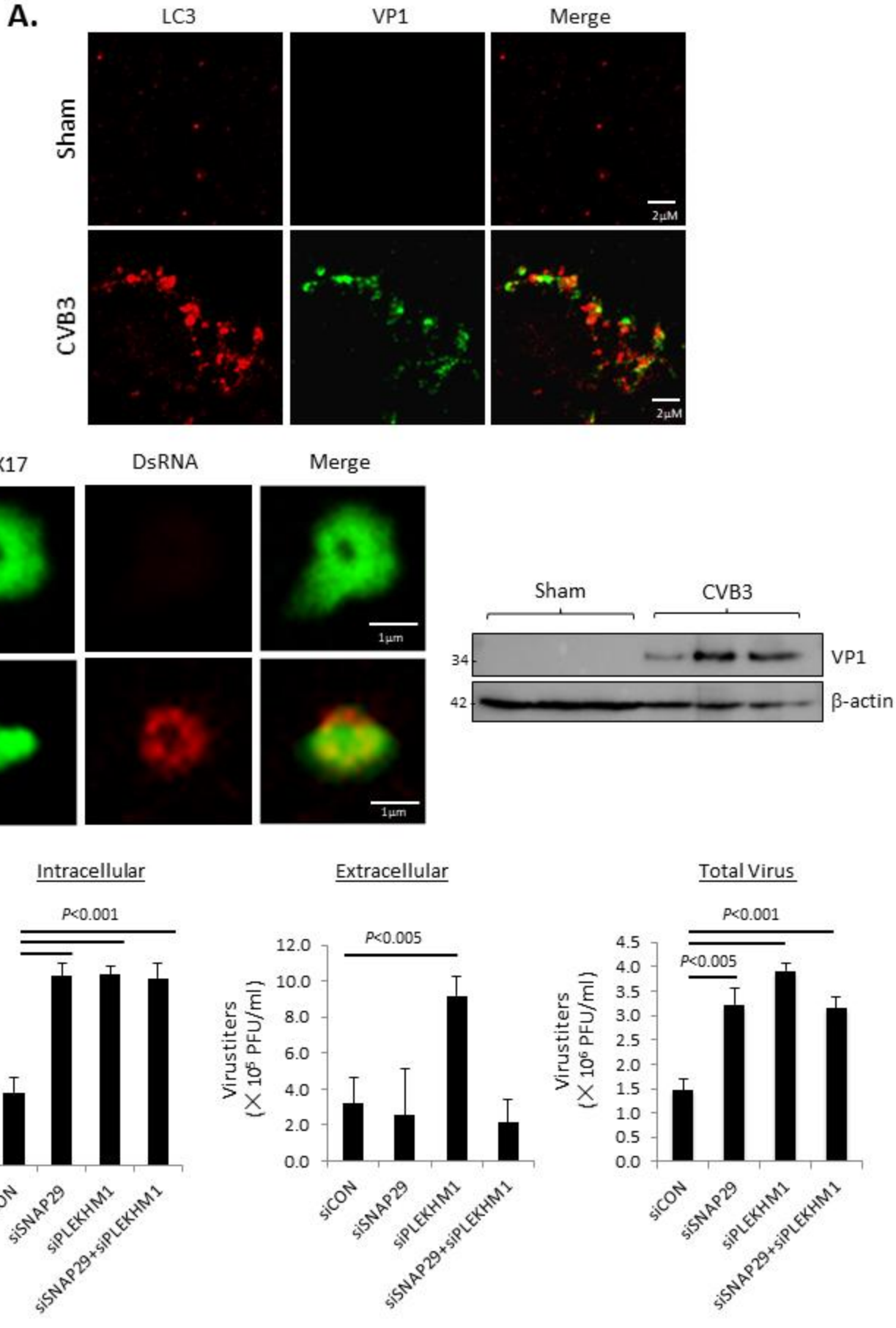
A.
LC3
VP1
Merge
Sham
CVB3
2μM
2μM
B.
STX17
DsRNA
Merge
Sham
CVB3
1μm
1μm
Sham
CVB3
34
42
VP1
β-actin
C.
Intracellular
Extracellular
Total Virus
P<0.001
P<0.005
P<0.001
P<0.005
Virustiters (× 10⁶ PFU/ml)
siCON
siSNAP29
siPLEKHM1
siSNAP29+siPLEKHM1

Figure 27. Depletion of SNAP29 limits spread of CVB3. (A) CVB3 infection causes non-lytic release of autophagosome-derived EMVs that are positive for viral protein. HeLa cells were sham- or CVB3-infected (MOI=0.1) for 16 h. EMVs were then isolated from cell culture medium, followed by immunostaining for LC3 (red) and VP1 (green). **(B)** EMVs isolated from CVB3-infected cells contain infectious viral particles. HeLa cells were treated with EMVs isolated as above and resuspended in PBS for 24 h. EMVs were then harvested for immunostaining of STX17 (green) and dsRNA (red, left panel) and cells for Western blot analysis of VP1 (right panel). **(C)** Effects of SNAP29/PLEKHM1 knockdown on viral release. HeLa cells were transfected with siSNAP29/siPLEKHM1 for 48 h, followed by CVB3 infection for 5 h. Plaque assay was conducted to determine intracellular and extracellular virus titers (mean ± SD from 3 replicates). Total virus titers were calculated as the sum of intracellular and extracellular virus titers.

Discussion

The current study identifies a novel mechanism by which CVB3 hijacks the autophagic pathway to permit effective viral propagation. I have previously discovered that p62/SQSTM1 is a bona fide substrate of CVB3 proteinase 2A [92], which is confirmed later upon poliovirus infection (data not shown). In light of this, endogenous p62/SQSTM1 is not a reliable marker to evaluate autophagic flux in the context of CVB3 and poliovirus infection, perhaps other picornavirus infection as well. Therefore, it is important to carefully examine autophagic flux using a combination of assays. By different approaches, including mRFP-GFP-LC3 reporter, non-cleavable p62/SQSTM1 degradation, and Lysotracker/LC3 co-localization, **I** demonstrate that CVB3 infection results in a significant, albeit incomplete, inhibition of autophagic flux by limiting the fusion of autophagosomes with lysosomes/endosomes. Our finding is in accordance with an early *in-vivo* report showing that CVB3 limits autophagosome-lysosome fusion, leading to the formation of megaphagosomes in virus-infected pancreatic acinar cells [67]. However, in contrast to the result from the same study that CVB3 permits autophagosome fusion with endosomes to form amphisomes, I found that the fusion between autophagosomes and late endosomes is also impaired. This result is further supported by the findings that CVB3 disrupts the SNARE complexes controlling not only autophagosome fusion with lysosomes but also with late endosomes. I speculate that methodological differences may account for this discrepancy. Furthermore, the reason for the inconsistency between our study and a recent report that CVB3 induces autophagic flux is not clear, but may relate to the differences in cell types, virus titers, infection duration, and the detection of endogenous versus exogenous LC3 [174].

Unlike the process of autophagosome formation, the underlying mechanism responsible for autophagosome fusion is poorly understood until the past few years. Studies suggest a pivotal role for the SNARE proteins, including the autophagosome-localized STX17, the lysosome/endosome-anchored VAMP8, and the adaptor protein SNAP29, in the fusion process [33]. Moreover, several tethering/adaptor proteins have also been reported to be involved in the fusion step of autophagy. For example, the PLEKHM1 protein was found to interact with Rab7, HOPS-SNARE complexes that are formed upon autophagy induction, and LC3 to facilitate autophagosome fusion [36, 37]. Another example is ATG14, which is an autophagy-specific regulator of the class III PI3K and was shown to directly bind to the binary SNARE protein complex (STX17-SNAP29) on autophagosomes to promote fusion by forming a complex with the

lysosomal/endosomal VAMP8 [35]. In addition to the observed cleavage for SNAP29 and PLEKHM1 and downregulation for STX17 and VAMP8 in the current report, I also found that ATG14 protein levels are decreased after infection (data not shown), indicating a mechanism by which CVB3 inhibits fusion via targeting different proteins at multiple levels. I suspect that disrupted formation of the SNARE complexes is a converging point for the diverse strategies that virus has evolved.

We are the first group to report cleavage of SNAP29 and PLEKHM1 as a mechanism of CVB3 evasion of autophagy. SNAP29 is a critical component of the SNARE complex and during the fusion step of autophagy, it serves as an adaptor protein that interacts directly with STX17 and VAMP8 via its N-terminal coiled-coil domain and C-terminal SNARE motif to form a ternary SNARE complex, driving fusion between autophagosomes and lysosomes/endosomes [35]. Previous studies have shown that loss or post-translational modification of SNAP29 by *O*-GlcNAcylation is sufficient to block autophagosome-lysosome/endosome fusion [33, 175]. The present data reveal another level of the regulatory mechanism of SNAP29. I show that CVB3-induced cleavage of SNAP29 takes place after Q161 in the loop region that separates its coiled-coil domain from the SNARE motif, resulting in the disruption of the STX17-SNAP29-VAMP8 complex. Similarly, I found that PLEKHM1 is also proteolytically targeted during CVB3 infection. Cleavage of PLEKHM1 occurs after Q668 to disassociate the N-terminal LIR and RUN domains that bind to LC3 and HOPS, respectively, from the C-terminal PH2 and C1 domains that interact with Rab7, leading to impaired formation of the LC3-PLEKHM1-Rab7-HOPS complexes. In addition to loss-of-function, I postulate that the resulting cleavage fragments of SNAP29 and PLEKHM1 can also negatively regulate the function of their respective native proteins in autophagosome fusion via a gain-of-function mechanism by competing for the same binding sites.

The CVB3 proteinase 3C, responsible for majority of the viral polyprotein processing, also mediates the cleavage of cellular proteins for viral advantages [171]. A number of 3C target proteins have been identified. The current study adds two additional substrates, i.e., SNAP29 and PLEKHM1, to the list and demonstrates the significance of such cleavage events in viral pathogenesis. Although it has yet to be determined in our model, overexpression of coxsackievirus A16 3C alone was shown to be sufficient to induce LC3 puncta formation and inhibits autophagic flux [70]. Given the conserved nature of 3C among all known picornaviruses, presumably, cleavage of SNAP29/PLEKHM1 would explain this observation of incomplete autophagy. Viral targeting

of the SNARE complexes has been previously reported for other viruses. For instance, infection with human parainfluenza virus was found to induce incomplete autophagy via a mechanism whereby viral phospho-protein binds to SNAP29 to prevent STX17-SNAP29 interaction [165], whereas direct interaction detected between non-structural protein 2BC of enterovirus A71 and the SNARE proteins, SNAP29 and STX17, was proposed to be responsible for virus-triggered complete autophagy although the detailed mechanism remains to be defined [176]. It was also reported that hepatitis C virus infection results in decreased levels of STX17 and overexpression of STX17 rescues the formation of autolysosomes [177]. There are currently no studies concerning viral targeting of PLEKHM1. However, other microorganisms, most notably the Salmonella were found to bind to the PH2 domain of PLEKHM1 to limit the formation of the PLEKHM1-Rab7-HOPS tethering complex [178].

The functional significance or consequence of CVB3 modification of the autophagic pathway may be at least three-fold. *First*, CVB3 inhibition of autophagosome degradation results in its accumulation to favor the replication of viral genomes by offering additional cytoplasmic membranes for the assembly of viral replication complex. It has long been known that RNA viruses, including picornaviruses, rely largely on intracellular membranous structures for replication [12]. Depending on the availability and abundance of other source of cytoplasmic membranes, such as ER, endosome, or mitochondrial membranes, autophagosome may not be absolutely required, but it does provide an additional option to be utilized by virus to maximize its replication. As noted earlier, SNAP29 and PLEKHM1 are ubiquitously expressed and participate in a wide range of intracellular vesicular trafficking events. Apart from regulating autophagosome fusion, they also play a vital role in the endocytic and exocytic (secretory) pathways [172, 173]. Thus, it is conceivable that loss of SNAP29/PLEKHM1 not only results in the accumulation of autophagosomes, but also leads to defective transport and recycling of endosomes and ER/Golgi-derived vesicles, contributing, at least partially, to the single- and double-membrane structures detected in infected cells and associated with viral RNA synthesis [79]. Whether absence of SNAP29/PLEKHM1 has a role in the modification of vesicular components, for example, transporting cholesterol to membranous replication sites, which has been shown to regulate viral polyprotein processing and promote viral RNA synthesis [64], has yet to be examined and warrants further investigation. *Second*, CVB3 inhibits autophagic flux to prevent viral RNA/protein degradation. Complete autophagy has been implicated as a host defense mechanism against

multiple viral infections, including picornavirus infection. It was recently shown that the danger receptor, galectin-8, responsible for monitoring endosomal integrity and pathogen-induced breaching can target picornavirus RNA for autophagic degradation [62]. Thus, it is expected that inhibition of a complete autophagy will also block autophagy-induced clearance of virus. *Third*, besides viral advantage, disrupted autophagy can also cause insufficient clearance of toxic protein aggregates/damaged organelles that are generated upon viral challenge [179], contributing to disease progression. Given that the removal of protein aggregates and damaged organelles is mainly through the lysosome pathway, our present data reveal a disease mechanism, in which CVB3 infection disrupts the function of protein quality control by preventing autophagy-mediated degradation, resulting in the accumulation of toxic protein conjugates/damaged organelles and consequent tissue damage.

Apart from its primary function in targeting cellular components for degradation (referred to as degradative autophagy), autophagy also plays a role in unconventional secretion of cytosolic cargo (termed secretory autophagy), such as the release of inflammatory cytokines and the transmission of protein aggregates [180]. Recent studies highlight the significance of non-lytic spread of picornavirus in viral pathogenesis and suggest a role for secretory autophagy and exosome pathway in such process [14, 15, 16, 17]. Although the exact mechanism remains uncertain, Altan-Bonnet *et al* propose a model that enterovirus-bearing autophagosomes, which fail to fuse with lysosomes, traffic to the cell periphery where they fuse with the plasma membrane to release inner vesicles [181]. Our results in this study appear to suggest that viral infection not only restricts autophagosome fusion with lysosomes, but also with plasma membrane, as evidenced by the observation that SNAP29 silencing limits viral egress despite significant elevation in viral replication. Indeed, a recent study has identified SNAP29 as a key component of the secretory autophagy pathway required for autophagosome fusion with plasma membranes [182]. Given the known function of SNAP29 in general membrane trafficking, this finding may not seem particularly surprising. However, it is unclear why CVB3 would target a protein that would otherwise help facilitate its non-lytic propagation. One explanation is that CVB3 only affects a particular pool of SNAP29 (e.g., SNAP29 specifically mediating autophagosome-lysosome/endosome fusion), whereas our experiments here systematically knocked down SNAP29. Alternatively, loss of SNAP29 prevents autophagosome recycling via fusion with plasma membrane to offer additional viral replication sites. Additionally, as enteroviruses have

only one open reading frame, it is conceivable that viral modulation of the function of essential host proteins involved in replication may hinder viral processes at different stages [183]. Future studies are warranted to determine whether virus is able to fine-tune the processing during various stages of the viral life cycle to maximize its propagation.

In conclusion, our data in this study provide compelling evidence that CVB3 targeting of the vesicular trafficking adaptor proteins, SNAP29 and PLEKHM1, ensures successful viral replication and acts as a novel mechanism to circumvent host xenophagic efforts.

In **Chapter 4**, I identified novel host factors that are targeted by CVB3 to disrupt autophagosome-lysosome fusion. Given the significance of the lysosome as an important cellular disposal chamber, in **Chapter 5** I explored the mechanisms by which CVB3 regulates lysosome biology and identified a novel host factor that is co-opted to facilitate viral pathogenesis.

Chapter 5: Coxsackievirus B3 targets TFEB to disrupt lysosomal function

Background

TFEB (transcription factor EB) is a master regulator of lysosome biogenesis and autophagy[184, 185, 186]. Expression, localization, and activity of TFEB is tightly regulated by post-translational modifications, including phosphorylation, ubiquitination, and acetylation[187, 188, 189]. Under physiological conditions, TFEB is phosphorylated by MTOR (mechanistic target of rapamycin kinase) complex 1 (MTORC1) on lysosomes and maintained in the cytosol. Upon starvation and cellular stress, MTORC1 is inactivated and/or PPP3/calcineurin phosphatase is activated, leading to the subsequent dephosphorylation and nuclear translocation of TFEB[184]. Nuclear TFEB then binds to a network of promoters (CLEAR; Coordinated Lysosomal Enhancement and Regulation) to induce the transcriptional activation of autophagy and lysosome target genes.

Rationale: Despite the demonstrated importance of autophagy in EV infections, the exact mechanism by which EVs subvert this pathway, particularly the interplay between EVs and the TFEB network, remains largely unclear. In the current study, I identified TFEB as a novel target of CVB3 that undergoes nuclear translocation, but transcriptional inactivation following infection. Further investigation revealed that TFEB is a bona fide substrate of viral proteinase 3C, leading to disrupted lysosomal function and enhanced viral propagation. The **specific aim** of this study was to investigate the mechanism by which CVB3 disrupts the host lysosome machinery.

Materials and methods

Plasmids and small interfering RNA (siRNA)

The 4×CLEAR luciferase reporter (66800), pEGFP-N1-TFEB (38119), pEGFP-N1-MITF-A (38132), and pEGFP-N1-TFE3 (38120) plasmids were obtained from Addgene (deposited by Albert La Spada and Shawn Ferguson). pEGFP-N1-TFEB [Δ60] plasmid was generated in the Luo lab. TFEB [Δ60] insert was amplified by PCR with Forward primer: AAATTTAAGCTTGCCACC ATGGGATCGCCACCACCTGTGC and Reverse primer: AAATTTGGTACCTTCAGCACATCGCCCTCCTC and cloned into pEGFP-N1 at HindIII and KpnI sites. 3×Flag-TFEB [Δ60] was generated in the current laboratory. TFEB [Δ60] insert was amplified by PCR with Forward primer: AAATTTGAATTCCTCGCCACCACCTGTGC and Reverse primer: AAATTTGGATCCTCACAGCACATCGCCCTCCTC and cloned into CMV10 vector at EcoRI and BamHI sites. $TFEB^{QS60LP}$, $TFEB^{QS73LP}$, and $TFEB^{QS86LP}$ were generated through site-directed mutagenesis with the following primers (QS60LP Forward: 5'CCGTCCACTTCCTGCCGCCACCAC-3' Reverse: 5' GTGGTGGCGGCAGGAAGTGGACGG-3'; QS73LP Forward: 5' GTGTTGAAGGTGCTGCCCTACCTGGAG-3' Reverse: 5' CTCCAGGTAGGGCAGCACCTTCAACAC-3'; QS86LP Forward: 5' CTACCATCTGCAGCTGCCGCAGCATCAG-3' Reverse: 5' CTGATGCTGCGGCAGCTGCAGATGGTAG-3'). The myc-tagged wild-type CVB3-3C (WT 3C) and C147A mutant CVB3-3C ($3C^{C147A}$) constructs were generous gifts from Dr. Carolyn Coyne at the University of Pittsburgh [190]. The siRNA targeting *TFEB* (sc-38509) and scrambled siRNA (sc-37007) were purchased from Santa Cruz Biotechnology. For transfection, cells were transiently transfected with plasmid cDNAs or siRNAs using Lipofectamine 2000 (Invitrogen, 11668-019) following the manufacturer's instructions.

Confocal microscopy

HeLa cells were cultured in 8-well chamber slides (Labtek, 155411) for 24 h prior to treatment. Cell membrane integrity was assessed with the amine-reactive dye LIVE/DEAD (L34958; Thermo Fisher Scientific) according to the manufacturer's instructions. After fixation in 4% paraformaldehyde, cells were washed thrice in PBS. For LAMP1 staining, cells were permeabilized with 0.1% Triton X-100 (Sigma, T8787), blocked with 3% BSA (Sigma, A7030),

and incubated overnight with Alexa Fluor 594-conjugated anti-LAMP1 (Santa Cruz Biotechnology, sc20011) before mounting with fluoroshield with 4, 6-diamidino-2-phenylindole (DAPI; Sigma-Aldrich, F6057). Images were captured with the Zeiss LSM 880 Inverted Confocal Microscopy using a 63×objective lens.

Measurement of nuclear TFEB was performed using HeLa cells expressing GFP-TFEB, GFP-TFEB [Δ60], or GFP-TFEB^{QS60LP}. Confocal images of control and treated cells were obtained from Zen Black software. Cells were manually quantified as positive for nuclear TFEB when nuclear GFP signal intensity was greater than cytoplasmic. A total of 30 GFP-positive cells across 3 biologically independent chambers was used for quantification and presented as percentage of positive cells (mean ± SD).

LysoTracker staining

Lysosomal colocalization was monitored using LysoTracker Red (LTR) DND-99 (L7528; Thermo Fisher Scientific) following the manufacturer's guideline. Briefly, HeLa cells were cultured in 8-well chamber slides (Labtek, 155411) for 24 h prior to treatment. Following construct transfection (24 h) and/or CVB3 infection (5 h), LTR (75 nM) was added into the culture medium and incubated at 37°C for 60 min. Cells were fixed in methanol-free 4% PFA and counterstained with DAPI. Images were captured with the Zeiss LSM 880 Inverted Confocal Microscopy/ Zen Black software using a 63×oil immersion lens. LTR mean intensity was analyzed using ImageJ software.

4×CLEAR luciferase assay

TFEB transcriptional activity was measured using the dual-luciferase reporter system (Promega, E1910). Briefly, HeLa cells were co-transfected with 4×CLEAR luciferase reporter (Addgene, 66800; deposited by Albert La Spada) and Renilla control luciferase plasmid (Addgene, 87121; deposited by Sanjiv Sam Gambhir). Cells were harvested at 16 h post transfection, and cell lysates were transferred to an opaque 96-well microplate (Greiner, 655074). Luciferase activity was detected using SpectraMax i3 Detection System.

Western blot analysis

Cells were lysed in buffer (10 mM HEPES, pH 7.4, 50 mM NaPyrophosphate, 50 mM NaF, 50 mM NaCl, 5 mM EDTA, 5 mM EGTA, 100 µM Na_3VO_4, 0.1% Triton X-100) supplemented with cOmplete Mini, EDTA-free protease inhibitor cocktail tablets (Sigma, #11836170001) and western blotting was conducted using the following primary antibodies: TFEB (Cell Signaling Technology, D2O7D), phospho (Ser211)-TFEB (Cell Signaling Technology, 376815), VP1 (Mediagnost, Cox mAb 31A2), ACTB (Sigma-Aldrich, A5316), GFP (Sigma-Aldrich, SAB5300167), FLAG (Sigma, F1804), and PPP3C/calcineurin (Santa Cruz Biotechnology, sc-17808).

Ex vivo cleavage assay

Ex vivo or cellular cleavage assay was performed as previously described[191]. Briefly, HeLa cells were transfected with $TFEB^{QS60LP}$, TFEB-QS73LP, or TFEB-QS86LP and either CVB3 WT 3C or catalytically inactive (C147A) mutant $3C^{mut}$ for 16 h. Lysates were harvested and subjected to western blot analysis with anti-GFP and anti-TFEB antibody to detect cleavage fragments.

Electrophoretic mobility shift assay (EMSA)

In vitro transcription/translation of TFEB and TFEB [Δ60] were performed using the TNT® T7 Quick Coupled Transcription/Translation System (Promega, L1170) according to the manufacturer's protocol. EMSA was carried out in 20 µl reaction containing 1 µl of reticulocyte translation product in binding buffer (5% glycerol, 100 mM KCl, 10 mM $MgCl_2$, 10 mM Tris, pH 7.4, 1 mM DTT) supplemented with 0.5 ng of TFEB consensus oligonucleotide sequence corresponding to an 18-nucleotide dsDNA sequence of 5'-GTAGGCCACGTGACCGGG-3' (Santa Cruz Biotechnology, sc-2621). Control reaction was supplemented with 1 µg of anti-TFEB antibody (Cell Signaling Technology, D2O7D). Reaction mixtures were incubated at room temperature for 20 min. and separated by 6% non-denaturing polyacrylamide gel. Nucleic acid was visualized with SYBR™ Safe DNA Gel Stain (Thermofisher Scientific, S33102) and imaged using the GBOX Chemi XRQ.

Immunoprecipitation

Immunoprecipitation (IP) of Flag-tagged TFEB [Δ60] was performed using EZview™ Red ANTI-FLAG ® M2 Affinity Gel (Sigma-Aldrich, F2426) according to the manufacturer's

instructions. In brief, HeLa cells were lysed with Flag Lysis Buffer (50 mM Tris HCl, pH 7.4, with 150 mM NaCl, 1 mM EDTA, and 1% TX-100) for 15min on ice. Lysates were cleared with a centrifugation at 12,000g for 15min. Supernatants (50uL) was partitioned for input control and the remaining lysate was incubated overnight with anti-Flag M2 agarose beads with end-over-end rotation at 4°C. After three washes with lysis buffer, the bound proteins were eluted with 2× SDS sample buffer and then subjected to Western blot analysis.

Viral entry assay

Viral particle uptake was performed as described previously[192]. In brief, HeLa cells treated with control or TFEB-targeting siRNA were infected with CVB3 for 1.5 h. After three washes with PBS, cells were harvested and subjected to RNA extraction. qPCR was performed to determine levels of viral genomic RNA using primer pairs of CVB3 2A (forward: 5′-GCT TTG CAG ACA TCC GTG ATC-3′; reverse: 5′-CAA GCT GTG TTC CAC ATA GTC CTT CA-3′) and normalized to β-actin mRNA (ACTB, forward primer: 5′-ACT GGA ACG GTG AAG GTG AC-3′; reverse primer: 5′-GTG GAC TTG TTG GGA GAG GAC TG-3′) levels.

Real-time quantitative RT-PCR

Total RNA was extracted using the RNeasy Mini kit (Qiagen, 74104). To determine gene expression levels, quantitative PCR targeting M6PR (forward primer: CTCAGTGTGGGTTCCATCTTAC; reverse primer: GGGAAACTGCTCCATTCCTT), CTSB (forward primer: GGACAAGCACTACGGATACAA; reverse primer: GTAGAGCAGGAAGTCCGAATAC) ATP6V1H (forward primer: CCCTGAAGAGAAGCAAGAGATG, reverse primer: TGCAGCATATCATCCACCATAG) RAB7A (forward primer: CCTGGAGTCTTGGCCATAAAG, reverse primer: GAGAAGGTCCAAGTTCTGGTTC) MCOLN1 (forward primer: GGAAAGCAGCTCCAGTTACA reverse primer: GATGAGGCTCTGGAGGTTAATG) was performed in a 10 μl reaction containing 1 μg of RNA using the TaqMan™ RNA-to-CT™ 1-Step Kit (Life Technologies, 4392653) and normalized to *ACTB* mRNA according to the manufacturer's instructions. The PCR reaction was performed on a ViiA 7 Real-Time PCR System (Applied Biosystems). Samples were run in triplicate and analyzed using comparative CT (2-ΔΔCT) method with control samples and presented as relative quantitation (RQ).

In vitro cleavage assay

In vitro cleavage assay was performed as previously described [171]. Briefly, HeLa cells were lysed with 25 strokes of dounce homogenization in 1X cleavage buffer assay buffer (20mM HEPES pH 7.4, 150 mM potassium acetate, and 1mM DTT). Lysates were clarified with a 15min centrifugation at 12,000g. Lysates (30 µg) was incubated with purified wild-type or catalytically inactive CVB3 proteinase 3C (0.1 µg) or 2A (0.3 µg) in a cleavage assay buffer for 16 h at 37ºC. Reaction was terminated with 6× SDS sample buffer, followed by 95ºC denaturation and subsequent Western blot analysis. Purified proteases were produced as described below.

Purification of CVB3 $2A^{pro}$ and $3C^{pro}$

pET-28a plasmids encoding wild-type (WT) CVB3 $2A^{pro}$ and WT CVB3 $3C^{pro}$ were transformed into C41 (DE3) *E. coli* and subsequently plated onto kanamycin (50 µg/mL) agar plates. A starter culture from a single colony was grown overnight and then diluted 100-fold in Terrific Broth [Sigma, T9179]. Expression was induced with 1mM isopropyl β-D-1-thiogalactopyranoside (IPTG) after cultures reached an OD600 of 0.6-0.8 and proceeded at 25°C for 5 additional hours. Protein was purified using Ni-NTA Fast Start (Qiagen, #30600) according to the manufacturer's instructions. Catalytically inactive $2A^{mut}$ (C109A) and $3C^{mut}$ (C147A) were generated as previously described [171].

Median Tissue Culture Infectious Dose (TCID50)

Samples were serially diluted and overlaid on 60-well micro test Terasaki plates (Sarstedt, #83.9923.972) of HeLa cells. After 48 h incubation, 50% tissue culture infective dose titer (TCID50) was calculated by the statistical method of Reed and Muench[193]. Titers were expressed as plaque forming unit (PFU)/mL with 1 infectious unit equal to 0.7 TCID50 as described previously [194].

Results

CVB3 induces nuclear localization but functional attenuation of TFEB

To evaluate the role of CVB3 infection in lysosomal biology, I first investigated the cellular protein TFEB, a master regulator of lysosomal biogenesis and autophagy. TFEB is basally situated in the cytoplasm but undergoes nuclear localization upon activation. HeLa cells were infected with CVB3 (multiplicity of infection [MOI] =10) following a time-course infection (*i.e.*, 1, 3, or 5 h) to monitor the cellular distribution of TFEB. TFEB was predominantly localized in the cytoplasm in mock-infected cells, while infection with CVB3 caused the re-distribution of TFEB to the nucleus, most evidently at 5 h post-infection (**Figure 28A & B**). It was previously established that nuclear localization of TFEB promotes transcriptional activation of the CLEAR network[195]. To investigate whether CVB3-induced nuclear localization of TFEB similarly activated the CLEAR network, I performed RT-qPCR to analyze several downstream gene targets of TFEB, including *M6PR* (mannose-6-phosphate receptor, cation dependent), *CTSB* (cathepsin B) encoding a lysosomal cysteine protease, *ATP6V1H* (ATPase H+ transporting V1 subunit H) encoding a vacuolar (V)-type proton ATPase subunit, *RAB7A* (RAB7A, member RAS oncogene family) encoding an endolysosomal trafficking small GTPase, and *MCOLN1* (mucolipin 1) encoing a lysosome-associated ion channel. Gene expression for all the aforementioned members of the CLEAR network was significantly reduced, while the mRNA level of house-keeping genes, *ACTB* and *GAPDH*, remained unaltered following CVB3 infection (**Figure 28C**), indicating impaired expression of TFEB target genes.

We next examined the effect of CVB3 infection on the transcriptional activity of TFEB, which can be measured using a luciferase reporter construct with 4 tandem CLEAR elements[196]. Consistent with transcriptional inactivation shown in **Figure 28C**, the 4×CLEAR luciferase activity was significantly disrupted in CVB3-infected cells (**Figure 28D**). I then biochemically assessed TFEB protein in CVB3-infected HeLa lysates. Western blot analysis following various time-points of CVB3 infection revealed a reduction in full-length TFEB and the emergence of a 63 kDa anti-TFEB reactive fragment at 5 h post-infection (**Figure 28E**), concomitant with the nuclear translocation of TFEB observed in **Figure 28A** and appearance of the proteolytically processed viral capsid protein VP1 (**Figure 1E**). Together, our data suggest that CVB3 infection causes nuclear translocation, but transcriptional inactivation and downregulation of full-length TFEB.

Viral proteinase 3C cleaves TFEB after Q60

Given that viral polyprotein processing is primarily mediated by the viral proteinase $3C^{197}$, I next investigated whether the lower-molecular-weight band observed with anti-TFEB antibody was a by-product of 3C. To that end, I conducted *in vitro* cleavage assays using purified recombinant wild-type (WT) 3C or the catalytically inactive (C147A) mutant of 3C ($3C^{C147A}$). **Figure 29A** showed the time-dependent emergence of a 63 kDa anti-TFEB-reactive fragment in the WT 3C-treated but not catalytically inactive $3C^{C147A}$-incubated condition. The observed fragment in the *in vitro* reaction was similar in size to that observed following CVB3 time-course infection. Consistent with this, HeLa cells co-transfected with TFEB-GFP and WT 3C, but not $3C^{C147A}$, recapitulated the appearance of the lower-molecular-weight TFEB fragment (**Figure 29B**), further supporting the requirement for 3C proteinase activity in TFEB cleavage.

To identify the precise location of proteolytic processing, I screened the TFEB open reading frame for potential cleavage sites with a focus mainly on the highly conserved glutamine (Q) residue at the P1 position (**Figure 29C**). I identified 6 potential sites that matched the consensus cleavage residues at the P1-P1' interface with variability being expanded at the P1' position to account for previously reported residues including glycine (G), asparagine (N), serine (S), and alanine (A)[198, 199, 200]. Site-directed mutagenesis was used to generate TFEB mutants in the N-terminal region by mutating glutamine (Q) and alanine (A) residues, designated as QA, to leucine (L) and proline (P) residues, which are designated as LP. The resulting mutants included QA15LP/QA28LP, Q112L, QS60LP, QS73LP, and QS86LP mutants (**Figure 2D**). Co-transfection of WT 3C with TFEB-QA15LP/QA28LP (**Figure 29E**), TFEB-Q112L (**Figure 29F**), TFEB-QS73LP or TFEB-QS86LP mutants (**Figure 29G**) resulted in cleavage of mutant TFEB, suggesting that these sites are not the targets of proteinase 3C. In contrast, co-expression of WT 3C with $TFEB^{QS60LP}$ led to complete blockage of 3C-mediated cleavage (**Figure 29G**). Collectively, these data demonstrate that TFEB is cleaved by viral proteinase 3C after Q60, leading to the generation of a TFEB fragment lacking the N-terminal 60 amino acids, designated as the TFEB [Δ60] fragment (**Figure 29H**).

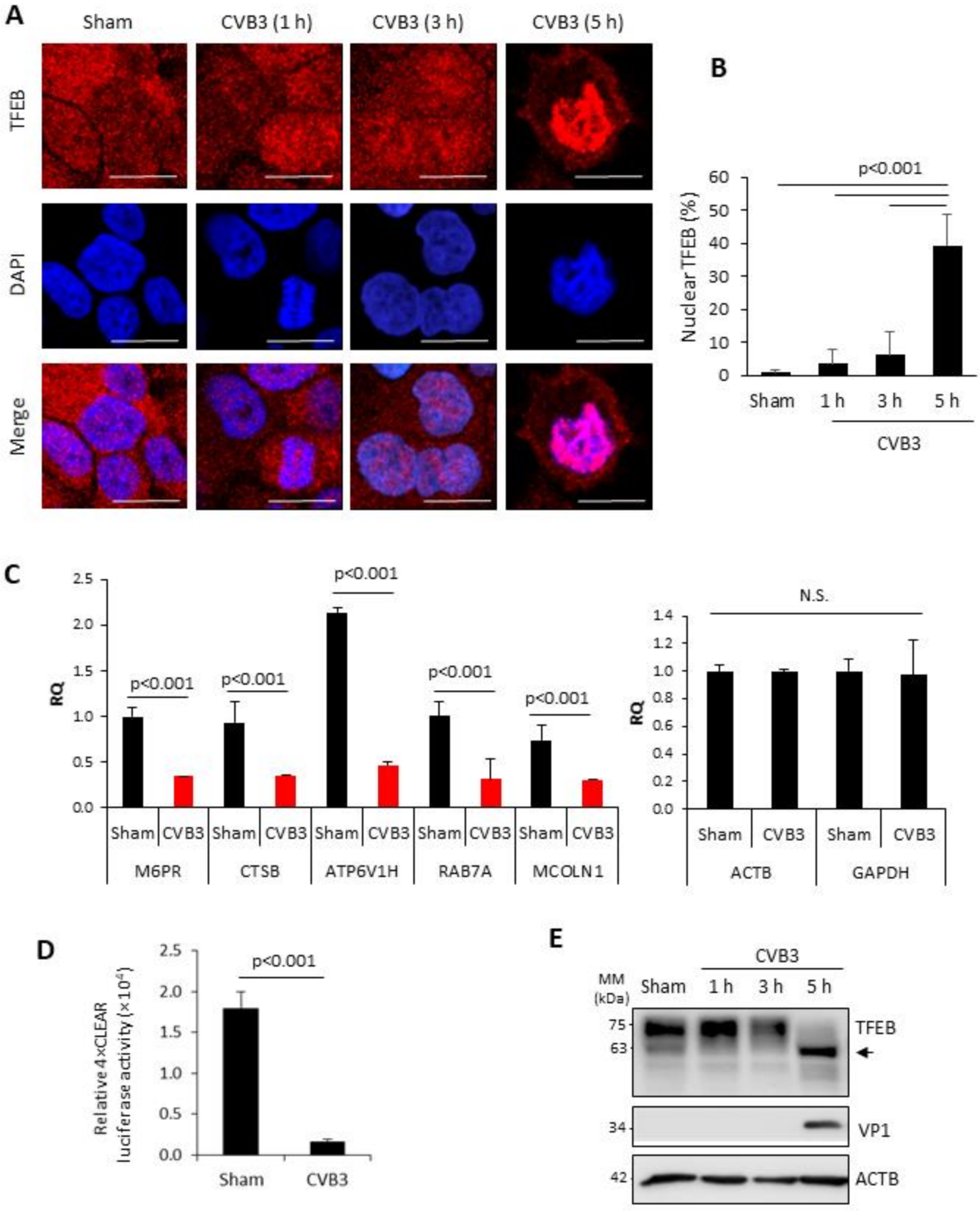
A
Sham
CVB3 (1 h)
CVB3 (3 h)
CVB3 (5 h)
TFEB
DAPI
Merge
B
p<0.001
Nuclear TFEB (%)
60
50
40
30
20
10
0
Sham
1 h
3 h
5 h
CVB3
C
RQ
2.5
2.0
1.5
1.0
0.5
0.0
p<0.001
p<0.001
p<0.001
p<0.001
p<0.001
Sham
CVB3
M6PR
CTSB
ATP6V1H
RAB7A
MCOLN1
N.S.
1.4
1.2
1.0
0.8
0.6
0.4
0.2
0.0
ACTB
GAPDH
D
Relative 4×CLEAR luciferase activity (×10⁴)
p<0.001
Sham
CVB3
E
CVB3
MM (kDa)
Sham
1 h
3 h
5 h
75
63
TFEB
34
VP1
42
ACTB

Figure 28. CVB3 induces nuclear localization but functional attenuation of TFEB. (**A**) Intracellular distribution of TFEB in HeLa cells following CVB3 infection. Immunocytochemical staining was performed to examine the localization of TFEB following time-course infection of CVB3 (MOI=10). Cell nuclei were counterstained with DAPI. Scale bars: 10 μm. (**B**) Quantification of percentage of TFEB nuclear localization in (A). More than 30 cells were analyzed. (**C**) mRNA levels of TFEB transcriptional targets in HeLa cells after CVB3 infection. Following 7-h CVB3 infection (MOI=10), the expression of several TFEB target genes as indicated was measured by real-time quantitative PCR and normalized to *ACTB* (mean ± SD, n=3). Transcriptional levels of house-keeping genes *ACTB* and *GAPDH* are shown on the right. (**D**) TFEB transcriptional activity in HeLa cells after CVB3 infection. TFEB transcriptional activity was measured using 4×CLEAR luciferase reporter (mean ± SD, n=3) following 5-h CVB3 infection (MOI=10). (**E**) Protein expression of TFEB in HeLa cells after CVB3 infection. Western blot analysis was conducted to examine protein levels of TFEB following CVB3 infection (MOI=10) at different time-points. Viral capsid protein (VP1) and ACTB were probed as controls for viral infection and protein loading, respectively. Arrow denotes lower molecular weight protein reactive to TFEB antibody.

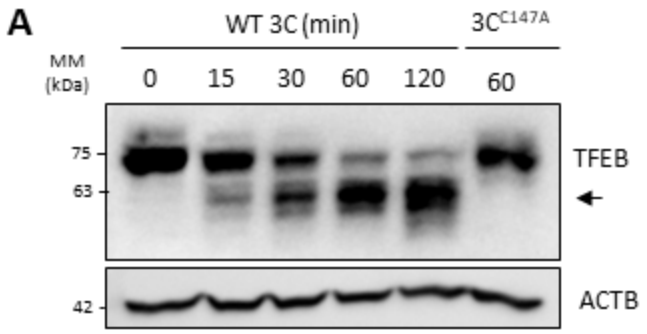

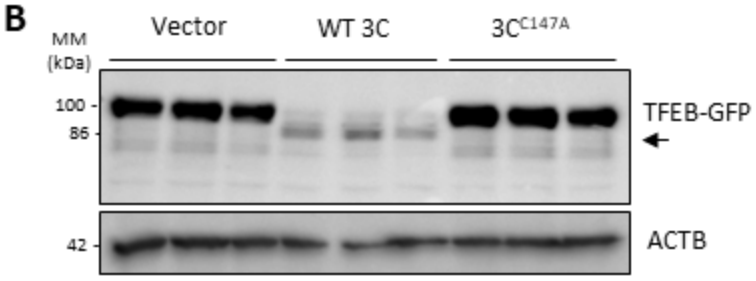

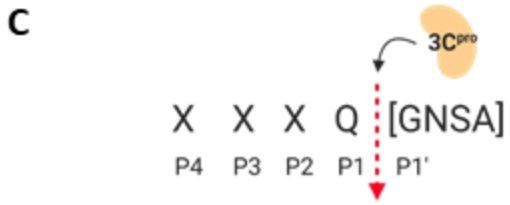

D

P1'	P4-P1'	Mutant Cleaved?
QA15	MREQA	Yes
QA28	MQQQA	Yes
QS60	VHFQS	No
QS73	IKVQS	Yes
QS86	HLQQS	Yes
QG112	SPAQG	Yes

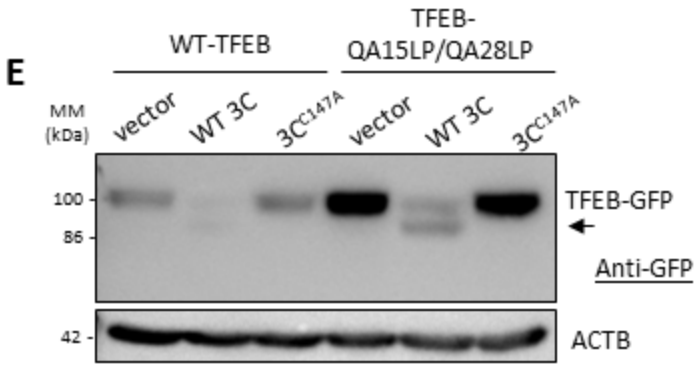

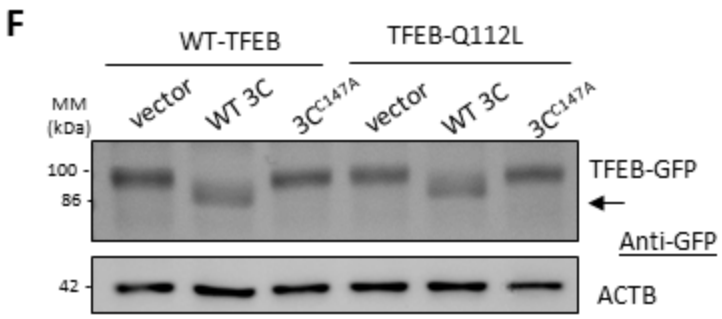

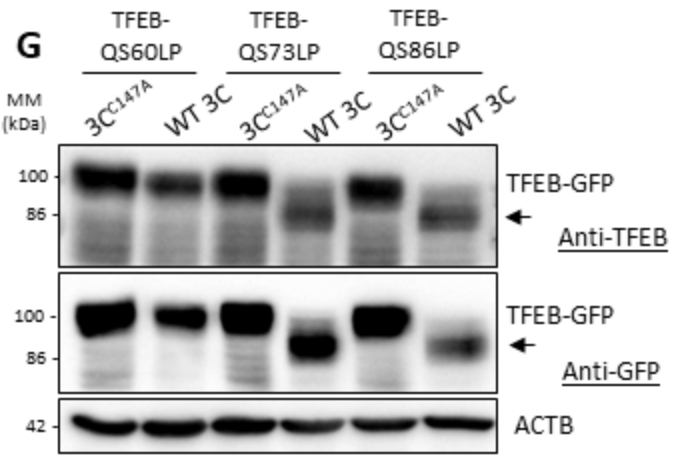

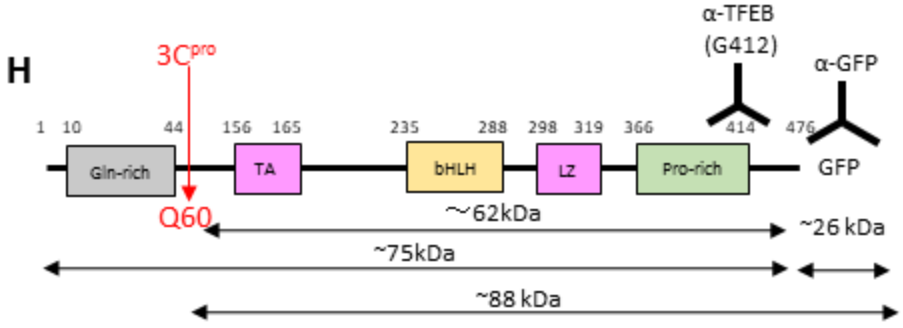

TA: Transcription activation
LZ: Leucine-zipper
bHLH: basic helix loop helix

Ser 142; Ser211
NLS & DNA binding: 230-250
14-3-3 binding: 209-213

Figure 29. Viral proteinase 3C cleaves TFEB after Q60.

(**A**) Viral proteinase 3C-mediated cleavage of TFEB by *in vitro* cleavage assay. HeLa lysates (30 μg) were subjected to *in vitro* cleavage assay by incubation with 0.1 μg of purified CVB3 wild-type proteinase 3C (WT 3C) or catalytically inactive (C147A) mutant of 3C ($3C^{C147A}$) for the indicated times. Cleavage product of TFEB was analyzed by western blotting with anti-TFEB antibody. Arrow denotes cleavage fragment.

(**B**) Viral proteinase 3C-dependent cleavage of TFEB by *ex vivo* (cellular) cleavage assay. HeLa cells were transfected with TFEB-GFP together with either empty vector, WT 3C, or $3C^{C147A}$. After 24 h, cell lysates were collected and analyzed by western blotting with anti-GFP antibody. Arrow denotes TFEB cleavage fragment.

(**C**) Schematic of $3C^{pro}$ consensus cleavage sequence. Q, Glutamine; G, Glycine; N, Asparagine; S, Serine; A, Alanine.

(**D**) Potential cleavage sites within open reading frame of TFEB. P4-P1' residues are provided in central column.

(**E-G**) Identification of the cleavage site on TFEB. HeLa cells were transfected with WT 3C or $3C^{C147A}$, together with either TFEB QA15LP/QA28LP (**E**), TFEB-Q112L (**F**), or $TFEB^{QS60LP}$, TFEB-QS73LP, or TFEB-QS86LP (**G**). After 24 h, cell lysates were harvested and subjected to western blot analysis using anti-TFEB and/or anti-GFP antibodies as indicated. Arrows denote TFEB cleavage fragments.

(**H**) Schematic illustration of the structural domains of TFEB, the identified cleavage site, the antibody recognition regions, and the resulting cleavage products of TFEB.

TFEB [Δ60] is non-phosphorylated and nuclear localized

To further study the function of the cleaved TFEB, I generated a GFP-labelled TFEB [Δ60]. Consistent with the results shown in **Figure 28A**, WT TFEB was predominantly distributed in the cytoplasm in mock-infected cells and underwent nuclear redistribution upon CVB3 infection. In contrast, TFEB [Δ60] was localized to the nucleus in either mock- or CVB3-infected cells (**Figure 30A & B**).

It was previously reported that a subset of cytoplasmic TFEB is anchored to lysosomal membranes and co-localized with LysoTracker Red (LTR, a red-fluorescent dye used as a marker of lysosome or acidic compartments)[201]. Unlike WT-TFEB, I found that TFEB [Δ60] failed to effectively co-localize with lysosomes (**Figure 30C & D**).

The lysosome-associated MTORC1 can suppress TFEB activity through inhibitory phosphorylation on Ser211[187]. As expected, expression of WT-TFEB resulted in the detection of Ser211 phosphorylation in mock-infected cells, while CVB3 infection led to decreased phosphorylation of WT-TFEB on Ser211 (**Figure 30E**). Remarkably, TFEB [Δ60] did not undergo phosphorylation at Ser211 in both mock- and CVB3-infected cells (**Figure 30E**). As a control, I showed that the exogenous WT-TFEB was cleaved whereas non-cleavable $TFEB^{QS60LP}$ and the truncated TFEB [Δ60] remained unaffected following CVB3 infection (**Figure 30F**). Together, our results reveal that the cleavage fragment of TFEB, TFEB [Δ60], is non-phosphorylated and localized to the nucleus.

TFEB [Δ60] impairs the signaling of lysosomal biogenesis

The nuclear localization nature of TFEB [Δ60] prompted us to evaluate whether this fragment retains the transcriptional activity of WT-TFEB. Following mock infection, cells expressing TFEB [Δ60] had significantly reduced 4×CLEAR transcriptional activity compared to WT-TFEB (**Figure 31A**). CVB3 infection further attenuated the transcriptional activity of both WT- and TFEB [Δ60] (**Figure 31A**). Most interestingly, I found a significant downregulation in gene targets of TFEB following the expression of TFEB [Δ60] as compared to the expression of vector control in HeLa cells (**Figure 31B**), suggesting a possible dominant-negative function of TFEB [Δ60] by competing with the endogenous WT-TFEB.

LTR serves as a functional proxy to assess the luminal acidity required for lysosomal protease activity[202]. Compared to control, I showed that CVB3-infected cells had significantly

reduced LTR intensity (**Figure 31C**). Furthermore, expression of TFEB [Δ60] alone in the absence of viral infection was able to recapitulate the impairment in lysosomal pH observed following CVB3-infection (**Figure 31D**), indicating disruption of the lysosomal function. Finally, I compared the impact of the TFEB [Δ60] mutant on lysosomes using lysosome-associated membrane protein 1 (LAMP1) as a marker. **Figure 31E** showed that compared to WT-TFEB, expression of TFEB [Δ60] mutant is associated with a significant reduction in the number of LAMP1-positive structures.

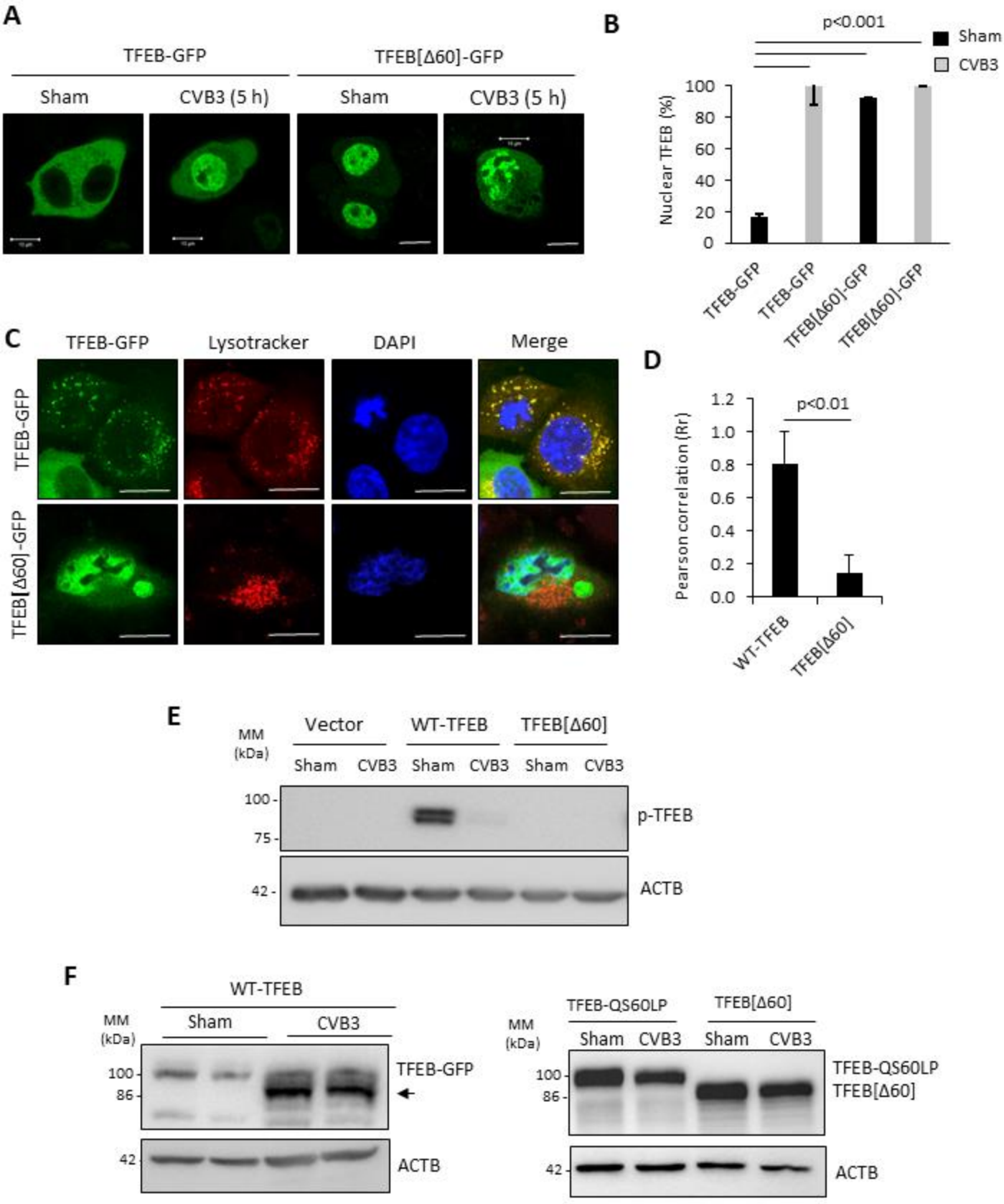
A
TFEB-GFP
TFEB[Δ60]-GFP
Sham
CVB3 (5 h)
Sham
CVB3 (5 h)
B
p<0.001
Sham
CVB3
Nuclear TFEB (%)
100
80
60
40
20
0
TFEB-GFP
TFEB-GFP
TFEB[Δ60]-GFP
TFEB[Δ60]-GFP
C
TFEB-GFP
Lysotracker
DAPI
Merge
TFEB-GFP
TFEB[Δ60]-GFP
D
p<0.01
Pearson correlation (Rr)
1.2
1.0
0.8
0.6
0.4
0.2
0.0
WT-TFEB
TFEB[Δ60]
E
MM (kDa)
Vector
WT-TFEB
TFEB[Δ60]
Sham
CVB3
Sham
CVB3
Sham
CVB3
100
75
p-TFEB
42
ACTB
F
WT-TFEB
MM (kDa)
Sham
CVB3
100
86
TFEB-GFP
42
ACTB
TFEB-QS60LP
TFEB[Δ60]
MM (kDa)
Sham
CVB3
Sham
CVB3
100
86
TFEB-QS60LP
TFEB[Δ60]
42
ACTB

Figure 30. TFEB [Δ60] is non-phosphorylated and nuclear-localized.

(**A**) Intracellular localization of TFEB and TFEB [Δ60] following CVB3 infection. HeLa cells were transfected with TFEB-GFP or TFEB [Δ60]-GFP for 24 h, followed by CVB3 infection (MOI=10) for an additional 5 h. GFP fluorescence was used to monitor TFEB localization. Scale bars = 10 μm.

(**B**) Quantification of percentage of TFEB-GFP and TFEB [Δ60]-GFP nuclear localization in (A). More than 30 cells were counted for statistical analysis and presented as mean ± SD as described in materials and methods.

(**C**) Lysosomal localization of TFEB or TFEB [Δ60]. HeLa cells transfected as above were incubated in medium containing the lysosome tracking dye Lysotracker Red DND-99 (75 nM). Scale bars=10 μm.

(**D**) Quantification of lysosome-localized TFEB-GFP or TFEB [Δ60]-GFP in (C) by ImageJ and presented as Pearson's correlation coefficient (Rr). More than 30 cells were counted.

(**E**) Dephosphorylation of TFEB following CVB3 infection. HEK293 cells were transfected with either vector, WT-TFEB-GFP, or TFEB [Δ60]-GFP for 24 h, followed by CVB3 infection (MOI=100) for 8 h. Cell lysates were analyzed by western blotting with anti p-TFEB (Ser211) and anti-ACTB antibodies.

(**F**) Cleavage of exogenous WT-TFEB-GFP following CVB3 infection. HeLa cells were transfected with either WT-TFEB-GFP, $TFEB^{QS60LP}$-GFP, or TFEB [Δ60]-GFP for 24 h followed by CVB3 infection (MOI=10) for 8 h. Cell lysates were analyzed by western blotting with anti-GFP antibody. Arrow denotes TFEB cleavage fragment.

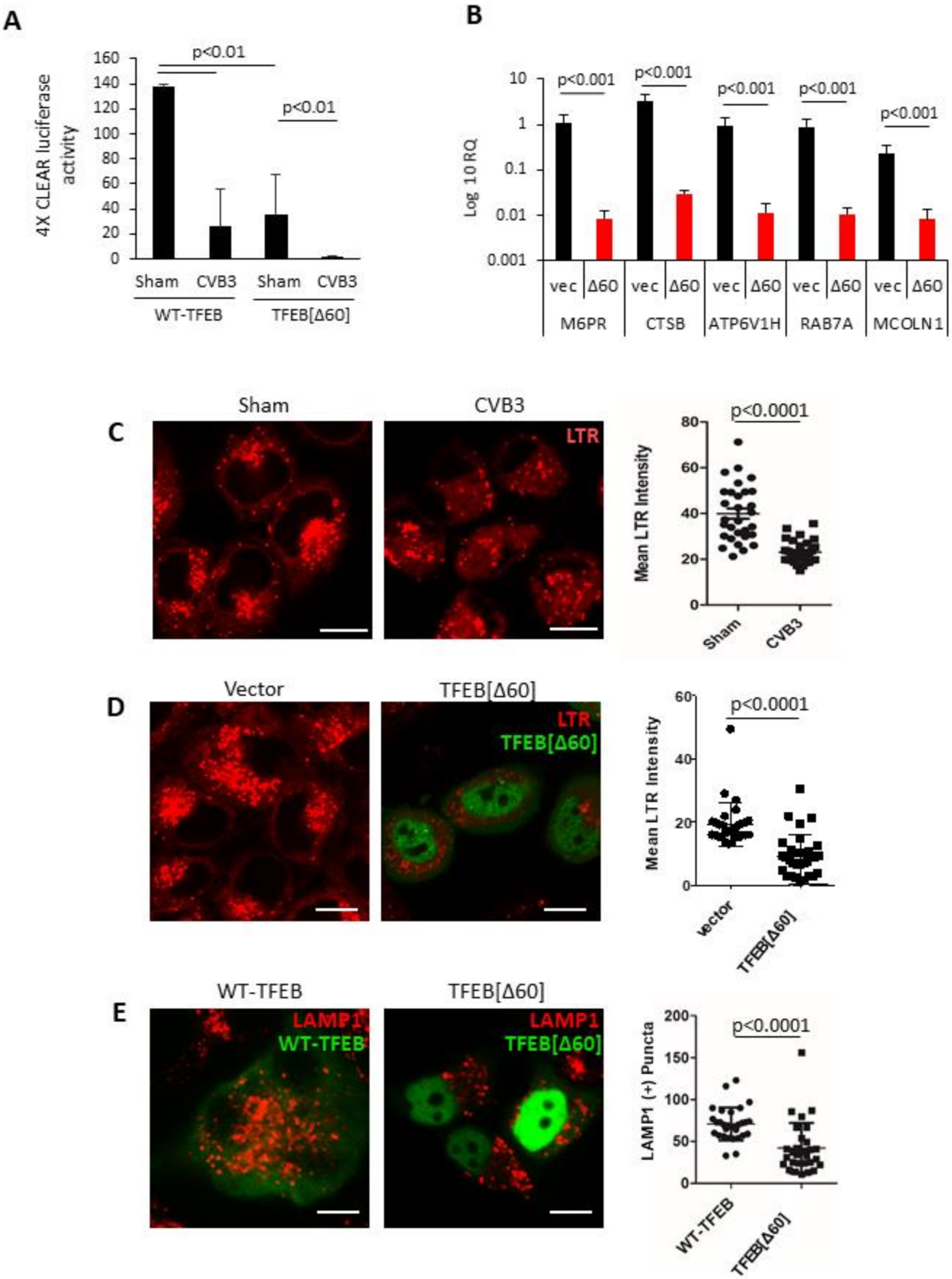
A
4X CLEAR luciferase activity
160
140
120
100
80
60
40
20
0
p<0.01
p<0.01
Sham
CVB3
Sham
CVB3
WT-TFEB
TFEB[Δ60]
B
Log 10 RQ
10
1
0.1
0.01
0.001
p<0.001
p<0.001
p<0.001
p<0.001
p<0.001
vec
Δ60
M6PR
CTSB
ATP6V1H
RAB7A
MCOLN1
C
Sham
CVB3
LTR
Mean LTR Intensity
p<0.0001
Sham
CVB3
D
Vector
TFEB[Δ60]
LTR
TFEB[Δ60]
Mean LTR Intensity
p<0.0001
vector
TFEB[Δ60]
E
WT-TFEB
TFEB[Δ60]
LAMP1
WT-TFEB
LAMP1
TFEB[Δ60]
LAMP1 (+) Puncta
p<0.0001
WT-TFEB
TFEB[Δ60]

Figure 31. TFEB [Δ60] impairs the signaling of lysosomal biogenesis.

(**A**) Transcriptional activity of WT-TFEB and TFEB [Δ60]. TFEB transcriptional activity was measured using 4×CLEAR luciferase reporter (mean ± SD, n=3) following 5 h CVB3 infection (MOI=10).

(**B**) mRNA levels of TFEB transcriptional targets following expression of TFEB [Δ60]. HeLa cells were transfected with control vector or TFEB [Δ60] for 24 h. Cellular RNA was analyzed by real-time quantitative PCR for the expression of several TFEB target genes as indicated and normalized to *ACTB* (mean ± SD, n=3).

(**C-D**) Lysotracker Red (LTR) signals following CVB3 infection (C) or expression of TFEB [Δ60]. HeLa cells were either sham or CVB3 infected (MOI=10) for 5 h (C) or transfected with control vector or TFEB [Δ60]-GFP for 24 h (D). Nuclear localized TFEB [Δ60] was visualized with GFP fluorescence (D). LTR dye was used as proxy for lysosomal pH measurement and mean LTR intensity was quantified in right panels. More than 30 cells were counted for statistical analysis. Scale bars=20 μm.

(**E**) LAMP1 signals following expression of WT-TFEB or TFEB [Δ60]. HeLa cells were transiently transfected with WT-TFEB-GFP or TFEB [Δ60]-GFP for 48 h. Cells were fixed and immunostained with anti-LAMP1 antibody. The number of LAMP1-positive structures was visualized by confocal microscopy and quantified from n=30 cells per condition and presented in the right panel. Scale bars=20 μm.

TFEB [Δ60] retains the ability to interact with CLEAR motif and MITF-family proteins

We next sought to determine the mechanism of TFEB [Δ60] functional deficiency. The transcriptional activity of WT-TFEB relies on its ability to recognize and bind the conserved CLEAR-box sequence (5'-GTCACGTGAC-3') that is present in the regulatory region of lysosomal target genes (**Figure 32A**). Electrophoretic mobility shift assay (EMSA) revealed that similar to WT-TFEB, the TFEB [Δ60] fragment retained its ability to bind the CLEAR E-box sequence (**Figure 32B & C**), consistent with a previous report in which deletion of 120 amino acids of the N-terminus did not impair DNA binding[203]. As expected, co-incubation with anti-TFEB antibody showed reduced mobility shift of the CLEAR probe (**Figure 32B & C**). In addition to nucleotide binding, TFEB transcriptional activity is dependent on hetero- or homodimerization of TFEB with members of the MITF-TFE family of transcription factors[204]. Co-immunoprecipitation studies demonstrated that TFEB [Δ60] could interact with members of the MITF/TFE family, including WT-TFEB (**Figure 32D**), MITF-A (**Figure 32E**), and TFE3 (**Figure 32F**). Collectively, these studies suggest that the functional deficiency of TFEB [Δ60] fragment is not due to impaired CLEAR E-box recognition/binding or hetero/ homodimerization with MITF/TFE transcription factors.

Non-cleavable TFEB rescues 3C-mediated disruption of TFEB

To test whether non-cleavable TFEB (QS60LP mutant) can rescue the functional deficiency of 3C-induced cleavage of TFEB, I first examined the cellular localization of $TFEB^{QS60LP}$ following CVB3 infection. Similar to WT-TFEB, non-cleavable TFEB was predominately cytoplasmic during mock infection. However, despite its resistance to cleavage, $TFEB^{QS60LP}$ was significantly trafficked to the nucleus following CVB3 infection (**Figure 33A**). Moreover, CVB3 infection resulted in the loss of the lysosomal localization of $TFEB^{QS60LP}$ (**Figure 33B**), suggesting that cleavage by viral proteinase 3C is unlikely the sole factor in regulating TFEB cellular distribution. To evaluate whether non-cleavable TFEB can rescue 3C-induced functional deficiency of TFEB, I expressed either WT- or $TFEB^{QS60LP}$ in the presence of the viral proteinase 3C in HeLa cells and found that non-cleavable TFEB was largely resistant to viral proteinase 3C-mediated disruption of TFEB transcriptional activity (**Figure 33C**).

The re-distribution of $TFEB^{QS60LP}$ to the nucleus following CVB3 infection prompted us to evaluate the mechanism of cleavage-independent trafficking of TFEB. Dephosphorylation of

TFEB by the calcium responsive phosphatase calcineurin was previously shown to regulate TFEB nuclear trafficking following lysosomal damage[184]. To investigate the potential involvement of calcineurin in CVB3-induced TFEB dephosphorylation, I infected $TFEB^{QS60LP}$ expressing cells treated with either siRNA targeting PPP3C (the catalytic subunit of calcineurin) or scrambled siRNA with CVB3. Protein expression of PPP3C was confirmed to be markedly reduced in siRNA-treated cells compared to scrambled control (**Figure 33D**). In a parallel experiment, the distribution of non-cleavable $TFEB^{QS60LP}$ was monitored following CVB3 infection. Compared to control cells, calcineurin-depleted cells had significantly reduced nuclear $TFEB^{QS60LP}$ (**Figure 33E**) and elevated phospho(p)-Ser211 (**Figure 33F**) without apparent alteration in viral replication as measured by VP1 expression (**Figure 33F**). Collectively, these results suggest that, in addition to processing TFEB, CVB3 infection also triggers a calcineurin-dependent trafficking of WT-TFEB to the nucleus.

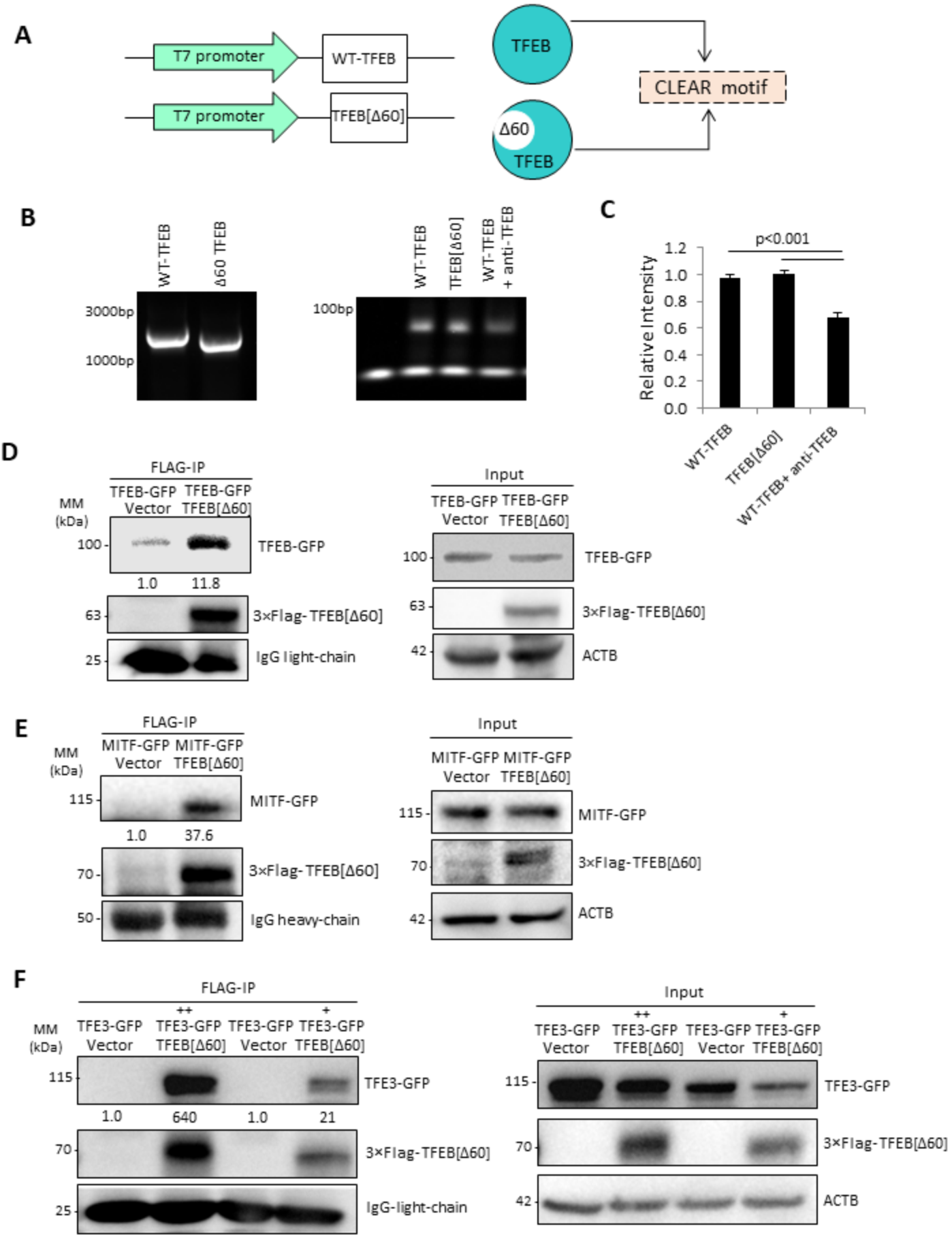
A
T7 promoter
WT-TFEB
T7 promoter
TFEB[Δ60]
TFEB
Δ60
TFEB
CLEAR motif
B
WT-TFEB
Δ60 TFEB
3000bp
1000bp
WT-TFEB
TFEB[Δ60]
WT-TFEB + anti-TFEB
100bp
C
p<0.001
Relative Intensity
1.2
1.0
0.8
0.6
0.4
0.2
0.0
WT-TFEB
TFEB[Δ60]
WT-TFEB+ anti-TFEB
D
FLAG-IP
TFEB-GFP Vector
TFEB-GFP TFEB[Δ60]
MM (kDa)
100
TFEB-GFP
1.0
11.8
63
3×Flag-TFEB[Δ60]
25
IgG light-chain
Input
TFEB-GFP Vector
TFEB-GFP TFEB[Δ60]
100
TFEB-GFP
63
3×Flag-TFEB[Δ60]
42
ACTB
E
FLAG-IP
MITF-GFP Vector
MITF-GFP TFEB[Δ60]
MM (kDa)
115
MITF-GFP
1.0
37.6
70
3×Flag-TFEB[Δ60]
50
IgG heavy-chain
Input
MITF-GFP Vector
MITF-GFP TFEB[Δ60]
115
MITF-GFP
70
3×Flag-TFEB[Δ60]
42
ACTB
F
FLAG-IP
++
+
TFE3-GFP Vector
TFE3-GFP TFEB[Δ60]
TFE3-GFP Vector
TFE3-GFP TFEB[Δ60]
MM (kDa)
115
TFE3-GFP
1.0
640
1.0
21
70
3×Flag-TFEB[Δ60]
25
IgG-light-chain
Input
++
+
TFE3-GFP Vector
TFE3-GFP TFEB[Δ60]
TFE3-GFP Vector
TFE3-GFP TFEB[Δ60]
115
TFE3-GFP
70
3×Flag-TFEB[Δ60]
42
ACTB

Figure 32. TFEB [Δ60] retains the ability to interact with CLEAR and MITF-family proteins.

(**A**) Schematic depiction of WT-TFEB and TFEB [Δ60] *in vitro* translation and EMSA assay.

(**B**) Binding of WT-TFEB and TFEB [Δ60] to TFEB consensus element. WT-TFEB and TFEB [Δ60] were PCR amplified with T7 promoter for *in vitro* transcription/translation (left). EMSA assay was performed with TFEB consensus binding element (CLEAR) in the presence of either WT-TFEB, TFEB [Δ60], or WT-TFEB supplemented with anti-TFEB antibody (1 μg).

(**C**) Quantification of EMSA assay in (B).

(**D-F**) Interaction of TFEB [Δ60] with WT-TFEB, MITF-A, and TFE3. HeLa cells were co-transfected with Flag-TFEB [Δ60] and either WT-TFEB-GFP (D), MITF-GFP (E) or TFE3-GFP (F) for 24 h. Immunoprecipitation was conducted with anti-Flag antibody coupled agarose beads, followed by western blot analysis with anti-GFP and anti-Flag antibodies. Densitometry was conducted by ImageJ to quantify the amount of WT-TFEB, MITF-A, and TFE3, normalized to level of antibody IgG light-chain. The fold changes are presented underneath the blots. Western blots of inputs for immunoprecipitation are shown in the right panels.

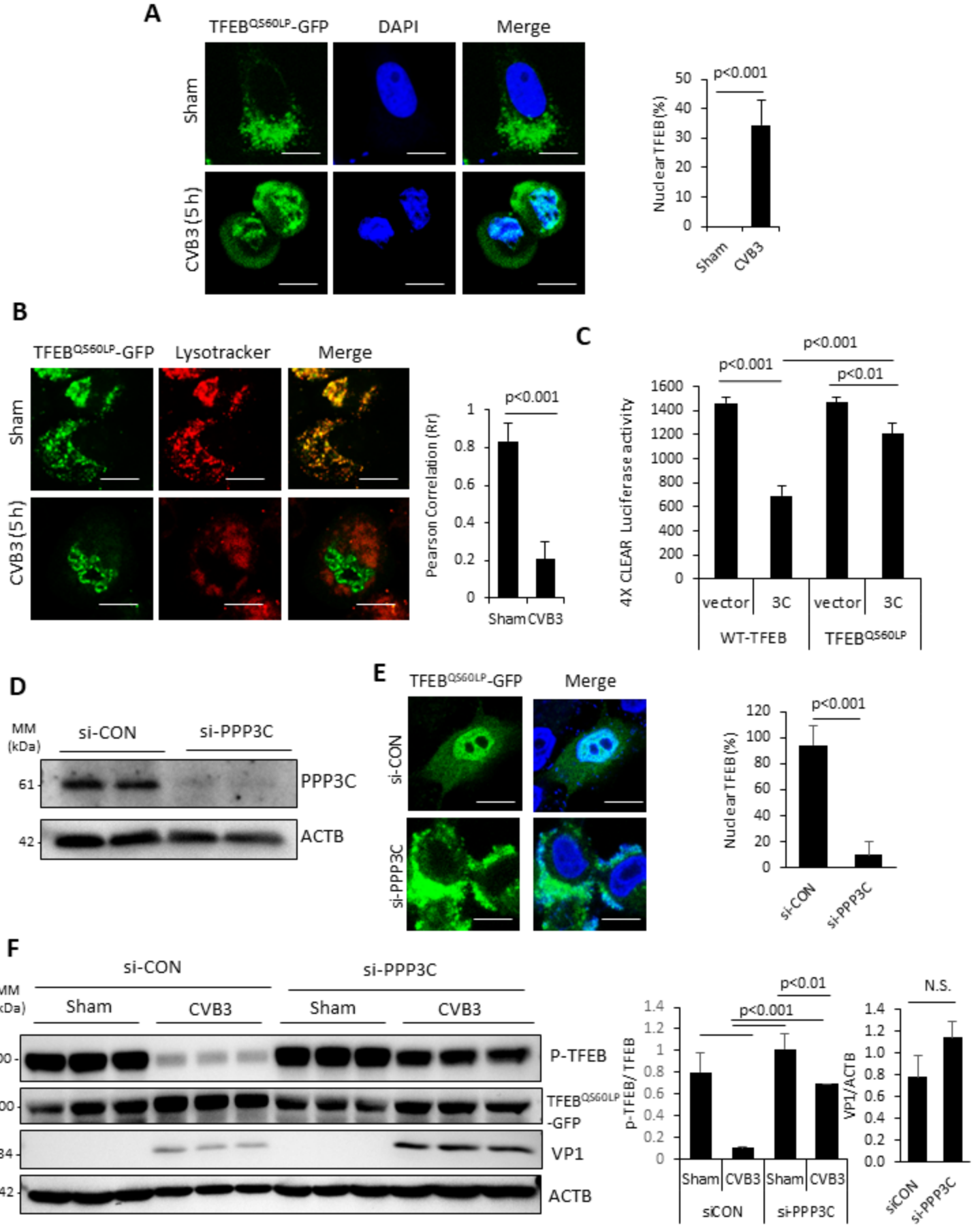
A
TFEB^QS60LP-GFP
DAPI
Merge
Sham
CVB3 (5 h)
p<0.001
Nuclear TFEB (%)
Sham
CVB3
B
TFEB^QS60LP-GFP
Lysotracker
Merge
Sham
CVB3 (5 h)
p<0.001
Pearson Correlation (Rr)
Sham
CVB3
C
p<0.001
p<0.001
p<0.01
4X CLEAR Luciferase activity
vector
3C
vector
3C
WT-TFEB
TFEB^QS60LP
D
MM (kDa)
si-CON
si-PPP3C
61
PPP3C
42
ACTB
E
TFEB^QS60LP-GFP
Merge
si-CON
si-PPP3C
p<0.001
Nuclear TFEB (%)
si-CON
si-PPP3C
F
si-CON
si-PPP3C
MM (kDa)
Sham
CVB3
Sham
CVB3
100
P-TFEB
100
TFEB^QS60LP -GFP
34
VP1
42
ACTB
p<0.01
p<0.001
p-TFEB/TFEB
Sham
CVB3
Sham
CVB3
siCON
si-PPP3C
N.S.
VP1/ACTB
siCON
si-PPP3C

Figure 33. Non-cleavable TFEB rescues 3C-mediated disruption of TFEB.

(**A**) Nuclear localization of non-cleavable TFEB. HeLa cells were transfected with $TFEB^{QS60LP}$-GFP for 24 h, followed by sham or CVB3 infection (MOI=10) for 5 h. Cells were fixed and nuclei were counterstained with DAPI. Percentage of nuclear localization of non-cleavable TFEB was quantified (right). More than 30 cells were selected for the analysis. Scale bar=20 μm.

(**B**) Lysosomal localization of non-cleavable TFEB. HeLa cells were transfected with $TFEB^{QS60LP}$-GFP for 24 h, followed by sham or CVB3 infection (MOI=10) for 5 h in medium containing lysosomal tracking dye LTR (75 nM). Lysosome-localized non-cleavable TFEB was quantified by ImageJ and presented as Pearson's correlation coefficient (right). More than 30 cells were analyzed. Scale bar=10 μm.

(**C**) Transcriptional activity of WT- and non-cleavable TFEB following WT 3C expression. HeLa cells were co-transfected with WT-TFEB or $TFEB^{QS60LP}$ and control vector or WT 3C with the addition of 4×CLEAR luciferase reporter construct. Luciferase activity was measured (mean ± SD, n=3).

(**D**) Knockdown of calcineurin/PPP3C by siRNA in HeLa cells. Cells were transfected with either control (si-CON) or PPP3C siRNA (si-PPP3C) for 48 h. Knockdown efficiency was validated by western blot analysis with anti-PPP3C antibody.

(**E**) Impairment of CVB3-induced trafficking of TFEB after gene-silencing of PPP3C. HeLa cells transfected with si-CON or si-PPP3C as above were infected with CVB3 (MOI=10) for 5 h. GFP-labeled $TFEB^{QS60LP}$ was analyzed by immunofluorescence. Nuclei were counterstained with DAPI. Nuclear TFEB was quantified in the right panel (number of analyzed cells >30). Scale bars=10 μm.

(**F**) Rescue of CVB3-induced dephosphorylation of $TFEB^{QS60LP}$ after gene-silencing of PPP3C. HeLa cells expressing $TFEB^{QS60LP}$ were treated with either si-CON or si-PPP3C for 48 h prior to CVB3 infection (MOI=10) for 5 h. Cell lysates were subjected to western blot analysis of p-TFEB (Ser211), $TFEB^{QS60LP}$-GFP, VP1 and ACTB. Densitometry was conducted to analyze the ratio of p-TFEB to TFEB and VP1/ACTB. Results (mean ± SD, n=3) are presented in the right panel.

TFEB [Δ60] enhances viral infection

EVs, such as CVB3, rely on various cellular factors for effective replication. To investigate the role of TFEB in viral infection, HeLa cells were transfected with siRNA targeting TFEB (si-TFEB) or scrambled siRNA (si-CON) for 48 h. Cells were subsequently infected with CVB3 (MOI=10) for an additional 7 h and the supernatant was collected for measurement of viral titers. Compared to control treatment, gene-silence of TFEB resulted in a significant attenuation of extracellular CVB3 titers without evident impacts on viral protein production (**Figure 34A**). To exclude the potential involvement of TFEB in viral entry, cells treated with si-CON or si-TFEB were incubated with CVB3 for 1.5 h. After thorough washes, cellular RNA was harvested and assessed for viral RNA expression. It was observed that two groups of cells had comparable post-entry viral RNA, suggesting that TFEB is dispensable for CVB3 entry (**Figure 34B**).

To further evaluate the functional consequence of TFEB cleavage in viral infection, HeLa cells were transiently transfected with constructs expressing either WT-TFEB, TFEB [Δ60], $TFEB^{QS60LP}$, or vector control for 24 h, followed by CVB3 infection (MOI=0.1) for an additional 24 h. A lower MOI and longer duration of infection was used to discern any subtle changes in viral propagation. I demonstrated that expression of TFEB [Δ60] was associated with a significant enhancement of viral titers, which appeared to be more evident than WT- and non-cleavable TFEB at this given MOI and length of viral infection (**Figure 34C**), suggesting a pro-viral function for the cleaved TFEB fragment. To assess the role of TFEB in non-lytic egress, I monitored cell membrane integrity following CVB3 infection with the amine-reactive LIVE/DEAD dye. These dyes can penetrate dead cells and fluoresce *via* laser excitation following chemical reactions with free amines (**Figure 34D**). During sham infection, the dye fluoresced on the surface of cells whereas prolonged CVB3 infection at 7 h and 9 h resulted in strong cytoplasmic signal, suggesting disrupted membrane integrity at these time-points (**Figure 34E**). Since the membrane integrity of cells was comparable between sham and 5 h infection, 5 h post-infection was selected for measurement of non-lytic egress. HeLa cells pre-treated with either control or si-TFEB for 48 h were subsequently reconstitution with WT-TFEB or TFEB [Δ60]. Following 24 h, cells were infected with CVB3 (MOI=10) for an additional 5 h and supernatants were collected for viral titer measurements. I showed that gene-silence of TFEB resulted in attenuated egress of CVB3 compared to control cells whereas expression of WT-TFEB was able to rescue this deficit (**Figure 34F**). Of note, expression of TFEB [Δ60] was associated with enhanced egress of CVB3.

Altogether, our data suggest that TFEB and TFEB [Δ60] have roles in viral egress albeit through differing mechanisms.

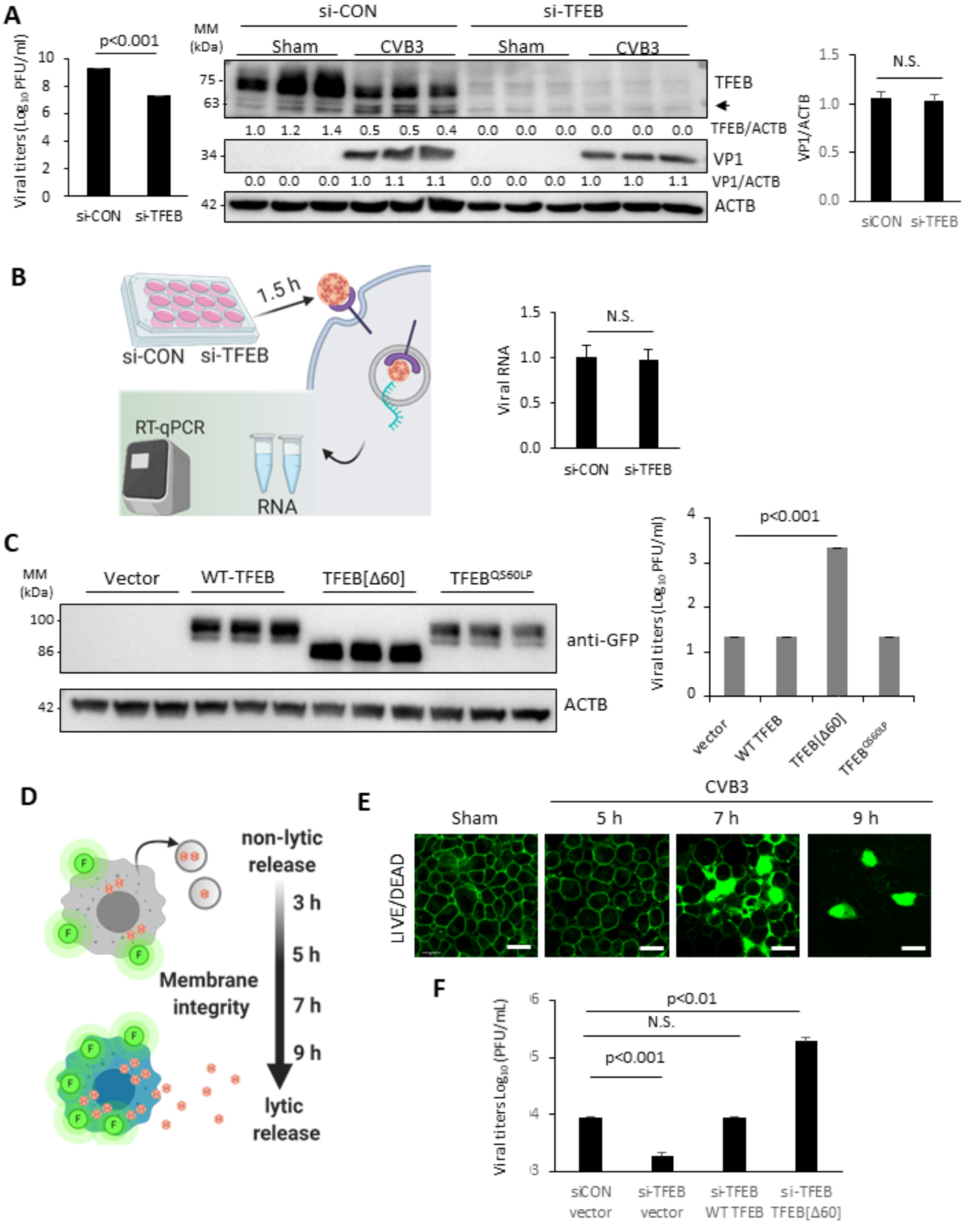
A
si-CON
si-TFEB
MM (kDa)
Sham
CVB3
Sham
CVB3
p<0.001
Viral titers (Log10 PFU/ml)
75
63
TFEB
1.0 1.2 1.4 0.5 0.5 0.4 0.0 0.0 0.0 0.0 0.0 0.0
TFEB/ACTB
34
VP1
0.0 0.0 0.0 1.0 1.1 1.1 0.0 0.0 0.0 1.0 1.0 1.1
VP1/ACTB
42
ACTB
N.S.
VP1/ACTB
siCON
si-TFEB
B
1.5 h
si-CON
si-TFEB
RT-qPCR
RNA
N.S.
Viral RNA
si-CON
si-TFEB
C
MM (kDa)
Vector
WT-TFEB
TFEB[Δ60]
TFEBQ560LP
100
86
anti-GFP
42
ACTB
p<0.001
Viral titers (Log10 PFU/ml)
vector
WT TFEB
TFEB[Δ60]
TFEBQ560LP
D
non-lytic release
3 h
5 h
7 h
9 h
Membrane integrity
lytic release
E
CVB3
Sham
5 h
7 h
9 h
LIVE/DEAD
F
p<0.01
N.S.
p<0.001
Viral titers Log10 (PFU/mL)
siCON vector
si-TFEB vector
si-TFEB WT TFEB
si-TFEB TFEB[Δ60]

Figure 34. TFEB [Δ60] enhances viral infection.

(**A**) Reduced viral titers after gene-silence of TFEB. HeLa cells were treated with si-CON or si-TFEB for 48 h, followed by CVB3 infection (MOI=10) for 7 h. Extracellular medium was harvested and viral titers were analyzed by $TCID_{50}$ (mean ± SD, n=3. left). Cell lysates were subjected to western blotting with anti-TFEB and anti-VP1 antibodies (middle). Densitometry was performed and the fold changes of TFEB and VP1 over ACTB are presented underneath the blots. VP1/ACTB is also shown in the bar plot (mean ± SD, n=3, right). Arrow denotes TFEB cleavage fragment.

(**B**) No impact on CVB3 entry after gene-silence of TFEB. HeLa cells were treated with si-CON or si-TFEB as in (A). Cells were incubated with CVB3 for 1.5 h, rinsed thrice with PBS, and subjected to RNA extraction. Viral RNA was assessed by RT-qPCR (mean ± SD, n=3).

(**C**) Enhanced CVB3 titers after overexpression of TFEB [Δ60]. HeLa cells were transfected with control vector, WT-TFEB, TFEB [Δ60], or $TFEB^{QS60LP}$ for 24 h. Cells were subsequently infected with CVB3 (MOI=0.1) for 24 h. Viral titers in the supernatant were analyzed by $TCID_{50}$ (mean ± SD, n=3). Protein expression was verified by western blotting using anti-GFP antibody.

(**D**) Schematic illustration of membrane integrity probe following CVB3 infection.

(**E**) HeLa cells were sham-infected or infected with CVB3 for the indicated time-points and stained with the LIVE/DEAD membrane integrity probe. Cells were fixed and visualized under confocal microscopy with an excitation wavelength of 580 nm. Scale bar=20 μm

(**F**) Enhanced non-lytic release after overexpression of TFEB [Δ60]. HeLa cells were transfected with si-CON or si-TFEB for 48 h, followed by reconstitution with either control vector, WT-TFEB, or TFEB [Δ60], for 24 h. Cells were subsequently infected with CVB3 for 5 h. Viral titers in the supernatant were analyzed by $TCID_{50}$ (mean ± SD, n=3) as a measure of non-lytic egress.

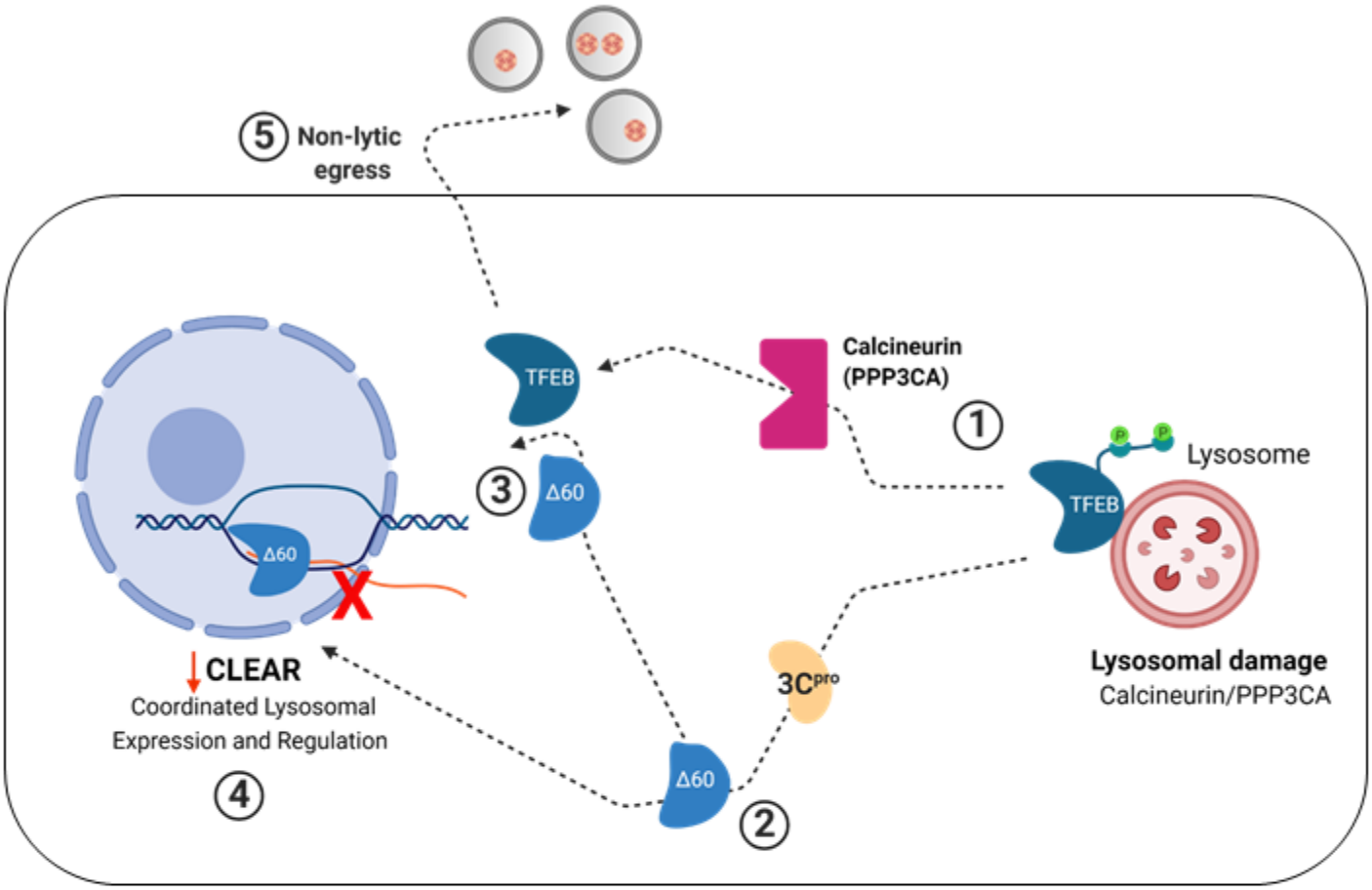

Figure 35. Proposed model of TFEB dysregulation following CVB3 infection.

(1) TFEB is dephosphorylated in a calcineurin-dependent manner following CVB3 infection. (2) TFEB is cleaved by viral proteinase 3C to generate TFEB [Δ60]. (3) TFEB [Δ60] interacts with TFEB and other members of MITF/TFE family as well as CLEAR elements. (4) TFEB [Δ60] is associated with attenuation of CLEAR network. (5) TFEB and TFEB [Δ60] play a role in non-lytic egress of CVB3.

Discussion

The subversion of cellular autophagy by EVs has become a topic of great interest ever since the first reported studies documenting the proliferation of double-membraned vesicles reminiscent of autophagosomes following EV infection[3, 205]. The normal function of autophagosomes is to enwrap cellular cargo, such as protein aggregates, damaged organelles, and invading pathogens, for clearance in lysosomes; but certain pathogens, such as EVs, have evolved strategies to evade the degradative capacity of autophagy. For example, CVB3 and EV-D68 can utilize viral proteinase 3C to target autophagic SNAREs that are required for autophagosomes-lysosome fusion for viral benefits[206, 207]. The current study identifies an additional mechanism by which EVs evade lysosomal degradation. Lysosomes are increasingly being recognized as more than a disposal chamber for cellular waste, being involved in various cellular processes from signaling and energy metabolism to secretions and membrane repair[208, 209]. I demonstrate that the viral proteinase 3C of CVB3 targets the master transcriptional regulator of lysosome biogenesis, TFEB, to impair lysosomal function and enhance viral propagation.

Following CVB3 infection, TFEB is re-distributed to the nucleus but paradoxically, gene expression of downstream targets is significantly attenuated. It was further identified that TFEB is cleaved by viral proteinase 3C at the N-terminus following Q60 to generate a fragment, designated as TFEB [Δ60]. This fragment retains the capacity to recognize and bind CLEAR-box elements as well as homo- and heterodimerize with members of the basic helix-loop-helix-leucine-zipper (bHLH-Zip) family of MITF/TFE transcription factors, but loses its function in transcriptional activation. Since TFEB [Δ60] lacks the Q-rich domain (residues 10-44), I speculate that functional deficiency in TFEB [Δ60] is related to this missing domain. Indeed, Q-rich domains are highly enriched in eukaryotic transcription factors and have been shown to modulate transcriptional activation[210]. It was reported that addition of homopolymeric stretches of the Q residues activates transcription when fused to the DNA binding domain of GAL4[211]. The precise cleavage of TFEB to eliminate its transactivation capacity while retaining its binding capabilities may be an unappreciated viral strategy to generate a dominant negative function. Additionally, the attenuation of TFEB transactivation may contribute to the downregulation of downstream CLEAR genes such as the vacuolar H+ ATPase, ATP6V1H, which acts to facilitate lysosome acidification.

Subcellular localization and activity of TFEB is controlled by its phosphorylation status at key residues such as Ser211. p-Ser211 serves as a docking site for the YWHA/14-3-3 family of

chaperones that sequester TFEB in the cytosol[187]. Phosphorylation of TFEB is mediated by MTORC1, which takes place at the lysosomal surface[212]. Our study reveals that CVB3 infection promotes the dephosphorylation of TFEB, consistent with recent findings by Alirezaei et al[213]. TFEB harbors a lysosome localization signal (LLS) within the first 30 amino acids at its N-terminus that mediates lysosomal localization of TFEB and consequent phosphorylation[187]. I therefore postulate that cleavage of TFEB after Q60 and the subsequent loss of the LLS contribute to the nuclear re-localization of TFEB observed following CVB3 infection. Interestingly, I found that, in addition to the cleavage fragment, non-cleavable TFEB is also re-localized to the nucleus following CVB3 infection, suggesting that CVB3 triggers additional mechanisms that facilitate nuclear redistribution of TFEB. Lysosomal calcium release was reported to activate the serine-threonine phosphatase calcineurin and promote the subsequent dephosphorylation of its substrate TFEB[184]. Using non-cleavable TFEB (QS60LP), I demonstrate that nuclear re-distribution of TFEB is partially mediated by calcineurin in a cleavage-independent manner. A proposed model of CVB3-induced dysregulation of TFEB and role in viral egress is summarized in **Figure 35**.

EVs have evolved to fine-tune efficient replication by differentially regulating host factors at various stages of the viral replication cycle. Certain host factors may be required during an early replicative stage but become dispensable or anti-viral during late infection[183]. In the present study, I demonstrate that gene-silencing of TFEB prior to infection leads to the attenuation of CVB3 titers, supporting recent evidence that TFEB serves as a pro-viral factor to facilitate viral replication [30] and non-lytic egress[214] at early viral infection. Interestingly, I discovered that during late stage of viral infection, TFEB is proteolytically processed and the cleavage fragment further enhances viral propagation. Our finding suggests that CVB3 has evolved to co-opt TFEB to shut-off its transcriptional activity and lysosomal repair mechanisms as a viral strategy to evade lysosomal degradation during late viral infection. The evidence of impaired transactivation by TFEB following CVB3 infection coupled with cleaved TFEB [Δ60] retaining its capacity to interact with full-length TFEB, likely supports that CVB3 may employ a two-pronged approach to incapacitate TFEB: (1) cleaved TFEB [Δ60] traffics to the nucleus to impair CLEAR network activation and/or (2) TFEB [Δ60] complexes with full-length TFEB to impair its transactivation capacity. Both outcomes result in the downregulation of lysosomal signaling that may ultimately favour CVB3 subversion of autophagy. EV proteinases are reported to target many host substrates leading to complex functional interplay within infected cells[199]. Although the current study

characterizes TFEB as a novel substrate of viral proteinase 3C, the complex interplay this event generates with other cleaved host-proteins still merits further study.

In summary, our study reveals that CVB3 directly targets TFEB for proteolytic cleavage and transcriptional inactivation, leading to impaired lysosomal function and increased viral propagation. These insights ultimately provide a better understanding of how EVs subvert cellular autophagy to promote viral pathogenesis.

Chapter 6: Closing remarks

Research summary and conclusions

Chapter 2: PI4KIIIβ is novel host factor in Coxsackievirus B3 induced non-canonical autophagy. The major findings of this chapter are:

1. CVB3 initiates autophagy independent of canonical factors
2. CVB3 cleaves several autophagy proteins, notably ULK1/2
3. PI4KIIIβ facilitates CVB3-induced autophagy

Chapter 3: CALCOCO2/NDP52 and SQSTM1/p62 differentially regulate Coxsackievirus B3 propagation. The major findings of this chapter are:

1. CALCOCO2 and SQSTM1 differentially regulate CVB3 replication
2. CALCOCO2 is cleaved by viral proteinase $3C^{pro}$ after Q139
3. CALCOCO2 modulates type I IFN through MAVS

Chapter 4: Enterovirus infection inhibits autophagic flux via disruption of the SNARE complex to enhance viral replication. The major findings of this chapter are:

1. CVB3 infection blocks autophagic flux.
2. CVB3 cleaves fusion adaptor proteins SNAP29 and PLEKHM1 through viral proteinase $3C^{pro}$.

Chapter 5: Coxsackievirus B3 targets TFEB to disrupt lysosomal function. The major findings of this chapter are:

1. CVB3 disrupts lysosomal functions
2. CVB3 cleaves TFEB through viral proteinase $3C^{pro}$
3. Cleaved TFEB[Δ60] has dominant negative effects on lysosome function

Collectively, the individual studies presented in this dissertation demonstrate that EV proteinases target multiple autophagy proteins at various stages of the autophagic pathway ultimately leading to disruption of cellular homeostasis in favour of viral pathogenesis.

Research significance

The hypothesis of this thesis is that CVB3 usurps the host autophagy pathway to promote viral propagation. In this dissertation, I outline the progress I have made in understanding the underlying mechanisms by which CVB3 disrupts cellular autophagy at multiple stages. As a small RNA virus equipped with only 11 viral proteins, CVB3 must heavily rely on its small arsenal to generate large disruptions in the infected host. In addition to processing the viral polyprotein, viral proteinases have demonstrated versatility in targeting many additional host proteins. As exemplified in this thesis, a significant advantage of viral proteinase versatility is the disruption of important cellular pathways including the host autophagy pathway. In addition to pro-viral functions, the disruption of autophagy is associated with detriments to the infected host with significant implications for human health. In particular, the significance of these findings is evident when examining the typical hallmarks of neurodegenerative and cardiovascular diseases which are characterized by loss of protein quality control and aberrant accumulation of toxic protein aggregates.

Autophagy is a cellular process that clears and recycles cellular waste including protein aggregates, damaged organelles, and invading pathogens. Although it is appreciated that CVB3 can hijack the host autophagy pathway to induce neurological and cardiovascular disorders, the underlying mechanisms remain poorly defined and novel therapeutic strategies are severely lacking. In this dissertation, I describe novel molecular insights by which CVB3 subverts cellular autophagy. In **chapter 2**, I demonstrate that CVB3 initiates autophagy independent of previously established canonical factors and identify the host factor PI4KIIIβ to be an important component of this process. In **chapter 3**, I also reveal that the process of selective autophagy is significantly compromised during EV infection in part through virus-mediated degradation of autophagy receptor proteins. Finally, I uncover in **chapters 4** that CVB3 impairs the critical step of autophagy whereby cellular waste inside autophagosome is degraded upon fusion with lysosome and in **chapter 5**, that lysosomal function in particular is compromised during infection. Collectively, these insights clarify our understanding of viral pathogenesis via the disruption of autophagy at multiple stages of the pathway including the initiation, proper recruitment of cellular waste, and appropriate clearance in disposal chambers. Ultimately the molecular targets identified in this dissertation may be useful in the development of anti-viral therapeutics to efficiently combat an emerging viral threat.

As mentioned in the introduction, autophagy can exist in multiple forms including macroautophagy, chaperone-mediated autophagy (CMA), and microautophagy. Much of the knowledge that exists in the literature and in the current thesis regarding enteroviral subversion of autophagy is limited to macroautophagy. There is a lack of appreciation and understanding of the underlying role of CMA and microautophagy in enteroviral propagation and pathogenesis. The findings from this dissertation clearly outline the mechanisms of enteroviral subversion of macroautophagy as much of the existing literature and understanding of autophagy pertains to this pathway. Additionally, chapters 2-4 demonstrate how EVs target autophagosomes specifically to disrupt initiation, sequestration, and fusion processes. Given that other forms of autophagy, particularly CMA and microautophagy rely directly on lysosome organelles, these forms of autophagy may be more enticing as therapeutic targets. Recent evidence from this dissertation (chapter 5) suggests that EVs can subvert lysosome function but consequences of EV infection on other forms of autophagy such as CMA and microautophagy require further investigation. Maintaining the integrity and function of lysosomes can serve as a potent anti-enteroviral strategy to bypasses the subversion of macroautophagy in favour of CMA and microautophagy signaling.

Similar to other RNA viruses, EVs usurp intracellular lipid surfaces to enhance viral replication and propagation. The early replicative stages in particular are characterized by viral replication organelle assembly (e.g. RNA-dependent RNA polymerases/ $3D^{pol}$) on topological lipid surfaces that help to orient and orchestrate viral genome expansion. It is widely appreciated that diverse RNA viruses including EVs, coronaviruses, noroviruses, and hepaciviruses generate viral-induced double membrane vesicles (DMV) in infected cells [215]. These replication organelles not only resemble autophagosomes in structure but also share molecular markers. The origin and biological significance of these structures has been a topic of keen interest to virologist and autophagy enthusiasts alike and continues to promise exciting therapeutic avenues for a diverse array of viral pathogens. Emerging research in this field is revealing DMVs as potential conduits for enhanced and concentrated viral dissemination [216] as well as defensive shields against host neutralizing antibodies [217]. Leveraging biotechnological advances may one day provide an opportunity to closely investigate potent and evasive populations of quasi-enveloped virus that uniquely hijack cellular membranes. Additionally, mechanistic understanding of how diverse

viruses acquire quasi-envelopes and the precise nature by which such membranes aid in viral migration across susceptible tissues promises to provide novel insights into viral pathogenesis.

Viruses have emerged as important environmental factors in the initiation and progression of neurological diseases such as amyotrophic lateral sclerosis (ALS) [218]. EVs such as poliovirus have long been suspected as etiological agents for ALS due to the identification of viral RNA signatures in the diseased tissue of ALS patients [7]. Recent experimental findings in murine models also support that EV infection can recapitulate the hallmark molecular phenotypes of ALS such as TDP-43 pathology and disrupted autophagy [219, 220]. Additionally, in vitro studies have recapitulated the role of EV proteinases in TDP-43 pathology [221]. Collectively, these studies point to a disease mechanism by which EV infection can trigger ALS pathogenesis and highlight the importance of studying viral infections outside of the typical infectious disease setting. Given that disrupted autophagy is a typical hallmark of neurodegenerative diseases [222], investigating the underlying mechanisms of autophagy disruption are paramount for future therapeutics. The current dissertation provides novel molecular insights by which pathogenic viruses such as CVB3 can disrupt autophagy. Targeting autophagy may serve as a novel therapeutic strategy to combat neurological diseases such as ALS for which no cure currently exists.

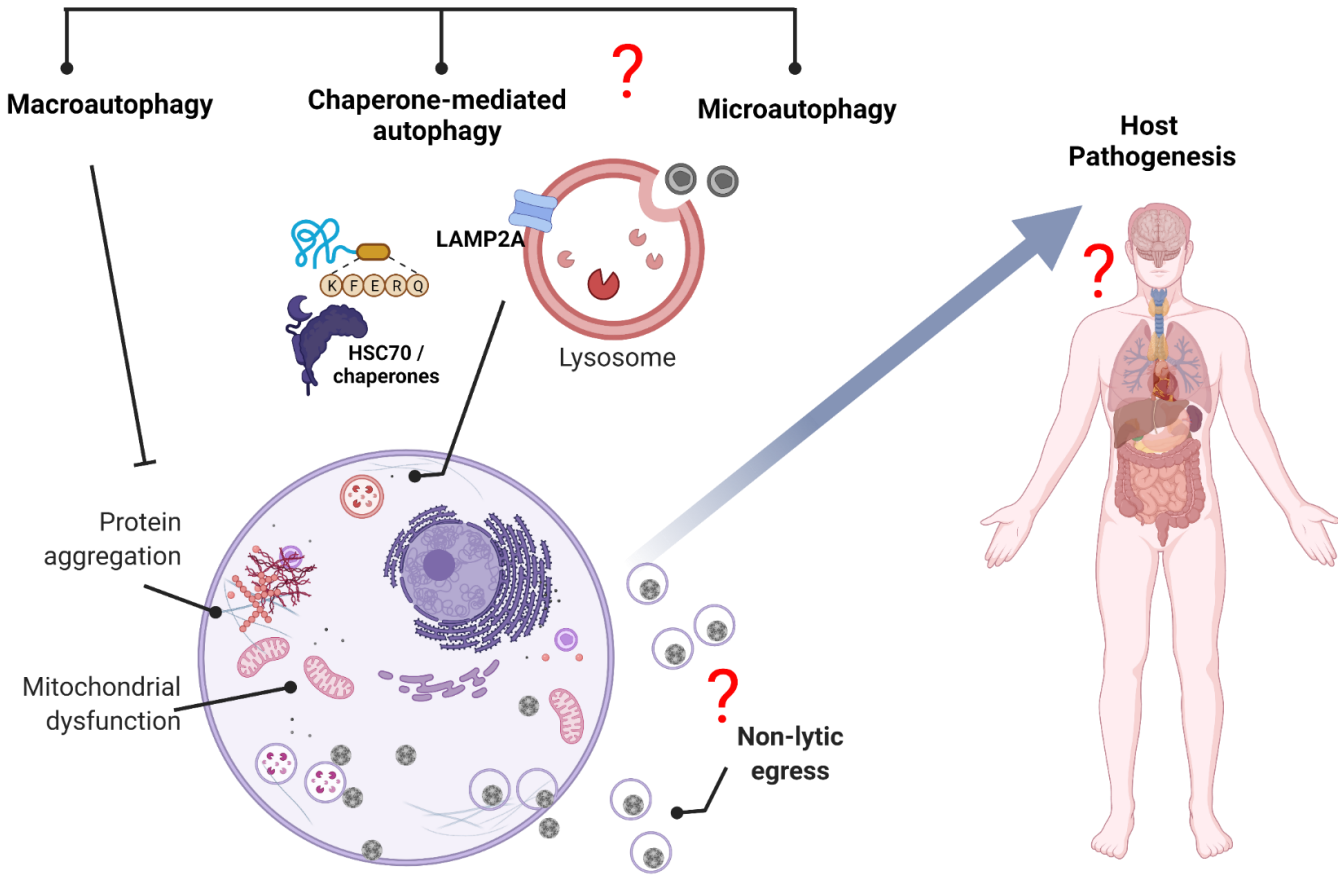

Figure 36. Remaining questions in EV subversion of autophagy. EV subversion of autophagy has primarily focused on the role of macroautophagy. Questions remain as to whether EV subverts other forms of autophagy including chaperone-mediated autophagy or microautophagy that bypass the requirement for autophagosomes in favour of direct lysosome mediated degradation. Additionally, understanding the mechanisms by which EVs subvert autophagy to facilitate non-lytic egress and precisely how these quasi-enveloped viruses facilitate host pathogenesis is a topic that warrants continued research effort.

Limitations and future direction

A major strength of the work presented in this thesis is the knowledge and insight gained by focusing on particular host proteins that are essential for cellular autophagy. Although this approach provides deeper molecular insights by dissecting the unique interactions of individual proteins during viral infection, it fails to fully grasp the complexity of viral pathogenesis. Challenges in capturing the complexity of viral pathogenesis are largely due to limitations in the simultaneous assessment of multiple viral targets, the appropriate considerations of temporal significance, and the differential susceptibilities and disruptions to unique biological tissues.

Ongoing advances in EV research continue to identify novel host proteins that are targets of viral proteinases. In an effort to address the complexity of viral pathogenesis, recent biotechnical advances have developed novel strategies to identify and study viral substrates on a global scale [171, 198, 223]. Techniques such as terminal amine isotopic labeling of substrates (TAILS) are proteomic-based approaches that allow for the simultaneous assessment of many substrates. One added benefit to utilizing TAILS is the ability to identify unique virally-induced cleavage fragments but this approach still requires researchers to experimentally validate the biological significance of individual fragments. As the technology continues to improve, future studies would benefit from investigating the proteomic signatures of virus-infected tissues. This *in vivo* approach may identify unique signatures across different organs/tissues that may be therapeutically targeted.

A second limitation in the field is the continuing challenges to better understand the temporal significance of identified cleavage events. It is appreciated that viral proteinases may target unique substrates at distinct stages of the viral life cycle and the significance of early, middle, and/or late cleavage events is only recently being appreciated. Recent advances in this area are beginning to address the temporal nature of host protein targeting[224]. These studies may shed additional light on the temporal significance of viral events and the special role this plays in the process of viral pathogenesis. For e.g., EVs routinely target certain host factors such as nucleoporin 98 (NUP98) and eukaryotic translation initiation factor 4G (EIF4G) at early stages of viral replication and these events have been proposed to facilitate enhanced viral replication by redirecting host cellular resources towards viral production. Additionally, viruses may utilize certain substrates for early pro-viral replication while dispensing such factors during late stages [225]. Understanding which factors are critical during the early stages of viral replication may instruct future therapeutic efforts to limit viral pathogenesis and preserve tissue function.

Lastly, a major limitation in our understanding of EV-induced pathogenesis particularly via disruptions of the host autophagy pathway is the relative contributions of differing viral tropism and susceptibilities of diverse tissues. In living organisms, terminally differentiated organs such as heart, pancreas, and brain are particularly susceptible to the damages of EV infection. Understanding the role of autophagy in viral pathogenesis needs to acknowledge the complex architecture of these organ systems and the presence of biologically diverse cell types. Recent findings suggest that cell-type specific autophagy may play an important role in disease progression[226]. Whether specific cell types with differing autophagy phenotypes are differentially susceptible to viral subversion requires further investigation.

Bibliography

1. Shi JY, Luo HL. Interplay between the cellular autophagy machinery and positive-stranded RNA viruses. *Acta Bioch Bioph Sin* 2012, **44**(5)**:** 375-384.

2. Harnett MM, Pineda MA, de Late PL, Eason RJ, Besteiro S, Harnett W, *et al.* From Christian de Duve to Yoshinori Ohsumi: More to autophagy than just dining at home. *Biomed J* 2017, **40**(1)**:** 9-22.

3. Dales S, Eggers HJ, Tamm I, Palade GE. Electron Microscopic Study of the Formation of Poliovirus. *Virology* 1965, **26:** 379-389.

4. Baggen J, Thibaut HJ, Strating J, van Kuppeveld FJM. The life cycle of non-polio enteroviruses and how to target it. *Nat Rev Microbiol* 2018, **16**(6)**:** 368-381.

5. Anastasina M, Domanska A, Palm K, Butcher S. Human picornaviruses associated with neurological diseases and their neutralization by antibodies. *J Gen Virol* 2017, **98**(6)**:** 1145-1158.

6. Huang HI, Shih SR. Neurotropic enterovirus infections in the central nervous system. *Viruses* 2015, **7**(11)**:** 6051-6066.

7. Xue YC, Feuer R, Cashman N, Luo H. Enteroviral infection: the forgotten link to amyotrophic lateral sclerosis? *Front Mol Neurosci* 2018, **11:** 63.

8. Fung G, Luo H, Qiu Y, Yang D, McManus B. Myocarditis. *Circulation research* 2016, **118**(3)**:** 496-514.

9. Yeung WCG, Rawlinson WD, Craig ME. Enterovirus infection and type 1 diabetes mellitus: systematic review and meta-analysis of observational molecular studies. *Brit Med J* 2011, **342**.

10. Sean P, Semler BL. Coxsackievirus B RNA replication: lessons from poliovirus. *Curr Top Microbiol Immunol* 2008, **323:** 89-121.

11. Altan-Bonnet N. Lipid tales of viral replication and transmission. *Trends Cell Biol* 2017, **27**(3)**:** 201-213.

12. Miller S, Krijnse-Locker J. Modification of intracellular membrane structures for virus replication. *Nat Rev Microbiol* 2008, **6**(5)**:** 363-374.

13. Yin J, Liu Y, Wimmer E, Paul AV. Complete protein linkage map between the P2 and P3 non-structural proteins of poliovirus. *J Gen Virol* 2007, **88**(Pt 8)**:** 2259-2267.

14. Bird SW, Maynard ND, Covert MW, Kirkegaard K. Nonlytic viral spread enhanced by autophagy components. *Proc Natl Acad Sci U S A* 2014, **111**(36)**:** 13081-13086.

15. Chen YH, Du W, Hagemeijer MC, Takvorian PM, Pau C, Cali A, *et al.* Phosphatidylserine vesicles enable efficient en bloc transmission of enteroviruses. *Cell* 2015, **160**(4)**:** 619-630.

16. Feng Z, Hensley L, McKnight KL, Hu F, Madden V, Ping L, *et al.* A pathogenic picornavirus acquires an envelope by hijacking cellular membranes. *Nature* 2013, **496**(7445)**:** 367-371.

17. Robinson SM, Tsueng G, Sin J, Mangale V, Rahawi S, McIntyre LL, *et al.* Coxsackievirus B exits the host cell in shed microvesicles displaying autophagosomal markers. *Plos Pathog* 2014, **10**(4)**:** e1004045.

18. Tang JW, Holmes CW. Acute and chronic disease caused by enteroviruses. *Virulence* 2017, **8**(7)**:** 1062-1065.

19. Filippi CM, von Herrath MG. Viral Trigger for Type 1 Diabetes Pros and Cons. *Diabetes* 2008, **57**(11)**:** 2863-2871.

20. Abzug MJ, Keyserling HL, Lee ML, Levin MJ, Rotbart HA. Neonatal Enterovirus Infection - Virology, Serology, and Effects of Intravenous Immune Globulin. *Clin Infect Dis* 1995, **20**(5)**:** 1201-1206.

21. Hayden FG, Turner RB, Gwaltney JM, Chi-Burris K, Gersten M, Hsyu P, *et al*. Phase II, randomized, double-blind, placebo-controlled studies of ruprintrivir nasal spray 2-percent suspension for prevention and treatment of experimentally induced rhinovirus colds in healthy volunteers. *Antimicrob Agents Ch* 2003, **47**(12)**:** 3907-3916.

22. Choi AM, Ryter SW, Levine B. Autophagy in human health and disease. *N Engl J Med* 2013, **368**(19)**:** 1845-1846.

23. Galluzzi L, Baehrecke EH, Ballabio A, Boya P, Bravo-San Pedro JM, Cecconi F, *et al.* Molecular definitions of autophagy and related processes. *Embo J* 2017, **36**(13)**:** 1811-1836.

24. Levine B, Kroemer G. Autophagy in the pathogenesis of disease. *Cell* 2008, **132**(1)**:** 27-42.

25. Yla-Anttila P, Vihinen H, Jokita E, Eskelinen EL. 3D tomography reveals connections between the phagophore and endoplasmic reticulum. *Autophagy* 2009, **5**(8)**:** 1180-1185.

26. Hailey DW, Rambold AS, Satpute-Krishnan P, Mitra K, Sougrat R, Kim PK, *et al.* Mitochondria supply membranes for autophagosome biogenesis during starvation. *Cell* 2010, **141**(4)**:** 656-667.

27. Hamasaki M, Furuta N, Matsuda A, Nezu A, Yamamoto A, Fujita N, *et al.* Autophagosomes form at ER-mitochondria contact sites. *Nature* 2013, **495**(7441)**:** 389-393.

28. Ge L, Schekman R. The ER-Golgi intermediate compartment feeds the phagophore membrane. *Autophagy* 2014, **10**(1)**:** 170-172.

29. Pavel M, Rubinsztein DC. Mammalian autophagy and the plasma membrane. *FEBS J* 2017, **284**(5)**:** 672-679.

30. Wong PM, Puente C, Ganley IG, Jiang X. The ULK1 complex: sensing nutrient signals for autophagy activation. *Autophagy* 2013, **9**(2)**:** 124-137.

31. Zachari M, Ganley IG. The mammalian ULK1 complex and autophagy initiation. *Essays Biochem* 2017, **61**(6)**:** 585-596.

32. Nakamura S, Yoshimori T. New insights into autophagosome-lysosome fusion. *J Cell Sci* 2017, **130**(7)**:** 1209-1216.

33. Itakura E, Kishi-Itakura C, Mizushima N. The hairpin-type tail-anchored SNARE syntaxin 17 targets to autophagosomes for fusion with endosomes/lysosomes. *Cell* 2012, **151**(6)**:** 1256-1269.

34. Itakura E, Mizushima N. Syntaxin 17: the autophagosomal SNARE. *Autophagy* 2013, **9**(6)**:** 917-919.

35. Diao J, Liu R, Rong Y, Zhao M, Zhang J, Lai Y, *et al.* ATG14 promotes membrane tethering and fusion of autophagosomes to endolysosomes. *Nature* 2015, **520**(7548)**:** 563-566.

36. Jiang P, Nishimura T, Sakamaki Y, Itakura E, Hatta T, Natsume T, *et al.* The HOPS complex mediates autophagosome-lysosome fusion through interaction with syntaxin 17. *Mol Biol Cell* 2014, **25**(8)**:** 1327-1337.

37. McEwan DG, Popovic D, Gubas A, Terawaki S, Suzuki H, Stadel D, *et al.* PLEKHM1 regulates autophagosome-lysosome fusion through HOPS complex and LC3/GABARAP proteins. *Mol Cell* 2015, **57**(1)**:** 39-54.

38. Corona AK, Jackson WT. Finding the Middle Ground for Autophagic Fusion Requirements. *Trends Cell Biol* 2018.

39. Johansen T, Lamark T. Selective autophagy mediated by autophagic adapter proteins. *Autophagy* 2011, **7**(3)**:** 279-296.

40. Komatsu M, Ichimura Y. Selective autophagy regulates various cellular functions. *Genes Cells* 2010, **15**(9)**:** 923-933.

41. Birgisdottir AB, Lamark T, Johansen T. The LIR motif - crucial for selective autophagy. *J Cell Sci* 2013, **126**(15)**:** 3237-3247.

42. Kraft C, Peter M, Hofmann K. Selective autophagy: ubiquitin-mediated recognition and beyond. *Nat Cell Biol* 2010, **12**(9)**:** 836-841.

43. Deretic V, Levine B. Autophagy balances inflammation in innate immunity. *Autophagy* 2018, **14**(2)**:** 243-251.

44. Deretic V, Saitoh T, Akira S. Autophagy in infection, inflammation and immunity. *Nat Rev Immunol* 2013, **13**(10)**:** 722-737.

45. Crotzer VL, Blum JS. Autophagy and its Role in MHC-Mediated Antigen Presentation. *J Immunol* 2009, **182**(6)**:** 3335-3341.

46. Jackson WT. Viruses and the autophagy pathway. *Virology* 2015, **479-480:** 450-456.

47. Shi XD, Chen ZJ, Tang SJ, Wu F, Xiong SD, Dong CS. Coxsackievirus B3 infection induces autophagic flux, and autophagosomes are critical for efficient viral replication. *Archives of Virology* 2016, **161**(8)**:** 2197-2205.

48. Mendelsohn CL, Wimmer E, Racaniello VR. Cellular receptor for poliovirus: molecular cloning, nucleotide sequence, and expression of a new member of the immunoglobulin superfamily. *Cell* 1989, **56**(5)**:** 855-865.

49. Greve JM, Davis G, Meyer AM, Forte CP, Yost SC, Marlor CW, *et al.* The major human rhinovirus receptor is ICAM-1. *Cell* 1989, **56**(5)**:** 839-847.

50. Bergelson JM, Cunningham JA, Droguett G, Kurt-Jones EA, Krithivas A, Hong JS, *et al.* Isolation of a common receptor for Coxsackie B viruses and adenoviruses 2 and 5. *Science* 1997, **275**(5304)**:** 1320-1323.

51. Bergelson JM, Mohanty JG, Crowell RL, St John NF, Lublin DM, Finberg RW. Coxsackievirus B3 adapted to growth in RD cells binds to decay-accelerating factor (CD55). *J Virol* 1995, **69**(3)**:** 1903-1906.

52. Baggen J, Thibaut HJ, Staring J, Jae LT, Liu Y, Guo H, *et al.* Enterovirus D68 receptor requirements unveiled by haploid genetics. *Proc Natl Acad Sci U S A* 2016, **113**(5)**:** 1399-1404.

53. Staring J, van den Hengel LG, Raaben M, Blomen VA, Carette JE, Brummelkamp TR. KREMEN1 is a host entry receptor for a major group of enteroviruses. *Cell Host Microbe* 2018, **23**(5)**:** 636-643 e635.

54. Bergelson JM, Coyne CB. Picornavirus Entry. *Viral Entry into Host Cells* 2013, **790:** 24-41.

55. Kim C, Bergelson JM. Echovirus 7 entry into polarized intestinal epithelial cells requires clathrin and Rab7. *MBio* 2012, **3**(2).

56. Hyttinen JM, Niittykoski M, Salminen A, Kaarniranta K. Maturation of autophagosomes and endosomes: a key role for Rab7. *Biochim Biophys Acta* 2013, **1833**(3)**:** 503-510.

57. McKnight NC, Zhong Y, Wold MS, Gong S, Phillips GR, Dou Z, *et al.* Beclin 1 is required for neuron viability and regulates endosome pathways via the UVRAG-VPS34 complex. *PLoS Genet* 2014, **10**(10)**:** e1004626.

58. Murrow L, Malhotra R, Debnath J. ATG12-ATG3 interacts with Alix to promote basal autophagic flux and late endosome function. *Nat Cell Biol* 2015, **17**(3)**:** 300-310.

59. Guo H, Chitiprolu M, Roncevic L, Javalet C, Hemming FJ, Trung MT, *et al.* Atg5 Disassociates the V1V0-ATPase to Promote Exosome Production and Tumor Metastasis Independent of Canonical Macroautophagy. *Dev Cell* 2017, **43**(6)**:** 716-730 e717.

60. Kim C, Bergelson JM. Echovirus 7 entry into polarized caco-2 intestinal epithelial cells involves core components of the autophagy machinery. *J Virol* 2014, **88**(1)**:** 434-443.

61. Patel KP, Coyne CB, Bergelson JM. Dynamin- and Lipid Raft-Dependent Entry of Decay-Accelerating Factor (DAF)-Binding and Non-DAF-Binding Coxsackieviruses into Nonpolarized Cells. *J Virol* 2009, **83**(21)**:** 11064-11077.

62. Staring J, von Castelmur E, Blomen VA, van den Hengel LG, Brockmann M, Baggen J, *et al.* PLA2G16 represents a switch between entry and clearance of Picornaviridae. *Nature* 2017, **541**(7637)**:** 412-416.

63. Hsu NY, Ilnytska O, Belov G, Santiana M, Chen YH, Takvorian PM, *et al.* Viral reorganization of the secretory pathway generates distinct organelles for RNA replication. *Cell* 2010, **141**(5)**:** 799-811.

64. Ilnytska O, Santiana M, Hsu NY, Du WL, Chen YH, Viktorova EG, *et al.* Enteroviruses harness the cellular endocytic machinery to remodel the host cell cholesterol landscape for effective viral replication. *Cell Host Microbe* 2013, **14**(3)**:** 281-293.

65. Roulin PS, Lotzerich M, Torta F, Tanner LB, van Kuppeveld FJ, Wenk MR, *et al.* Rhinovirus uses a phosphatidylinositol 4-phosphate/cholesterol counter-current for the formation of replication compartments at the ER-Golgi interface. *Cell Host Microbe* 2014, **16**(5)**:** 677-690.

66. Jackson WT, Giddings TH, Taylor MP, Mulinyawe S, Rabinovitch M, Kopito RR, *et al.* Subversion of cellular autophagosomal machinery by RNA viruses. *Plos Biology* 2005, **3**(5)**:** 861-871.

67. Kemball CC, Alirezaei M, Flynn CT, Wood MR, Harkins S, Kiosses WB, *et al.* Coxsackievirus infection induces autophagy-like vesicles and megaphagosomes in pancreatic acinar cells in vivo. *J Virol* 2010, **84**(23)**:** 12110-12124.

68. Wong J, Zhang J, Si X, Gao G, Mao I, McManus BM, *et al.* Autophagosome supports coxsackievirus B3 replication in host cells. *J Virol* 2008, **82**(18)**:** 9143-9153.

69. Yoon SY, Ha YE, Choi JE, Ahn J, Lee H, Kweon HS, *et al.* Coxsackievirus B4 uses autophagy for replication after calpain activation in rat primary neurons. *J Virol* 2008, **82**(23)**:** 11976-11978.

70. Shi Y, He X, Zhu G, Tu H, Liu Z, Li W, *et al.* Coxsackievirus A16 elicits incomplete autophagy involving the mTOR and ERK pathways. *Plos One* 2015, **10**(4)**:** e0122109.

71. Fu Y, Xu W, Chen D, Feng C, Zhang L, Wang X, *et al.* Enterovirus 71 induces autophagy by regulating has-miR-30a expression to promote viral replication. *Antiviral Res* 2015, **124:** 43-53.

72. Huang SC, Chang CL, Wang PS, Tsai Y, Liu HS. Enterovirus 71-induced autophagy detected in vitro and in vivo promotes viral replication. *J Med Virol* 2009, **81**(7)**:** 1241-1252.

73. Corona AK, Saulsbery HM, Corona Velazquez AF, Jackson WT. Enteroviruses Remodel Autophagic Trafficking through Regulation of Host SNARE Proteins to Promote Virus Replication and Cell Exit. *Cell Rep* 2018, **22**(12)**:** 3304-3314.

74. Klein KA, Jackson WT. Human rhinovirus 2 induces the autophagic pathway and replicates more efficiently in autophagic cells. *J Virol* 2011, **85**(18)**:** 9651-9654.

75. Alirezaei M, Flynn CT, Wood MR, Whitton JL. Pancreatic acinar cell-specific autophagy disruption reduces coxsackievirus replication and pathogenesis in vivo. *Cell Host Microbe* 2012, **11**(3)**:** 298-305.

76. Delorme-Axford E, Morosky S, Bomberger J, Stolz DB, Jackson WT, Coyne CB. BPIFB3 Regulates Autophagy and Coxsackievirus B Replication through a Noncanonical Pathway Independent of the Core Initiation Machinery. *Mbio* 2014, **5**(6).

77. Tabor-Godwin JM, Tsueng G, Sayen MR, Gottlieb RA, Feuer R. The role of autophagy during coxsackievirus infection of neural progenitor and stem cells. *Autophagy* 2012, **8**(6)**:** 938-953.

78. Richards AL, Soares-Martins JA, Riddell GT, Jackson WT. Generation of unique poliovirus RNA replication organelles. *MBio* 2014, **5**(2)**:** e00833-00813.

79. Belov GA, Nair V, Hansen BT, Hoyt FH, Fischer ER, Ehrenfeld E. Complex dynamic development of poliovirus membranous replication complexes. *J Virol* 2012, **86**(1)**:** 302-312.

80. Wang H, Sun HQ, Zhu X, Zhang L, Albanesi J, Levine B, *et al.* GABARAPs regulate PI4P-dependent autophagosome:lysosome fusion. *Proc Natl Acad Sci U S A* 2015, **112**(22)**:** 7015-7020.

81. Bestebroer J, V'Kovski P, Mauthe M, Reggiori F. Hidden behind autophagy: the unconventional roles of ATG proteins. *Traffic* 2013, **14**(10)**:** 1029-1041.

82. Subramani S, Malhotra V. Non-autophagic roles of autophagy-related proteins. *EMBO Rep* 2013, **14**(2)**:** 143-151.

83. Alirezaei M, Flynn CT, Wood MR, Harkins S, Whitton JL. Coxsackievirus can exploit LC3 in both autophagy-dependent and -independent manners in vivo. *Autophagy* 2015, **11**(8)**:** 1389-1407.

84. Mauthe M, Langereis M, Jung J, Zhou X, Jones A, Omta W, *et al.* An siRNA screen for ATG protein depletion reveals the extent of the unconventional functions of the autophagy proteome in virus replication. *J Cell Biol* 2016, **214**(5)**:** 619-635.

85. Corona Velazquez A, Corona AK, Klein KA, Jackson WT. Poliovirus induces autophagic signaling independent of the ULK1 complex. *Autophagy* 2018**:** 1-14.

86. Suhy DA, Giddings TH, Kirkegaard K. Remodeling the endoplasmic reticulum by poliovirus infection and by individual viral proteins: an autophagy-like origin for virus-induced vesicles. *J Virol* 2000, **74**(19)**:** 8953-8965.

87. Taylor MP, Kirkegaard K. Modification of cellular autophagy protein LC3 by poliovirus. *J Virol* 2007, **81**(22)**:** 12543-12553.

88. Wang J, Ptacek JB, Kirkegaard K, Bullitt E. Double-membraned liposomes sculpted by poliovirus 3AB protein. *J Biol Chem* 2013, **288**(38)**:** 27287-27298.

89. Wu H, Zhai X, Chen Y, Wang R, Lin L, Chen S, *et al*. Protein 2B of coxsackievirus B3 induces autophagy relying on Its transmembrane hydrophobic sequences. *Viruses* 2016, **8**(5).

90. Bjorkoy G, Lamark T, Pankiv S, Overvatn A, Brech A, Johansen T. Monitoring autophagic degradation of p62/SQSTM1. *Methods Enzymol* 2009, **452:** 181-197.

91. Richards AL, Jackson WT. Intracellular vesicle acidification promotes maturation of infectious poliovirus particles. *Plos Pathog* 2012, **8**(11)**:** e1003046.

92. Shi J, Wong J, Piesik P, Fung G, Zhang J, Jagdeo J, *et al.* Cleavage of sequestosome 1/p62 by an enteroviral protease results in disrupted selective autophagy and impaired NFKB signaling. *Autophagy* 2013, **9**(10)**:** 1591-1603.

93. Mutsafi Y, Altan-Bonnet N. Enterovirus transmission by secretory autophagy. *Viruses* 2018, **10**(3).

94. Taylor MP, Burgon TB, Kirkegaard K, Jackson WT. Role of microtubules in extracellular release of poliovirus. *J Virol* 2009, **83**(13)**:** 6599-6609.

95. Ponpuak M, Mandell MA, Kimura T, Chauhan S, Cleyrat C, Deretic V. Secretory autophagy. *Curr Opin Cell Biol* 2015, **35:** 106-116.

96. Sin J, McIntyre L, Stotland A, Feuer R, Gottlieb RA. Coxsackievirus B Escapes the Infected Cell in Ejected Mitophagosomes. *J Virol* 2017, **91**(24).

97. Too IH, Yeo H, Sessions OM, Yan B, Libau EA, Howe JL, *et al.* Enterovirus 71 infection of motor neuron-like NSC-34 cells undergoes a non-lytic exit pathway. *Scientific reports* 2016, **6:** 36983.

98. Corona AK, Mohamud Y, Jackson WT, Luo H. Oh, SNAP! How enteroviruses redirect autophagic traffic away from degradation. *Autophagy* 2018, **14**(8)**:** 1469-1471.

99. Mohamud Y, Shi JY, Qu JY, Poon T, Xue YC, Deng HY, *et al.* Enteroviral Infection Inhibits Autophagic Flux via Disruption of the SNARE Complex to Enhance Viral Replication. *Cell Rep* 2018, **22**(12)**:** 3292-3303.

100. Han J, Pluhackova K, Bockmann RA. The multifaceted role of SNARE proteins in membrane fusion. *Front Physiol* 2017, **8:** 5.

101. Ma Y, Galluzzi L, Zitvogel L, Kroemer G. Autophagy and cellular immune responses. *Immunity* 2013, **39**(2)**:** 211-227.

102. Dong X, Levine B. Autophagy and viruses: adversaries or allies? *J Innate Immun* 2013, **5**(5)**:** 480-493.

103. Richetta C, Faure M. Autophagy in antiviral innate immunity. *Cell Microbiol* 2013, **15**(3)**:** 368-376.

104. Kim BW, Kwon DH, Song HK. Structure biology of selective autophagy receptors. *BMB Rep* 2016, **49**(2)**:** 73-80.

105. Judith D, Mostowy S, Bourai M, Gangneux N, Lelek M, Lucas-Hourani M, *et al.* Species-specific impact of the autophagy machinery on Chikungunya virus infection. *EMBO Rep* 2013, **14**(6)**:** 534-544.

106. Orvedahl A, MacPherson S, Sumpter R, Talloczy Z, Zou ZJ, Levine B. Autophagy Protects against Sindbis Virus Infection of the Central Nervous System. *Cell Host Microbe* 2010, **7**(2)**:** 115-127.

107. Lei X, Xiao X, Wang J. Innate Immunity Evasion by Enteroviruses: Insights into Virus-Host Interaction. *Viruses* 2016, **8**(1).

108. Gorbea C, Makar KA, Pauschinger M, Pratt G, Bersola JL, Varela J, *et al.* A role for Toll-like receptor 3 variants in host susceptibility to enteroviral myocarditis and dilated cardiomyopathy. *J Biol Chem* 2010, **285**(30)**:** 23208-23223.

109. Song J, Hu Y, Li J, Zheng H, Wang J, Guo L, *et al.* Suppression of the toll-like receptor 7-dependent type I interferon production pathway by autophagy resulting from enterovirus 71 and coxsackievirus A16 infections facilitates their replication. *Arch Virol* 2018, **163**(1)**:** 135-144.

110. Mohamud Y, Luo H. The Intertwined Life Cycles of Enterovirus and Autophagy. *Virulence* 2018.

111. Velazquez AC, Corona AK, Klein KA, Jackson WT. Poliovirus induces autophagic signaling independent of the ULK1 complex. *Autophagy* 2018, **14**(7)**:** 1201-1213.

112. Kuma A, Hatano M, Matsui M, Yamamoto A, Nakaya H, Yoshimori T, *et al.* The role of autophagy during the early neonatal starvation period. *Nature* 2004, **432**(7020)**:** 1032-1036.

113. Ran FA, Hsu PD, Wright J, Agarwala V, Scott DA, Zhang F. Genome engineering using the CRISPR-Cas9 system. *Nat Protoc* 2013, **8**(11)**:** 2281-2308.

114. Harris KG, Coyne CB. Unc93b Induces Apoptotic Cell Death and Is Cleaved by Host and Enteroviral Proteases. *Plos One* 2015, **10**(10)**:** e0141383.

115. DeSelm CJ, Miller BC, Zou W, Beatty WL, van Meel E, Takahata Y, *et al.* Autophagy proteins regulate the secretory component of osteoclastic bone resorption. *Dev Cell* 2011, **21**(5)**:** 966-974.

116. de Chaumont F, Dallongeville S, Chenouard N, Herve N, Pop S, Provoost T, *et al.* Icy: an open bioimage informatics platform for extended reproducible research. *Nat Methods* 2012, **9**(7)**:** 690-696.

117. Kuma A, Mizushima N. Chromosomal mapping of the GFP-LC3 transgene in GFP-LC3 mice. *Autophagy* 2008, **4**(1)**:** 61-62.

118. Wang C, Wong J, Fung G, Shi J, Deng H, Zhang J, *et al.* Dysferlin deficiency confers increased susceptibility to coxsackievirus-induced cardiomyopathy. *Cellular microbiology* 2015, **17**(10)**:** 1423-1430.

119. Tanida I, Minematsu-Ikeguchi N, Ueno T, Kominami E. Lysosomal turnover, but not a cellular level, of endogenous LC3 is a marker for autophagy. *Autophagy* 2005, **1**(2)**:** 84-91.

120. Klein KA, Jackson WT. Human Rhinovirus 2 Induces the Autophagic Pathway and Replicates More Efficiently in Autophagic Cells. *J Virol* 2011, **85**(18)**:** 9651-9654.

121. Moloughney JG, Monken CE, Tao HL, Zhang HY, Thomas JD, Lattime EC, *et al.* Vaccinia virus leads to ATG12-ATG3 conjugation and deficiency in autophagosome formation. *Autophagy* 2011, **7**(12)**:** 1434-1447.

122. Kimura S, Noda T, Yoshimori T. Dissection of the autophagosome maturation process by a novel reporter protein, tandem fluorescent-tagged LC3. *Autophagy* 2007, **3**(5)**:** 452-460.

123. Zachari M, Ganley IG. The mammalian ULK1 complex and autophagy initiation. *Essays Biochem* 2017, **61**(6)**:** 585-596.

124. Hara T, Takamura A, Kishi C, Iemura S, Natsume T, Guan JL, *et al.* FIP200, a ULK-interacting protein, is required for autophagosome formation in mammalian cells. *J Cell Biol* 2008, **181**(3)**:** 497-510.

125. Hosokawa N, Hara T, Kaizuka T, Kishi C, Takamura A, Miura Y, *et al.* Nutrient-dependent mTORC1 association with the ULK1-Atg13-FIP200 complex required for autophagy. *Mol Biol Cell* 2009, **20**(7)**:** 1981-1991.

126. Petherick KJ, Conway OJ, Mpamhanga C, Osborne SA, Kamal A, Saxty B, *et al.* Pharmacological inhibition of ULK1 kinase blocks mammalian target of rapamycin (mTOR)-dependent autophagy. *J Biol Chem* 2015, **290**(48)**:** 28726.

127. Funderburk SF, Wang QJ, Yue ZY. The Beclin 1-VPS34 complex - at the crossroads of autophagy and beyond. *Trends Cell Biol* 2010, **20**(6)**:** 355-362.

128. Polson HEJ, de Lartigue J, Rigden DJ, Reedijk M, Urbe S, Clague MJ, *et al.* Mammalian Atg18 (WIPI2) localizes to omegasome-anchored phagophores and positively regulates LC3 lipidation. *Autophagy* 2010, **6**(4)**:** 506-522.

129. Mari M, Griffith J, Rieter E, Krishnappa L, Klionsky DJ, Reggiori F. An Atg9-containing compartment that functions in the early steps of autophagosome biogenesis. *J Cell Biol* 2010, **190**(6)**:** 1005-1022.

130. Wong J, Zhang JC, Gao G, Esfandiarei M, Si XN, Wang YH, *et al.* Liposome-mediated transient transfection reduces cholesterol-dependent coxsackievirus infectivity. *J Virol Methods* 2006, **133**(2)**:** 211-218.

131. Judith D, Jefferies HBJ, Boeing S, Frith D, Snijders AP, Tooze SA. ATG9A shapes the forming autophagosome through Arfaptin 2 and phosphatidylinositol 4-kinase IIIbeta. *J Cell Biol* 2019, **218**(5)**:** 1634-1652.

132. Vicinanza M, Korolchuk VI, Ashkenazi A, Puri C, Menzies FM, Clarke JH, *et al.* PI(5)P regulates autophagosome biogenesis. *Mol Cell* 2015, **57**(2)**:** 219-234.

133. Altan-Bonnett N. Lipid Tales of Viral Replication and Transmission. *Trends Cell Biol* 2017, **27**(3)**:** 201-213.

134. Lee YK, Lee JA. Role of the mammalian ATG8/LC3 family in autophagy: differential and compensatory roles in the spatiotemporal regulation of autophagy. *BMB Rep* 2016, **49**(8)**:** 424-430.

135. Cheong H, Lindsten T, Wu J, Lu C, Thompson CB. Ammonia-induced autophagy is independent of ULK1/ULK2 kinases. *Proc Natl Acad Sci U S A* 2011, **108**(27)**:** 11121-11126.

136. Boyle KB, Randow F. Rubicon swaps autophagy for LAP. *Nat Cell Biol* 2015, **17**(7)**:** 843-845.

137. Martinez J, Malireddi RKS, Lu Q, Cunha LD, Pelletier S, Gingras S, *et al.* Molecular characterization of LC3-associated phagocytosis reveals distinct roles for Rubicon, NOX2 and autophagy proteins. *Nat Cell Biol* 2015, **17**(7)**:** 893-906.

138. Heckmann BL, Green DR. LC3-associated phagocytosis at a glance. *J Cell Sci* 2019, **132**(5).

139. Oh HS, Banerjee S, Aponte-Diaz D, Sharma SD, Aligo J, Lodeiro MF, *et al.* Multiple poliovirus-induced organelles suggested by comparison of spatiotemporal dynamics of membranous structures and phosphoinositides. *PLoS Pathog* 2018, **14**(4)**:** e1007036.

140. Shi J, Fung G, Piesik P, Zhang J, Luo H. Dominant-negative function of the C-terminal fragments of NBR1 and SQSTM1 generated during enteroviral infection. *Cell Death Differ* 2014, **21**(9)**:** 1432-1441.

141. Ran FA, Hsu PD, Wright J, Agarwala V, Scott DA, Zhang F. Genome engineering using the CRISPR-Cas9 system. *Nat Protoc* 2013, **8**(11)**:** 2281-2308.

142. Lazarou M, Sliter DA, Kane LA, Sarraf SA, Wang C, Burman JL, *et al.* The ubiquitin kinase PINK1 recruits autophagy receptors to induce mitophagy. *Nature* 2015, **524**(7565)**:** 309-314.

143. Orvedahl A, MacPherson S, Sumpter R, Jr., Talloczy Z, Zou Z, Levine B. Autophagy protects against Sindbis virus infection of the central nervous system. *Cell Host Microbe* 2010, **7**(2)**:** 115-127.

144. Althof N, Harkins S, Kemball CC, Flynn CT, Alirezaei M, Whitton JL. In vivo ablation of type I interferon receptor from cardiomyocytes delays coxsackieviral clearance and accelerates myocardial disease. *J Virol* 2014, **88**(9)**:** 5087-5099.

145. Burke JD, Platanias LC, Fish EN. Beta interferon regulation of glucose metabolism is PI3K/Akt dependent and important for antiviral activity against coxsackievirus B3. *J Virol* 2014, **88**(6)**:** 3485-3495.

146. Jin S, Tian S, Luo M, Xie W, Liu T, Duan T, *et al.* Tetherin suppresses type I interferon signaling by targeting MAVS for NDP52-mediated selective autophagic degradation in human cells. *Mol Cell* 2017, **68**(2)**:** 308-322 e304.

147. Seth RB, Sun L, Ea CK, Chen ZJ. Identification and characterization of MAVS, a mitochondrial antiviral signaling protein that activates NF-kappaB and IRF 3. *Cell* 2005, **122**(5)**:** 669-682.

148. Jagdeo JM, Dufour A, Klein T, Solis N, Kleifeld O, Kizhakkedathu J, *et al.* N-Terminomics TAILS identifies host cell substrates of poliovirus and coxsackievirus B3 3C proteinases that modulate virus infection. *Journal of virology* 2018.

149. Jackson WT, Giddings TH, Jr., Taylor MP, Mulinyawe S, Rabinovitch M, Kopito RR, *et al.* Subversion of cellular autophagosomal machinery by RNA viruses. *Plos Biol* 2005, **3**(5)**:** e156.

150. Staring J, von Castelmur E, Blomen VA, van den Hengel LG, Brockmann M, Baggen J, *et al.* PLA2G16 represents a switch between entry and clearance of Picornaviridae. *Nature* 2017, **541**(7637)**:** 412-+.

151. Mohamud Y, Shi, J., Qu, J., Poon, T.X., Y.C., Deng, H., Zhang, J. Luo, H. Enteroviral infection inhibits autophagic flux via disruption of the SNARE complex to enhance viral replication. *Cell Rep* 2018.

152. Cemma M, Kim PK, Brumell JH. The ubiquitin-binding adaptor proteins p62/SQSTM1 and NDP52 are recruited independently to bacteria-associated microdomains to target Salmonella to the autophagy pathway. *Autophagy* 2011, **7**(3)**:** 341-345.

153. Thurston TL, Ryzhakov G, Bloor S, von Muhlinen N, Randow F. The TBK1 adaptor and autophagy receptor NDP52 restricts the proliferation of ubiquitin-coated bacteria. *Nat Immunol* 2009, **10**(11)**:** 1215-1221.

154. von Muhlinen N, Akutsu M, Ravenhill BJ, Foeglein A, Bloor S, Rutherford TJ, *et al.* LC3C, bound selectively by a noncanonical LIR motif in NDP52, is required for antibacterial autophagy. *Mol Cell* 2012, **48**(3)**:** 329-342.

155. Leymarie O, Meyer L, Tafforeau L, Lotteau V, Costa BD, Delmas B, *et al.* Influenza virus protein PB1-F2 interacts with CALCOCO2 (NDP52) to modulate innate immune response. *J Gen Virol* 2017, **98**(6)**:** 1196-1208.

156. Petkova DS, Verlhac P, Rozieres A, Baguet J, Claviere M, Kretz-Remy C, *et al.* Distinct Contributions of Autophagy Receptors in Measles Virus Replication. *Viruses-Basel* 2017, **9**(5).

157. Petkova DS, Verlhac P, Rozieres A, Baguet J, Claviere M, Kretz-Remy C, *et al.* Distinct Contributions of Autophagy Receptors in Measles Virus Replication. *Viruses* 2017, **9**(5).

158. Feng Q, Langereis MA, Lork M, Nguyen M, Hato SV, Lanke K, *et al.* Enterovirus 2Apro targets MDA5 and MAVS in infected cells. *J Virol* 2014, **88**(6)**:** 3369-3378.

159. Mukherjee A, Morosky SA, Delorme-Axford E, Dybdahl-Sissoko N, Oberste MS, Wang T, *et al.* The coxsackievirus B 3C protease cleaves MAVS and TRIF to attenuate host type I interferon and apoptotic signaling. *Plos Pathog* 2011, **7**(3)**:** e1001311.

160. Kraft C, Peter M, Hofmann K. Selective autophagy: ubiquitin-mediated recognition and beyond. *Nat Cell Biol* 2010, **12**(9)**:** 836-841.

161. Khaminets A, Behl C, Dikic I. Ubiquitin-Dependent And Independent Signals In Selective Autophagy. *Trends in cell biology* 2016, **26**(1)**:** 6-16.

162. Kirkin V, McEwan DG, Novak I, Dikic I. A role for ubiquitin in selective autophagy. *Mol Cell* 2009, **34**(3)**:** 259-269.

163. Lippai M, Low P. The role of the selective adaptor p62 and ubiquitin-like proteins in autophagy. *Biomed Res Int* 2014, **2014:** 832704.

164. Corona AK, Saulsbery HM, Corona Velazquez AF, Jackson WT. Enteroviruses remodel autophagic trafficking through regulation of host SNARE proteins to promote virus replication and cell exit. *Cell Rep* 2018, **(In press)**.

165. Ding B, Zhang G, Yang X, Zhang S, Chen L, Yan Q, *et al.* Phosphoprotein of human parainfluenza virus type 3 blocks autophagosome-lysosome fusion to increase virus production. *Cell Host Microbe* 2014, **15**(5)**:** 564-577.

166. Kong BW, Foster LK, Foster DN. A method for the rapid isolation of virus from cultured cells. *Biotechniques* 2008, **44**(1)**:** 97-99.

167. Mizushima N. Methods for monitoring autophagy using GFP-LC3 transgenic mice. *Methods in enzymology* 2009, **452:** 13-23.

168. Talloczy Z, Jiang W, Virgin HWt, Leib DA, Scheuner D, Kaufman RJ, *et al.* Regulation of starvation- and virus-induced autophagy by the eIF2alpha kinase signaling pathway. *Proc Natl Acad Sci U S A* 2002, **99**(1)**:** 190-195.

169. Gutierrez MG, Munafo DB, Beron W, Colombo MI. Rab7 is required for the normal progression of the autophagic pathway in mammalian cells. *J Cell Sci* 2004, **117**(Pt 13)**:** 2687-2697.

170. Hubert V, Peschel A, Langer B, Groger M, Rees A, Kain R. LAMP-2 is required for incorporating syntaxin-17 into autophagosomes and for their fusion with lysosomes. *Biology open* 2016, **5**(10)**:** 1516-1529.

171. Jagdeo JM, Dufour A, Fung G, Luo H, Kleifeld O, Overall CM, *et al.* Heterogeneous Nuclear Ribonucleoprotein M Facilitates Enterovirus Infection. *J Virol* 2015, **89**(14)**:** 7064-7078.

172. McEwan DG, Dikic I. PLEKHM1: Adapting to life at the lysosome. *Autophagy* 2015, **11**(4)**:** 720-722.

173. Morelli E, Ginefra P, Mastrodonato V, Beznoussenko GV, Rusten TE, Bilder D, *et al.* Multiple functions of the SNARE protein Snap29 in autophagy, endocytic, and exocytic trafficking during epithelial formation in Drosophila. *Autophagy* 2014, **10**(12)**:** 2251-2268.

174. Shi X, Chen Z, Tang S, Wu F, Xiong S, Dong C. Coxsackievirus B3 infection induces autophagic flux, and autophagosomes are critical for efficient viral replication. *Archives of virology* 2016, **161**(8)**:** 2197-2205.

175. Guo B, Liang Q, Li L, Hu Z, Wu F, Zhang P, *et al.* O-GlcNAc-modification of SNAP-29 regulates autophagosome maturation. *Nat Cell Biol* 2014, **16**(12)**:** 1215-1226.

176. Lai JKF, Sam IC, Verlhac P, Baguet J, Eskelinen EL, Faure M, *et al.* 2BC Non-Structural Protein of Enterovirus A71 Interacts with SNARE Proteins to Trigger Autolysosome Formation. *Viruses* 2017, **9**(7).

177. Ren H, Elgner F, Jiang B, Himmelsbach K, Medvedev R, Ploen D, *et al.* The Autophagosomal SNARE Protein Syntaxin 17 Is an Essential Factor for the Hepatitis C Virus Life Cycle. *J Virol* 2016, **90**(13)**:** 5989-6000.

178. McEwan DG, Richter B, Claudi B, Wigge C, Wild P, Farhan H, *et al.* PLEKHM1 regulates Salmonella-containing vacuole biogenesis and infection. *Cell Host Microbe* 2015, **17**(1)**:** 58-71.

179. Gao G, Zhang J, Si X, Wong J, Cheung C, McManus B, *et al.* Proteasome inhibition attenuates coxsackievirus-induced myocardial damage in mice. *American journal of physiology Heart and circulatory physiology* 2008, **295**(1)**:** H401-408.

180. Zhang M, Schekman R. Cell biology. Unconventional secretion, unconventional solutions. *Science* 2013, **340**(6132)**:** 559-561.

181. Altan-Bonnet N, Chen YH. Intercellular Transmission of Viral Populations with Vesicles. *J Virol* 2015, **89**(24)**:** 12242-12244.

182. Kimura T, Jia J, Kumar S, Choi SW, Gu Y, Mudd M, *et al.* Dedicated SNAREs and specialized TRIM cargo receptors mediate secretory autophagy. *Embo J* 2017, **36**(1)**:** 42-60.

183. Lloyd RE. Nuclear proteins hijacked by mammalian cytoplasmic plus strand RNA viruses. *Virology* 2015, **479-480:** 457-474.

184. Medina DL, Di Paola S, Peluso I, Armani A, De Stefani D, Venditti R, *et al.* Lysosomal calcium signalling regulates autophagy through calcineurin and TFEB. *Nat Cell Biol* 2015, **17**(3)**:** 288-299.

185. Napolitano G, Ballabio A. TFEB at a glance. *J Cell Sci* 2016, **129**(13)**:** 2475-2481.

186. Settembre C, Di Malta C, Polito VA, Garcia Arencibia M, Vetrini F, Erdin S, *et al.* TFEB links autophagy to lysosomal biogenesis. *Science* 2011, **332**(6036)**:** 1429-1433.

187. Roczniak-Ferguson A, Petit CS, Froehlich F, Qian S, Ky J, Angarola B, *et al.* The transcription factor TFEB links mTORC1 signaling to transcriptional control of lysosome homeostasis. *Sci Signal* 2012, **5**(228)**:** ra42.

188. Sha YB, Rao L, Settembre C, Ballabio A, Eissa NT. STUB1 regulates TFEB-induced autophagy-lysosome pathway. *Embo J* 2017, **36**(17)**:** 2544-2552.

189. Zhang JB, Wang JG, Zhou ZH, Park JE, Wang LM, Wu S, *et al.* Importance of TFEB acetylation in control of its transcriptional activity and lysosomal function in response to histone deacetylase inhibitors. *Autophagy* 2018, **14**(6)**:** 1043-1059.

190. Harris KG, Coyne CB. Unc93b Induces Apoptotic Cell Death and Is Cleaved by Host and Enteroviral Proteases. *Plos One* 2015, **10**(10).

191. Mohamud Y, Qu J, Xue YC, Liu H, Deng H, Luo H. CALCOCO2/NDP52 and SQSTM1/p62 differentially regulate coxsackievirus B3 propagation. *Cell Death Differ* 2019, **26**(6)**:** 1062-1076.

192. Deng HY, Liu HT, de Silva T, Xue YC, Mohamud Y, Ng CS, *et al.* Coxsackievirus Type B3 Is a Potent Oncolytic Virus against KRAS-Mutant Lung Adenocarcinoma. *Mol Ther-Oncolytics* 2019, **14:** 266-278.

193. L.J. Reed HM. A Simple Method of Estimationg Fifty Per Cent Endpoints *American Journal of Epidemiology* 1938, **27**(3)**:** 493-497.

194. Davis BD DR, Eisen HN, Ginsberg HS, Wood WB. Nature of viruses. *Microbiology*. New York: Harper and Row; 1972. pp. 1044-1053.

195. Settembre C, Zoncu R, Medina DL, Vetrini F, Erdin S, Erdin S, *et al.* A lysosome-to-nucleus signalling mechanism senses and regulates the lysosome via mTOR and TFEB. *Embo J* 2012, **31**(5)**:** 1095-1108.

196. Cortes CJ, Miranda HC, Frankowski H, Batlevi Y, Young JE, Le A, *et al.* Polyglutamine-expanded androgen receptor interferes with TFEB to elicit autophagy defects in SBMA. *Nat Neurosci* 2014, **17**(9)**:** 1180-1189.

197. Sun D, Chen S, Cheng AC, Wang MS. Roles of the Picornaviral 3C Proteinase in the Viral Life Cycle and Host Cells. *Viruses-Basel* 2016, **8**(3).

198. Jagdeo JM, Dufour A, Klein T, Solis N, Kleifeld O, Kizhakkedathu J, *et al.* N-Terminomics TAILS Identifies Host Cell Substrates of Poliovirus and Coxsackievirus B3 3C Proteinases That Modulate Virus Infection. *J Virol* 2018, **92**(8).

199. Saeed M, Kapell S, Hertz NT, Wu XF, Bell K, Ashbrook AW, *et al.* Defining the proteolytic landscape during enterovirus infection. *Plos Pathogens* 2020, **16**(9).

200. Blom N, Hansen J, Blaas D, Brunak S. Cleavage site analysis in picornaviral polyproteins: Discovering cellular targets by neural networks. *Protein Sci* 1996, **5**(11)**:** 2203-2216.

201. Bampton ETW, Goemans CG, Niranjan D, Mizushima N, Tolkovsky AM. The dynamics of autophagy visualized in live cells - From autophagosome formation to fusion with endo/lysosomes. *Autophagy* 2005, **1**(1)**:** 23-36.

202. Kliosnky D. Guidelines for the Use and Interpretation of Assays for Monitoring Autophagy (3rd edition) (vol 12, pg 1, 2015). *Autophagy* 2016, **12**(2)**:** 443-443.

203. Fisher DE, Carr CS, Parent LA, Sharp PA. Tfeb Has DNA-Binding and Oligomerization Properties of a Unique Helix Loop Helix Leucine-Zipper Family. *Gene Dev* 1991, **5**(12A)**:** 2342-2352.

204. Slade L, Pulinilkunnil T. The MiTF/TFE Family of Transcription Factors: Master Regulators of Organelle Signaling, Metabolism, and Stress Adaptation. *Mol Cancer Res* 2017, **15**(12)**:** 1637-1643.

205. Horne RW, Nagington J. Electron Microscope Studies of the Development and Structure of Poliomyelitis Virus. *J Mol Biol* 1959, **1**(4-5)**:** 333-&.

206. Corona AK, Saulsbery HM, Velazquez AFC, Jackson WT. Enteroviruses Remodel Autophagic Trafficking through Regulation of Host SNARE Proteins to Promote Virus Replication and Cell Exit. *Cell Reports* 2018, **22**(12)**:** 3304-3314.

207. Mohamud Y, Shi J, Qu J, Poon T, Xue YC, Deng H, *et al.* Enteroviral Infection Inhibits Autophagic Flux via Disruption of the SNARE Complex to Enhance Viral Replication. *Cell Rep* 2018, **22**(12)**:** 3292-3303.

208. Reddy A, Caler EV, Andrews NW. Plasma membrane repair is mediated by Ca2+-regulated exocytosis of lysosomes. *Cell* 2001, **106**(2)**:** 157-169.

209. Settembre C, Fraldi A, Medina DL, Ballabio A. Signals from the lysosome: a control centre for cellular clearance and energy metabolism. *Nat Rev Mol Cell Biol* 2013, **14**(5)**:** 283-296.

210. Gemayel R, Chavali S, Pougach K, Legendre M, Zhu B, Boeynaems S, *et al.* Variable Glutamine-Rich Repeats Modulate Transcription Factor Activity. *Mol Cell* 2015, **59**(4)**:** 615-627.

211. Gerber HP, Seipel K, Georgiev O, Hofferer M, Hug M, Rusconi S, *et al.* Transcriptional Activation Modulated by Homopolymeric Glutamine and Proline Stretches. *Science* 1994, **263**(5148)**:** 808-811.

212. Sancak Y, Bar-Peled L, Zoncu R, Markhard AL, Nada S, Sabatini DM. Ragulator-Rag complex targets mTORC1 to the lysosomal surface and is necessary for its activation by amino acids. *Cell* 2010, **141**(2)**:** 290-303.

213. Alirezaei M, Flynn CT, Garcia SD, Kimura T, Whitton JL. A food-responsive switch modulates TFEB and autophagy, and determines susceptibility to coxsackievirus infection and pancreatitis. *Autophagy* 2020**:** 1-18.

214. Giansanti P, Strating J, Defourny KAY, Cesonyte I, Bottino AMS, Post H, *et al.* Dynamic remodelling of the human host cell proteome and phosphoproteome upon enterovirus infection. *Nat Commun* 2020, **11**(1)**:** 4332.

215. Wolff G, Melia CE, Snijder EJ, Barcena M. Double-Membrane Vesicles as Platforms for Viral Replication. *Trends Microbiol* 2020, **28**(12)**:** 1022-1033.

216. Mutsafi Y, Altan-Bonnet N. Enterovirus Transmission by Secretory Autophagy. *Viruses-Basel* 2018, **10**(3).

217. Feng ZD, Hensley L, McKnight KL, Hu FY, Madden V, Ping LF, *et al.* A pathogenic picornavirus acquires an envelope by hijacking cellular membranes. *Nature* 2013, **496**(7445)**:** 367-+.

218. Celeste DB, Miller MS. Reviewing the evidence for viruses as environmental risk factors for ALS: A new perspective. *Cytokine* 2018, **108:** 173-178.

219. Xue YC, Ruller CM, Fung G, Mohamud Y, Deng HY, Liu HT, *et al.* Enteroviral Infection Leads to Transactive Response DNA-Binding Protein 43 Pathology in Vivo. *Am J Pathol* 2018, **188**(12)**:** 2853-2862.

220. Masaki K, Sonobe Y, Ghadge G, Pytel P, Roos RP. TDP-43 proteinopathy in Theiler's murine encephalomyelitis virus infection. *Plos Pathogens* 2019, **15**(2).

221. Fung G, Shi J, Deng H, Hou J, Wang C, Hong A, *et al.* Cytoplasmic translocation, aggregation, and cleavage of TDP-43 by enteroviral proteases modulate viral pathogenesis. *Cell Death Differ* 2015, **22**(12)**:** 2087-2097.

222. Nixon RA. The role of autophagy in neurodegenerative disease. *Nat Med* 2013, **19**(8)**:** 983-997.

223. Kleifeld O, Doucet A, auf dem Keller U, Prudova A, Schilling O, Kainthan RK, *et al.* Isotopic labeling of terminal amines in complex samples identifies protein N-termini and protease cleavage products. *Nat Biotechnol* 2010, **28**(3)**:** 281-288.

224. Saeed M, Kapell S, Hertz NT, Wu X, Bell K, Ashbrook AW, *et al.* Defining the proteolytic landscape during enterovirus infection. *Plos Pathogens* 2020, **16**(9)**:** e1008927.

225. Mohamud Y, Xue YC, Liu H, Ng CS, Bahreyni A, Jan E, *et al.* The papain-like protease of coronaviruses cleaves ULK1 to disrupt host autophagy. *Biochem Biophys Res Commun* 2021, **540:** 75-82.

226. Rudnick ND, Griffey CJ, Guarnieri P, Gerbino V, Wang X, Piersaint JA, *et al.* Distinct roles for motor neuron autophagy early and late in the SOD1(G93A) mouse model of ALS. *Proc Natl Acad Sci U S A* 2017, **114**(39)**:** E8294-E8303.